

AD-A171 084

NUMERICAL SIMULATION OF CURRENT ARTILLERY CHARGES USING 1/3

THE TDNOVA CODE(U) GOUGH (PAUL) ASSOCIATES INC

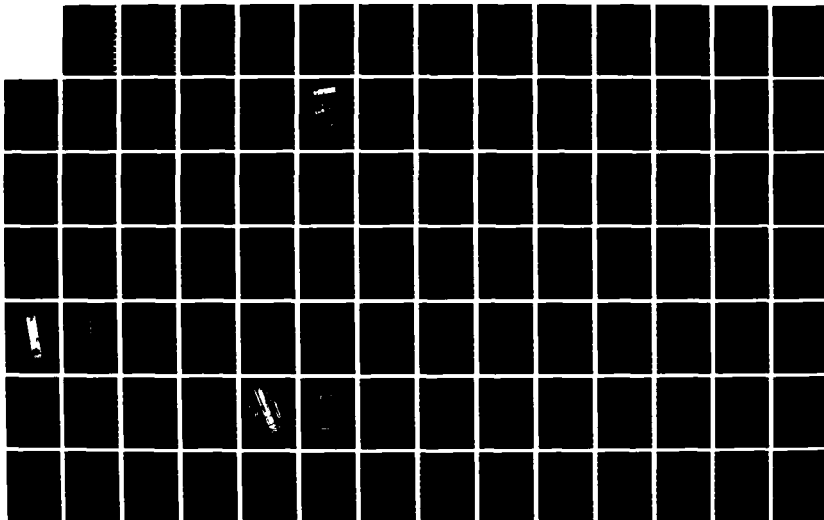
PORTSMOUTH NH P S GOUGH JUN 86 BRL-CR-555

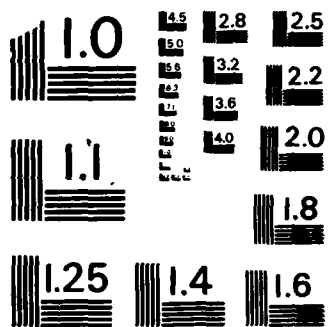
UNCLASSIFIED

DAAK11-83-C-0051

F/G 19/4

NL





MICROCOPY RESOLUTION TEST CHART
NATIONAL BUREAU OF STANDARDS-1963-A

AD-A171 084

AD

12



CONTRACT REPORT BRL-CR-555

NUMERICAL SIMULATION OF CURRENT
ARTILLERY CHARGES USING
THE TDNOVA CODE

Paul Gough Associates, Inc.
P.O. Box 1614
Portsmouth, NH 03801

June 1986

APPROVED FOR PUBLIC RELEASE; DISTRIBUTION UNLIMITED.

US ARMY BALLISTIC RESEARCH LABORATORY
ABERDEEN PROVING GROUND, MARYLAND



86 8 21 06 7

DTIC FILE COPY

UNCLASSIFIED

SECURITY CLASSIFICATION OF THIS PAGE (When Data Entered)

REPORT DOCUMENTATION PAGE		READ INSTRUCTIONS BEFORE COMPLETING FORM
1. REPORT NUMBER Contract Report BRL-CR-555	2. GOVT ACCESSION NO. AD-A171084	3. RECIPIENT'S CATALOG NUMBER
4. TITLE (and Subtitle) Numerical Simulation of Current Artillery Charges Using the TDNOVA Code		5. TYPE OF REPORT & PERIOD COVERED Final Report July 1983 - July 1985
7. AUTHOR(s) Paul S. Gough		6. PERFORMING ORG. REPORT NUMBER
9. PERFORMING ORGANIZATION NAME AND ADDRESS Paul Gough Assoc., Inc. P.O. Box 1614 Portsmouth, NH 03801		8. CONTRACT OR GRANT NUMBER(s) DAAK11-83-C-0051
11. CONTROLLING OFFICE NAME AND ADDRESS US Army Ballistic Research Laboratory ATTN: SLCBR-DD-T Aberdeen Proving Ground, MD 21005-5066		10. PROGRAM ELEMENT, PROJECT, TASK AREA & WORK UNIT NUMBERS 1L161102AH43
14. MONITORING AGENCY NAME & ADDRESS (if different from Controlling Office) U.S. Army Ballistic Research Laboratory ATTN: SLCBR-IB Aberdeen Proving Ground, MD 21005-5066		12. REPORT DATE June 1986
		13. NUMBER OF PAGES 253
		15. SECURITY CLASS. (of this report) Unclassified
		15a. DECLASSIFICATION DOWNGRADING SCHEDULE
16. DISTRIBUTION STATEMENT (of this Report) Approved for public release; Distribution Unlimited.		
17. DISTRIBUTION STATEMENT (of the abstract entered in Block 20, if different from Report)		
18. SUPPLEMENTARY NOTES		
19. KEY WORDS (Continue on reverse side if necessary and identify by block number) Interior Ballistics Computer Code Numerical Simulations		
20. ABSTRACT (Continue on reverse side if necessary and identify by block number) The TDNOVA Code provides a digital simulation of the interior ballistics of gun propelling charges. The code is based on a numerical solution of the two-dimensional balance equations for the macroscopic or average properties of a heterogeneous two-phase flow with embedded discontinuities of porosity. Multi-increment charges may be simulated and individual increments may consist of granular or stick propellant. When perforated sticks are considered, the code distinguishes between the processes in the interstices and the		

DD FORM 1 JAN 73 1473

EDITION OF 1 NOV 65 IS OBSOLETE

UNCLASSIFIED

SECURITY CLASSIFICATION OF THIS PAGE (When Data Entered)

UNCLASSIFIED

SECURITY CLASSIFICATION OF THIS PAGE(When Data Entered)

perforations. the containers of the individual increments are modeled as attributes of the boundaries of the increments. The container attributes include thickness, resistance to normal penetration by the gas, and reactivity on both outer and inner surfaces. Highly localized ignition elements such as basepads are treated as surface attributes - sources of hot gas - within the macroscopic model framework. Centercore igniters are modeled as quasi-one-dimensional two-phase flows.

The code has been developed and tested at various stages in earlier work. The principal objective of the present effort has been to make such revisions and corrections as proved necessary in an attempt to model three artillery charges of current interest. All such revisions are documented here. We demonstrate the applicability of the revised code to the M203, M203E2, and XM216 Propelling Charges for the 155-mm Howitzer. The M203 Charge is a single-increment granular charge with a centercore igniter and is initially contained in a cloth bag. The M203E2 Charge is a single-increment slotted stick charge with a highly structured base igniter and is enclosed in a rigid nitrocellulose container. The XM216 Charge consists of three increments of stick propellant each enclosed in a separate nitrocellulose container and has a base igniter similar to that of the M203E2 Charge.

We present the results of studies of the dependence of the solutions on numerical parameters for both the M203 and M203E2 Charges, treating the base igniter for the M203E2 Charge as a surface term. We then examine the influence of the permeability of the containers on the interior ballistics of the M203E2 and XM216 Charges, treating the base igniter as a separate charge increment. Solutions are also presented to demonstrate other features of the code including finite rate gas-phase chemistry, heat transfer to the tube and programmed fracture of stick charges.

In addition, we describe the development of an implicit solver for the regions of ullage which it is intended to use in future studies to provide fully two-dimensional solutions for the ullage regions as well as the propelling charges. Since the algorithm includes the effects of viscosity and heat conduction it is also hoped that it will permit insights into the influence of charge packaging on tube erosion. Operability of the algorithm is demonstrated by reference to a simplified ballistic problem for which an analytical solution exists.

UNCLASSIFIED

SECURITY CLASSIFICATION OF THIS PAGE(When Data Entered)

Acknowledgments

This work was performed under the technical cognizance of A. Horst, Jr., of the Ballistic Research Laboratory at Aberdeen Proving Ground, Maryland. The author acknowledges with gratitude the patient encouragement extended to him by Mr. Horst during the performance of what proved to be a rather demanding exercise. He also wishes to record the extensive and generous assistance of Dr. G. Keller and Mr. F. Robbins of Interior Ballistics Division at BRL who made it possible for him to gain the necessary access to the CYBER 7600.

Accession For		
NTIS GRA&I	<input checked="" type="checkbox"/>	
DTIC TAB	<input type="checkbox"/>	
Unannounced	<input type="checkbox"/>	
Justification		
By		
Distribution/		
Availability Codes		
Dist	Avail and/or	
	Special	
A-1		



TABLE OF CONTENTS

	<u>Page</u>
Acknowledgments	iii
List of Illustrations	ix
List of Tables	xiii
1.0 INTRODUCTION	1
1.1 Background Information	2
1.2 Scope of Investigation	5
2.0 DESCRIPTION OF THE TINOVA CODE	8
2.1 Overview of Code	8
2.2 Charge Representation by TINOVA	10
2.2.1 Main Charge Increment	11
2.2.1.1 Rheology	12
2.2.1.2 Interphase Drag and Heat Transfer	13
2.2.1.3 Analysis of Slotted Propellant	14
2.2.1.4 Other Constitutive Laws	15
2.2.2 Igniter Increment	15
2.2.3 The Case	16
2.2.3.1 Chemical Properties	16
2.2.3.2 Mechanical Properties	17
2.3 Summary of Code Revisions	18
2.3.1 General Topics	19
2.3.2 Transverse Boundary Instability	22
2.3.3 Global Mass Balancing	26
2.3.4 Editing of Boundary Positions	29
2.3.5 Analysis of Boundary Values	31
2.3.5.1 Governing Equations	32
2.3.5.2 Rupture of the Case	32
2.3.5.3 Boundary Value Algorithm	33
3.0 THE M203 PROPELLING CHARGE	36
3.1 Nominal Data Base	36
3.2 Nominal Solution	38
3.3 Influence of Computational Parameters	39

TABLE OF CONTENTS continued		<u>Page</u>
4.0	THE M203E2 PROPELLING CHARGE — SINGLE-INCREMENT REPRESENTATION	57
4.1	Nominal Data Base	57
4.2	Nominal Solution	58
4.3	Influence of Computational Parameters	59
5.0	THE M203E2 PROPELLING CHARGE — TWO-INCREMENT REPRESENTATION	76
5.1	Nominal Data Base and Solution	76
5.2	Effects of Container Permeability	79
6.0	THE XM216 PROPELLING CHARGE	96
6.1	Nominal Data Base and Solution	96
6.2	Effects of Container Properties	98
7.0	MISCELLANEOUS APPLICATIONS OF TENOVA	121
7.1	Programmed Fracture Stick Charge	121
7.2	Finite Rate Chemistry	122
7.3	Heat Transfer to the Tube	124
8.0	IMPLICIT SOLVER FOR REGIONS OF ULLAGE	135
8.1	Background Information	135
8.2	Governing Equations	140
8.3	Method of Solution	144
8.4	A Sample Calculation	148
9.0	CONCLUSIONS AND RECOMMENDATIONS	151
	REFERENCES	153
APPENDIX A	SOLUTION OF THE GAS-PHASE MECHANICAL BOUNDARY CONDITIONS	159
A.1	The Boundary Conditions	161
A.2	Exterior State Open	163
A.2.1	Subsonic Fluxes	163
A.2.2	Sonic Fluxes	168
A.3	Exterior State Closed	169
A.3.1	Subsonic Fluxes	169
A.3.2	Sonic Fluxes	170
A.4	Treatment of Slotted Sticks	170

TABLE OF CONTENTS continued		<u>Page</u>
APPENDIX B	INPUT DATA FOR NOMINAL SIMULATION OF M203 CHARGE	173
APPENDIX C	INPUT DATA FOR NOMINAL SIMULATION OF M203E2 CHARGE (SINGLE-INCREMENT REPRESENTATION)	185
APPENDIX D	INPUT DATA FOR NOMINAL SIMULATION OF M203E2 CHARGE (TWO-INCREMENT REPRESENTATION)	199
APPENDIX E	INPUT DATA FOR NOMINAL SIMULATION OF XM216 CHARGE	215
NOMENCLATURE		235
DISTRIBUTION LIST		237

LIST OF ILLUSTRATIONS

<u>Figure</u>	<u>Title</u>	<u>Page</u>
1.1	Propelling Charges for the 155-mm Howitzer	6
2.1	Charge Representation by TDNOVA	9
3.1	The M203 Propelling Charge	43
3.2	Representation of M203 Charge by TDNOVA	44
3.3	Pressure Distributions for M203 Charge Obtained with Nominal Mesh (30 X 7 @ 0.01)	45
3.4	Solid-Phase Velocity Fields for M203 Charge Obtained with Nominal Mesh (30 X 7 @ 0.01)	47
3.5	Gas-Phase Velocity Fields for M203 Charge Obtained with Nominal Mesh (30 X 7 @ 0.01)	48
3.6	Influence of Number of Axial Mesh Points on Pressure Distribution for M203 Charge at 2.0 msec	49
3.7	Influence of Number of Axial Mesh Points on Pressure Distribution for M203 Charge at 3.5 msec	50
3.8	Influence of Number of Axial Mesh Points on Pressure Distribution for M203 Charge at 4.0 msec	51
3.9	Influence of Number of Radial Mesh Points on Pressure Distribution for M203 Charge at 2.0 msec	52
3.10	Influence of Number of Radial Mesh Points on Pressure Distribution for M203 Charge at 3.5 msec	53
3.11	Influence of Number of Radial Mesh Points on Pressure Distribution for M203 Charge at 4.0 msec	54
3.12	Influence of Mesh on Flamespreading Through M203 Charge (Contours correspond to intervals of 0.32 msec)	55
3.13	Influence of Mesh on Pressure Difference History in M203 Charge	56

List of Illustrations continued

	<u>Page</u>
4.1 The M203E2 Propelling Charge	61
4.2 Single-Increment Representation of M203E2 Charge by TINOVA	62
4.3 Pressure Distributions for M203E2 Charge Obtained with Nominal Mesh (30 X 7 @ 0.01)	63
4.4 Influence of Number of Axial Mesh Points on Pressure Distribution for M203E2 Charge at 0.5 msec	65
4.5 Influence of Number of Axial Mesh Points on Pressure Distribution for M203E2 Charge at 1.0 msec	66
4.6 Influence of Number of Axial Mesh Points on Pressure Distribution for M203E2 Charge at 1.5 msec	67
4.7 Influence of Number of Radial Mesh Points on Pressure Distribution for M203E2 Charge at 0.5 msec	68
4.8 Influence of Number of Radial Mesh Points on Pressure Distribution for M203E2 Charge at 1.0 msec	69
4.9 Influence of Number of Radial Mesh Points on Pressure Distribution for M203E2 Charge at 1.5 msec	70
4.10 Solid-Phase Velocity Field Just Prior to Transformation to a Quasi-Two-Dimensional Representation for M203E2 Charge	71
4.11 Influence of Mesh on External (Interstitial) Flamespreading Through M203E2 Charge (Contours correspond to intervals of 0.17 msec.)	73
4.12 Influence of Mesh on Internal (Perforation) Flamespreading Through M203E2 Charge (Contours correspond to intervals of 0.17 msec.)	74
4.13 Influence of Mesh on Pressure Difference History in M203E2 Charge (Pressure at 0.01 cm minus pressure at 87.37 cm on centerline)	75
5.1 Two-Increment Representation of M203E2 Charge by TINOVA	82
5.2 Pressure Distributions for the M203E2 Case 1 (Nominal) Data Base	83
5.3 Solid-Phase Velocity Fields for the M203E2 Case 1 (Nominal) Data Base	85

List of Illustrations continued

	Page
5.4 Pressure Distributions for the M203E2 Case 2 Data Base	86
5.5 Pressure Distributions for the M203E2 Case 3 Data Base	87
5.6 Pressure Distributions for the M203E2 Case 4 Data Base	88
5.7 Pressure Distributions for the M203E2 Case 5 Data Base	89
5.8 Pressure Distributions for the M203E2 Case 6 Data Base	90
5.9 Solid-Phase Velocity Fields for the M203E2 Case 6 Data Base	91
5.10 Influence of Case Permeability on External (Interstitial) Flamespreading Through M203E2 Charge	92
5.11 Influence of Case Permeability on Internal (Perforation) Flamespreading Through M203E2 Charge	93
5.12 Influence of Case Permeability on Pressure Difference History in M203E2 Charge (Pressure at 0.01 cm minus pressure at 87.37 cm on centerline)	94
6.1 The XM216 Propelling Charge	103
6.2 Representation of XM216 Charge by TDNOVA	104
6.3 Pressure Distributions for the XM216 Case 1 (Nominal) Data Base	105
6.4 Solid-Phase Velocity Fields for the XM216 Case 1 (Nominal) Data Base	108
6.5 Pressure Distributions for the XM216 Case 4 Data Base	109
6.6 Pressure Distributions for the XM216 Case 5 Data Base	110
6.7 Solid-Phase Velocity Fields for the XM216 Case 5 Data Base	111
6.8 Pressure Distributions for the XM216 Case 6 Data Base	112
6.9 Solid Phase Velocity Fields for the XM216 Case 6 Data Base	114

List of Illustrations continued

	<u>Page</u>
6.10 Pressure Distributions for the XM216 Case 7 Data Base	115
6.11 Solid-Phase Velocity Fields for the XM216 Case 7 Data Base	116
6.12 Pressure Distributions for the XM216 Case 8 Data Base	117
6.13 Influence of Case Permeability on Pressure Difference History in XM216 Charge (Pressure at 0.01 cm minus pressure at 87.37 cm on centerline)	118
7.1 Pressure Distributions in Programmed Fracture Stick Charge	126
7.2 Flamespreading, Pressure and Projectile Velocity Histories and Pressure Difference History in Programmed Fracture Stick Charge	127
7.3 Pressure Distributions in the M203 Charge with Finite Rate Gas-Phase Reaction	128
7.4 Distributions of Pyrolysis Product Mass Fraction in the M203 Charge with Finite Rate Gas-Phase Reaction	129
7.5 Flamespreading, Pressure and Projectile Velocity Histories and Pressure Difference History in M203 Charge with Finite Rate Gas-Phase Reaction	130
7.6 Tube Surface Temperature Distributions for M203 Charge and Flat Plate Correlation	131
7.7 Tube Surface Temperature Distributions for M203 Charge and Pipe Flow Correlation	132
7.8 Tube Surface Temperature Distributions for M203E2 Charge and Flat Plate Correlation	133
7.9 Tube Surface Temperature Distributions for M203E2 Charge and Pipe Flow Correlation	134

LIST OF TABLES

<u>Table</u>	<u>Page</u>
3.1 Effect of Computational Parameters on Simulation of M203 Propelling Charge	40
3.2 Effect of Pressure Tolerance Factor on Simulation of Propelling Charge with Perfect Mass Balancing	41
4.1 Effect of Computational Parameters on Simulation of M203E2 Propelling Charge	60
5.1 Values of Container Flow Resistance Coefficients for Simulations of M203E2 Propelling Charge (Two-Increment Representation)	79
5.2 Effect of Container Permeability on Simulations of M203E2 Propelling Charge (Two-Increment Representation)	80
6.1 Values of Container Bond Strength and Flow Resistance for Simulations of XM216 Propelling Charge	99
6.2 Effect of Container Bond Strength and Permeability on Simulations of XM216 Propelling Charge	100
7.1 Kinetic Data for Finite Rate Chemistry Problem	123
7.2 Thermal Properties of Tube Wall	124
8.1 Definition of Lagrange Ballistic Problem	149
8.2 Conditions at Muzzle Exit According to Analytical Solution, TDNOVA and TDLADIS	149
8.3 Comparison of TDNOVA and TDLADIS Predictions of Breech and Base Pressure for Lagrange Ballistic Problem	150

1.0 INTRODUCTION

The TDNOVA code provides a simulation of interior ballistic phenomena in guns. Interest is focussed on flamespreading through the charge and the development of pressure waves within the gun chamber. The code is designed to address the manner in which these phenomena are influenced by such details of design as the distribution of the igniter elements, the distribution of ullage, and the permeability, reactivity and strength of the containers used to package each of the charge increments. The model is based on a numerical solution of the governing equations for the macroscopic equations of two-phase heterogeneous flow with embedded discontinuities. The code is intended to be broadly applicable to gun propelling charges in general; however, medium caliber artillery charges have been of special interest.

The principal objective of this report is to demonstrate the application of TDNOVA to a number of artillery charges of current interest. We discuss the representation of each of the charges by TDNOVA, the degree to which the simulation is affected by the numerical solution technique, and the sensitivity of the solutions to certain aspects of the packaging of the charge.

A second objective of this report is to document the code revisions which were incorporated during the course of the present contract. We do not provide herein a complete description of TDNOVA. The mathematical basis and the method of solution have been described previously in detail. However, for the sake of completeness we do describe the physical content of the model and the general manner of representation of each of the charge components.

A third objective is to describe work which has been performed in connection with algorithm developments which are intended to support future extensions to the scope of applicability of the code.

The TDNOVA code is described, in its present form, in Chapter 2.0 which also documents all the revisions incorporated in the present contract. The discussion of Chapter 2.0 is supported by Appendix A. In Chapters 3.0 through 7.0 we present numerical solutions for a variety of problems. In Chapter 8.0 we discuss the topic of ongoing algorithm development and provide a numerical solution for an idealized interior ballistic problem.

The balance of this introduction consists of two sections. In Section 1.1 we provide some discussion of background information. In Section 1.2 we outline the scope of the present investigation.

1.1 Background Information

The literature which documents the relationship between the occurrence of pressure oscillations in the gun chamber and ignition anomalies of a potentially dangerous nature has been reviewed by Budka and Knapton¹ and, more recently, by May and Horst.² The influence of annular ullage, or spaces between the charge sidewalls and the tube, had been observed at an early date by Kent.³ The influence of axial ullage, or spaces between the ends of the charge and the breechface or projectile base, and the influence of the location of the ignition stimulus were studied by Heddon and Nance.⁴ The importance of the distribution of ullage and the location of the igniter stimulus in respect to the development of pressure oscillations is connected with the phenomenon of flow resistance. Flow resistance, or impermeability of the propelling charge, prevents locally produced igniter or combustion gases from penetrating the bed and therefore promotes the development of pressure gradients during flamespreading. Flow impediments can also arise from the presence of the bag or other container material used to package the charge initially. The properties of the container are surprisingly significant in respect to the occurrence of ignition anomalies. May and Horst describe an incident in which the substitution of an alternative cloth for a 155-mm charge resulted in a breechblow.²

The NOVA code, most recently described in Reference 5, was one of several one-dimensional, two-phase interior ballistic codes developed for the purpose of studying ignition-induced pressure waves. It was shown to predict well the influence of axial ullage and the location of the ignition

- 1 Budka, A.J. and Knapton, J.D.
"Pressure Wave Generation in Gun Systems -- A Survey"
Ballistic Research Laboratory Memorandum Report 2567
(AD B008893L) 1975
- 2 May, I.W. and Horst, A.W.
"Charge Design and Pressure Waves in Guns"
Progress in Astronautics and Aeronautics, Vol. 68,
Interior Ballistics of Guns, edited by H. Krier and M. Summerfield 1979
- 3 Kent, R.H.
"Study of Ignition of 155-mm Gun"
Ballistic Research Laboratory Report 22 (AD 494703) 1935
- 4 Heddon, S.E. and Nance, G.A.
"An Experimental Study of Pressure Waves in Gun Chambers"
Naval Proving Ground Report 1534 1957
- 5 Gough, P.S.
"The NOVA Code: A User's Manual"
Naval Ordnance Station Contract Report IHCR 80-8 1980

stimulus.^{6,7} Further analytical studies,^{8,9} based on a quasi-two-dimensional model to reflect the presence of annular ullage and certain of the bag properties, exhibited a theoretical sensitivity of pressure waves to annular ullage and container material similar to that which had been observed experimentally.

It was therefore determined that a two-dimensional, two-phase flow code should be developed in order to model systematically the combined influence of ignition scheme, ullage distribution and container properties on the path of flamespreading and the development of pressure waves in gun propelling charges. In Reference 10 the general strategy for the development of TINOVA was described and two-dimensional convective flamespreading solutions were obtained. In Reference 11 the code was extended to treat the ullage and certain of the container properties, and the complete interior ballistic

-
- 6 Horst, A.W., Smith, T.C. and Mitchell, S.E.
 "Key Design Parameters in Controlling Gun Environment Pressure Wave Phenomena — Theory versus Experiment"
 Proc. 13th JANNAF Combustion Meeting 1976
 - 7 Horst, A.W. and Gough, P.S.
 "Influence of Propellant Packaging on Performance of Navy Case Gun Ammunition"
 J. Ballistics Vol. 1, p. 229 1977
 - 8 Gough, P.S.
 "Theoretical Study of Two-Phase Flow Associated with Granular Bag Charges"
 Ballistic Research Laboratory Contract Report ARBRL-CR-00381
 (AD A062144) 1978
 - 9 Horst, A.W. and Gough, P.S.
 "Modeling Ignition and Flamespread Phenomena in Bagged Artillery Charges"
 Ballistic Research Laboratory Technical Report ARBRL-TR-02263
 (AD 091790) 1980
 - 10 Gough, P.S.
 "Two-Dimensional Convective Flamespreading in Packed Beds of Granular Propellant"
 Ballistic Research Laboratory Contract Report ARBRL-CR-00404
 (AD A075326) 1979
 - 11 Gough, P.S.
 "A Two-Dimensional Model of the Interior Ballistics of Bagged Artillery Charges"
 Ballistic Research Laboratory Contract Report ARBRL-CR-00452
 (AD A100751) 1981

cycle of an M203 granular propelling charge was simulated. In Reference 12 the code was extended to treat multi-increment charges. Most recently, in Reference 13, we described the extension of the code to treat stick as well as granular charges.

Evaluations and demonstrations of the TDNOVA code have been presented at various stages of its development. The accuracy of the code and consistency of its predictions with those of the NOVA code were evaluated by Horst.¹⁴ Accuracy was also evaluated by Robbins using an idealized problem for which an analytical solution was available.¹⁵ Studies were made of the influence, on flamespreading through a 155-mm granular charge, of various details of the packaging of the propellant.¹⁶ The application of TDNOVA to a 155-mm stick charge was discussed by Horst, Robbins and Gough.¹⁷ In this study, based on the code version described in Reference 13, attempts were made to model the base igniter as a separate two-phase increment. This representation of the base igniter may be contrasted with the previous approach in which the igniter was treated as a surface source term. The attempt to treat it as a separate increment was not successful and it became

- 12 Gough, P.S.
"Two-Dimensional, Two-Phase Modeling of Multi-Increment Bagged Artillery Charges"
Ballistic Research Laboratory Contract Report ARBRL-CR-00503
(AD A125482) 1982
- 13 Gough, P.S.
"Modeling of Rigidized Gun Propelling Charges"
Ballistic Research Laboratory Contract Report ARBRL-CR-00518
(AD A135860) 1983
- 14 Horst, A.W.
"Baseline Evaluation of the TDNOVA Code"
Ballistic Research Laboratory Memorandum Report ARBRL-MR-03198
(AD A120718) 1982
- 15 Robbins, F.W.
"Comparison of TDNOVA Results with an Analytic Solution"
Ballistic Research Laboratory Memorandum Report ARBRL-MR-03299
(AD A132969) 1983
- 16 Horst, A.W., Robbins, F.W. and Gough, P.S.
"A Two-Dimensional, Two-Phase Flow Simulation of Ignition, Flamespread, and Pressure-Wave Phenomena in the 155-mm Howitzer"
Ballistic Research Laboratory Technical Report ARBRL-TR-02414
(AD A119148) 1982
- 17 Horst, A.W., Robbins, F.W. and Gough, P.S.
"Multidimensional, Multiphase Flow Analysis of Flamespreading in a Stick Propelling Charge"
Ballistic Research Laboratory Memorandum Report ARBRL-MR-03372
(AD A145731) 1984

of interest to explore the extent to which the code could be made sufficiently rugged as to withstand the numerical strain imposed by simulations of this type.

In the present contract we have pursued the objective of increasing the ruggedness of the algorithm to treat not only the example considered in Reference 17 but also another more complex charge consisting of several increments. Both these charges are discussed briefly in the next section.

A second objective of the present contract has been to lay the groundwork for future extensions of TDNOVA. To date the two-dimensional solutions have been obtained by representing the main charge as two-dimensional and the ullage as quasi-one-dimensional. For high zone granular charges in which the ullage occupies only a small portion of the combustion chamber, this modeling approach is reasonable. For low zone charges in which the ullage may involve one half of the available volume, a fully two-dimensional treatment of the ullage is desirable. The same may be true in the context of stick charges of any zone since the ullage occupies an increasing proportion of the available volume as the projectile moves down the tube.

Our approach to each of these contract objectives and the scope of the present effort are outlined in the next section.

1.2 Scope of Investigation

The demonstration of the present capability of TDNOVA is conducted with reference to three propelling charges, illustrated in Figure 1.1. The first is a granular charge, the M203 propelling charge for the 155-mm Howitzer. The second and third charges are also designed for the 155-mm Howitzer, but they consist of slotted stick propellant. The M203E2 contains a single increment of stick propellant while the XM216 charge contains three separately packaged increments.

The M203 granular charge is essentially the same as that which was previously simulated by Horst¹⁴ using an earlier version of the code. We include it in the present study in order to assess the degree to which the code predictions and accuracy have been affected by the extensions necessary to treat stick charges. In Chapter 3.0 we present the results of studies of the numerical convergence of TDNOVA by reference to the M203 charge.

The M203E2 stick charge was the subject of Reference 17. As we noted in the previous section, it was found possible to obtain solutions at that time only if the base igniter was represented as a surface source term. Because the igniter has so much structure it is desirable to treat it as a separate increment and much of the effort in the present enquiry has been devoted to achieving that goal. In chapter 4.0 we use the surface representation of the igniter to generate solutions for the purpose of assessing the numerical convergence of TDNOVA when applied to stick charges. Then, in Chapter 5.0, we present solutions with the igniter represented as a separate increment. We will refer to the single-increment and two-increment representations of the M203E2 charge. The solutions in Chapter 5.0 are

generated for a number of data bases in which the initial permeability of the case is varied. Some aspects of this topic have already been reported.^{18, 19}

Solutions for the XM216 charge are presented in Chapter 6.0. We examine the influence of variations in the permeability of the containers and of the strength of the bonds between the increments. In Chapter 7.0 we present some results pertaining to three other problems of interest. We illustrate the use of TDNOVA to analyze the programmed fracture of a stick charge, using the single-increment M203E2 data base as a starting point. The M203 data base is used to study the effect of gas-phase chemical reactions which cause the full energy of the propellant to be released at a finite rate following a preliminary exothermic decomposition at the surface of the solid-phase. Results pertaining to this topic have also been reported elsewhere.²⁰ Finally, we use the M203 and M203E2 charges as vehicles to examine heat transfer to the tube wall. A comparison of the heating rates due to granular and stick charges was previously reported by Horst²¹ based on solutions generated with the NOVA code.

Progress towards a fully two-dimensional representation of the ullage is described in Chapter 8.0. An implicit algorithm is developed to solve the balance equations for the gas-phase. An implicit solver was selected even though the present gas-phase equations do not contain any diffusive terms. Implicitness is required to circumvent the time step constraint which can arise due to mesh concentration in the ullage as the mixture approaches external boundaries. However, given the selection of an implicit solver, it becomes of interest to add the diffusive terms for future studies of boundary layer phenomena. In Chapter 8.0 we describe the implicit algorithm and we present a solution for an idealized interior ballistic cycle.

-
- 18 Gough, P.S.
"Theoretical Effects of Packaging on Two-Dimensional Flamespread
Through Slotted Stick Propelling Charges"
Proc. 21st JANNAF Combustion Meeting 1984
- 19 Minor, T.C. and Horst, A.W.
"Theoretical and Experimental Investigation of Flamespreading
Processes in Combustible-Cased, Stick Propellant Charges"
Proc. 21st JANNAF Combustion Meeting 1984
- 20 Fickie, K.D. and Keller, G.E.
"Analysis of Solid Propellants as a Reactive-Diffusive System:
Dynamics of Ignition"
Proc. 21st JANNAF Combustion Meeting 1984
- 21 Horst, A.W.
"A Comparison of Barrel-Heating Processes for Granular and
Stick Propellant Charges"
Ballistic Research Laboratory Memorandum Report ARBRL-MR-03193
(AD A118394) 1982

2.0 DESCRIPTION OF THE TDNOVA CODE

The purpose of this chapter is to provide a description of the physical content of the model and the method of solution. The governing equations are not documented here. They are not changed in any significant way from the forms given in Reference 13. Only the revisions are noted here. The structure of this chapter is as follows. In Section 2.1 we first provide a brief overview of the code. In Section 2.2 we then discuss, in some detail, the representation of a propelling charge by the code, proceeding component by component. The discussion of Section 2.2 incorporates a description of some of the revisions to the code which were made during the present effort. For completeness, we note in Section 2.3 all the substantive code revisions; that is to say the revisions to the model equations or the solution algorithm as opposed to the correction of programming errors.

It should be understood that the discussion of the TDNOVA code given here excludes any reference to the implicit solver for the regions of ullage. The implicit solver, referred to in Chapter 1.0, is not presently linked to TDNOVA and does not represent a current capability in respect to the modeling of complete propelling charges.

2.1 Overview of Code

The general representation of a propelling charge by TDNOVA is illustrated in Fig. 2.1. The breechface and tube walls are taken to be rigid impermeable boundaries. The projectile is viewed as a rigid body and the base and afterbody constitute a moving impermeable boundary. The computational domain defined by these boundaries is divided into subregions within each of which the solution is assumed to be continuous and to vary sufficiently smoothly, both in time and from point to point, to permit the partial derivatives in the governing equations to be well approximated by finite differences. Each main charge increment defines a computational region within which the flow is assumed to be represented with sufficient accuracy by the macroscopic equations for a heterogeneous two-phase mixture. The macroscopic formulation models the flow in terms of averages of the state variables. The average is not explicit but may be viewed conceptually as formed over a volume which is large in comparison with the scale of heterogeneity of the mixture. The use of a macroscopic formulation introduces the porosity or the fraction of a unit macroscopic volume which is occupied by the gas-phase. Closure of the macroscopic equations requires that constitutive relations be defined to describe the microscopic interactions between the phases due to mass, momentum and energy transfer. We use empirical correlations to relate the microprocesses to the explicitly modeled macroscopic variables. In the general case each main charge increment envelopes a centercore igniter which is modeled as a quasi-one-dimensional two-phase flow.

The ullage is decomposed into subregions which are predicated on the instantaneous geometry of each of the increments. Each of the boundaries of each of the increments defines a quasi-one-dimensional region of ullage.

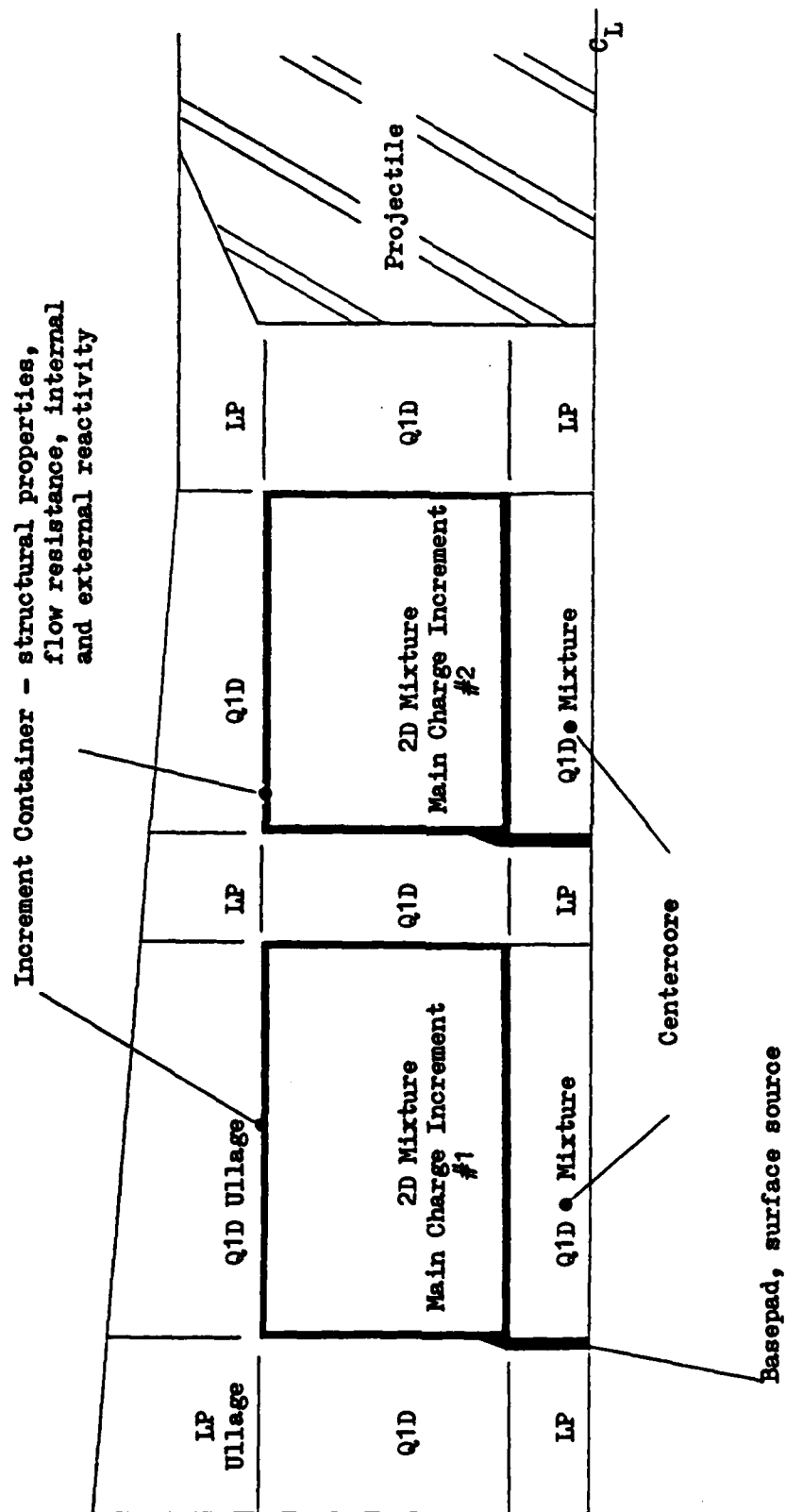


Figure 2.1 Charge Representation by TTNNOVA

These continuous regions of ullage are linked by lumped parameter regions located at the corners of the increments. The gas in the ullage is assumed to be single-phase and inviscid. However, the conditions which link the pressure at the boundaries of the continuous regions to the pressure in the lumped parameter regions admit the possibility of losses as the flow turns the corner. The continuous regions of ullage are linked to the flow in each of the main charge increments through internal boundary conditions. The boundaries of each of the increments are viewed as surfaces on which the porosity jumps discontinuously. The physical boundary conditions then follow from the jump conditions at a macroscopic discontinuity. By allowing the finite balances of mass, momentum and energy to incorporate source or loss terms we are able to model the reactivity, flow resistance and mechanical restraint associated with the presence of the case. The case is therefore viewed as an attribute of the boundaries of the increment which it encloses and, except as specifically noted below in the discussion of the rigidized case, we do not consider its motion independently of that of the boundaries of the increment. We always consider the thickness of the case but its inertia is only taken into account when it is rigidized.

The computational mesh within each two-dimensional region is established using the time-dependent boundary fitting algorithm of Thompson et al.²² The mesh in the regions of ullage is attached to that on the boundary of the relevant increment. The finite difference solution is advanced in time using a scheme based on the explicit two step marching algorithm of MacCormack.²³ Complete interior ballistic solutions are not obtained using the fully two-dimensional model. When flamespread is complete, all container sidewalls have ruptured, and radial pressure gradients have subsided to within a user-selectable tolerance, the model is converted to a quasi-two-dimensional representation based on coupled regions of coaxial one-dimensional flow.

2.2 Charge Representation by TDNOVA

We now enlarge on the foregoing summary. We discuss the charge component by component. We also pay attention to the differences between granular and stick propellant. Emphasis is given to the latter for three reasons. First, current charge designs appear to be increasingly dependent on the use of stick propellant. Second, the bulk of the present effort has centered around the simulation of stick charges. Third, the analysis of stick charges involves many more difficulties than their granular counterparts, particularly when the sticks are perforated and slotted.

-
- 22 Thompson, J.F., Thames, F.C. and Mastin, C.W.
 "Automatic Numerical Generation of Body-Fitted Curvilinear
 Coordinate Systems for Field Containing Any Number of
 Arbitrary Two-Dimensional Bodies"
 J. Comp. Phys. Vol. 15, p. 299 1974
- 23 MacCormack, R.W.
 "The Effect of Viscosity in Hypervelocity Impact Cratering"
 AIAA Paper No. 69-354 1969

2.2.1 Main Charge Increment

When the main charge increment consists of granular propellant we model average or macroscopic values of the following: gas-phase density, pressure and velocity; solid-phase velocity, intergranular stress and either surface temperature or surface regression, depending on whether the propellant is locally ignited; and the porosity or fraction of a unit macroscopic volume occupied by the gas-phase. As we have discussed previously, stick propellant is at least as amenable as granular propellant to analysis in terms of the macroscopic equations.²⁴ However, it is necessary to introduce double valued state variables for the gas-phase properties and for the solid-phase surface properties. We identify external properties formed by averaging over the interstitial regions and the outer surfaces of the sticks, and internal properties formed by averaging over the perforation regions and the internal surfaces of the sticks. We refer to the resulting set of equations as a dual-voidage model of flamespreading. At each location within the mixture we have the exterior porosity, or fraction of a unit macroscopic volume occupied by the gas-phase within the interstices, and the interior porosity, or fraction of a unit macroscopic volume occupied by the gas-phase within the perforations.

We emphasize that the average does not need to be viewed as formed over a region which is large in comparison with the length of the sticks. If we introduce coordinates aligned with the stick bundle we may define the longitudinal direction as parallel to the axes of the sticks and the transverse direction as normal to the axes. We assume that the bundle retains orderly packing characteristics so that the natural coordinates are uniquely defined at each location. This is certain to be true initially, is probably true during flamespreading, and probably becomes untrue only when the charge is substantially consumed by combustion. Then since the point of averaging is simply to remove intractable microstructure from the solution it is evident that longitudinal averaging is unnecessary and that the average need be formed only in the transverse direction. As with granular charges, we note the caveat that the chamber dimensions are not as large in comparison with the scale of heterogeneity as we would like: they are separated by only one order of magnitude whereas two or more orders would be desirable to validate the macroscopic approach.

In addition to the introduction of the concept of a dual-voidage formulation (which is, of course, only necessary if the sticks are perforated) it is necessary to revise several of the constitutive laws when we

²⁴ Gough, P.S.

"Continuum Modeling of Stick Charge Combustion"
Proc. 20th JANNAF Combustion Meeting

1983

consider stick rather than granular propellant.¹⁴ The constitutive laws which depend on the type of grain are those governing the rheology of the solid-phase and the interphase drag and heat transfer. In the subsequent discussion we first note the approach taken for the granular charge and then comment on the revisions pertinent in the case of a stick charge. We also discuss the method of treating the presence of a slot in the stick charge. Slotted sticks are used in both foreign and domestic charges. Finally, we comment on those constitutive laws which are common to both granular and stick charges.

2.2.1.1 Rheology

The law of interest here is that which defines the intergranular stress or that part of the solid-phase stress tensor which is not due to the direct local influence of the gas-phase. For granular charges we assume the intergranular stress to be isotropic and a path-dependent function of porosity. We assume the existence of a well-defined settling porosity at which the grains just make contact with one another. Above the settling porosity the intergranular stress is assumed to vanish. Below the settling porosity changes in the stress are proportional to changes in porosity, but the proportionality coefficient, or the bulk modulus, depends on whether the porosity is decreasing (loading) or increasing (unloading). There is no conceptual difference between the one- and two-dimensional laws for the granular charge.

In the one-dimensional theory the law governing the intergranular stresses in stick propellant expresses the assumption that each stick behaves like an elastic rod subjected to the pressure of the interstitial gas over its external surfaces. Using the elastic theory one may express the axial stress in terms of the axial strain and, through the Poisson effect, the transversely applied gas pressure. The stick bundle is assumed to support both compressive and axial stresses and the relationship between stress and strain is reversible. In contrast the granular charge supports only compressive intergranular stresses and the relationship between stress and strain is irreversible. For both types of charge, however, it is possible to recast the relationship between stress and strain into one between stress and porosity.

The two-dimensional model of stick charge rheology is anisotropic and incorporates features of both the stick and granular one-dimensional rheology. The longitudinal stress is assumed to be related to the longitudinal strain according to a reversible elastic law and, through the Poisson effect, to the sum of the gas pressure and the transverse component of intergranular stress which acts on the exterior surfaces of the individual sticks. On the other hand, the transverse component of stress is assumed to be governed by a law identical to that for granular charges: the transverse component of intergranular stress is assumed to be limited to compressive states and to depend irreversibly on the external porosity. In the natural coordinate frame of the bundle, the stress tensor is assumed to be diagonal. In principle we should speak of two transverse components, one

essentially radial and the other essentially azimuthal. We assume that the two components are equal in magnitude; this is tantamount to the assumption that the bundle does not resist deformation in the transverse plane. To have the stress tensor diagonal it is also necessary for the sticks to offer no resistance to bending.

2.2.1.2 Interphase Drag and Heat Transfer

For the granular charge the interphase drag and heat transfer are assumed to be isotropic, reflecting the random packing of the bed. The heat transfer is assumed to be given by the correlation of Gelperin and Einstein.²⁵ The interphase drag for a packed bed may be modeled either according to the correlation of Ergun²⁶ or the more recent data of Robbins and Gough.²⁷ In the fluidized regime, where the porosity exceeds the settling porosity, the packed bed friction factor is faired into the value for a single particle according to the tortuosity factor of Andersson.²⁸

When we turn to the stick charge, the interphase drag and heat transfer are posed in anisotropic forms. For purely longitudinal flow the drag and heat transfer are assumed to be given by empirical correlations for pipe flow in the same form as in the one-dimensional theory. For purely transverse flow the drag and heat transfer are assumed to be defined by correlations describing the flow through rod bundles. In the general situation of oblique flow we define both longitudinal and transverse components of drag which when combined are found to give reasonable agreement with some empirical results reported by Kutateladze.²⁹ The transverse component of drag for the internal flow through the perforations is

-
- | | | |
|----|---|------|
| 25 | Gelperin, N.I. and Einstein, V.G.
"Heat Transfer in Fluidized Beds"
<u>Fluidization</u> , edited by Davidson, J.F. and Harrison, D.
Academic Press, N.Y. | 1971 |
| 26 | Ergun, S.
"Fluid Flow Through Packed Columns"
Chem. Eng. Progr. Vol. 48, p.89 | 1952 |
| 27 | Robbins, F.W. and Gough, P.S.
"Influence of Length and Diameter of Cylinders on Packed
Bed Flow Resistance"
Proc. 16th JANNAF Combustion Meeting | 1979 |
| 28 | Andersson, K.E.B.
"Pressure Drop in Ideal Fluidization"
Chem. Eng. Sci. Vol. 15, p. 276 | 1961 |
| 29 | Kutateladze, S.S. and Borishanskii, V.M.
"A Concise Encyclopedia of Heat Transfer"
Pergamon Press | 1966 |

taken to be infinite. Accordingly the internal flow is formally modeled as though it were two-dimensional. Its inherently one-dimensional nature is imposed by the infinite transverse drag component. Transverse and longitudinal components of heat transfer are also defined and combined by forming an inner product with the relative velocity vector. The resulting dependence on obliquity is speculative and requires confirmation. Of course, only the longitudinal component of heat transfer is considered for the internal flow.

Heat transfer is only computed during the ignition phase of the interior ballistic cycle. The heat transfer is used to define a boundary condition for the heat conduction equation in the solid phase. It is assumed that there is no interaction between the external and internal thermal waves. When the surface temperature reaches the specified ignition temperature of the propellant, steady state combustion is assumed to begin. The subsequent surface regression is assumed to depend on the ambient gas-phase pressure according to an empirical law. The exterior ignition and combustion events are completely independent of those in the interior.

2.2.1.3 Analysis of Slotted Propellant

If the propellant is slotted it is assumed that the slot is initially closed. From the theory of thick elastic cylinders the hoop stress at the inner surface may be computed: the external pressure is taken to be the sum of the exterior gas-phase pressure and the transverse component of intergranular stress; the internal pressure is the interior gas-phase pressure. When the hoop stress is found to exceed a prespecified value the slot is assumed to open irrevocably and to allow mass transfer between the exterior and interior regions thereafter. As an alternative criterion, the user may allow the slot to open when the internal pressure exceeds the sum of the external pressure and the transverse component of the intergranular stress. The rate of mass transfer is assumed to be such as to equilibrate exactly the interior and exterior gas-phase pressures. An allowance is made for the mass addition due to the burning of the faces of the slot. Although the exterior and interior gas-phase pressures are made locally equal wherever the slot is open, the same is not true of the other gas-phase state variables and the dual-voidage model is still used. However, when the slots are open everywhere in a given bundle of sticks and flamespread is complete throughout the bundle, the dual-voidage model is terminated. The exterior and interior state variables are combined to define equivalent single-voidage state variables using the principles of local balance of mass, momentum and energy. We also note that the transition of the representation of the solution to a quasi-two-dimensional form is delayed until each slotted stick increment has been converted to a single-voidage representation.

2.2.1.4 Other Constitutive Laws

Other constitutive laws pertaining to the main charge are as follows. The gas is assumed to obey a covolume equation of state. The specific heats and molecular weight are taken to vary with the composition of the mixture. The viscosity is assumed to obey a Sutherland type dependence on temperature and to be independent of pressure. The thermal conductivity follows from the assumption of a fixed value of the Prandtl number.

Normally, the propellant is assumed to burn at a rate which depends on the local pressure in accordance with an empirical exponential law. As an option the user may define the combustion rate by reference to a quasi-steady thermal wave theory in which the unsteady thermal response of the solid-phase is driven by a steady-state gas-phase heat feedback subject to a pyrolytic boundary condition. As an additional feature, the user may specify that only a part of the chemical energy is released locally when the propellant surface decomposes. The balance of the energy may be taken to be released in the gas-phase according to an Arrhenius reaction rate law.

2.2.2 Igniter Increment

Originally it was intended to represent the igniter stimulus in TDNOVA according to any or all of three different methods:

[1] As in NOVA⁵ the igniter may be specified as a distributed source term. This method has not been used except to compare solutions with those of NOVA.¹⁴

[2] Basepads and combustible case components may be represented as surface source terms. This method has been used in connection with many problems and is illustrated in all the non-trivial examples in the present report.

[3] If the increment has a centercore igniter, the igniter is modeled as a two-phase flow. This method has also been exercised and is illustrated in the present report in connection with the M203 charge.

In some instances, as for example the M203E2 charge, the igniter does not easily fall into any of the three foregoing categories. It is tempting then to represent the igniter as a separate increment of propellant and model it as a two-dimensional two-phase flow. Due to the fine granulation of the igniter charge, when compared with that of the main charge, certain computational difficulties arise. Because of these difficulties, which we will discuss in a moment, we have found it necessary to encode special procedures for any charge increment which is identified by the user as an igniter increment.

Because the grains of the igniter material are very small they are strongly susceptible to drag forces. Moreover, in a charge like the M203E2, the igniter increment has a very low loading density. Under conditions of strong rearward blowing the igniter grains can be compacted against the breechface. The computational mesh can become very compressed with the result that the time step, which is constrained in accordance with the Courant-Lewy-Friedrichs stability condition,³⁰ becomes extremely small. The cost of the calculation may then become prohibitive. We therefore eliminate the igniter increment if it is compacted to less than 10% of its original length. Second, the igniter increment may burn out early in the ballistic cycle. When burnout occurs, the solid-phase streamlines default to those of the gas-phase, and the increment may deform excessively. In fact, it is possible for the increment to deform to the point where the transformation into the computational plane becomes singular. Therefore we eliminate the igniter increment whenever burnout occurs at any point. We note that in all the calculations presented here the igniter was eliminated due to burnout rather than compression. Elimination of the igniter increment means that the solid-phase and case are dropped from further analysis. The volume occupied by the igniter increment is consolidated with that of the contiguous regions of ullage.

2.2.3 The Case

We discuss first the chemical properties of the case and second the mechanical properties.

2.2.3.1 Chemical Properties

At each point the case may be specified as having up to four reactive substrates, two on the outside and two on the inside. A pair is specified on each side to permit modeling of the regression of the surface of the case and also the combustion of an attached component such as a basepad. The rate of combustion of each substrate may be prespecified in tabular form or it may be modeled explicitly. In the latter case we compute the heat transfer to the surface according to an empirical pipe flow correlation and compute the surface temperature in the same manner as for the propellant. When ignition occurs the surface is assumed to regress according to an exponential dependence on pressure. The pipe flow correlation requires that a characteristic length scale be defined. For the exterior of the case we use the hydraulic diameter defined by the cross-section between the case and the gun surface. For the interior of the case we use the external diameter of the propellant grains. When combustion of the case occurs the local thickness of the wall is taken to decrease correspondingly.

30 Richtmyer, R.D. and Morton, K.W.
"Difference Methods for Initial Value Problems"
Interscience

2.2.3.2 Mechanical Properties

The case of any increment may be specified as rigidized. In such an instance we model explicitly the longitudinal displacement of the case sidewall independently of the motion of the boundary of the charge. However, the motion of the case in the direction normal to the charge boundary is not modeled explicitly and is assumed to coincide with that of the propellant. The sidewall is assumed to be a linear elastic solid. Friction due to the normal force exerted by the propellant on the inner wall is taken into account. The endwalls are assumed to be rigid. The motion of the endwalls is determined by the forces due to the sidewall and the integral of the sum of the gas pressure and intergranular stress on each side of the endwall. If the endwall is ruptured at some radial location, the integral is performed only over values of radius larger than that at the point of rupture. We note that the inertia of the case is only taken into account when it is modeled as rigidized. Each rigidized case may be bonded to its neighbors. Once the tensile force between the increments exceeds the bond strength, the bond is broken irrevocably. The case ceases to be modeled as rigidized whenever an unbonded endwall is completely ruptured or when the equivalent stress at any point in the sidewall exceeds the tensile strength of the sidewall material. Only when the case is rigidized do we consider the endwalls to impede directly the motion of the solid-phase. The solid-phase is permitted to separate from the inner surface of the endwall but is not allowed to penetrate it. The sidewalls on the other hand may impede the radial motion of the solid-phase whether or not the case is rigidized. Until it is fully ruptured in the sense to be discussed below, the outer sidewall of the case cannot be expanded beyond its initial diameter.

Once the case is determined to be no longer rigidized it is modeled in accordance with our earlier flexible case model.¹³ It is determined to rupture when the sum of the gas-pressure and intergranular stress on the inside exceed the sum on the outside by a prespecified amount. The only exception to this rule pertains to the centercore sidewall for which the absolute value of the difference is used. When rupture occurs the case becomes increasingly permeable to the gas-phase. The initial permeability of the case is defined at each point by specifying the value of a dimensionless flow resistance coefficient K . The pressure drop across the surface of the case is proportional to the product of K with the density of the gas and the square of the normal component of velocity. Appendix A may be consulted for further details. If K is greater than or equal to 100, the surface is treated as completely impermeable. When rupture occurs the local value of K decreases to zero over a prespecified interval of time.

Originally,¹⁴ the failure of a rigidized case had no other consequence than the elimination of a constraint on the motion of the solid-phase by the endwalls of the container. The actual rupture of the various segments of the container could only occur as a result of overpressurization from within. For some propelling charges, like the XM216 charge considered in

the present report, this model of case rupture may preclude the theoretical prediction of ignition of one or more of the increments. If an increment is completely enclosed by an impermeable container whose inner walls are inert it may be impossible for rupture to occur as a result of overpressure from within. Without rupture the container remains impermeable and the propellant is never ignited. To circumvent such a possibility we have encoded an obvious physical extension to the rupture model. If failure of the rigidized case occurs at the endwall or the mesh point adjacent to the endwall, the entire endwall is taken to commence rupturing at that time. If the rupture occurs at any other point on the sidewall of the case, rupture is taken to commence for the point in question and also for each of its neighbors. Thus the transition to the flexible wall model occurs in such a way that some portion of the container is in the process of rupturing and therefore of becoming permeable to the gas-phase.

An additional option was encoded according to which the user may specify that a given type of container material begins to rupture whenever the main charge is locally ignited. This option is useful in cases where the container is initially specified as being very permeable to the gas-phase. In such cases the pressure differential required to rupture the segment may never occur. Rupture following main charge ignition provides a phenomenologically reasonable criterion for container failure in such cases.

2.3 Summary of Code Revisions

We summarize here the revisions to TDNOVA which have been incorporated since the last final report.¹⁴ We describe substantive revisions only; that is to say that we only consider revisions to the model equations or the method of solution. Coding errors or logical flaws which were corrected during the present effort are not described here except for one error which affects previous simulations of the M203 charge. The revisions described here have for the most part been motivated by direct computational experience. Revisions required in order to circumvent or remedy algorithm weaknesses have been formulated and incorporated into the code at various times and in connection with various data bases. Occasionally, the algorithm revision which enables a stable solution to be obtained with some new and complicated charge has the consequence that other data bases, previously capable of being run with the code, are found to result in instabilities. On the other hand, it may well be the case that earlier revisions are in some sense superseded by new revisions. The revisions discussed here are those which have been retained in the single code version which has been used to generate all the results presented in this report. We attempt to describe as completely as possible the motivation for each revision and the implications in respect to limitations on the scope of applicability of the code. The set of revisions given here should be viewed as sufficient but not as completely necessary, since as noted above, it is possible that some of the earlier revisions may have been rendered redundant or unnecessary as a consequence of other later revisions.

We do not attempt to order the revisions chronologically. Instead, we have attempted to organize them into groups. Several revisions have no direct logical association with any others and are dealt with in Section 2.3.1. Section 2.3.2 deals with revisions which were made in response to observations of instability of the transverse boundaries in the quasi-two-dimensional representation. Section 2.3.3 discusses revisions which were made to improve the global mass balancing properties of the integration scheme. In Section 2.3.4 we discuss revisions to the analysis of the motion of the boundaries of the computational regions and in Section 2.3.5 we consider the revisions to the analysis of boundary values. The discussion of Section 2.3.5 is supplemented by Appendix A.

As a final remark here it should be stated that the process of code revision is certainly not yet complete. When we review the computational results in Chapters 3.0 through 7.0 we will note various numerical anomalies. For some of these the remedy will be apparent while for others the solutions will have to await further and deeper study.

2.3.1 General Topics

[1] In order for the representation of the solution to be converted from fully two-dimensional to quasi-two-dimensional, it is necessary that flamespreading be complete throughout all increments of the charge, that all outer sidewalls of all increments be fully ruptured, and that the difference between the values of pressure at the tube wall and the centerline vanish to within a user-specified tolerance throughout the gun chamber. That is, for each axial location z we require $|p(z,R) - p(z,o)| \leq PTOL * p(z,o)$ where $PTOL$ is the pressure tolerance factor and $p(z,R)$, $p(z,o)$ are respectively the pressures at the tube wall and the centerline. We have revised slightly the pressure tolerance criterion. Previously, we evaluated the pressure difference at every axial location within each of the charge increments. We have found that for very small values of the pressure tolerance factor, $PTOL < 0.01$, conversion to a quasi-two-dimensional representation was precluded by numerical noise associated with the corners of the charge increment regions. This is no doubt a result of the relatively crude techniques used to define corner boundary values in TDNOVA. We provide further discussion of the corner boundary values below in Section 2.3.5. The revision made in response to this problem was simply to exclude the corner positions from the set of axial locations at which compliance with the pressure tolerance criterion is evaluated.

[2] Previously, all regions of axial ullage were represented as lumped parameter following the transformation to a quasi-two-dimensional representation. By axial ullage we mean regions of gas contiguous with the ends of one or more increments. The radial ullage contiguous with the increment sidewalls is treated as a one-dimensional continuum. This approach was acceptable for granular charges which, in general, tend to be dispersed nearly uniformly over the region between the breech and the base of the

projectile. For stick charges, however, a revision was clearly required since the stick bundle never changes in length appreciably and therefore occupies a continually decreasing fraction of the available length of the tube.

We have revised the code to transform the forward region of axial ullage, that is to say the region adjacent to the projectile base, to a continuum when it becomes sufficiently large. Only the forward region of axial ullage is affected. Other regions of axial ullage continue to be treated as lumped parameter.

The conversion to a continuum occurs when the projectile is found to be moving faster than the forward boundary of the charge and when the region of ullage has a length greater than or equal to $2/(\text{INDIMZ} - 1)$ times the axial location of the front of the charge. Here INDIMZ is the number of axial mesh points used to represent the charge. The length criterion is approximately equivalent to a requirement that the length of the ullage exceed two mesh intervals in the charge. Subsequently, the mesh spacing in the ullage is compared with that for the forward increment of propellant. Whenever the mesh in the ullage exceeds that in the forward increment, points are added to the ullage so as to halve the mesh spacing. Such additions continue until either the ullage is assigned more than INDIMZ points or the storage limit for the solution arrays is reached.

[3] An option was encoded to permit the simulation of programmed fracture of single-perforation stick propellant. Two modes of fracture are possible. In the first mode the stick bundle is converted to a different granulation according to a criterion based on the state of stress at the midpoint of the bundle. In the second mode, the stick bundle is replaced by two bundles of shorter sticks. These, in turn, are capable of subdividing until the original bundle is reduced to eight smaller bundles. A final transformation of the granulation of each of the one-eighth length bundles may also occur. Revisions were also made to the criteria for the opening of the slots of slotted stick propellant and for the rupture of unslotted single-perforation propellant.

We describe the various stress criteria in terms of the nomenclature of Reference 13. Let σ_{p1} , σ_{p2} , σ_{p3} be the principal stresses in the intrinsic coordinate frame of the stick bundle. We identify σ_{p1} as a longitudinal or axial stress and σ_{p3} as a hoop stress. Moreover, we adopt the normal convention of continuum mechanics according to which a positive value is assigned to a tensile stress. We use σ_{eq} to represent the von Mises equivalent stress, $\sigma_{eq}^2 = 1/2 \{(\sigma_{p1} - \sigma_{p2})^2 + (\sigma_{p2} - \sigma_{p3})^2 + (\sigma_{p3} - \sigma_{p1})^2\}$. Then we may state the stress criteria for the foregoing events in the following forms, where p_c is a user-defined critical value of stress.

Event	Stress Criterion
Change of Granulation in Programmed Fracture	$\sigma_{p3} > 0$ and $\sigma_{eq} > p_*$ at midpoint
Bundle Subdivision in Programmed Fracture	$\sigma_{p1} > 0$ and $\sigma_{eq} > p_*$ at midpoint
Opening of Slot of Slotted Stick	$\sigma_{p3} > p_*$ locally
Rupture of Single-Perforation Stick	$\sigma_{p3} > 0$ and $\sigma_{eq} > p_*$ at any radial location

For convenience, however, we have retained as an option the previous criterion for slot opening and rupture of single-perforation sticks, namely that the internal gas pressure exceed the sum of the external pressure and the transverse intergranular stress.

[4] We had previously encoded an input datum NOLDCD which allowed the user to select either the Ergun or the Robbins-Gough correlation for the packed bed. Because of computational difficulties associated with the unbounded behavior of the idealized transverse interphase friction factor we extended the meaning of NOLDCD to allow the user to limit the transverse components of both friction factor and heat transfer to the values for a granular bed of particles having the same external diameter as the sticks. This option has been exercised in all the stick charge calculations presented here. Only the external transverse friction factor is affected. The internal transverse friction factor remains infinite so as to force the flow through the perforations of the sticks to conform with the orientation of the sticks.

[5] Originally,¹⁰ we had encoded a one-sided second order corrector for the formation of spacewise differences. The use of this second order corrector was dropped in connection with the evaluation of derivatives normal to the region boundaries when it was found to be destabilizing. However, it was retained in connection with the determination of convective derivatives at interior mesh points. Experience during the present effort revealed that for the most highly structured solutions, namely those for the XM216 charge, more harm than good was resulting from this second order corrector to the convective derivative and it was eliminated. Accordingly, all derivatives normal to region boundaries and all convective derivatives are evaluated using a first order one-sided difference.

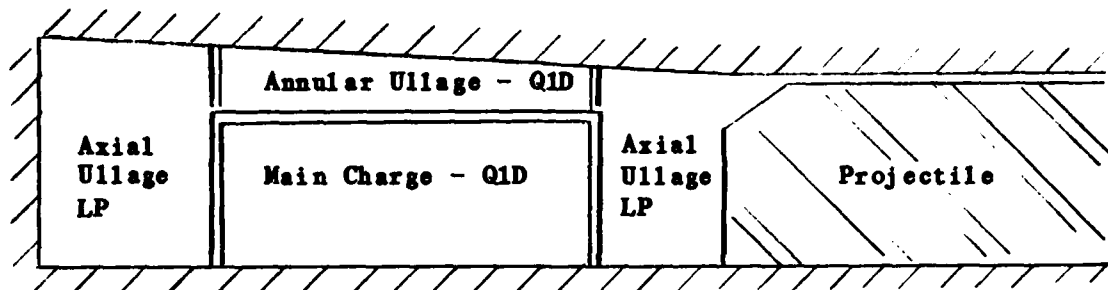
2.3.2 Transverse Boundary Instability

The topic of interest here is the behavior of the transverse boundaries of the main charge increments in the quasi-two-dimensional representation. When TDNOVA was originally formulated it was expected that as the propelling charge was consumed, the transverse boundaries would expand, the inner boundary moving to the centerline and the outer boundary moving to the tube wall. The principal mechanism for this expansion was expected to be the drag exerted on the solid-phase by the transverse fluxes as they were expelled from a region of strong gas generation to a region of weak or zero gas generation. However, with increasing computational experience with data bases of increasing complexity — particularly the multi-increment charges — it became apparent that our original expectation would not always be satisfied. In fact, exactly the opposite behavior was occasionally observed, particularly near the ends of the charge and particularly at increment-to-increment interfaces. Rather than expanding to fill uniformly the tube, the charge was found, in some cases, to contract in an unstable manner with the result that the calculation either could not be completed or else was contaminated with pressure wiggles. This was a very difficult problem to treat and we are not certain that our present revisions are necessarily complete, although they have proved adequate for all the data bases of interest here.

The difficulty is that unstable boundary motion is not excluded from the physics of the problem. It is possible that very non-uniform radial distributions of propellant might occur in the gun, particularly toward burnout, which is precisely where the computations run into trouble. As we will discuss further, the governing equations do admit unstable behavior. Thus in dealing with the problem one has to consider whether the observed effect is a physical event; a feature of the governing equations which could be eliminated by reformulation; a weakness in the numerical algorithm; or given the complexity of the programming, a simple coding error.

A basic assumption of the quasi-two-dimensional analysis is that the gas-phase pressure is uniform over the cross-section of the tube. Since the flow is modeled as a number of coaxial flows with slip boundaries, the potential exists for instability of the Helmholtz type. We note however that mass transfer between the regions may have a stabilizing effect. To understand how the governing equations originally formulated for TDNOVA can lead to unstable behavior we briefly outline the solution method.

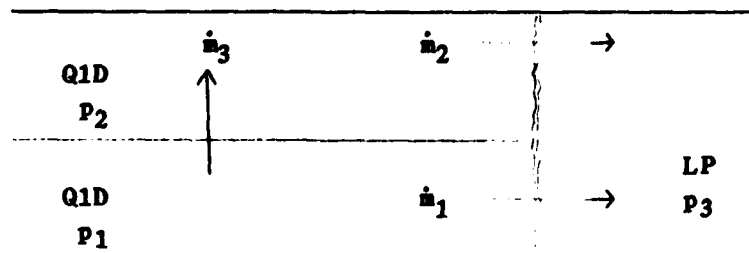
For simplicity consider a single increment charge with no centercore but with external annular ullage. The charge and the ullage are represented as coaxial one-dimensional flows. The ends of the region occupied by the charge and the annular ullage are terminated by regions of axial ullage, each of which is represented as lumped parameter. We illustrate the situation in the following sketch. The geometry of the problem is determined by the motion of the projectile and the boundaries of the main charge.



The motion of the ends of the charge follows from the boundary values of the solid-phase. The radial motion is determined mainly by the drag force on the solid-phase due to mass transfer to the annular ullage. We model not only the axial velocity of the solid-phase but also, in general, an outer and an inner radial velocity. Once the mass transfer to the outer annular ullage has been determined, as described below, it is used to define a radial drag force which modifies the outer radial velocity of the solid-phase and hence the boundary motion. A principle of equilibration of the transverse intergranular stress also plays a role in defining the radial motion of the charge in the quasi-two-dimensional representation, but it is usually of secondary importance.

The state of the gas-phase in each of the continuum regions is governed by equations perfectly analogous to those for the flow of an inviscid gas through a duct of variable area and with an allowance for mass and heat addition. At any interior mesh point (not on the boundaries or ends of the charge) the pressure in the main charge and in the ullage, at the same axial location, are first updated assuming that there is no transverse flux or exchange between the ullage and the main charge. The assumption that the pressure in the ullage is equal to that in the main charge, at the same axial location, then serves to define a unique value of the transverse flux.

Now consider the situation at the boundaries of the continuum regions. As shown in the sketch below, let \dot{m}_1 and \dot{m}_2 be the mass fluxes from the continua to the adjacent lumped parameter region. Let \dot{m}_3 be the transverse flux from the main charge to the ullage. Let p_1 , p_2 , p_3 respectively denote



the pressures in the main charge, the ullage and the lumped parameter region. From the equations of motion, with the help of the theory of characteristics,¹⁰ it emerges that one can establish the following linear relationships for sufficiently small changes of state:

$$\Delta p_1 = a_{11}\Delta \dot{m}_1 + a_{13}\Delta \dot{m}_3 , \quad (2.3.2.1)$$

$$\Delta p_2 = a_{22}\Delta \dot{m}_2 + a_{23}\Delta \dot{m}_3 . \quad (2.3.2.2)$$

$$\Delta p_3 = a_{31}\Delta \dot{m}_1 + a_{32}\Delta \dot{m}_2 . \quad (2.3.2.3)$$

The principle of pressure equilibration implies

$$p_1 = p_2 = p_3 . \quad (2.3.2.4)$$

We therefore have five independent relations to determine six quantities and the solution is underdetermined. From a physical standpoint the equations may be viewed as admitting an infinite set of fluxes with an arbitrary circulation. To close the equations we originally defined the transverse flux \dot{m}_3 by assuming that the boundary value was equal to that at the neighboring interior mesh point. However, unstable transverse boundary motion was observed on occasion, usually at the internal boundary associated with the presence of a centercore. Moreover, a symptom of the instability was the development of unbounded increases in circulation at the ends of the charges. The following revisions were made, successively, to deal with this problem.

[1] The solid-phase momentum equation includes the gradient of the gas-phase pressure. Originally, we evaluated this term at the boundaries by means of a first order one-sided difference. It was observed that during the early stages of transverse instability, the pressure wiggle at the boundary was exacerbated by the effect of the gradient term on the solid-phase motion and excessive condensation of the solid-phase was observed. To circumvent this anomaly, we have evaluated the pressure gradient in the solid-phase momentum equation using the first and second neighbors of the boundary point. Thus if the boundary is at mesh point n , we evaluate $p_{n-1} - p_{n-2}$ to compute the pressure gradient. We emphasize that this revision pertains only to the solid-phase and only during the quasi-two-dimensional representation.

[2] It was observed that transverse instability generally manifested itself towards the burnout stage of the interior ballistic cycle. Since the rationale for modeling the positions of the transverse boundaries is to keep track of low permeability flow channels which can affect the development of ignition-induced pressure waves, interest in the boundary positions

diminishes as the propellant is consumed. We also recognize the incompleteness of the model phenomenology which makes it likely that estimates of transverse boundary position are increasingly inaccurate as burnout is approached. Accordingly, we have revised the code to terminate the analysis of transverse boundary position once slivering occurs in a multiperforated grain. For single-perforation grains the analysis is still continued through burnout. The decision to discontinue the analysis of the motion is made locally. The boundary radius is then frozen until burnout occurs throughout the increment.

[3] In order to compute the transverse flux it is necessary to determine the derivative of pressure with respect to the flux. The derivative depends on the sign of the flux since an entering flux introduces irreversible heating or cooling while an exiting flux has the effect of an isentropic expansion. Originally, we used the current sign of the transverse flux to determine its direction and hence the derivative. During the transverse instability it was observed that the flux could oscillate between predictor and corrector steps with the result that the computed derivative was always inconsistent with the sign of the flux. We have revised the code to perform an additional iteration, recomputing the derivatives of pressure with respect to mass whenever the transverse fluxes turn out to have signs different from those which were first assumed.

[4] As discussed previously, we originally determined the transverse fluxes at the endpoints of the charge by assuming that they were equal to the values at the neighboring point. We revised this slightly. If \dot{m}_n is the transverse flux at the boundary point n , we put $\dot{m}_n = 1/2(\dot{m}_{n-1} + \dot{m}_{n-2})$.

[5] All the foregoing revisions alleviated the problem of transverse instability to some extent but it still persisted. Although many data bases were rendered tractable, others remained intractable. Because the assumption of pressure equilibrium clearly allowed unbounded circulation around the ends of the charge it was decided to relax this assumption at the ends and to allow the pressure in the ullage to differ from that in the main charge. Moreover we have constructed the potential pressure difference in such a way that it introduces a stabilizing energy penalty on gas recirculated around the end points. If the gas is exiting the continuum region of ullage we take its pressure to be equal to that in the contiguous lumped parameter region of ullage. However, if the gas is entering the continuum region, we assume that the transfer from the lumped parameter region is adiabatic and isentropic. The pressure in the main charge is assumed to be equal to that in the ullage independently of the sign of the boundary value of velocity. The centercore is treated in the same way as the continuum ullage. To compute the pressure drop associated with the isentropic transfer one needs to know the gas velocity in the lumped parameter region of ullage. This is computed by averaging all the mass fluxes to and from the lumped parameter region.¹³

This revision is thought to be the most significant change as regards the problem of transverse instability. Possibly, the preceding revisions are no longer necessary. However, testing to confirm that suspicion has not been conducted.

2.3.3 Global Mass Balancing

Finite difference schemes may be classified as conservative or non-conservative. Conservative schemes are designed so that the total mass, momentum and energy of the system being simulated are necessarily conserved with a precision limited only by the round-off accuracy of the computer. It should be noted that the automatic global conservation property is assured only relative to a specific numerical algorithm for evaluating the integral, usually the trapezoidal rule. Moreover, although the global conservation property is obviously a desirable attribute of a numerical scheme, it does not follow that the accuracy of the solution is necessarily improved in any other respect relative to a non-conservative scheme.

The algorithm used in TDNOVA is non-conservative. We use the balance equations in non-divergence form, discretized at interior mesh points according to the MacCormack scheme and at the boundaries by reference to the characteristic forms. The degree to which TDNOVA fails to conserve total system mass and energy is clearly of interest.

Many revisions were made in order to improve the global conservation properties of the code, but most of these revisions constituted coding corrections rather than algorithm changes. Of the three topics noted below, it might be argued that only the third is a genuine revision. However the first two were thought to be worth noting for future reference.

We will pay considerable attention to the global conservation of mass and energy when we discuss the numerical examples in Chapter 3.0 through 7.0. Accordingly, we now note the manner in which we analyze the global balances in TDNOVA. Let M be the total mass of the two phases within the complete computational domain, as defined below, and let M_0 be the initial value of M . Then we define the mass defect at any time as

$$\Delta m\% = 100 \left[\frac{M - M_0}{M_0} \right] \quad (2.3.3.1)$$

and we note that this quantity is expressed as a percentage. The total initial mass M_0 includes the mass of the gas-phase and the solid-phase but excludes the mass defined by combustible case segments or other surface source terms. Obviously, with this definition an apparent defect would arise due to the real addition of mass to the computational domain as the basepads and sidewalls were consumed. Accordingly, the value of M is corrected at each time step to subtract the accumulated contribution from

the surface terms. The quantity $\Delta m\%$ as used in subsequent chapters is therefore to be understood primarily as a measure of the accuracy of the numerical scheme and secondarily, as a reflection of errors in the numerical evaluation of total mass at any time.

Let ρ be the density of the gas-phase and let ϵ be the porosity. Then M is evaluated as a sum of contributions from lumped parameter, quasi-one-dimensional, and two-dimensional cells. The contribution from a lumped parameter cell is $\epsilon \rho V$ where the volume V is computed from the formula

$$V = \frac{\pi}{2} (r_1 + r_2 + r_3 + r_4) \text{area}(r_1, r_2, r_3, r_4) \quad (2.3.3.2)$$

where the r_i , $i = 1, \dots, 4$, are position vectors of the four corners of the cell and r_i is the corresponding radial coordinate. The term $\text{area}(r_1, r_2, r_3, r_4)$ denotes the area of the trapezoid defined by the position vectors. This is computed exactly using the formula for the area of a triangle. The contribution from a quasi-one-dimensional cell is computed as $\bar{\rho} \bar{\epsilon} \bar{A}$ where $\bar{\rho} = 1/2(\rho_1 + \rho_2)$ is the average value of the mesh point values ρ_1 and ρ_2 , and A is the cross-sectional area of the flow. The contribution from a two-dimensional cell is computed as $\bar{\rho} \bar{\epsilon} V$ where V is as in 2.3.3.2 and $\bar{\rho} = 1/4 (\rho_1 + \rho_2 + \rho_3 + \rho_4)$. The mass of the solid-phase is computed analogously. The contribution of the surface source terms is computed using a trapezoidal rule to integrate over the surface and a first order predictor scheme to integrate in time. Then M is computed as the sum of all the gas-phase and solid phase contributions less the cumulative sum of all the surface flux contributions.

The energy defect $\Delta e\%$ is defined analogously to $\Delta m\%$. The total energy E includes the internal and kinetic energy of both phases, the kinetic energy of the projectile and the work done against bore resistance. From this total is subtracted the energy due to the surface fluxes. Not presently taken into account are the heat loss to the tube and the kinetic energy of gas in lumped parameter regions. The calculation of internal energy does include the contribution of the chemical energy stored in any unreacted pyrolysis products in the gas-phase.

The following are the revisions connected with the global balances.

[1] Originally, trial values of the gas-phase fluxes through the boundaries were computed prior to the imposition of the solid-phase boundary conditions. The subsequent adjustment of the solid-phase boundary velocity was not reflected in the fluxes, creating an error in mass and energy balancing. The code was revised so that the fluxes would be computed following the determination of the corrected boundary velocities.

[2] As we discuss in the next section, there are a number of instances in which the mixture boundary is moved slightly for bookkeeping reasons. For example, when the mixture boundary approaches a stationary external boundary to within a distance less than 1 mm, it is placed in contact. When this displacement occurs on the outer circumferential boundary of the propelling charge, a detectable contribution to the mass defect may result. Accordingly, care was taken, in the fully two-dimensional part of the calculation, to adjust the gas-phase density and the porosity whenever a bookkeeping displacement was introduced at the outer circumferential boundary. Adjustments were also made in the quasi-two-dimensional part of the calculation whenever a bookkeeping displacement occurred at either the outer or the inner boundary of the main charge.

[3] In order to update the state of the quasi-one-dimensional regions it is necessary to have an estimate of the time derivative of cross-sectional area $\partial A/\partial t$. For the lumped parameter regions a knowledge of $\partial V/\partial t$ is required where V is the volume. Originally this was evaluated using the MacCormack second order predictor/corrector scheme. However, in a simulation of a two-phase flow consisting of a gas and a highly dispersed aggregate of small inert particles, we observed the development of a large mass defect which was traced to the use of the MacCormack evaluation of $\partial V/\partial t$ for the lumped parameter equations in non-conservative form.

It may be verified that the following representation of $\partial V/\partial t$ leads to perfect mass balancing, insofar as volume changes are concerned, when applied to the balance equations in non-conservative form

$$\frac{\partial V}{\partial t} = \begin{cases} \frac{V^n}{\tilde{V}} \left[\frac{\tilde{V} - V^n}{\Delta t} \right] & , \text{ predictor step} \\ \frac{\hat{\rho}}{\tilde{\rho}} \frac{\tilde{A}}{A^{n+1}} \left[\frac{A^{n+1} - \frac{1}{2\hat{\rho}} (\tilde{\rho} \tilde{A} + \rho^n A^n)}{\Delta t/2} \right] & , \text{ corrector step} \end{cases}$$

where $\hat{\rho} = 1/2(\tilde{\rho} + \rho^n)$. Here we have used superscripts n , \sim , and $n+1$ to denote present, future predictor and future corrector values respectively. An analogous expression is used to evaluate $\partial A/\partial t$ for the quasi-one-dimensional regions.

Although this revision was evidently necessary in connection with the cited problem, for which satisfactory results were then obtained, it appears to have no discernable consequences for the calculations presented in this report.

2.3.4 Editing of Boundary Positions

The boundaries of the computational regions are determined by the external surfaces — the breech, the tube and the projectile — and by the internal surfaces which envelop each of the main charge increments. In the fully two-dimensional representation the main charge increments are modeled as two-dimensional while the contiguous regions of ullage and the centercores are modeled as quasi-one-dimensional. Lumped parameter corner regions terminate the quasi-one-dimensional regions. The mesh in the one-dimensional regions is attached to the contiguous boundary of the main charge. Hence, the mesh is determined in all regions by the motion of the main charge increments. However, although a solid-phase Lagrangian mesh option is available, we do not normally tie the two-dimensional mesh to the solid-phase. The two-dimensional mesh points are assigned velocity vectors according to the following algorithm. On the boundaries of each main charge increment the normal velocity component of the mesh equals that of the solid-phase. But tangential slip is allowed in order to maintain uniform spacing along the boundary. The interior mesh and its velocity field are determined from the boundary distributions using an equipotential algorithm.²²

As the boundary of a main charge increment approaches an external boundary — the tube wall for example — the contiguous region of ullage begins to collapse. Collapse is taken to be complete once the transverse dimension is less than 1 mm. Once the ullage is collapsed at any point it is no longer possible to update the solution from the equations of motion. The state is assumed to be the same as that at the neighboring main charge point. It may therefore be anticipated that some numerical strain will occur at a mesh point in the ullage which is adjacent to a point at which the ullage is collapsed. In some instances it is possible for the case of the charge to be fully ruptured over part of its length and fully expanded to the tube wall while the remainder of the charge is still at its original diameter. Under such conditions the flow area of the ullage will vary abruptly near the point of attachment of the mixture to the wall. Difficulties can then arise from the derivatives of the area as well as of the state variables in the ullage. Other numerical difficulties can arise if, for example, an isolated point on the mixture boundary has not yet attached to the tube wall, while both its neighbors are attached. Alternatively, an isolated point may begin to separate from the wall.

It should not be surprising, therefore, that a certain amount of essentially ad hoc editing of the mixture boundary positions might be desirable to keep the solution from wandering through computational paths which are not only potentially destabilizing but also outside the resolving power of the macroscopic framework on which the model rests. Our approach to this topic has been to introduce such editing only when absolutely necessary and only after exploring the benefits of various differencing techniques at points adjacent to a collapsed region of ullage. The following revisions represent the set of boundary restrictions necessary to permit the complete simulation of all the data bases discussed in the succeeding chapters.

[1] A point on the mixture boundary is assumed to be in contact with an external boundary when the separation between them is less than or equal to 1 mm. To eliminate problems associated with spurious separations in which a point might approach the wall to slightly less than 1 mm and then move slightly further away, we edit the mixture boundary points, moving them into precise contact with the external boundaries whenever the separation is less than or equal to 1 mm. Moreover, on the stationary boundaries — the breech, the tube wall and, prior to any motion, the projectile base — we assume that once contact has been made by the mixture, separation never occurs. This assumption rules out the possible blowing away of the mixture from the wall due to a vigorously burning case segment and also, the inertial separation which might occur as the mixture flows past a corner. Of course, when the projectile is moving, the possibility of separation from the mixture must be considered. At the base of the moving projectile, therefore, the attachment logic takes into account the relative normal velocity component of the solid-phase.

If a mesh point on the boundary of the mixture is separated from the external boundaries by more than 1 mm while both of its neighbors are attached, the point is moved into contact. This closing of ullage 'pockets' is performed even more stringently in the quasi-two-dimensional representation. In this case a group of separated points, terminated at each end by points of attachment, will also be moved into contact with the external boundary.

Finally, in the quasi-two-dimensional representation, at a separated boundary mesh point adjacent to an attached boundary mesh point, the normal velocity component is defaulted to zero if it corresponds to increasing separation.

[2] In order to determine the velocity field for the mesh on the boundaries of the mixture we use the conditions that the normal velocity component be equal to that of the solid-phase while the tangential velocity is such as to preserve uniformity of the mesh. Previously, the components of the tangent vector to the boundary were determined using centered differences. For stability we found it necessary to use first order upwind differences instead.

[3] For igniter increments the axial positions of the corners are assumed to be equal to those of the neighboring points on the endwalls. This revision was made necessary by the extreme volatility of the igniter increment boundaries due to the fine granulation of the igniter charge.

[4] As an added safeguard against extreme compression of the igniter increment we encoded logic to terminate compression if the thickness became less than 0.5 cm at a given radius.

2.3.5 Analysis of Boundary Values

The boundary conditions for the mixture are complex, both physically and computationally. As might be expected, numerous revisions were made in connection with the determination of the boundary values of both phases. However, the basic approach, as documented in previous work,¹³ was not modified. The essential strategy for both phases is as follows. Pseudo-characteristic forms are used to update the stress and pressure fields assuming trial values of the normal solid- and gas-phase velocity components. The tangential component of velocity is given a trial value from the equations of motion for the gas-phase and by continuation from the interior for the solid-phase. The porosity is updated either from the continuity equation for the solid-phase or from a characteristic form, the choice of the latter depending on the boundary orientation in the case of a stick charge. The density and other thermodynamic parameters of the gas-phase are updated using characteristic forms to maintain compatibility with the trial value of pressure.

Together with the trial future boundary values we identify quasi-linear relationships among them from the characteristic forms. Then the trial values are adjusted, subject to the characteristic constraints, to satisfy the physical boundary conditions. For the solid-phase either the normal stress or the normal velocity component is specified and the solution is completed in a straightforward manner. For the gas-phase the situation is more complicated. The mechanical boundary condition may couple the boundary values of several flows. For example, at an interface between two stick charges, the pressures and mass fluxes of each of the two external (interstitial) and internal (perforation) flows are all coupled through the macroscopic mechanical boundary condition. Moreover, the mechanical relationships are further complicated by the possibility of sonic flow for any or all of the fluxes. Additional complications arise when reactive components are placed on the interfaces and when the interfaces are impermeable. Finally, special considerations have to be taken into account when the sticks are slotted so that the internal and external pressures are equal, even though the gas-phase velocities may differ.

We have taken the approach of solving the mechanical boundary conditions — continuity and momentum — assuming that the density or temperature of the gas-phase does not vary over the time step. Following the determination of the gas-phase pressures and velocities, the enthalpies and other thermodynamic properties — molecular weight, specific heats, pyrolysis product mass fraction — are updated using either the characteristic data or the macroscopic jump conditions, according as the flow is an efflux or an influx respectively. The solution of the mechanical equations is then repeated using these updated values of density. Iteration continues until the solution converges.

The revisions pertaining to this topic are grouped into three categories. Two revisions pertain to the governing equations themselves. A second category pertains to the physical model of the rupture of the case. The third category pertains to the algorithm for the determination of the boundary values.

2.3.5.1 Governing Equations

[1] A coding error was detected in respect to the analysis of flow resistance through the case. This is the only coding error mentioned here. It is noted because it has the effect of changing certain details of the solution for the M203 charge. If K is the dimensionless friction factor which characterizes the resistance of the case to normal penetration by the gas (see Appendix A) then the error had the result that prior calculations used an effective value equal to $K\varepsilon^2/p$ where ε is the porosity of the main charge at the boundary point in question and p is the pressure. The error only pertained to situations in which $K < 100$. Values of $K \geq 100$ were correctly interpreted as representing a completely impermeable case element.

[2] Among the physical boundary conditions which apply at the boundary of the propelling charge is the finite balance of the tangential component of momentum. We have previously discussed the need to modify the obvious direct statement of this principle.¹¹ Large velocity gradients can be produced if influx occurs at a given point on the boundary while an efflux occurs at a neighboring point. We have used a "relaxed" tangential velocity component which reflects the tendency of entering gas to be made conformable with the gas in the mixture due to the effect of the interphase drag. An additional compromise was made in connection with the reactive case segments. The gas produced by combustion on the mixture side of the case is assumed to have a tangential component equal to that of the gas-phase at the boundary. Thus the momentum defect which must be overcome to accelerate the products of combustion of the case to a velocity comparable to that of the mixture is neglected. The physical consequences of this assumption are thought to be small. We also note that this assumption was introduced at an early stage in the shakedown process for TDNOVA. Possibly, it could be eliminated, but testing to confirm this has not been conducted.

2.3.5.2 Rupture of the Case

The data base for TDNOVA admits the prescription of container properties which vary discontinuously from point to point, either initially or as a result of the evolution of the flow. Naturally, such discontinuities place a strain on the numerical scheme. As with the analysis of boundary motion, our approach has been initially to admit all possible situations and then to impose such restrictions as are proved necessary in the search for stable numerical solutions. We have made the following revisions.

[1] If a segment of the case which is burning on its external surface is forced sufficiently close to an external boundary the solution in the ullage is discontinued. If the segment is impermeable, there is no volume to receive the products of combustion of the case. Rather than also discontinuing the model of external burning, which may affect the overall progressivity of the charge, we allow an impermeable case segment, which is both burning on the outside and in contact with an external boundary, to begin to rupture at the time when contact occurs.

[2] If a case segment is described as being very permeable to the gas-phase it may happen that the sum of the intergranular stress and the pressure differential are never sufficiently large to cause rupture. Accordingly, we have provided an option which causes rupture to begin locally for a case segment whenever the main charge is locally ignited, and independently of whether or not the mechanical forces are capable of inducing rupture. The option can be applied independently to each of the case segment types or uniformly, through a global switch.

[3] The revision of interest here has already been discussed in Section 2.2.3.2. As noted there, when a rigidized case fails we consider that the case is locally ruptured in the sense of the flexible case model. We do not repeat the details of motivation or implementation here.

[4] It may happen that part of the case sidewall is ruptured quite early in the calculation, as for example if the rigidized model leads to failure at any interior point. Failure of the remainder of the sidewall may be delayed until igniter gases penetrate the failed, and therefore increasingly permeable, sidewall section and ignite the main charge increment. If the failed section of the sidewall is permitted to expand freely during this ignition interval, the shape of the boundary will become sufficiently structured as to introduce numerical strain which will clearly manifest itself in the form of wiggles in the pressure field. To ease the numerical strain somewhat we have revised the code to permit radial expansion of the sidewall at a point where the case is fully ruptured only if both the neighboring points are also fully ruptured.

2.3.5.3 Boundary Value Algorithm

We note six revisions here. The last four of these relate to the determination of gas-phase pressures and mass fluxes on all boundary points other than the corners. In the present section the discussion of these four revisions is confined to a brief statement of the reasons for and nature of each of them. Because of the importance of this topic, however, and also because the revisions are non-trivial, we provide a self-contained discussion of the solution of the pressure/mass-flux boundary conditions in Appendix A.

[1] In the previous version of TDNOVA,¹⁴ values of pressure at the corners of the two-dimensional regions were determined by taking the average of the values of the neighboring points on the two boundary elements which defined the corner. For purely one-dimensional flows this approach introduces an obvious amount of computational noise. Following some experimentation, the algorithm for the definition of the boundary values was revised to use either the value on the $\tau - \xi$ or the $\tau - \eta$ boundary according as $|\xi_z u_\xi + \xi_r v_\xi| > |\eta_z u_\eta + \eta_r v_\eta|$. Here τ, ξ, η are the computational coordinates which

correspond approximately to t , z and r where t is time and z and r are cylindrical coordinates. We have also used u and v as the velocity components of the gas-phase. The inequality amounts to a test of the flow dilatation rates in each of the two coordinate directions, and was used in our first studies of two-dimensional flow.¹⁰ If the flow is one-dimensional, the corner value will be chosen so as to maintain one-dimensionality.

[2] At quite an early stage in the development of TDNOVA,¹¹ it was decided to determine the tangential velocity component of the solid-phase by continuation from the interior rather than by using the equations of motion on the boundary itself. This decision was connected with the possibility that due to the transfer of gas into the mixture, an anomalously high tangential interphase drag component might cause excessive boundary deformation. The necessity of using the continued tangential component has not been investigated subsequently. Since many other code revisions have been incorporated it is possible that testing might reveal that the continuation is no longer required. However, such testing has not been done and the following revisions were made in connection with the determination of porosity and intergranular stress on the boundaries. For stick charges we also use continued values of porosity and transverse intergranular stress on the $\tau - \zeta$ boundaries; on the $\tau - \eta$ boundaries we use a continued value of the longitudinal stress.

[3] A revision was made to the determination of the pressure and mass flux at a boundary having a finite value of surface flow resistance. A Newton-Raphson scheme was coded to account for the influence of the quadratic terms in the momentum equation. The revised analysis is described in Appendix A.

[4] The gas-phase momentum balance is factored to determine the ratios of the pressures of each of the streamlines intercepting the boundary element. The pressures are all related through coefficients which are functions of the Mach number. Previously, these coefficients were based on data in current storage. This has been revised to limit the coefficients explicitly to the values obtainable in a sonic flow. Further details are given in Appendix A.

[5] Previously, we determined the boundary values of pressure for a slotted stick charge, when the slot was open, in the following way. First we obtained trial values of the external and internal pressure from the characteristic forms. Second we determined a mass flux through the slot which would equilibrate the internal and external pressures. Third, we adjusted the pressures and fluxes to satisfy the physical boundary conditions. As a result of the third step the internal and external pressures could fail to be equilibrated on the boundary. Some oscillation of boundary values was observed under some conditions. Accordingly, the scheme for the determination of the boundary values was modified to maintain the equilibration of the internal and external gas-phase pressures for the slotted stick. Details are given in Appendix A.

[6] In TIDNOVA we consider that two adjacent charge increments are always separated by a region of ullage which may be either open, if they are sufficiently far apart, or closed, if the increments are sufficiently close. The two-dimensional method of solution entails a continuum analysis of the ullage, in the tangential direction, only when it is open. Previously, the decision to treat a region of ullage as locally closed was based solely on the criterion that its transverse dimension exceed 1 mm. Under some conditions, at low pressure during flamespreading, involving ullage between two increments with large values of through flux, the predicted density in the ullage may become negative. Accordingly, we modified the criterion to treat the ullage as closed so as to take into account the ratio of the through flux to the gas contained in the mesh cell. Details are given in Appendix A.

3.0 THE M203 PROPELLING CHARGE

In the present chapter we consider the M203 Propelling Charge for the 155-mm Howitzer. We have previously reported on the applicability of TDNOVA to the simulation of this charge¹¹ and it was the subject of a study by Horst.¹⁴ The study by Horst included a comparison with NOVA and an assessment of the influence of computational elements of the data base. Since the time of these prior studies TDNOVA has undergone substantial development and revision.^{12,13} It is therefore of interest to determine the implications of the code revisions insofar as previous important milestone conclusions are concerned.

In Section 3.1 we describe the charge from a physical standpoint and discuss the representation by TDNOVA. Differences from the previous representation are noted. In Section 3.2 we present some details of the solution based on nominal computational parameters. Then, in Section 3.3, we study the influence of the computational parameters on various aspects of the solution.

The M203 Charge is also used in Chapter 7.0 as a baseline to examine the effects of heat transfer to the tube and a finite rate of release of energy in the gas-phase.

3.1 Nominal Data Base

The M203 Charge is illustrated in Figure 3.1. It consists of approximately 12 kg of M30A1 granular propellant contained in a cloth bag. The charge includes a basepad igniter and a centercore tube igniter which runs the length of the charge. While the bag is gas-permeable, the centercore tube is not. In addition, the forward two-thirds of the outer sidewall of the bag includes a lead foil liner which obstructs penetration by the gas-phase. A further impediment to penetration of the bag by ignition gas is due to the salt bag attached to the front of the bag. Since the diameter of the bag is less than that of the chamber, annular ullage is initially present and the initial configuration is not axisymmetric. The charge is normally spaced away from the spindle face. Therefore, axial ullage is normally present at each end of the charge.

The representation of the charge by TDNOVA is defined by the tabulation of the input data given in Appendix B and also by Figure 3.2. Appendix B contains the tabulation of data in essentially the same format as the TDNOVA printout. Figure 3.2 illustrates the axisymmetric representation of the charge which is necessarily assumed by the code. Little is known about the consequences of neglecting three-dimensional details of the charge distribution. Some experimental steps towards understanding three-dimensional details have been reported by Minor.³¹

³¹ Minor, T.C.

"MultiDimensional Influences on Ignition, Flamespread and Pressurization in Artillery Propelling Charges"

Proc. 20th JANNAF Combustion Meeting

1983

The boundaries of the main charge are considered to be the rear and forward endwalls, the outer sidewall and the centercore tube. These boundary elements are considered to have neither thickness nor inertia. However we do attribute flow resistance to each segment and we attribute reactivity to the outer part of the rear endwall, thereby simulating the basepad as a surface source term. The basepad is also represented as extending over the rear endwall of the centercore tube. We note the convention for the reactivity file pointer, a four digit number. The digits, read from left to right, point to files for the inner attached, inner surface, outer surface and outer attached reactive substrates. Figure 3.2 shows that four different sets of permeability data are used to represent the charge. Referring to Appendix B we see that the initial value of K_1 is 0.01 so that the rear portions of the bag, including part of the outer sidewall, are represented as very permeable. On the other hand, the initial values of K_2 , K_3 and K_4 are 101. so that the remaining sections of the container are represented as initially impermeable.

We note that the rate of combustion of the basepad is prespecified. Because both the rear endwall of the bag and the end of the centercore are permeable, the igniter gas will stimulate both the centercore and the main charge. The centercore is taken to contain black powder. Because of uncertainties about the role of condensed phases in promoting flamespread through black powder, the ignition temperature is set to an artificially low value, namely 300°K . Accordingly, our representation of the charge will strongly favor ignition of the centercore before the main charge increment.

The representation given here differs from that considered by Horst.¹⁴ First, as we have already described, in Chapter 2.0. a correction has been made to the dimensionless friction factor which defines the flow resistance of the bag. Second, at one stage in the present effort it was discovered that a stable calculation of the M203 Charge could no longer be obtained. The breakdown was associated with the sudden change in permeability of the forward endwall following rupture. The data base considered by Horst¹⁴ defined the rupture interval for the forward endwall as zero. Accordingly, the flow was required to adjust instantaneously from a condition of complete impermeability to complete permeability. Although the code was able to withstand this requirement in its earlier versions, the more recent versions were found to break down. Accordingly, the data base was revised to include an arbitrarily selected 2 msec interval of rupture for the forward endwall. Third, following the other revisions of the present effort, it was found that the rear part of the outer sidewall would not rupture. Accordingly, transition to a quasi-two-dimensional representation would not occur. Therefore, we exercised the code option which allows rupture to commence when the main charge is locally ignited. This option was applied only to the rear part of the outer sidewall for which $K_1 = 0.01$ initially.

We note the computational elements of the data base. These are the number of axial mesh points assigned to the main charge, the number of radial mesh points assigned to the main charge and the pressure tolerance factor which controls the transformation to a quasi-two-dimensional representation. Denoting these parameters by Z, R and P respectively, we note the convention that we will refer to the computational set in the form Z X R @ P. Thus the nominal mesh is described as the 30 X 7 @ 0.01 case.

3.2 Nominal Solution

Aspects of the nominal solution are presented in Figures 3.3, 3.4 and 3.5. Figure 3.3 illustrates the pressure distribution at a variety of times. Figures 3.4 and 3.5 depict the solid- and gas-phase velocity fields respectively.

Referring to Figure 3.3, we see that at 1 msec the centercore is substantially ignited. Since the centercore tube is initially impermeable it confines the products of combustion of the black powder. Thus the pressure in the centercore exceeds that in the main charge. The pressure differential increases until the rupture criterion for the centercore tube is satisfied. Subsequently, the pressure differential is moderated by the increasing permeability of the tube and eventually becomes negligible. By 2.0 msec rupture of the tube is nearly complete over the rear section and the main charge is pressurized. Towards the front, however, the interior of the centercore tube is still at a higher pressure than the main charge. We also see a pressure jump across the forward end wall. By 3.5 msec the main charge is fully ignited and the solution is becoming increasingly one-dimensional, as far as the pressure field is concerned. The inner part of the forward endwall has ruptured. As the gas flows out, it drags the solid-phase towards the projectile base. By 4.0 msec impact against the projectile has occurred.

Figures 3.4 and 3.5 reveal the degree to which the forward endwall is deformed at 4.0 msec. The sharp variation in flow area in the forward axial ullage creates numerical strain which is responsible for the pressure wiggle seen at 4.0 msec in Figure 3.3.

By 5.421 msec however, the charge has made full contact with the projectile base—see Figure 3.4—and the pressure field has become almost perfectly one-dimensional—see Figure 3.3. At this point the pressure tolerance criterion is satisfied and the transformation to a quasi-two-dimensional representation occurs. Figure 3.3 contains distributions from this phase of the calculation at times equal to 5.421, directly after the transformation occurs, at 9.0 msec, near maximum pressure, and at 16.0 msec, just prior to muzzle exit.

The simulation of the M203 Charge presented here differs from that obtained by Horst¹⁴ with the earlier representation. The persistent pressure differential across the forward endwall was not seen previously. The present calculation continues much further in the fully-two-dimensional mode than the earlier simulation. As a consequence the present calculation is required to treat the fully-two-dimensional impact of the solid-phase against the base of the projectile.

The nominal solution required 289 seconds of CPU time on the CYBER 7600 computer.

3.3 Influence of Computational Parameters

The influence of computational parameters on various details of the simulation of the M203 Charge is illustrated by Figures 3.6 through 3.13 and by Table 3.1.

The effect of the number of axial mesh points on the pressure distributions at 2.0, 3.5 and 4.0 msec is shown in Figures 3.6, 3.7 and 3.8 respectively. No substantial differences are seen. We do note, in Figure 3.6, an increasing resolution of detail near the forward part of the outer sidewall. A small excursion due to the flow resistance of the bag is seen to emerge progressively with increases in the number of axial mesh points. We also note, in Figure 3.8, that the wiggles associated with partial collapse of the forward axial ullage are exacerbated as the number of mesh points increases. This increase in the amplitude of the wiggles reflects the fact that the underlying cause is a discontinuous variation of bag properties as we move along the boundary.

The effect of the number of radial mesh points is shown in Figures 3.9, 3.10 and 3.11 which focus on the same three points in time, namely 2.0, 3.5 and 4.0 msec. Again, additional mesh points do not help the situation in the forward axial ullage near the time of impact of the solid-phase against the projectile. In fact, a smoother solution is obtained by reducing the number of radial mesh points, as we see in Figure 3.11.

In general, Figures 3.6 through 3.11 indicate that the nominal choices of 30 axial mesh points and 7 radial mesh points are adequate and that the solution is little changed by increases in those computational parameters. Possibly, smaller values could be used without undue loss of accuracy.

The adequacy of the mesh is also confirmed by Figures 3.12 and 3.13. Here we demonstrate the effect of mesh refinement on the path of flamespreading—Figure 3.12—and the structure of the ignition-induced pressure wave—Figure 3.13. Figure 3.13 represents the difference between the pressure at the breech and that at the mouth of the combustion chamber. In both cases the centerline value is used. Although some differences in fine structure are observed in Figure 3.13, the mesh indifference is very good.

Further information concerning the influence of the computational parameters is given in Table 3.1. Here, in addition to the number of mesh points, we consider the influence of the pressure tolerance factor. We also examine the behavior of the mass defect as defined in Section 2.3.3. Each run is identified by its computational parameters according to the convention of Section 3.1. We then tabulate the maximum breech pressure (p_{max}), the muzzle velocity (m.v.), the first minimum of the pressure difference history (Δp_{min}), the time at which transformation to a quasi-two-dimensional representation occurs (t_{2QD}), and three values of the percent mass defect ($\Delta m\%$). We present the maximum, minimum and final values of $\Delta m\%$.

Table 3.1 Effect of Computational Parameters on Simulation of M203 Propelling Charge

Run	p_{max} (MPa)	m.v. (m/s)	Δp_{min}^* (MPa)	t_{Q2D} (msec)	max	$\Delta m\%(-)$ min final	
Nominal Case							
30 X 7 @ 0.01	360.7	836.2	-11.4	5.42	0.00	-1.87	-1.44
Effect of Number of Axial Mesh Points							
15 X 7 @ 0.01	354.2	831.6	-12.6	5.02	0.00	-1.75	-0.88
45 X 7 @ 0.01	362.2	834.1	-12.5	5.58	0.00	-1.81	-1.81
Effect of Number of Radial Mesh Points							
30 X 5 @ 0.01	372.3	845.8	-18.4	5.47	0.84	-1.29	0.30
30 X 9 @ 0.01	357.9	836.9	-11.3	4.44	0.00	-1.53	-1.42
30 X 11 @ 0.01	356.7	835.1	-11.8	4.41	0.31	-1.14	-1.03
Effect of Pressure Tolerance Factor							
30 X 7 @ 0.05	358.4	838.9	- 2.6	3.15	0.56	-0.98	-0.16
30 X 7 @ 0.10	358.4	838.9	- 2.6	3.15	0.56	-0.98	-0.16
30 X 7 @ 0.005	379.2	848.5	-12.2	5.92	0.70	-1.05	0.14

* First minimum of pressure at 87.37 cm minus pressure at 0.01 cm on centerline

The preceding observations concerning the indifference of the simulation to the number of mesh points are confirmed by the results of Table 3.1. With the exception of the 30 X 5 @ 0.01 case, the predictions of p_{max} , m.v. and Δp_{min} all show an acceptable level of insensitivity to the number of mesh points. Excepting the 30 X 5 @ 0.01 case, the variation in p_{max} is less than 2% while that of m.v. is less than 0.5%.

The range of values of the mesh parameters is too limited to permit us to say that convergence is demonstrated. However, we note that the variations in the ballistic predictions are of approximately the same magnitude as the external values of $\Delta m\%$. As discussed in Section 2.3.3. the value of $\Delta m\%$ may be viewed as providing an independent estimate of the accuracy of global aspects of the solution.

We turn now to the influence of the pressure tolerance factor. The results of Table 3.1 show that the ballistic predictions are not indifferent to the value of this parameter. The cases with values of the pressure tolerance factor equal to 0.10 and 0.05 appear to give essentially identical results. While these two cases give predictions of p_{\max} and m.v. which are in close agreement with the nominal 30 X 7 @ 0.01 case, they produce a noticeably lower value of Δp_{\min} . On the other hand, the 30 X 7 @ 0.005 case produces a value of Δp_{\min} close to that of the nominal mesh, but the predictions of p_{\max} and m.v. are significantly higher than the nominal values.

If we examine the mass defects we see that all three values for the 30 X 7 @ 0.005 case exceed those of the nominal case by approximately 1%. This differential suggests that the higher values of p_{\max} and m.v. obtained with the 30 X 7 @ 0.005 case might be due to mass balancing errors. However, the possibility that other factors might be at work is immediately suggested when we examine the values of $\Delta m\%$ for the 30 X 7 @ 0.05 and 30 X 7 @ 0.10 cases. These values are in close agreement with those for the 30 X 7 @ 0.005 case. Nevertheless, we considered it to be of interest to prepare a temporary version of the code in which perfect mass balancing was enforced after every time step. In this temporary version we computed the mass defect and then adjusted all values of gas-phase density and porosity by a common factor which restored the value of $\Delta m\%$ to zero.

We ran the 30 X 7 @ 0.01 and the 30 X 7 @ 0.005 cases with the temporary code version. Although the values of $\Delta m\%$ are necessarily zero, the same is not true of the values of $\Delta e\%$ and we examine them to see whether some other global balancing error might be of significance. In Table 3.2 we summarize the values of p_{\max} , m.v., t_{Q2D} and three values of $\Delta e\%$. All three

Table 3.2 Effect of Pressure Tolerance Factor on Simulation of Propelling Charge with Perfect Mass Balancing

Run	p_{\max} (MPa)	m.v. (m/s)	t_{Q2D} (msec)	$\Delta e\%$		
				max	min	final
30 X 7 @ 0.01	363.9	839.9	5.16	0.37	-0.52	-0.31
30 X 7 @ 0.005	371.3	843.5	5.64	0.38	-0.46	-0.24

values of $\Delta e\%$ are seen to be in close agreement for the two computational cases. We also see that the values of p_{\max} and m.v. are brought into closer agreement when perfect mass balancing is performed. Nevertheless, the residual differences are larger than those induced by changes in the number of mesh points.

The present dependence of the results on the value of the pressure tolerance factor may be contrasted with the previous finding of Horst who saw little effect.¹⁴ In that study, however, the values of t_{Q2D} were 3.49 and 3.51 msec for the 30 X 7 @ 0.01 and 30 X 7 @ 0.005 cases respectively. Here we see a more substantial delay: Tables 3.1 and 3.2 both indicate a delay of approximately 0.5 msec to satisfy the smaller value of the pressure tolerance factor. Moreover, the transformation to a quasi-two-dimensional representation occurs at much higher pressures in the present calculations than in those of Horst.¹⁴ At 3.5 msec the breech pressure is approximately 20 MPa whereas at 5.5 msec it is approximately 80 MPa.

The sensitivity to the time at which transformation to a quasi-two-dimensional representation occurs will require further study. A basic assumption of the modeling approach of TDNOVA has been that detailed radial structure of the flow could be neglected beyond a certain point in time. Moreover, it has been assumed that radial uniformity of the pressure distribution provides an appropriate criterion for the transformation to a quasi-two-dimensional representation. To verify these assumptions one would ideally like to have the complete two-dimensional solution. But stable solutions for the complete interior ballistic cycle have not been obtained as of this date. In the absence of the complete two-dimensional solution one can only seek, as we have done here, to demonstrate indifference of the results to the point at which the transformation to a quasi-two-dimensional solution is effected. From a practical standpoint this goal must be confined to showing indifference to a range of values of the pressure tolerance factor larger than some minimum which corresponds to the onset of instability in the fully-two-dimensional mode. It may be that the value 0.005 is too close to the minimum and that the observed increases in P_{max} and m.v. are symptomatic of latent instability. Or, it may be that the fully-two-dimensional solutions actually do differ from their quasi-two-dimensional counterparts. In either case, our inability to show complete indifference to the pressure tolerance factor makes it necessary to pursue the goal of obtaining complete two-dimensional solutions in subsequent work.

It may also be desirable to provide the mass balance correction as an option. Tracking of the cumulative correction would serve as a guide to accuracy in the same way as the present tabulation of $\Delta m\%$. Such an option would be useful provided that the cumulative correction did not exceed a few percent.

CHARGE, PROPELLING, 155MM, M203 (RED BAG, ZONE 8S)

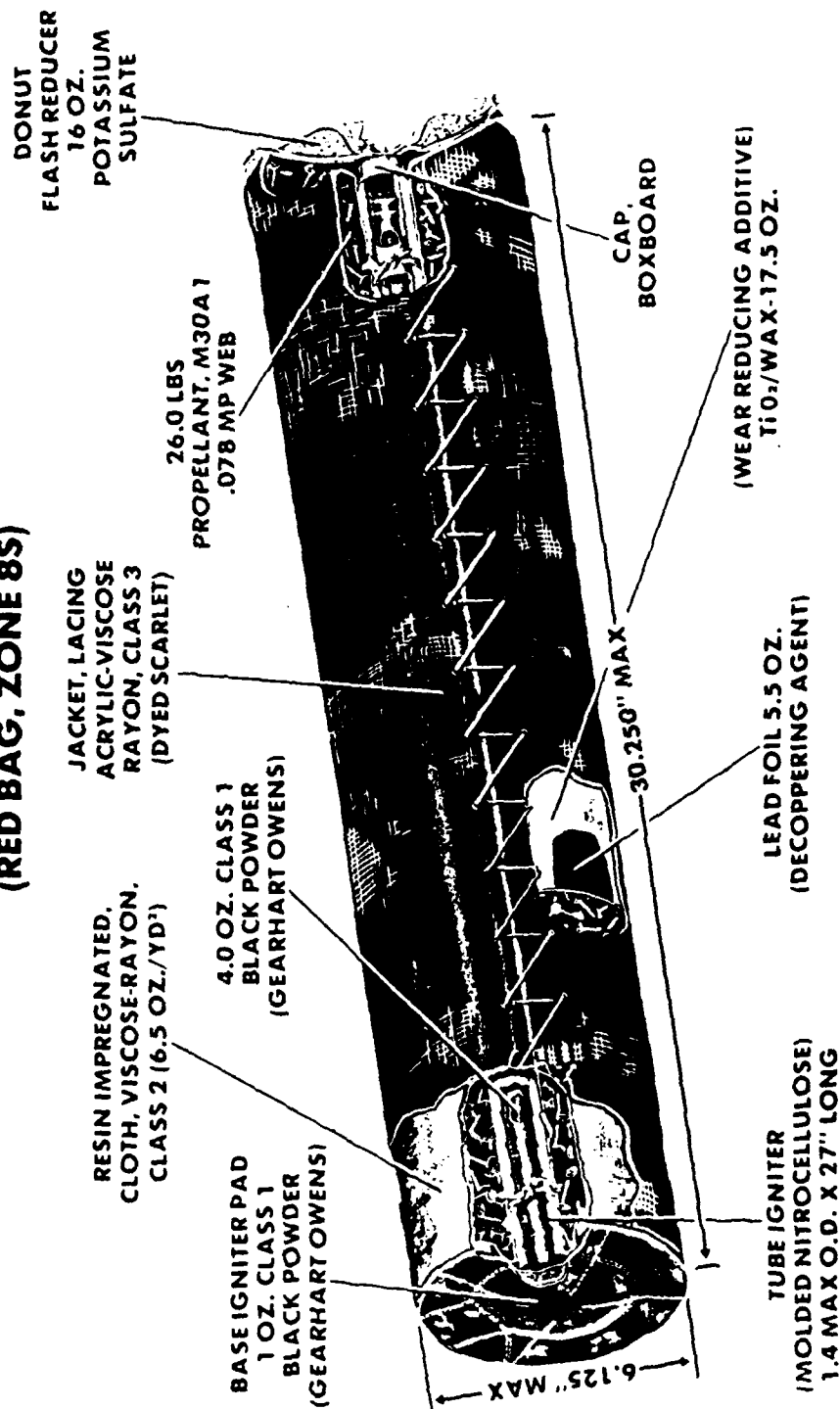


Figure 3.1 The M203 Propelling Charge

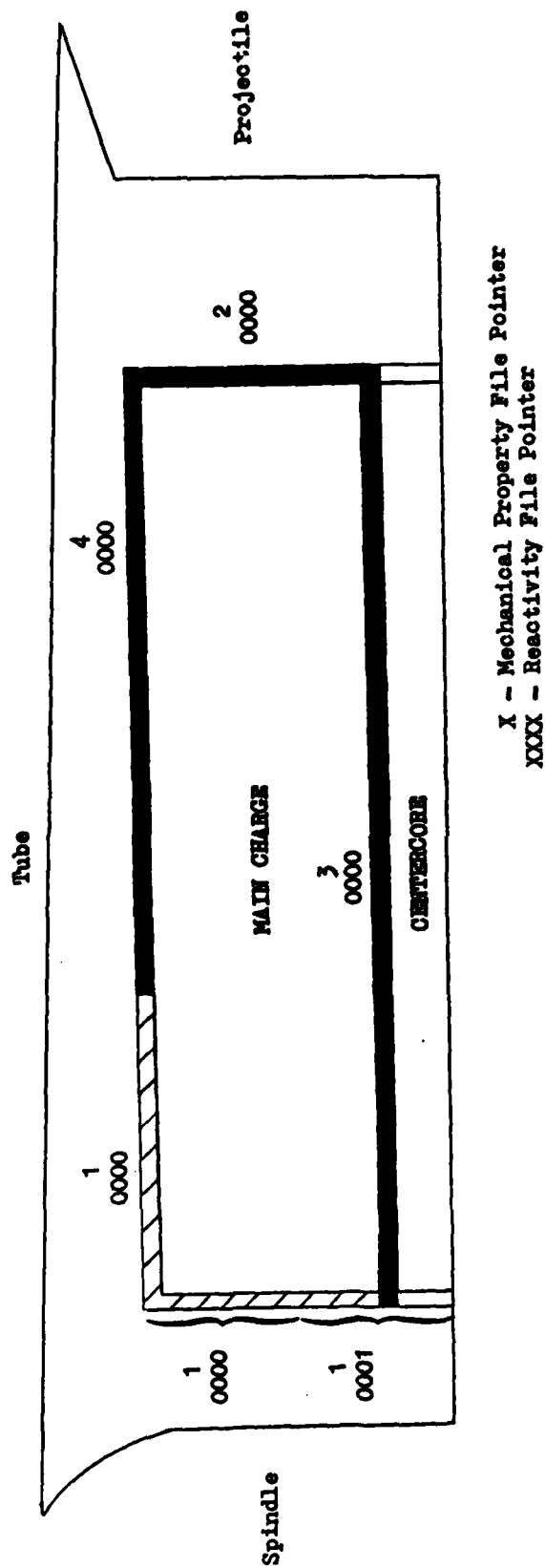


Figure 3.2 Representation of M203 Charge by TUNOVA

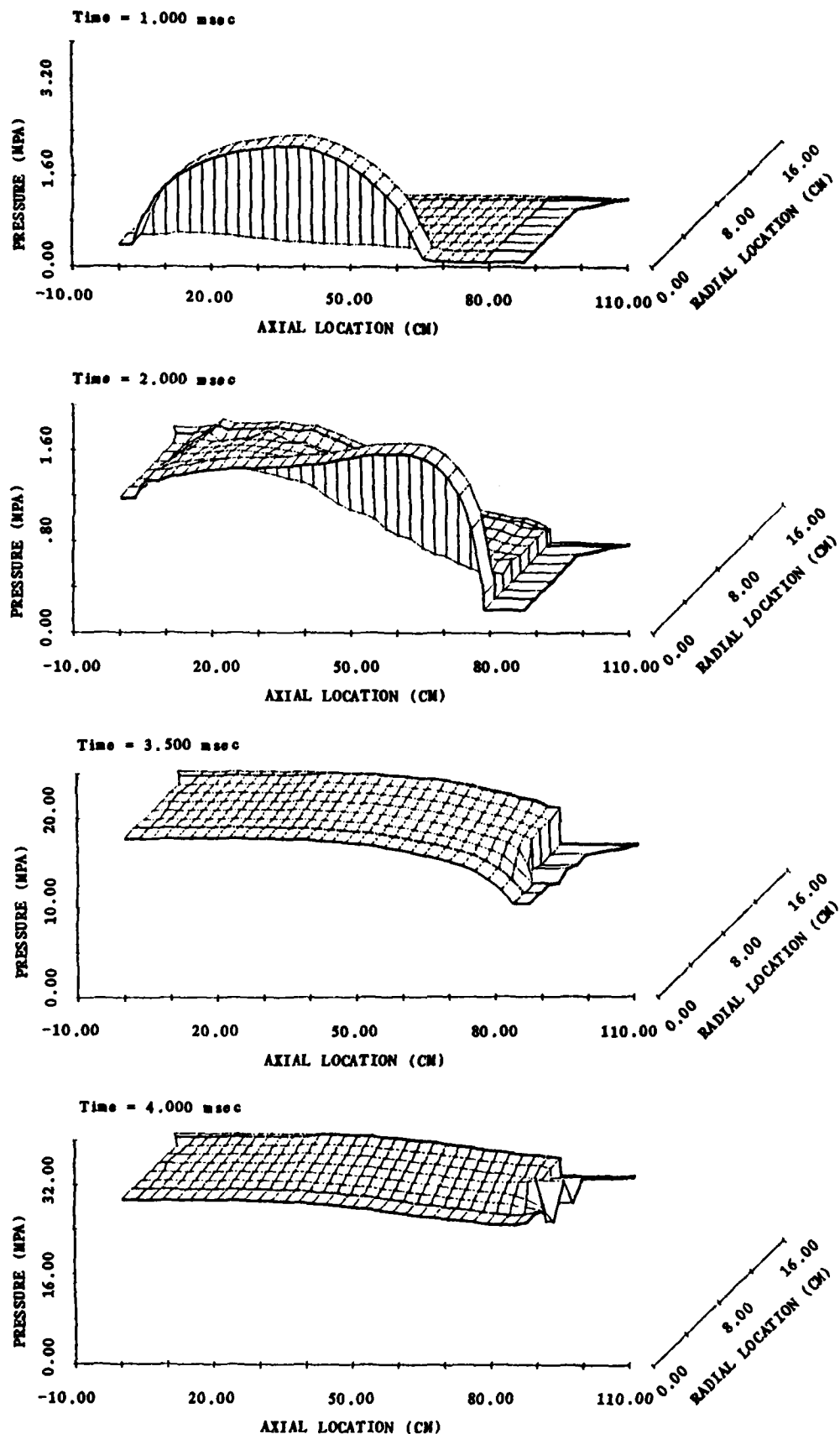


Figure 3.3 Pressure Distributions for M203 Charge Obtained with Nominal Mesh (30 X 7 @ 0.01)

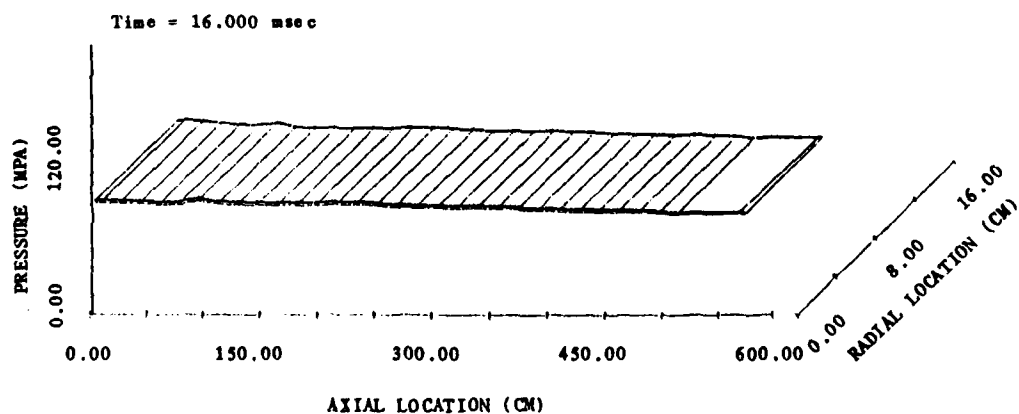
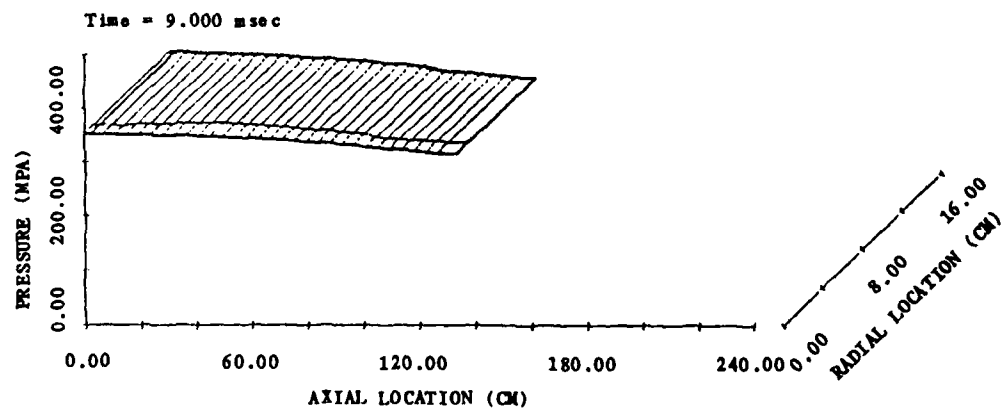
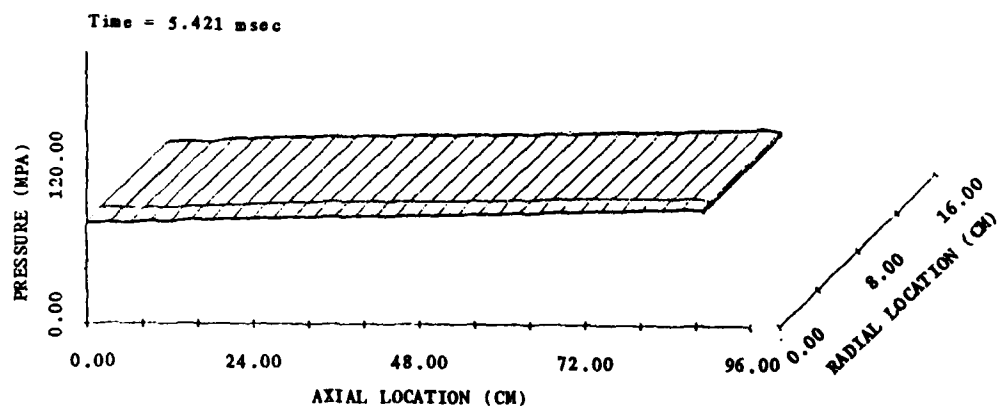
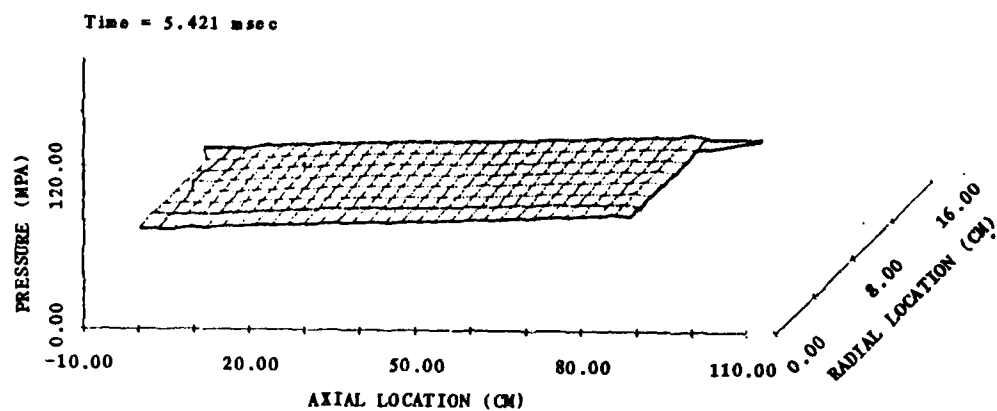


Figure 3.3 Continued

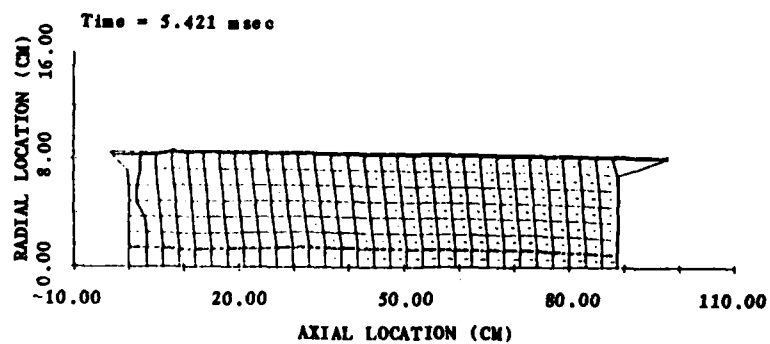
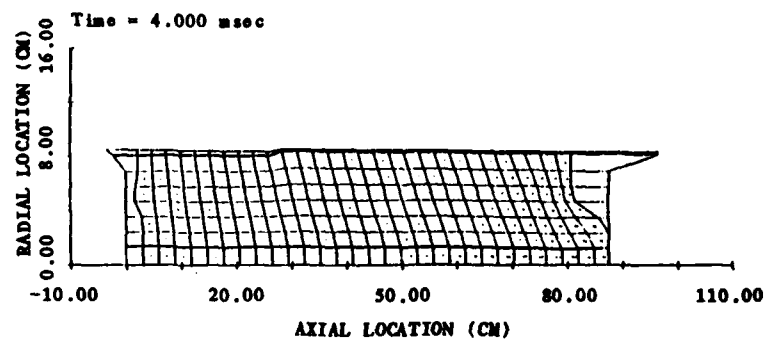
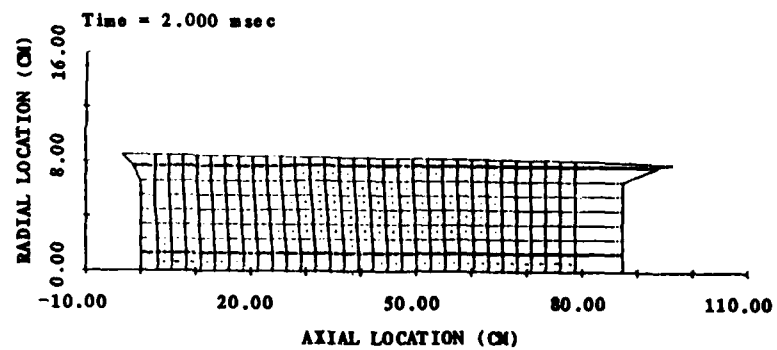
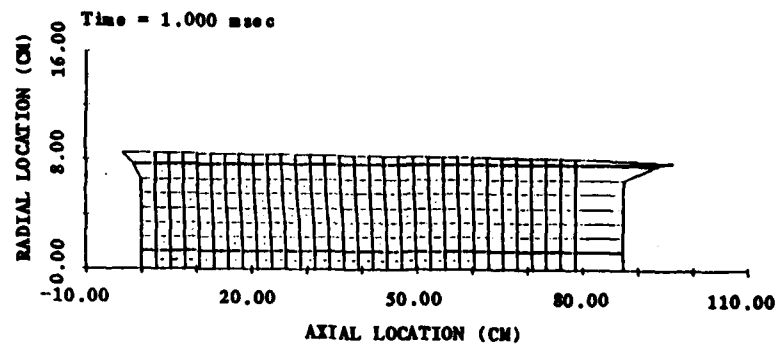


Figure 3.4 Solid-Phase Velocity Fields for M203 Charge Obtained with Nominal Mesh (30 X 7 @ 0.01)

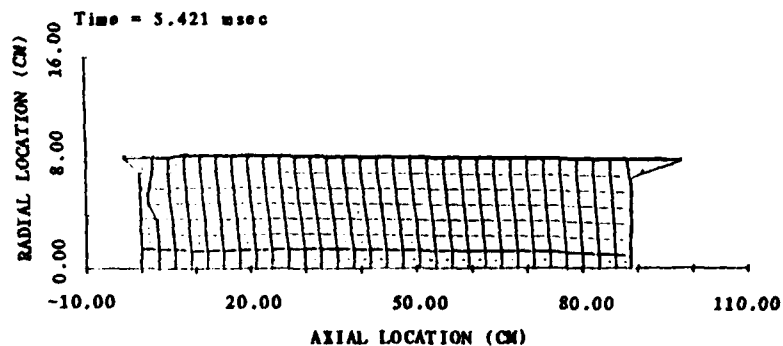
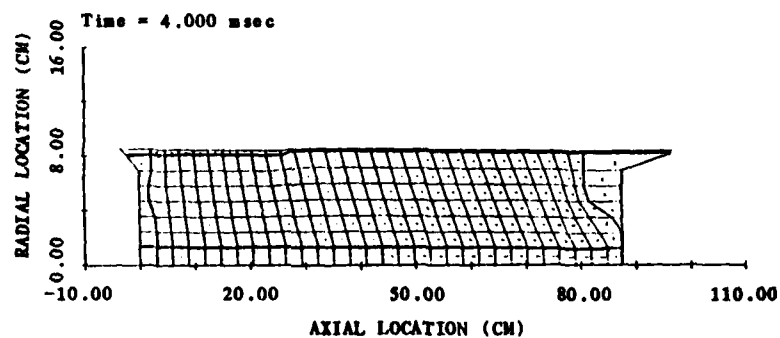
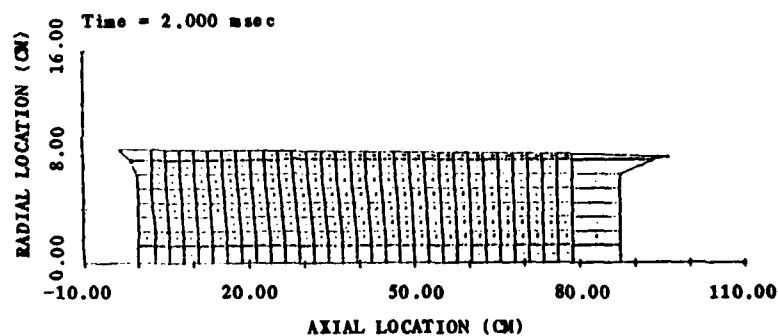
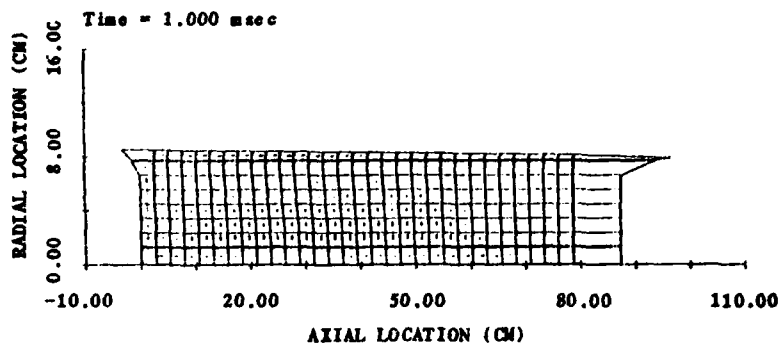


Figure 3.5 Gas-Phase Velocity Fields for M203 Charge Obtained with Nominal Mesh (30 X 7 @ 0.01)

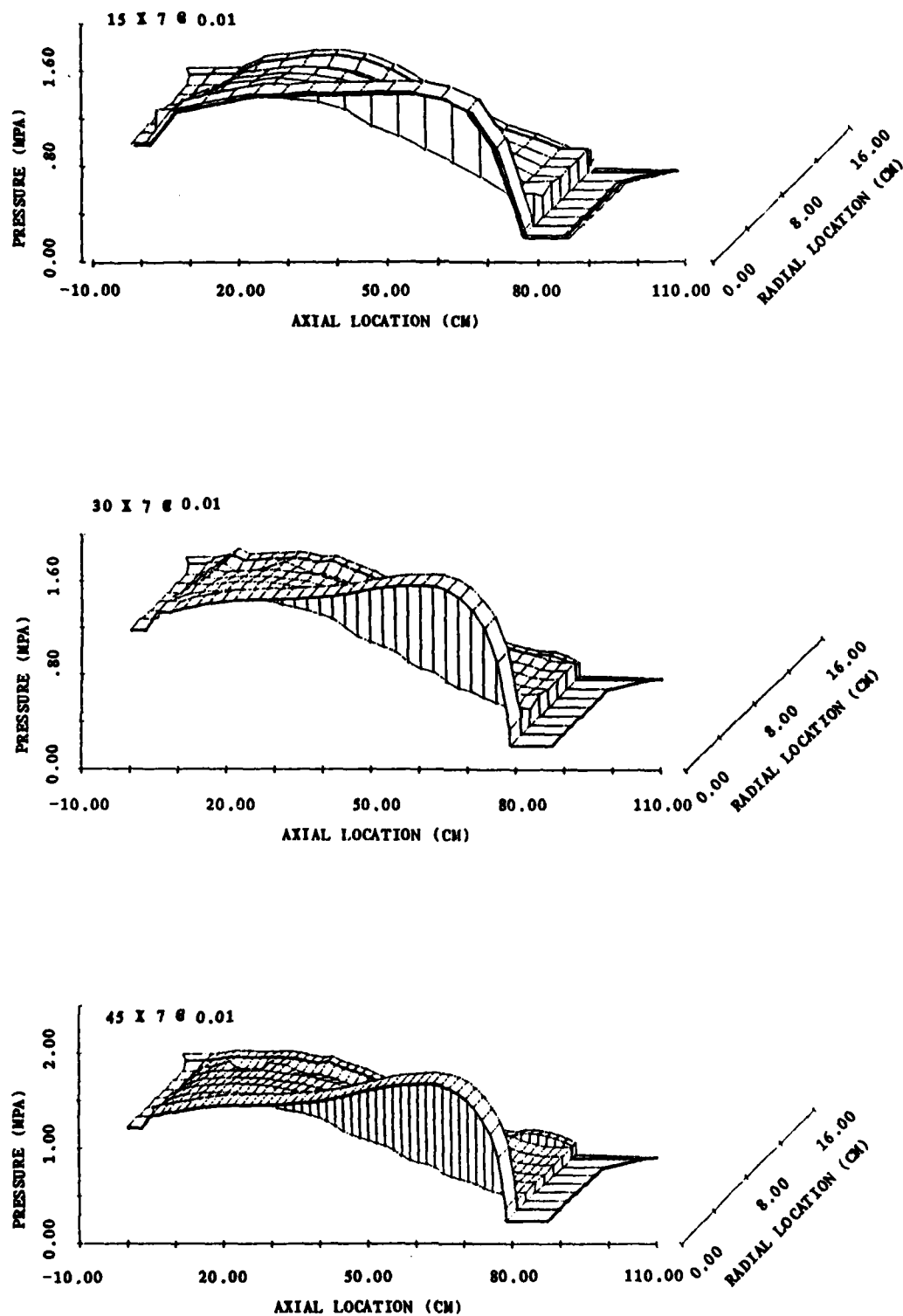


Figure 3.6 Influence of Number of Axial Mesh Points on Pressure Distribution for M203 Charge at 2.0 msec

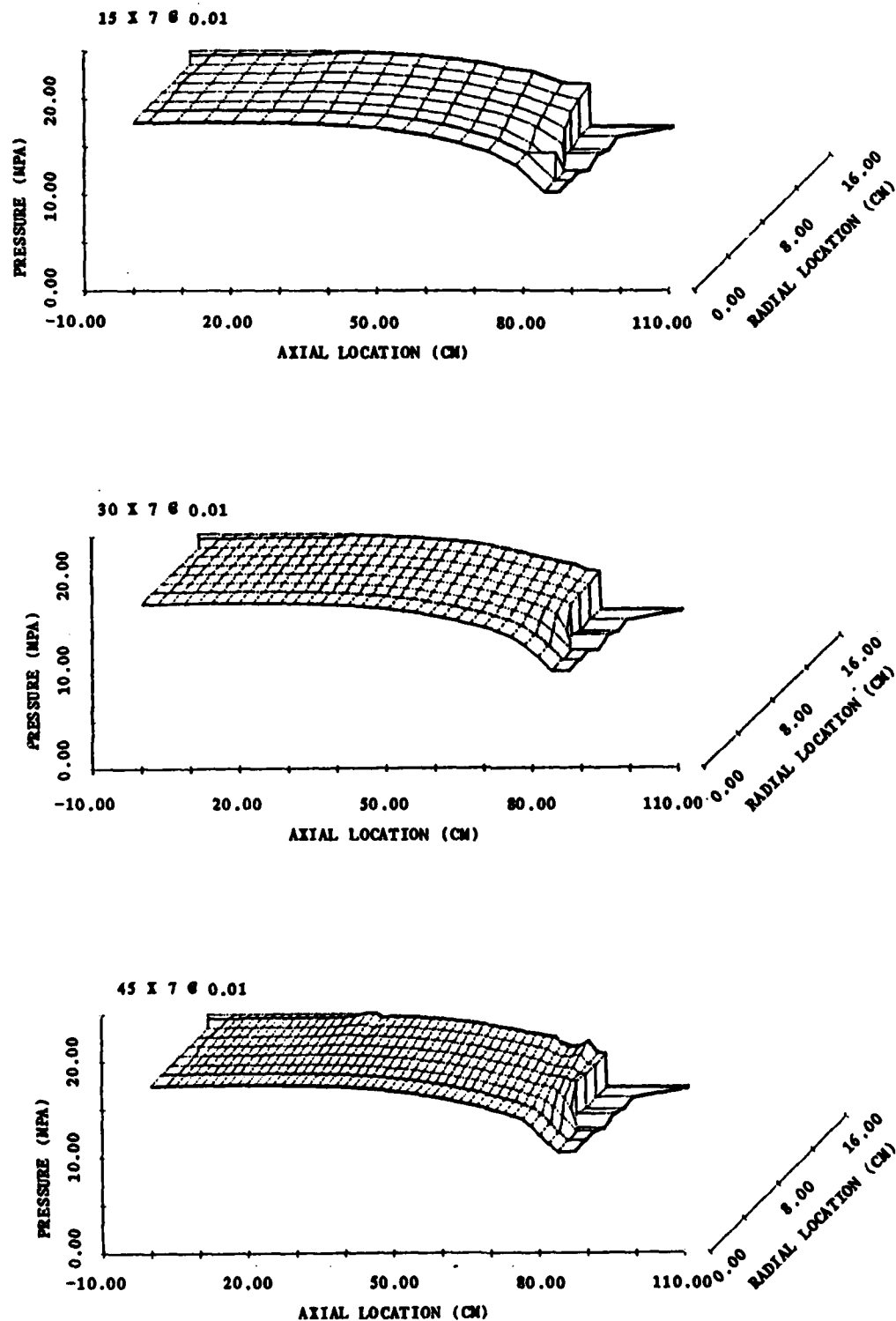


Figure 3.7 Influence of Number of Axial Mesh Points on Pressure Distribution for M203 Charge at 3.5 msec

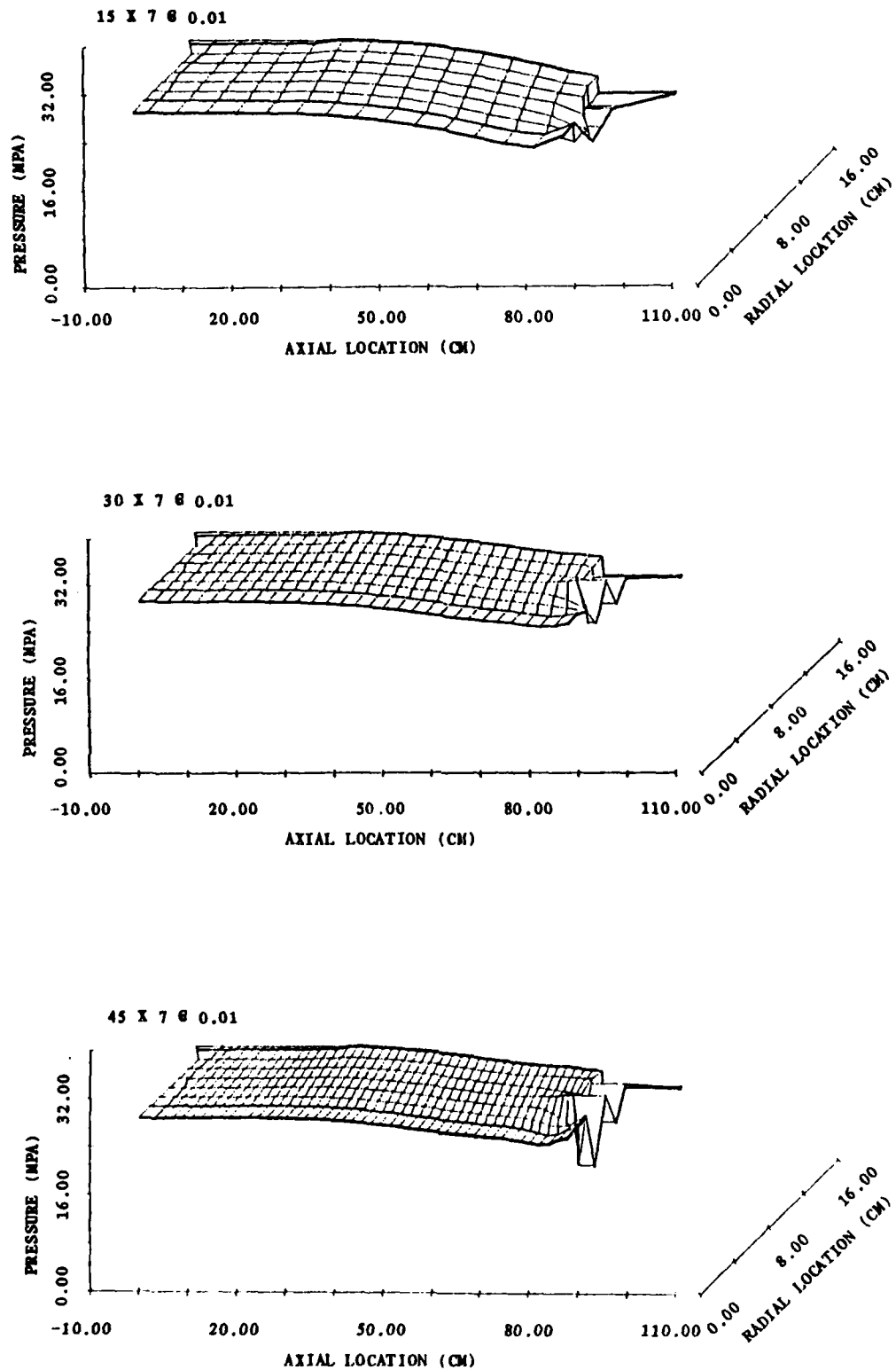


Figure 3.8 Influence of Number of Axial Mesh Points on Pressure Distribution for M203 Charge at 4.0 msec

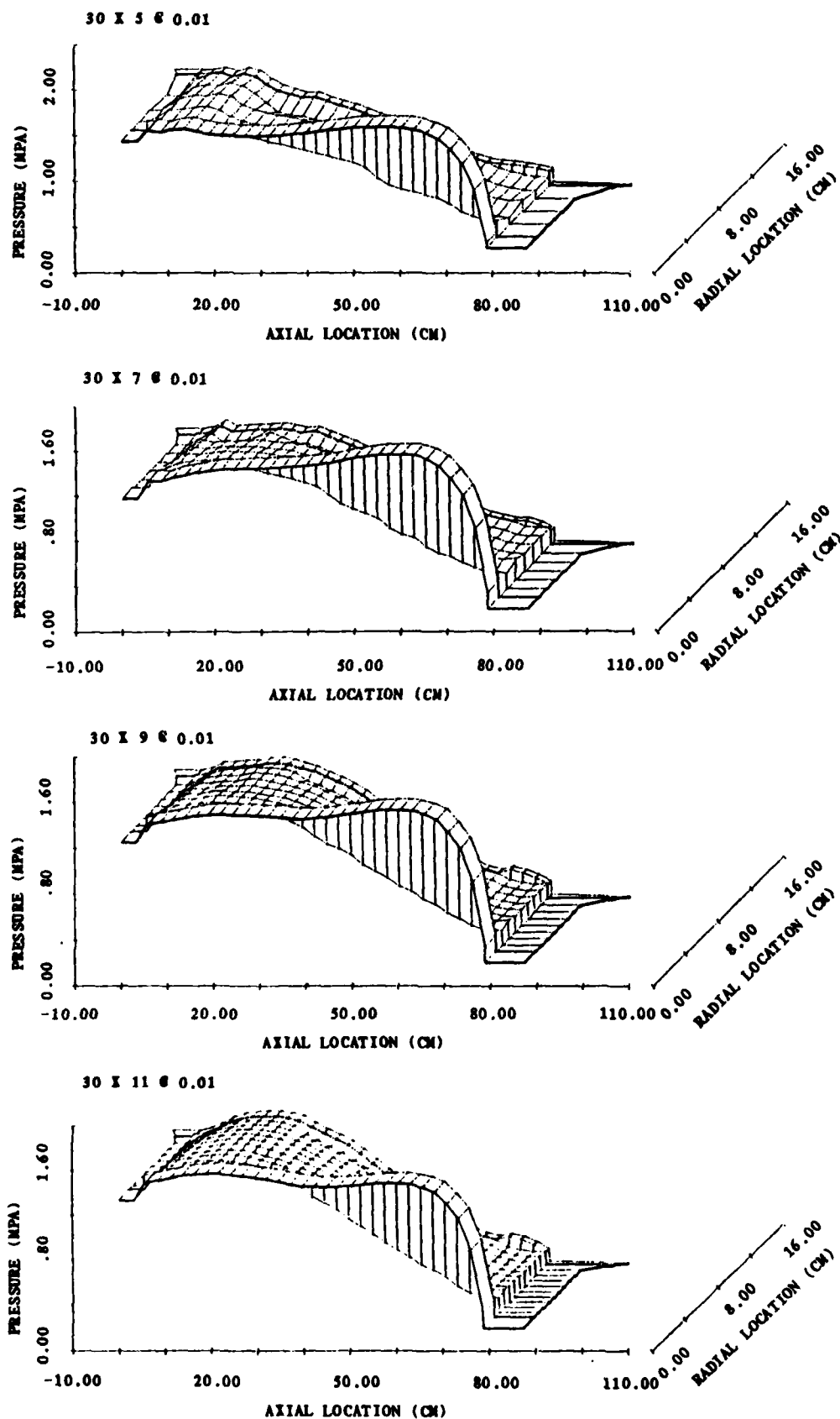


Figure 3.9 Influence of Number of Radial Mesh Points on Pressure Distribution for M203 Charge at 2.0 msec

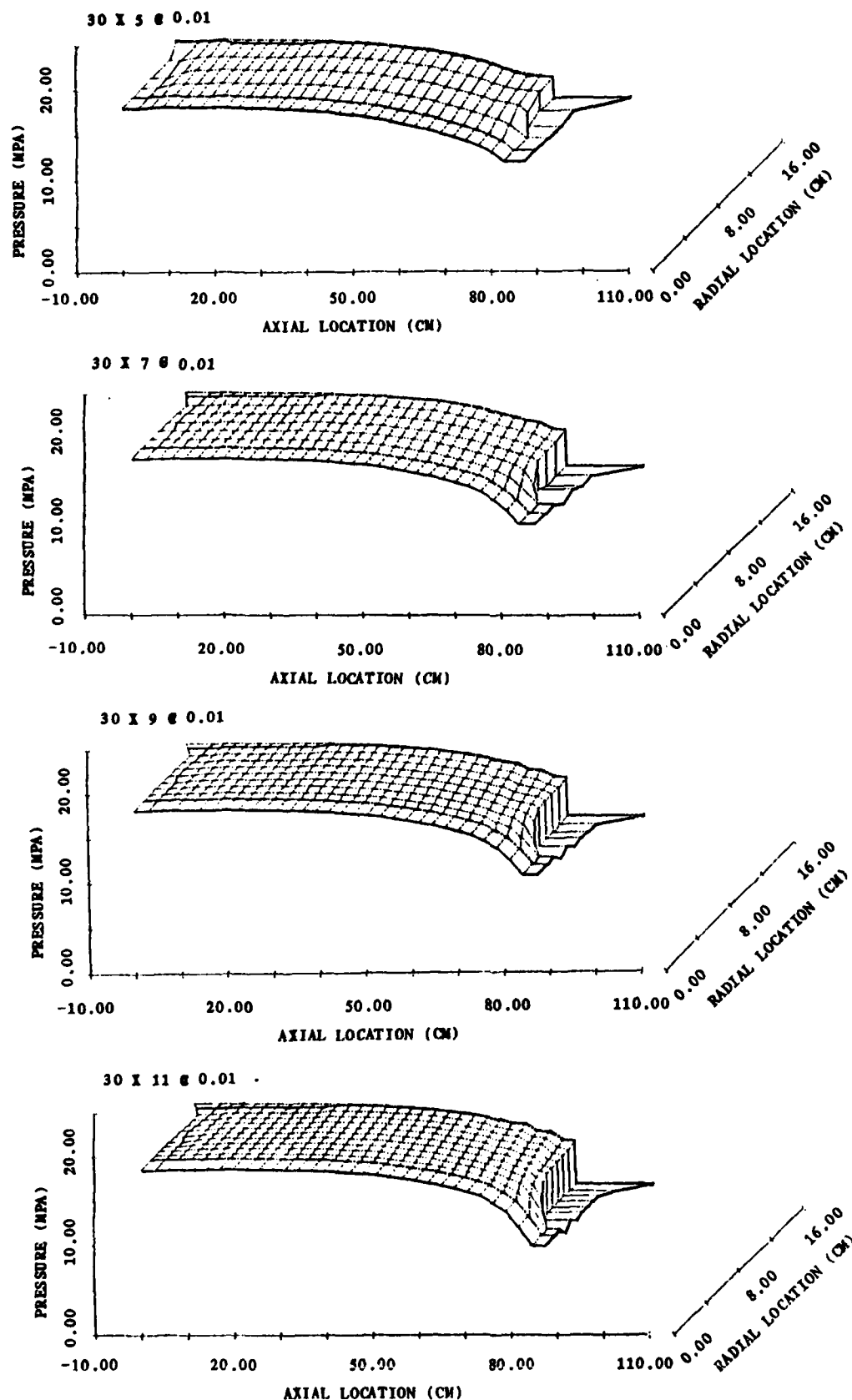


Figure 3.10 Influence of Number of Radial Mesh Points on Pressure Distribution for M203 Charge at 3.5 msec

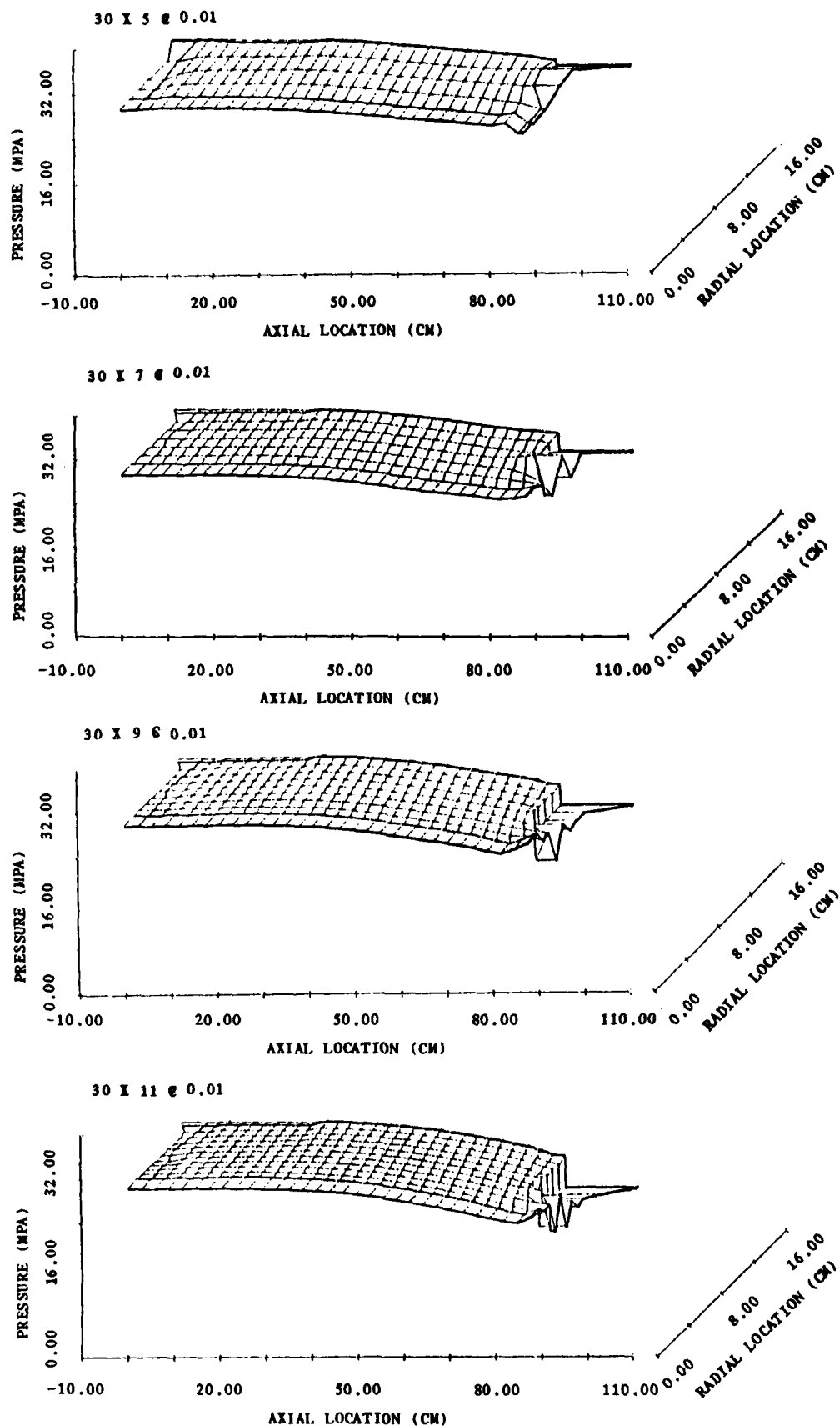


Figure 3.11 Influence of Number of Radial Mesh Points on Pressure Distribution for M203 Charge at 4.0 msec

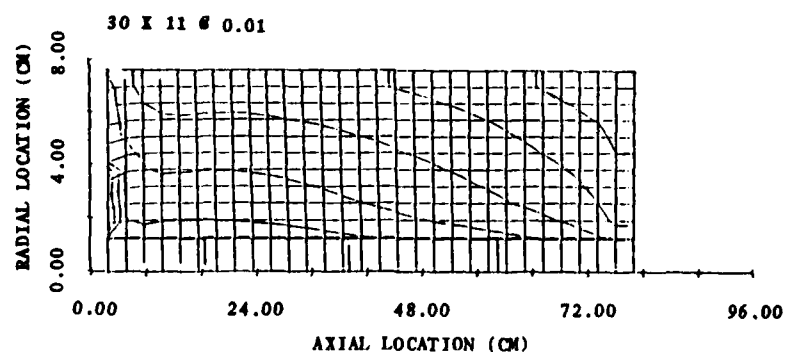
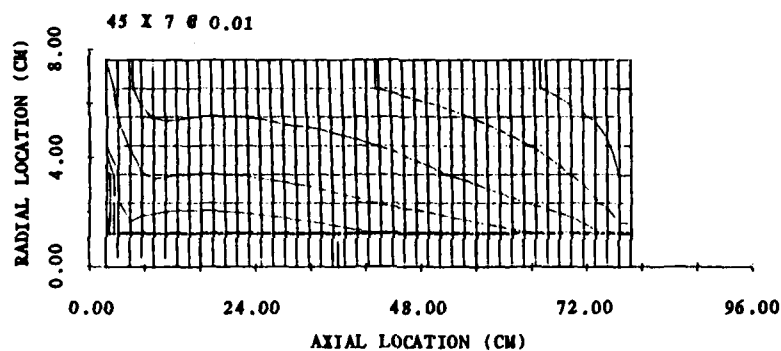
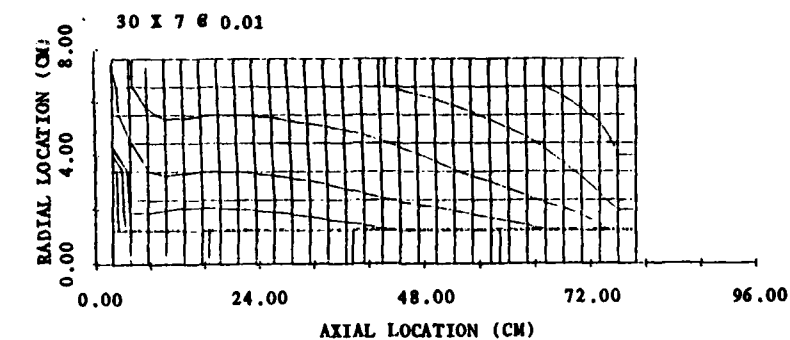


Figure 3.12 Influence of Mesh on Flamespreading Through M203 Charge
(Contours correspond to intervals of 0.32 msec)

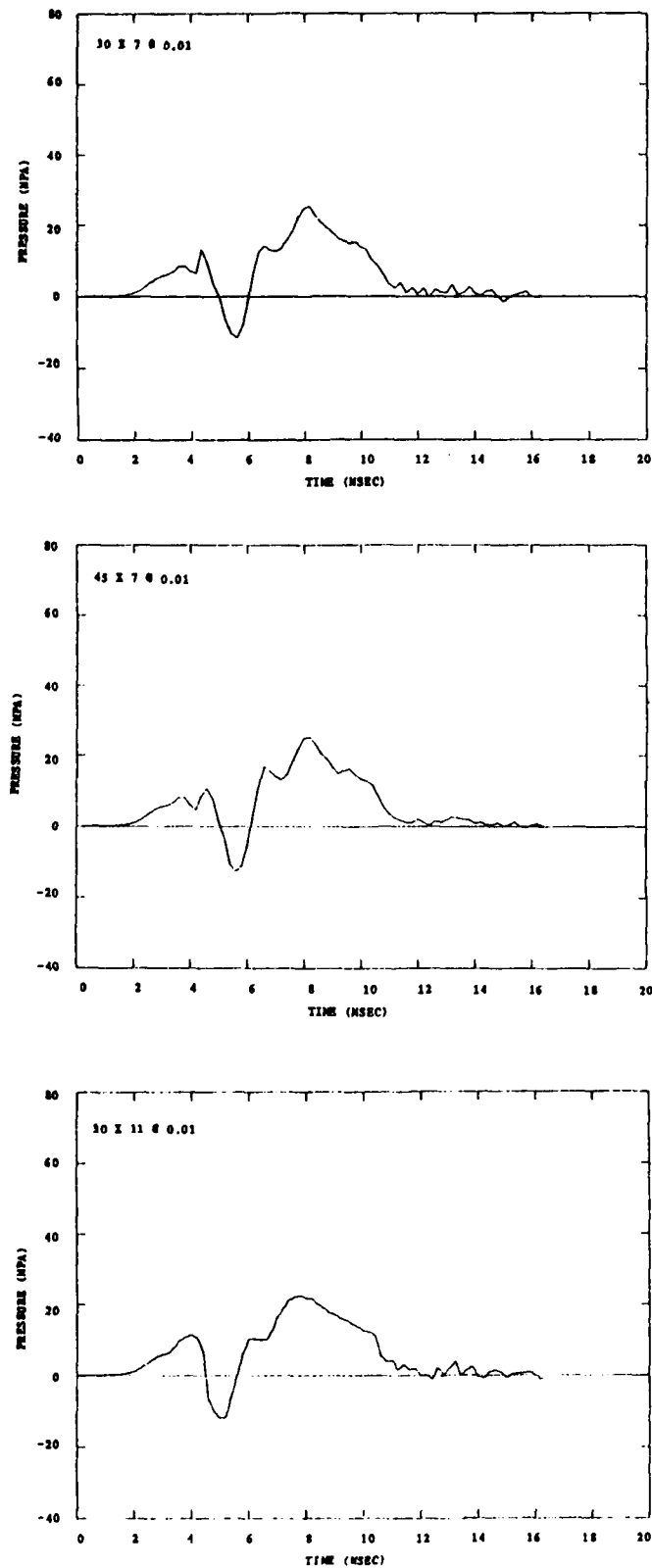


Figure 3.13 Influence of Mesh on Pressure Difference History in M203 Charge

4.0 THE M203E2 PROPELLING CHARGE — SINGLE-INCREMENT REPRESENTATION

We now consider the M203E2 Propelling Charge for the 155-mm Howitzer. In the present section we consider a single-increment representation in which the base igniter is modeled as a surface source term. Results for this representation have previously been presented by Horst et al.¹⁷ In this chapter we will use the single-increment representation as a vehicle to assess the influence of computational parameters on the interior ballistics of a stick propelling charge. We will also use the single-increment representation in Chapter 7.0 when we illustrate the modeling of programmed fracture. In Chapter 5.0 we will present solutions based on a two-increment representation of the M203E2 Charge in which the igniter is modeled as a two-phase flow.

The format of this chapter is the same as that of the previous one. In Section 4.1 we describe the charge and discuss the data base. In Section 4.2 we present some details of the nominal solution and in Section 4.3 we study the influence of the computational parameters.

4.1 Nominal Data Base

The M203E2 Propelling Charge is illustrated in Figure 4.1. It consists of 12.7 kg of M31A1E1 slotted stick propellant loaded in a rigid combustible cartridge case. The rear end closure has a permeable wall to allow the base igniter combustion products to flow into the stick charge. The base igniter consists of a small amount of CBI which is ignited by a black powder spot. The igniter is held in place by an end cap which has a central hole to allow ignition of the black powder by the primer located in the spindle. As with the M203 Charge, the initial condition involves axial ullage at both ends of the charge as well as annular ullage around it.

The single-increment representation of the M203E2 Charge by TDNOVA is defined by the tabulation of the input data given in Appendix C and by Figure 4.2. We see, in Figure 4.2, that the main charge is completely enclosed by the case and that all the surfaces of the case are taken to be reactive. Referring to Appendix C we see that the rate of combustion of the surfaces of the case is represented in a predetermined tabular format. Moreover we include an attached reactive substrate on the outside of the rear end wall. This attached substrate represents the action of the igniter which is therefore collapsed to a surface effect. Like the case, its rate of combustion is represented in a predetermined tabular format. The case is represented as rigidized. Thus we consider the longitudinal strain of the outer sidewall until such time as it is determined to have failed. Referring to Appendix C we see that the initial values of the flow resistance coefficients are $K_6 = 10$, $K_4 = K_5 = 101$. Therefore only the rear endwall is represented as initially permeable to the gas-phase.

In contrast to the M203 Charge, we take into account the thickness of the container in the present problem.

The main charge consists of slotted stick propellant. Accordingly, we model the interstitial flow independently of that in the perforations until flamespread is complete and all the slots are fully open. In the present instance the pressure required to open the slots is set so that they are represented as open from the initial instant. Accordingly, the dual-voidage model will be terminated as soon as flamespread is complete on all inner and outer propellant surfaces. Because the slots are always open, the interstitial and perforation pressures will always be identical at each location. However, the other gas-phase properties may differ as may the solid-phase surface properties.

4.2 Nominal Solution

In the present simplified representation of the M203E2 Charge the combustion of the case is specified in a predetermined tabular format according to which all internal and external surfaces begin to burn at the start of the calculation. Therefore the case plays an important role in respect to the ignition of the charge in this representation. In Chapter 5.0 combustion of the case will be modeled in a more physically correct manner.

Because of the combustion of the case all the surfaces of the container are pressurized early on. At the forward endwall the pressure differential creates a sufficiently large stress in the sidewall, according to the model of the rigidized case, that failure of the sidewall is predicted to occur at the forward end in approximately 0.1 msec. Since the rupture interval for all case segments is taken to be zero, in the present problem, the forward endwall becomes fully permeable when the structural failure occurs.

Figure 4.3 presents the distributions of pressure at various times. Since the slots are always open, the figure applies equally well to the interstitial and perforation flows.

At 0.5 msec we see the elevated pressure in the rear ullage due to the combustion of the igniter under the confinement of the endwall of the charge. Although the endwall is initially permeable, it offers significant resistance to penetration by the igniter gas. We see an even more pronounced excursion in the outer annular ullage where the products of combustion of the case are confined by the impermeable sidewall. Since the forward endwall has been fully permeable for some time we see that the internal case combustion products have been substantially vented into the forward region of axial ullage. Not only is the pressure continuous across the forward boundary of the charge, but the boundary condition has been impressed on a significant part of the charge. Near the rear outer corner, however, the pressure within the charge is still elevated.

By 1.0 msec the rear portions of the charge are ignited on both the inner and outer surfaces of the sticks. Although the rear endwall has not ruptured, the pressure differential across it has nearly disappeared. The rear portion of the outer sidewall of the case will soon rupture due to the overpressure created by propellant combustion. By 1.5 msec flamespread and case rupture are nearly complete and the pressure is rapidly becoming nearly uniform throughout the chamber. The dual-voidage model is terminated at 1.56 msec. By 2.224 msec the radial pressure gradients have disappeared to within 1% as required by the pressure tolerance factor, set equal to 0.01. Transformation to a quasi-two-dimensional representation occurs. We present the pressure distribution just before and just after the transformation.

We include the distributions of pressure at various times during the balance of the interior ballistic cycle. These exhibit no important physical details. However, we draw attention to the continuum representation of the forward region of axial ullage.

The nominal solution was generated using the 30 X 7 @ 0.01 computational parameter set. It required 246 seconds of CPU time on the CYBER 7600 computer.

4.3 Influence of Computational Parameters

The influence of the computational parameters is illustrated in Figures 4.4 through 4.13 and by the data of Table 4.1. The results are seen to be similar to those of the previous chapter. Very good indifference of the calculations is seen insofar as the number of mesh points is concerned. But some sensitivity of the maximum chamber pressure is seen as the value of the pressure tolerance factor is reduced. The absolute values of the mass defect reach maximum values of about 2%.

Figure 4.4 through 4.6 illustrate the influence of the number of axial mesh points on the pressure distributions at three times. The agreement is seen to be very good. The only noteworthy feature occurs in Figure 4.6 where the 45 X 7 @ 0.01 case exhibits some small wiggles on the outer boundary. This is thought to be associated with the non uniform rupture of the sidewall which occurs between 1.0 and 1.5 msec. As the mesh is refined it becomes more sensitive to non-analyticities in the boundary conditions. We saw a similar result in Chapter 3.0 in connection with the collapse of the forward axial ullage as the charge approached the base of the projectile.

The effect of the number of radial mesh points is illustrated in Figures 4.7 through 4.9. The indifference of the pressure distribution is seen to be very good.

Due to the permeability of the stick charge and the relatively early equilibration of pressure across the rear end closure, the propellant does not move significantly during flamespreading. This is illustrated in Figure 4.10 in which we display the solid-phase velocity field at the instant of transformation to a quasi-two-dimensional representation. It should be noted that the flow fields of Figure 4.10 are at a variety of times. Accordingly, the shape of the charge boundary may vary from mesh to mesh.

Table 4.1 Effect of Computational Parameters on Simulation of M203E2 Propelling Charge

Run	P _{max} (MPa)	m. v. (m/s)	ΔP _{min} [*] (MPa)	t _{Q2D} (msec)	max	Δm%(-) min Final	
Nominal Case							
30 X 7 @ 0.01	357.9	799.4	- 4.4	2.22	2.11	0.00	1.06
Effect of Number of Axial Mesh Points							
15 X 7 @ 0.01	354.5	794.6	- 5.5	2.27	1.48	-0.37	-0.37
45 X 7 @ 0.01	354.6	794.3	- 2.1	3.47	1.51	-1.73	-1.73
Effect of Number of Radial Mesh Points							
30 X 5 @ 0.01	352.0	793.7	- 3.6	2.45	1.37	0.00	0.23
30 X 9 @ 0.01	357.4	799.0	- 4.4	2.22	2.04	0.00	1.01
30 X 11 @ 0.01	357.0	796.2	- 2.7	2.45	1.57	0.00	0.19
Effect of Pressure Tolerance Factor							
30 X 7 @ 0.05	356.0	798.2	- 4.8	2.04	2.00	0.00	0.91
30 X 7 @ 0.10	356.0	798.2	- 4.8	2.04	2.00	0.00	0.91
30 X 7 @ 0.005	364.3	798.5	- 2.4	3.73	2.31	-0.47	-0.47

* First minimum of pressure at 87.37 cm minus pressure at 0.01 cm on centerline

Figures 4.11 and 4.12 illustrate the influence of the mesh on the path of flamespreading through the interstices and the perforations of the stick charge. Good indifference is seen. We also note only minor differences between the external and internal flamespread rates. In Figure 4.13 we note the influence of the mesh on the pressure difference history. As with the M203 Charge in the previous chapter, the indifference of the solution is good, although there are differences in the fine structure. We note an anomaly in the solution for the 30 X 7 @ 0.01 case. The excursion at around 12 msec represents a flaw in the treatment of burnout. This algorithm defect will be corrected in subsequent code versions. It was not judged to be of sufficient importance to warrant repeating the present set of runs.

CHARGE, PROPELLING, 155MM M203E2 (STICK PIP)

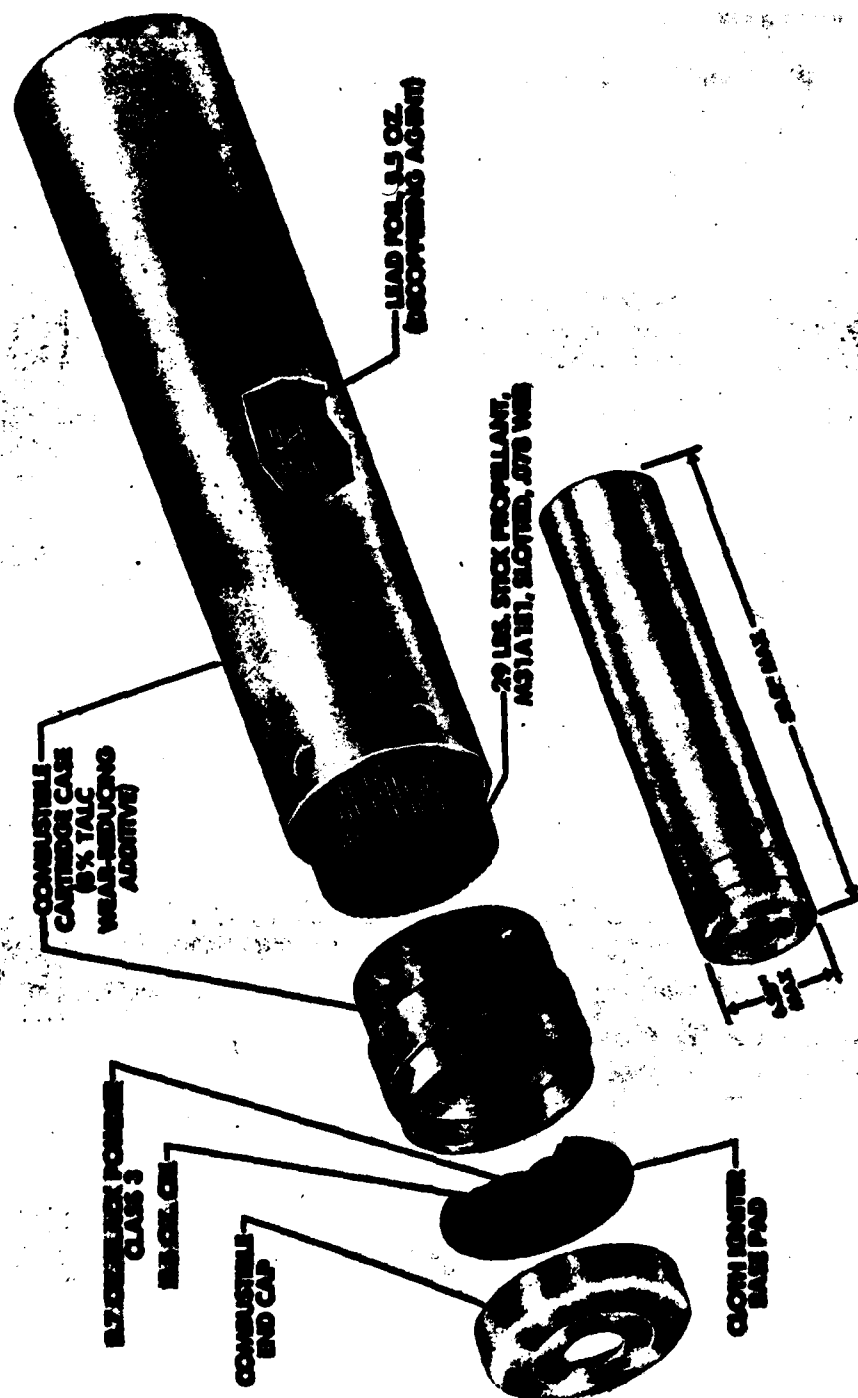
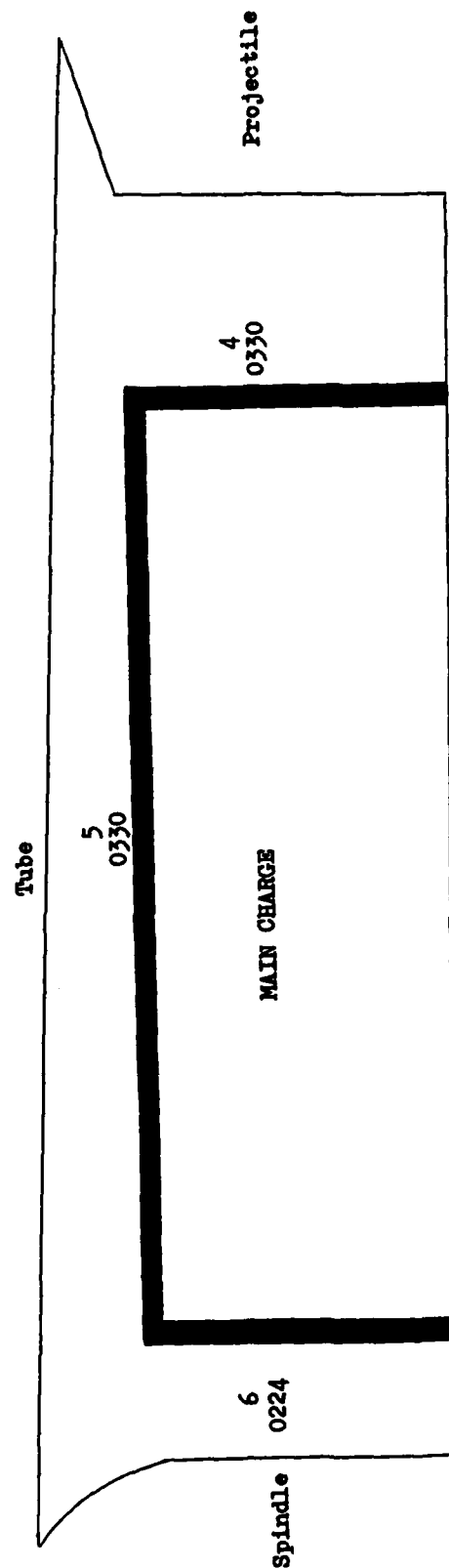


Figure 4.1 The M203E2 Propelling Charge



X - Mechanical Property File Pointer
 XXXX - Reactivity File Pointer

Figure 4.2 Single-Increment Representation of M203E2 Charge by TDNOVA

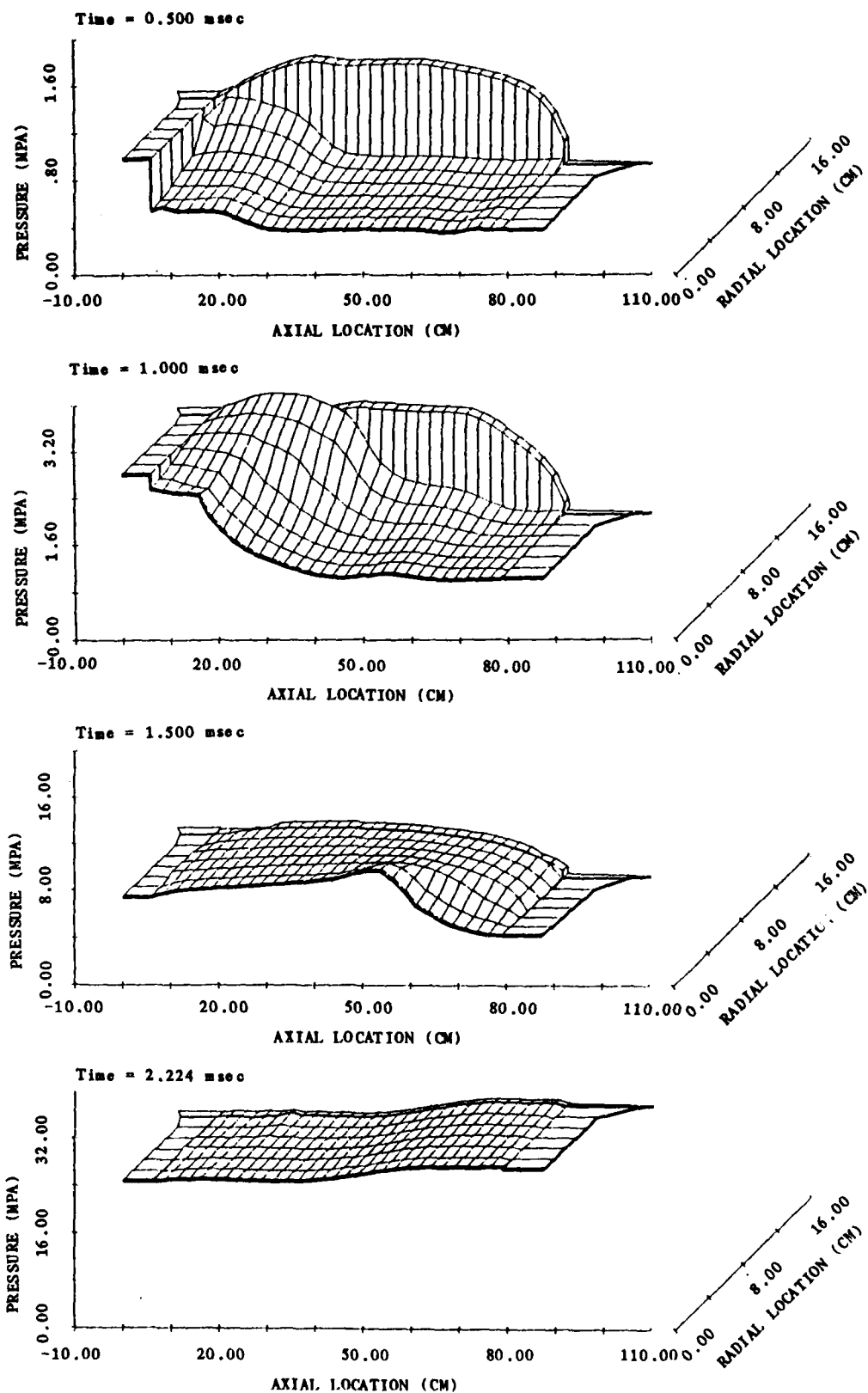


Figure 4.3 Pressure Distributions for M203E2 Charge Obtained with Nominal Mesh (30 X 7 @ 0.01)

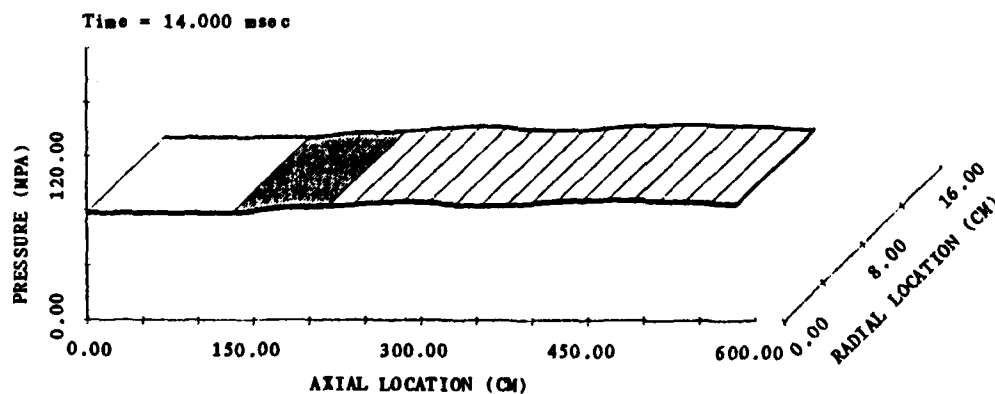
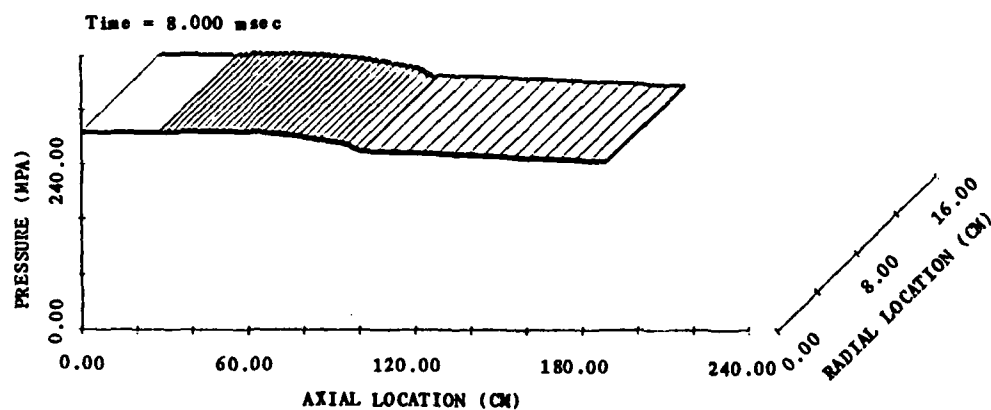
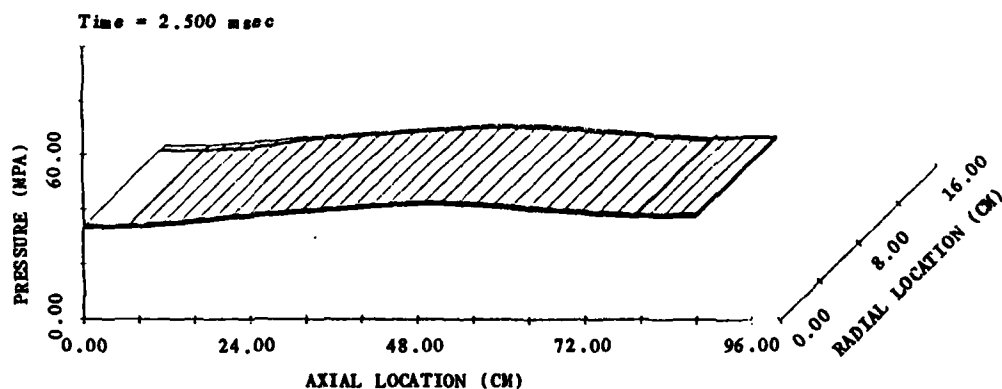
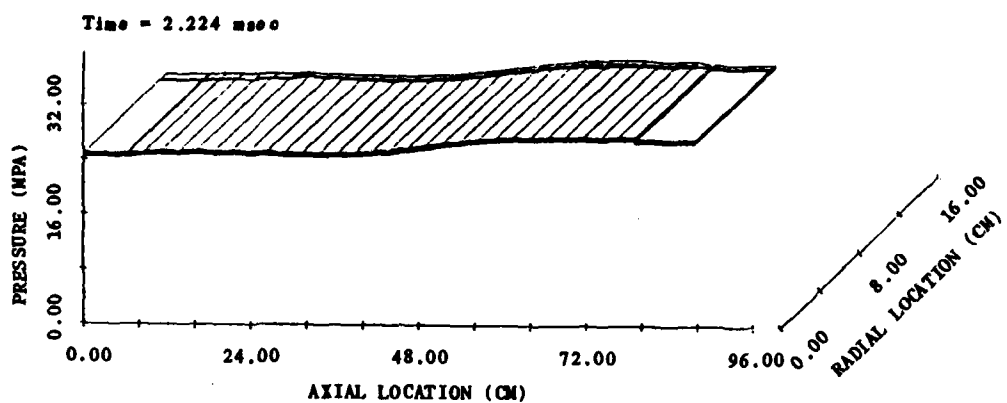


Figure 4.3 Continued

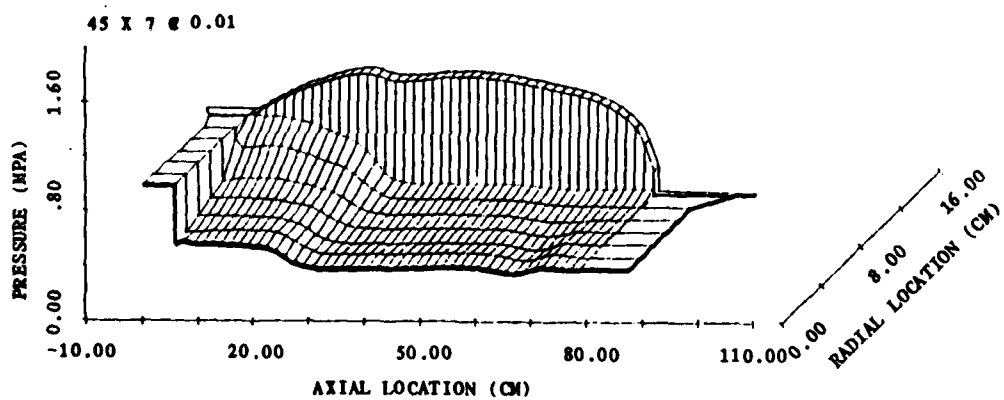
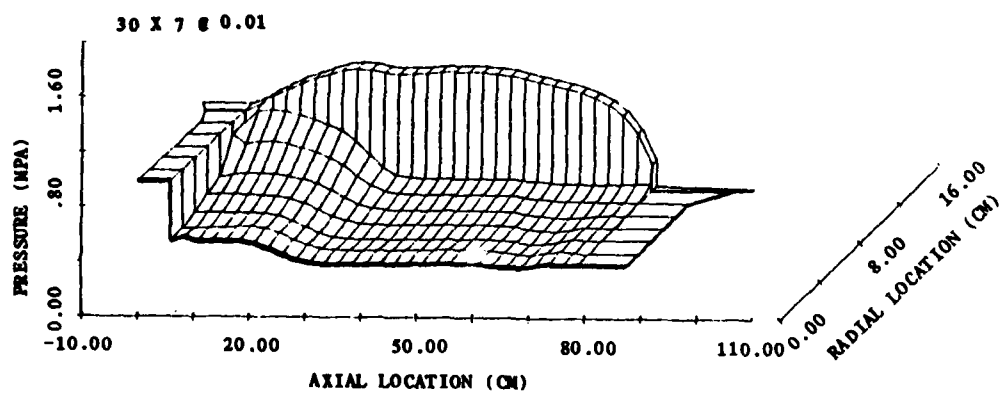
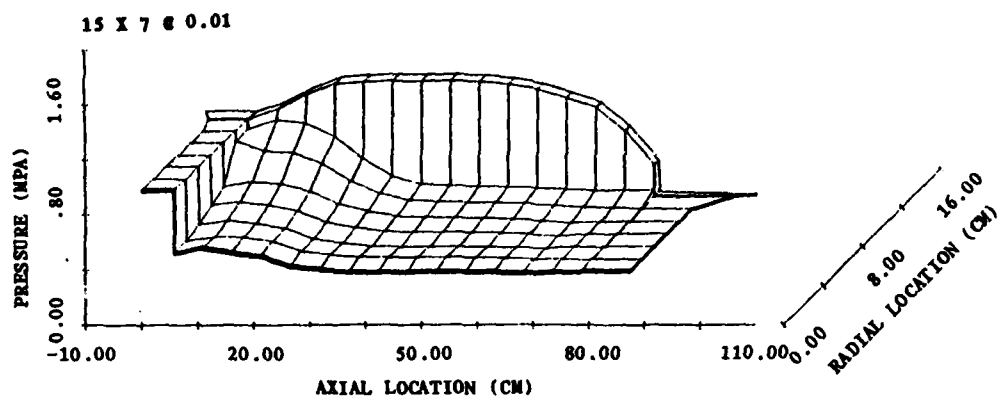


Figure 4.4 Influence of Number of Axial Mesh Points on Pressure Distribution for M203E2 Charge at 0.5 msec

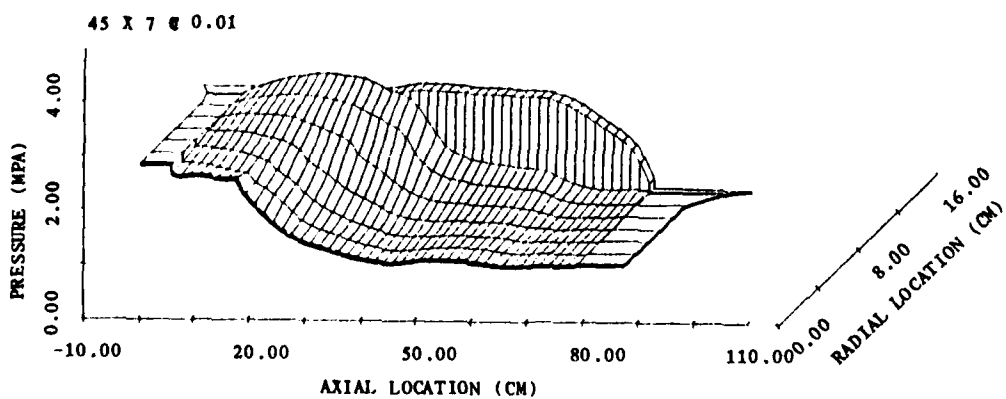
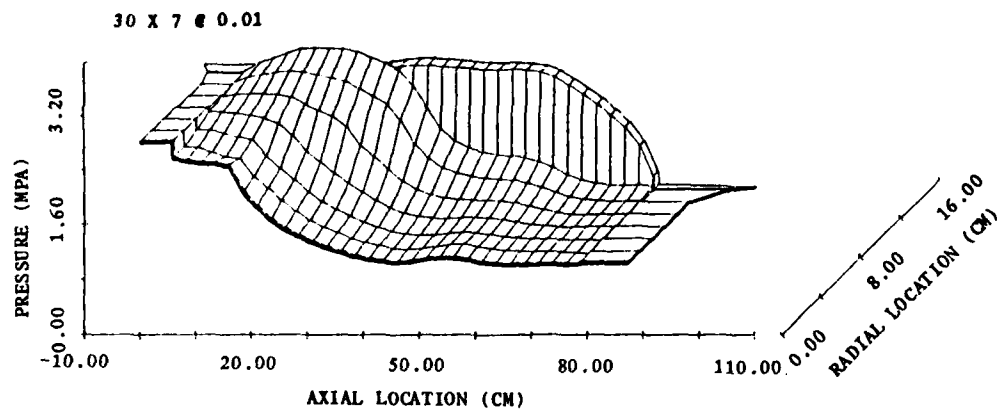
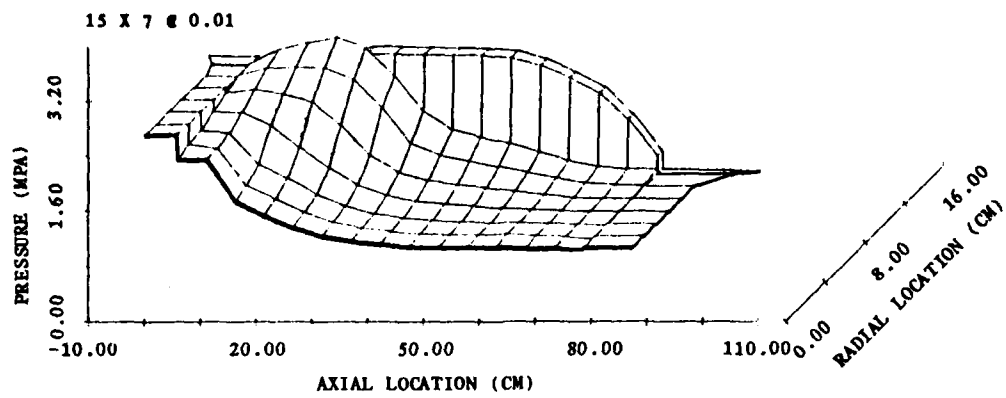


Figure 4.5 Influence of Number of Axial Mesh Points on Pressure Distribution for M203E2 Charge at 1.0 msec

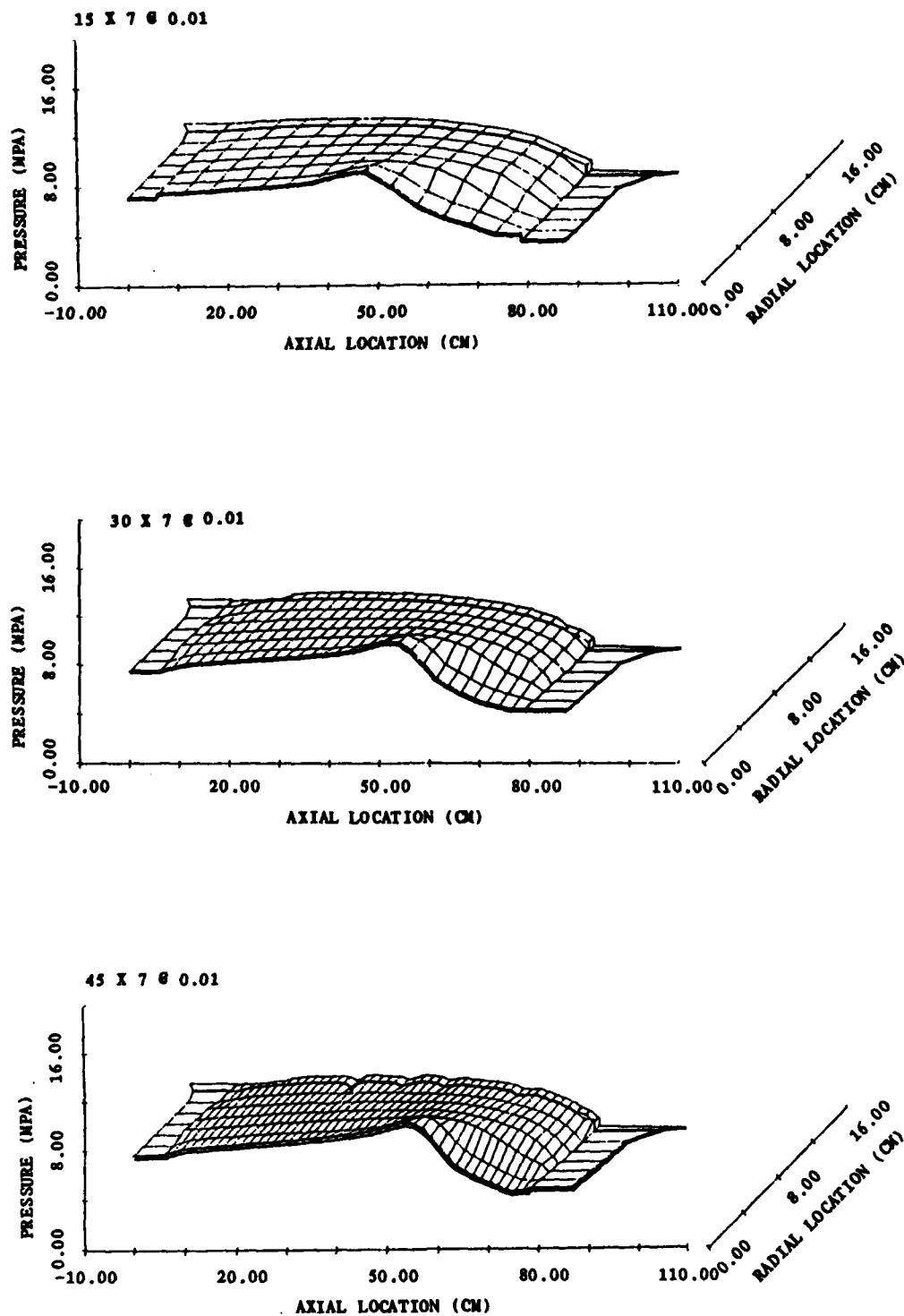


Figure 4.6 Influence of Number of Axial Mesh Points on Pressure Distribution for M203E2 Charge at 1.5 msec

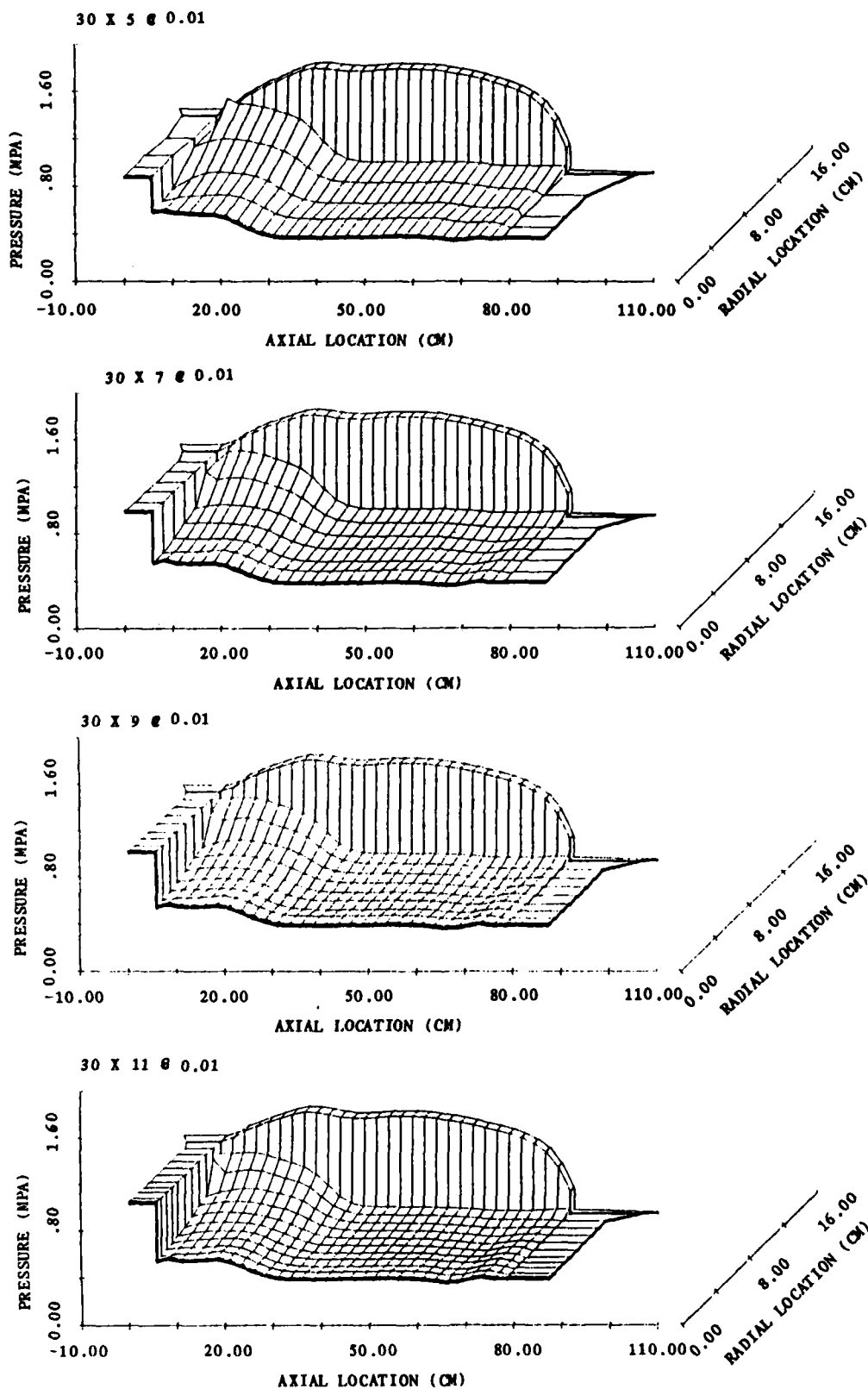


Figure 4.7 Influence of Number of Radial Mesh Points on Pressure Distribution for M203E2 Charge at 0.5 msec

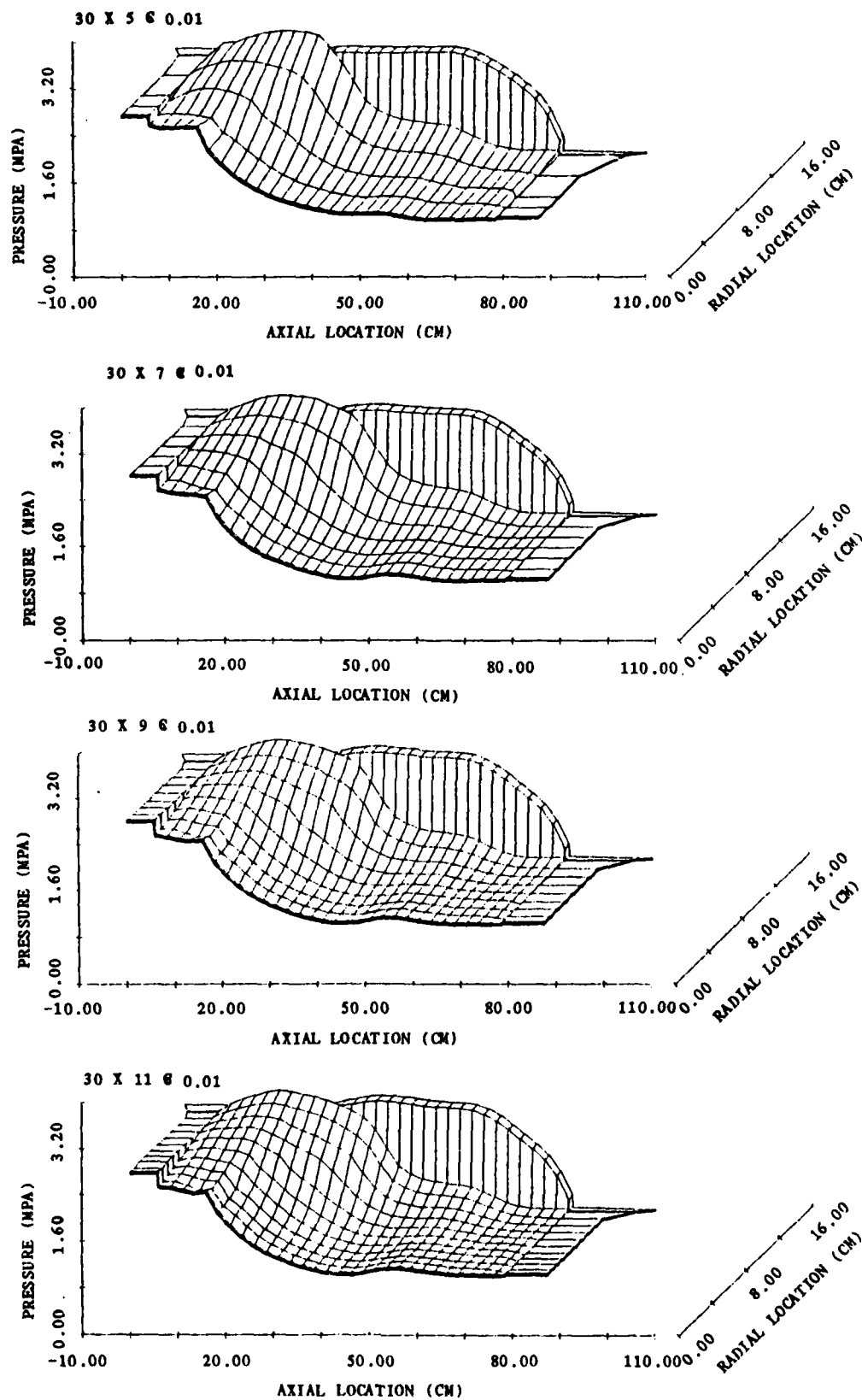


Figure 4.8 Influence of Number of Radial Mesh Points on Pressure Distribution for M203E2 Charge at 1.0 msec

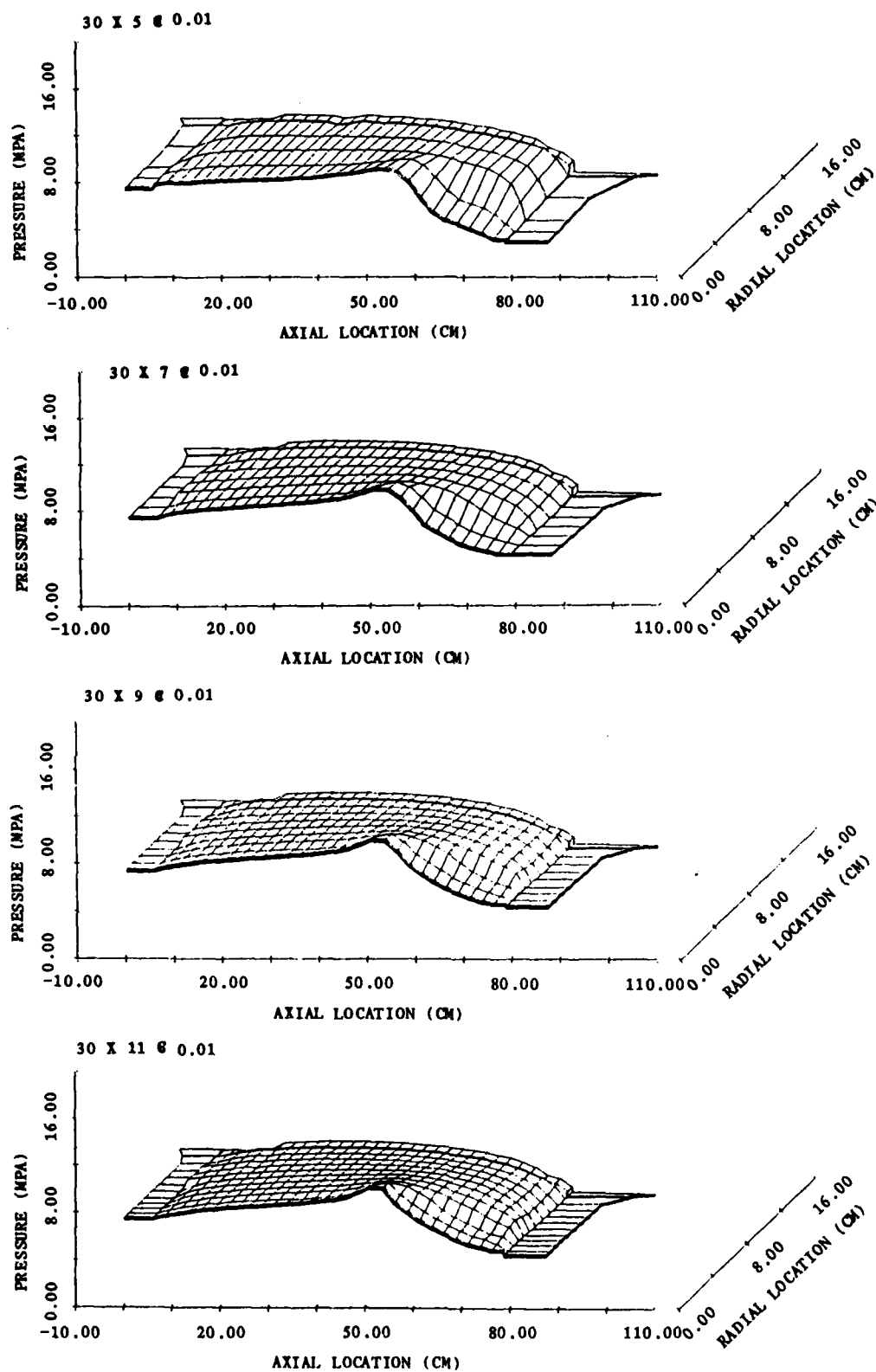


Figure 4.9 Influence of Number of Radial Mesh Points on Pressure Distribution for M203E2 Charge at 1.5 msec

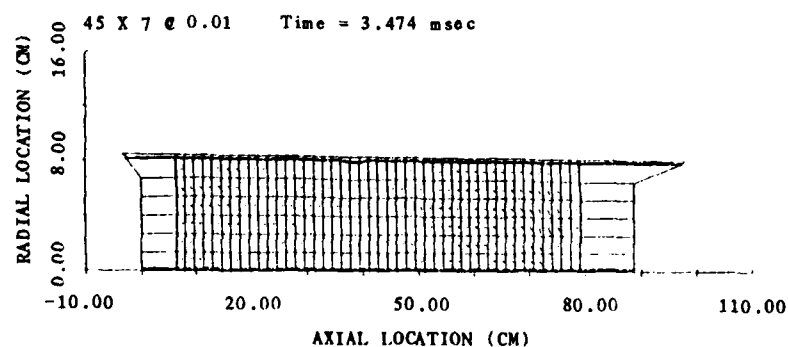
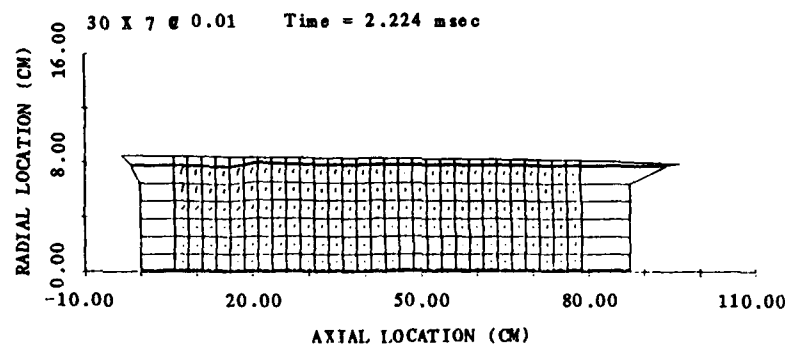
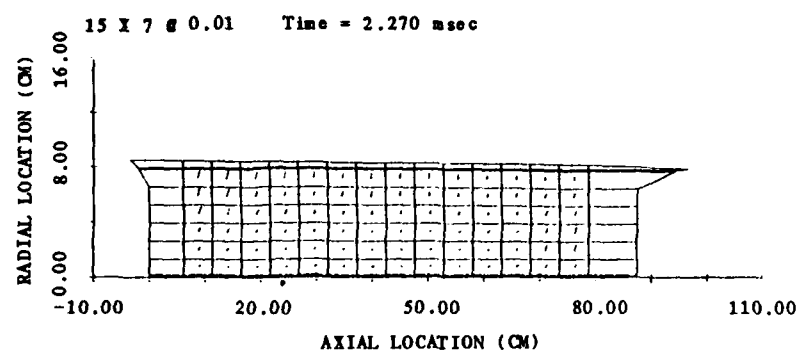


Figure 4.10 Solid-Phase Velocity Field Just Prior to Transformation to a Quasi-Two-Dimensional Representation for M203E2 Charge

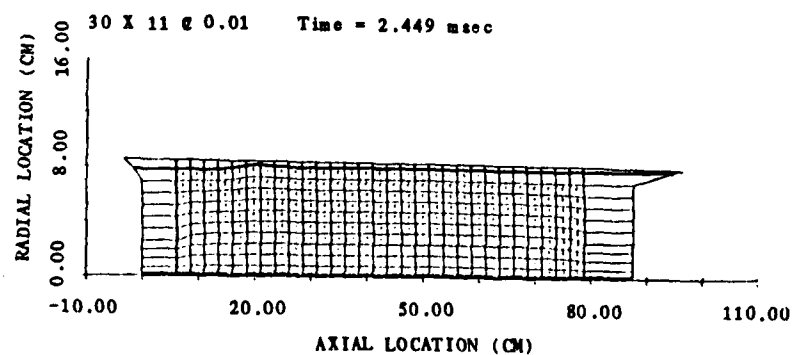
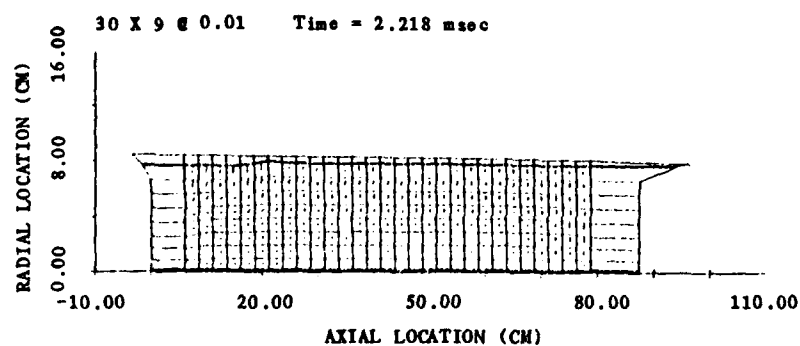
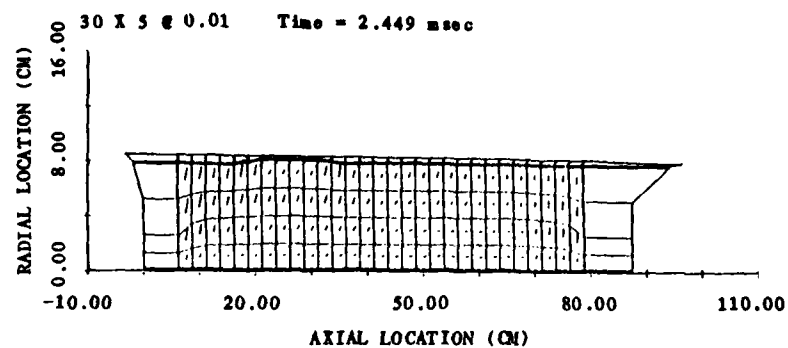


Figure 4.10 Continued

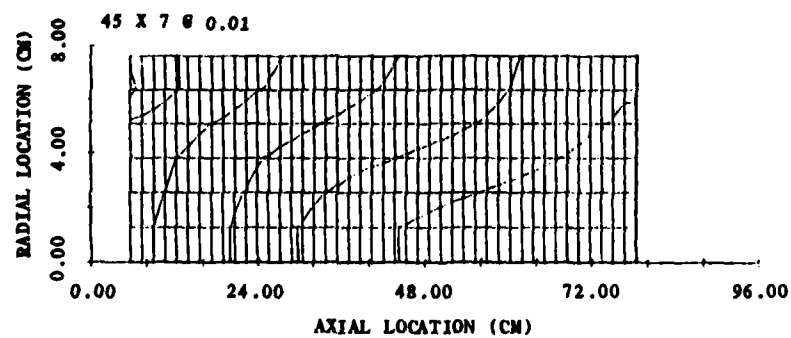
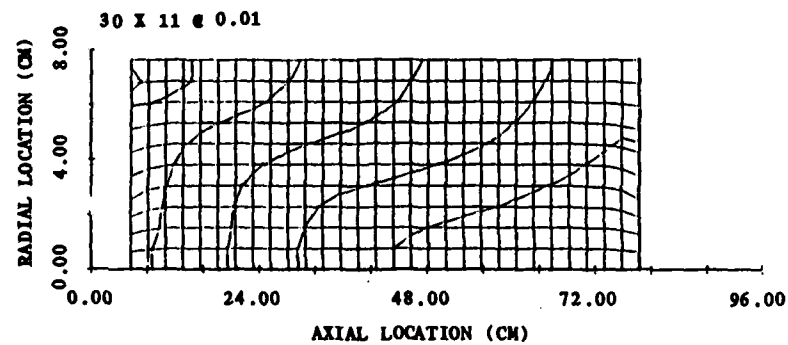
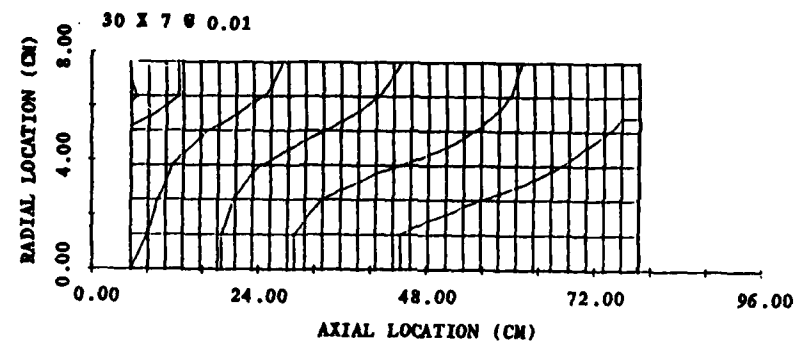


Figure 4.11 Influence of Mesh on External (Interstitial) Flamespreading Through M203E2 Charge (Contours correspond to intervals of 0.17 msec.)

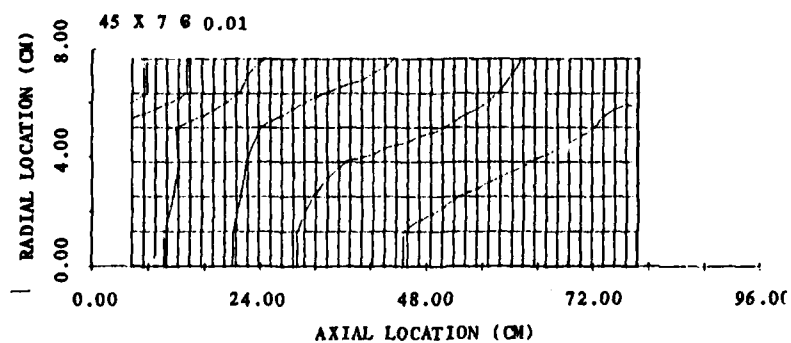
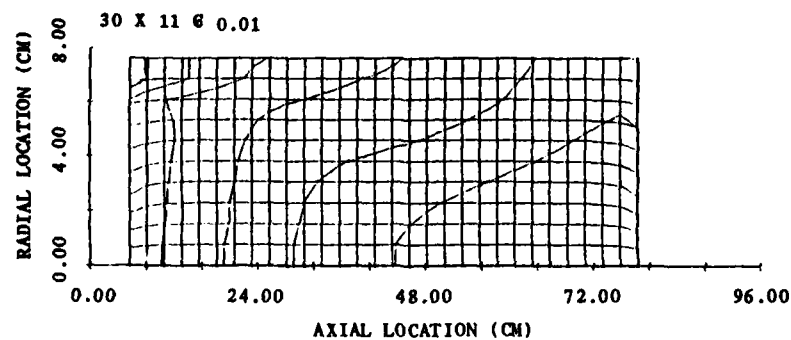
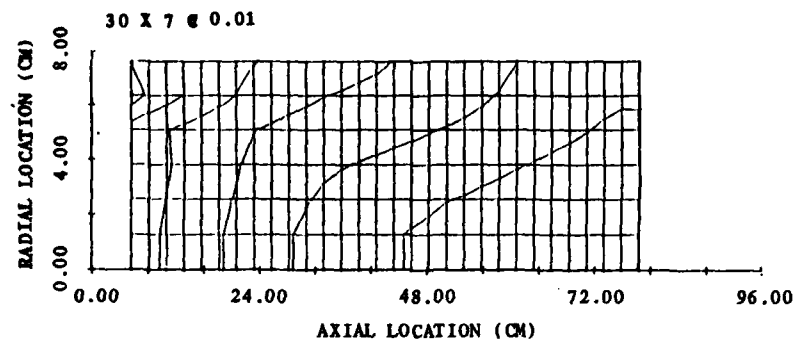


Figure 4.12 Influence of Mesh on Internal (Perforation) Flamespreading Through M203E2 Charge (Contours correspond to intervals of 0.17 msec.)

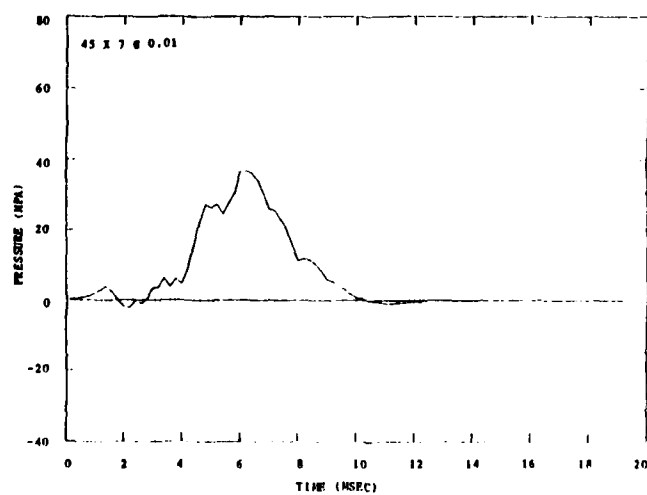
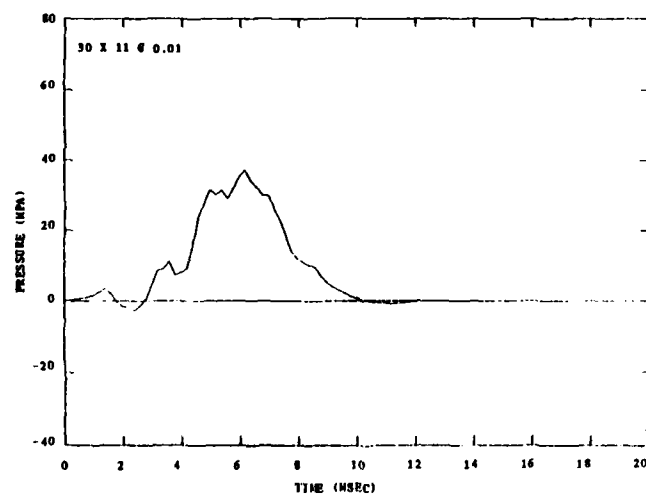
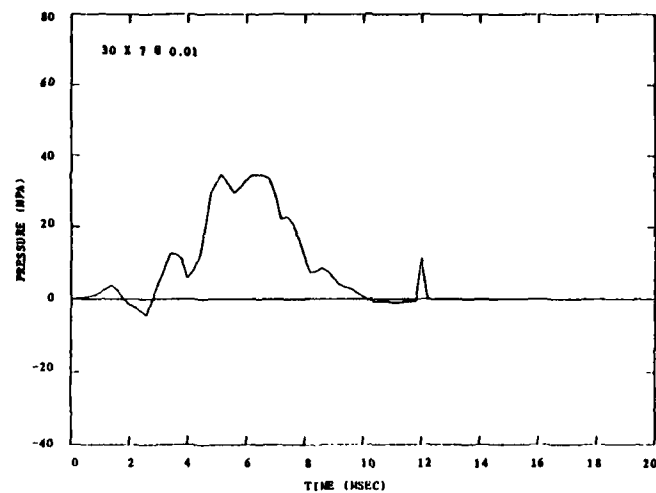


Figure 4.13 Influence of Mesh on Pressure Difference History in M203E2 Charge (Pressure at 0.01 cm minus pressure at 87.37 cm on centerline)

5.0 THE M203E2 PROPELLING CHARGE — TWO-INCREMENT REPRESENTATION

In the previous chapter we presented simulations of the M203E2 Propelling Charge in which the igniter was represented as a surface source term. The base igniter contains a number of structural details, as may be seen from an inspection of Figure 4.1, and it is therefore tempting to represent the igniter as a separate increment, modeled according to the same two-phase flow formulation as the main charge. Early attempts to perform a two-increment simulation of the M203E2 Charge were unsuccessful¹⁷ and much of the effort in the present contract has been directed towards ruggedizing the code to meet this goal.

In this chapter we present solutions which demonstrate the achievement of the goal of treating the igniter as a separate increment. The nominal data base and certain details of the solution are presented in Section 5.1. Then, in Section 5.2 we examine the theoretical influence of the permeability of the propellant container.

5.1 Nominal Data Base and Solution

The two-increment representation of the M203E2 Propelling Charge is illustrated in Figure 5.1. The complete nominal data base is tabulated in Appendix D. Most of the details of the representation are as in the preceding chapter. The major differences are due to the treatment of the reactivity of the container and, of course, the model of the base igniter.

Figure 5.1 identifies the mechanical property and reactivity file pointers which are used to characterize the various sections of the container. We note that all the container walls are taken to be initially impermeable ($K=101$), except for the endwall between the increments which is characterized by a value of $K=10$. We recall that the reactivity pointer is a four digit number. Each digit points to a file of data for one of the four possible reactive substrates in each segment of the container. A zero value implies that the corresponding substrate is non-reactive. Referring to Appendix D we see that with the exception of the black powder spot located on the rear endwall of the main charge increment, all container substrates are characterized by modeled combustion rates. Due to uncertainties in the rate of convective heat transfer to the container we have set the ignition temperature of the container material to be 300°K or slightly more than the initial temperature of 294°K . Accordingly, combustion of the container will begin shortly after the onset of any appreciable convection of high temperature gases. The combustion rate depends on pressure according to the familiar exponential law.

We note that the rear endwall of the igniter increment is defined by two segments. The inner segment represents the venthole shown in Figure 4.1 and is accordingly given zero values for the mechanical property and reactivity pointers. The igniter increment is also depicted as having no forward endwall. We have taken the forward endwall of the igniter to be the rear endwall of the main charge even though, as shown in Figure 4.1, it is

physically a part of the igniter case. Our purpose in so doing is twofold. First of all, since TDNOVA will treat the endwall as moving with the boundary of the increment to which it is ascribed, it is physically more appropriate to identify it with the main charge. The ignition of the charge has as its initial stimulus the venting of the black powder basepad located on the rear face of the endwall. This will have the effect of blowing the igniter grains rearward while at the same time thrusting the endwall against the main charge. Second, ascribing the endwall to the main charge permits us to retain the reactive stimulus and flow resistance of the endwall after the igniter increment has been eliminated due to burnout.

Both the igniter and main charge containers are taken to be rigidized. The containers are represented as bonded together with a bond strength of 10^6 N. The maximum tensile stress for the container sidewall is 20.68 MPa. This value is used to determine the point at which the analysis of sidewall longitudinal strain is to be terminated. Subsequently, in the flexible case mode, the endwalls offer no direct constraint to the motion of the solid-phase. Rupture is taken to begin in the flexible case mode at an over-pressure of 0.86 MPa and to require 1 msec for completion. All segments of the containers are taken to have an initial thickness of 0.32 cm.

The igniter charge consists of 0.0283 gm of CBI (Clean Burning Igniter). We take the ignition temperature of the CBI to be 300°K , ensuring that it begins to burn shortly after the basepad starts to vent. The initial porosity of the igniter increment is 0.963, very close to unity.

In order to prevent complete collapse of the igniter increment it was decided, at an early stage, to set the settling porosity equal to the initial porosity. Accordingly, the igniter will tend to resist compaction. The necessity of this compromise of the data base in the context of subsequent code improvements has not been verified. We note that since the igniter increment has an initial length of 2.54 cm, the requirement that it compress to a length no less than 0.5 cm, as discussed in Section 2.3.4, implies that the igniter increment will never be eliminated due to excessive compression. As discussed in Section 2.2.2, elimination due to compression occurs when the igniter increment is compressed to less than 10% of its original length which, in this case, would be 0.25 cm.

The solution is performed with the computational parameter set $30 \times 7 @ 0.05$. The complete nominal solution requires 406 CPU seconds on the CYBER 7600 computer.

Details of the nominal solution are presented in Figures 5.2 and 5.3. Figure 5.2 illustrates the distributions of pressure at various times while 5.3 displays the solid-phase velocity field at a somewhat different set of times. As in Chapter 5.0, the interstitial and perforation pressures are always equal at every location in the main charge increment.

The pressure distributions of Figure 5.2 are similar in many ways to those presented in Chapter 4.0 with the single-increment representation. However, pressurization at the rear of the charge is much more rapid in the present case. Also, since the container does not begin to burn prior to the onset of a sufficiently strong thermal stimulus, we do not see the rupture of the main charge container at the forward endwall as occurred with the single-increment representation. Rupture still occurs quite early on, at approximately 0.1 msec. For both containers the sidewall fails at the connecting endwall which then begins to become fully permeable.

The constitutive revision to allow the endwall to begin to rupture when the sidewall fails at an endpoint in the analysis of rigidization was not part of the code version used to produce previously reported results for this problem.¹⁸ The present solutions differ from those of Reference 18, particularly as regards propellant motion. While the endwall is unruptured it always allows the pressure differential across it to be transmitted into the sticks, propelling them forward. Propellant motion is reduced in the present simulations when compared with those reported previously.¹⁸

As in the single-increment representation we see elevated pressures in the rear of the charge at 0.5 msec. But the outer annular ullage is barely pressurized. By 1.5 msec the annular ullage shows an excess of pressure over that inside the charge, due at least in part to combustion of the outer surface of the sidewall. By 2.5 msec flamespread is nearly complete but the front endwall has not yet fully ruptured and the pressure in the charge is greater than that in the forward axial ullage.

At 2.86 msec burnout occurs locally within the igniter increment. It is eliminated as a separate increment at this time and consolidated with the rear axial ullage. Any remaining unburned igniter solid-phase is ignored in the balance of the calculation. At 3.03 msec flamespread is complete. Since the data base specifies that the slots of the sticks are open from the initial instant, the dual voidage representation is terminated at this time. At 3.207 msec the transformation to a quasi-two-dimensional representation occurs. We display the pressure distributions just before and just after the transformation.

At 3.5 msec the forward axial ullage is large enough to warrant a continuum analysis. Figure 5.2 concludes with the distribution at 14.0 msec, just prior to muzzle exit.

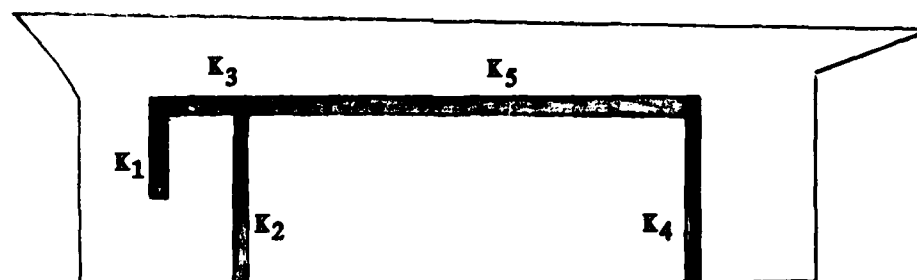
Figure 5.3 displays the solid-phase velocity field at four times up to the instant at which the igniter increment is eliminated due to local burnout. Although the igniter is initially blown rearward and compacted against the spindle, it subsequently expands forward when combustion of the igniter propellant overwhelms the blowing action of the black powder spot. We note that expansion of the igniter increment also occurs in the radial direction. Due to their much larger inertia, the sticks hardly move.

5.2 Effects of Container Permeability

We now consider the influence of the permeability of the container on the theoretical behavior of the M203E2 Charge. In addition to the nominal case we consider five other cases all predicated on the data base of Appendix D. Only the initial flow resistance coefficients for the container segments vary from run to run. The values of the K_i are shown in Table 5.1 together with a sketch which identifies the segments to which they pertain.

Table 5.1 Values of Container Flow Resistance Coefficients for Simulations of M203E2 Propelling Charge (Two-Increment Representation)

Case	K_1^*	K_2	K_3	K_4	K_5
1	101	10	101	101	101
2	101	20	101	101	101
3	101	0	101	101	101
4	101	10	0	101	0
5	0	0	101	0	101
6	0	0	0	0	0



* Nomenclature for values of K_i as in sketch

In Case 2 the value of K_2 is doubled, making the endwall between the igniter and main charge increments less permeable to the gas-phase. In Case 3 the value of K_2 is set equal to zero. In Case 4 we let the sidewalls be fully permeable by setting $K_3 = K_5 = 0$. In Case 5 we allow all endwalls to be fully permeable by setting $K_1 = K_2 = K_4 = 0$. Finally, in Case 6 the entire container is made fully permeable with all values of the K_i set equal to zero.

In Table 5.2 we summarize the predictions of maximum pressure (p_{\max}), muzzle velocity (m.v.) and the first minimum of the pressure difference history (Δp_{\min}). We also present the maximum, minimum and final values of the percent mass defect ($\Delta m\%$).

Table 5.2 Effect of Container Permeability on Simulations of M203E2 Propelling Charge (Two-Increment Representation)

Case	p_{\max} (MPa)	m.v. (m/s)	Δp_{\min}^* (MPa)	$\Delta m\%$		
				max	min	final
1	380.1	831.5	-2.4	1.48	-1.06	-0.25
2	375.7	828.5	-1.4	0.98	-1.18	-0.75
3	383.9	836.8	-4.7	1.96	-0.38	0.05
4	373.0	825.5	-3.7	0.65	-1.04	-1.04
5	381.7	831.4	-2.6	1.28	-1.48	-0.53
6	373.0	826.6	-5.8	0.96	-0.77	-0.77

*First minimum of pressure at 87.37 cm minus pressure at 0.01 cm on centerline.

The values of $\Delta m\%$ are all reasonably small, the extrema do not exceed 2% and the final values are all 1% or less. Accordingly it is reasonable to assume that the mesh indifference of the present solutions is similar to that of the single-increment representation of Chapter 4.0. It follows that the ballistic predictions of Table 5.2 do not exhibit a dependence on container permeability which can be discriminated from the computational noise. This finding is consistent with the experimental results of Minor and Horst.³²

Details of the individual solutions are presented in Figure 5.4 through 5.9. In Figures 5.10 through 5.12 we compare the paths of flamespreading and the pressure difference histories for the various data bases.

³² Minor, T.C. and Horst, A.W

"Ignition Phenomena in Developmental, Stick Propellant, Combustible-Cased, 155-mm, M203E2 Propelling Charges"

Ballistic Research Laboratory Report ARBRL-TR-02568

1984

Doubling the initial flow resistance coefficient for the endwall between the igniter and main charge increments does not have a large effect on the pressure distributions, as shown in Figure 5.4. However, it should be borne in mind that failure of the container in the rigidized mode induces an early rupture of the dividing endwall. On the other hand, setting the flow resistance of the dividing endwall equal to zero has a more pronounced effect on the pressure field, as we see in Figure 5.5. Without the confining influence of the endwall, the CBI burns more slowly. We see continuity of the pressure across the dividing endwall. In addition the pressure increases much more slowly as a function of time.

Figure 5.6 illustrates the pressure distributions obtained with permeable sidewalls while 5.7 presents the solution with permeable endwalls. Finally, in Figure 5.8 we see the solution corresponding to the fully permeable container. These three figures display the expected continuity of pressure across the permeable surfaces. We do note a small excursion near the rear of the charge in Figures 5.7 and 5.8. This is due to the blowing effect of the black powder spot which is attributed to the dividing endwall. We also note that for Case 6 the igniter increment was not eliminated until after the transformation to a quasi-two-dimensional representation. Figure 5.9 presents the solid-phase velocity field for Case 6. We note the extreme compression of the igniter increment at 1.5 msec.

Figures 5.10 and 5.11 illustrate the path of flamespreading over the outer and inner surfaces of the stick charges. In spite of the fact that the slots are always open, the outer and inner flamespread path differ. We recall that transverse flow occurs only in the interstices so that the outer and inner flow fields differ. Moreover, the outer and inner heat transfer coefficients are expected to differ due to the differing characteristic length scales used to evaluate the heat transfer correlation.

Figure 5.12 compares the pressure difference histories for the six cases. Small differences of detail are seen but in no case do we observe what would be described as a dangerous level of pressure waves. This tolerance of design variations by the stick charge is in agreement with the previously mentioned finding of Minor and Horst.³²

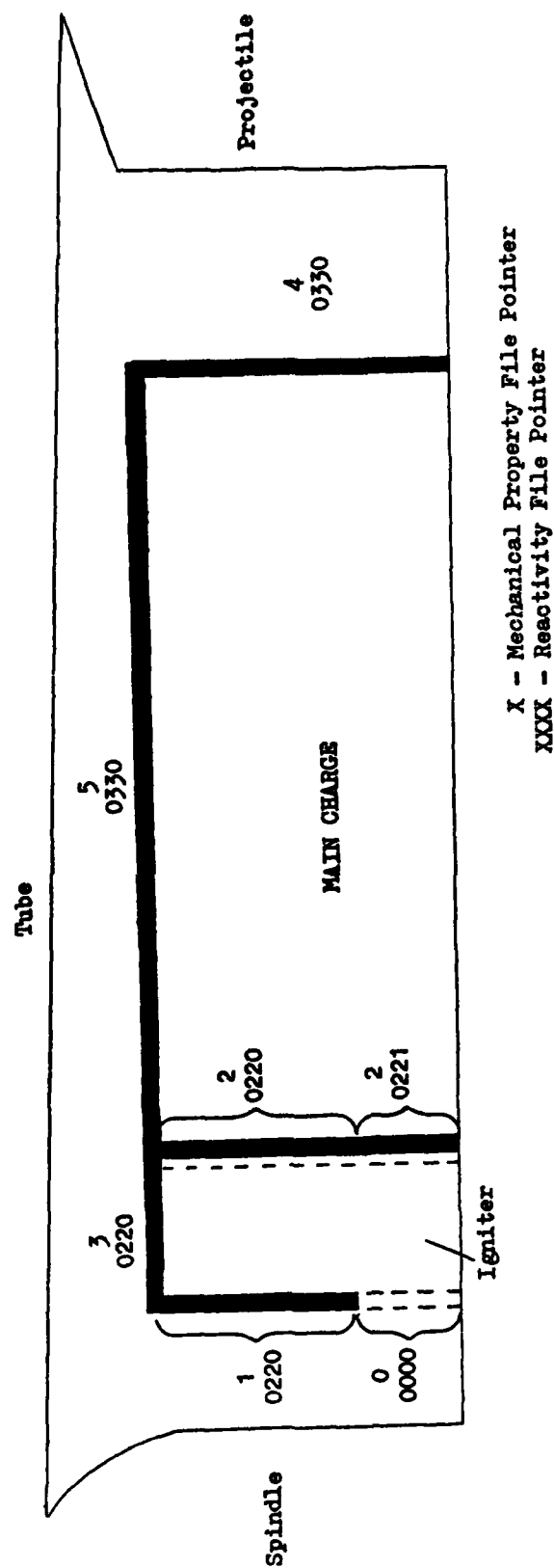


Figure 5.1 Two-Increment Representation of M203E2 Charge by TDNOVA

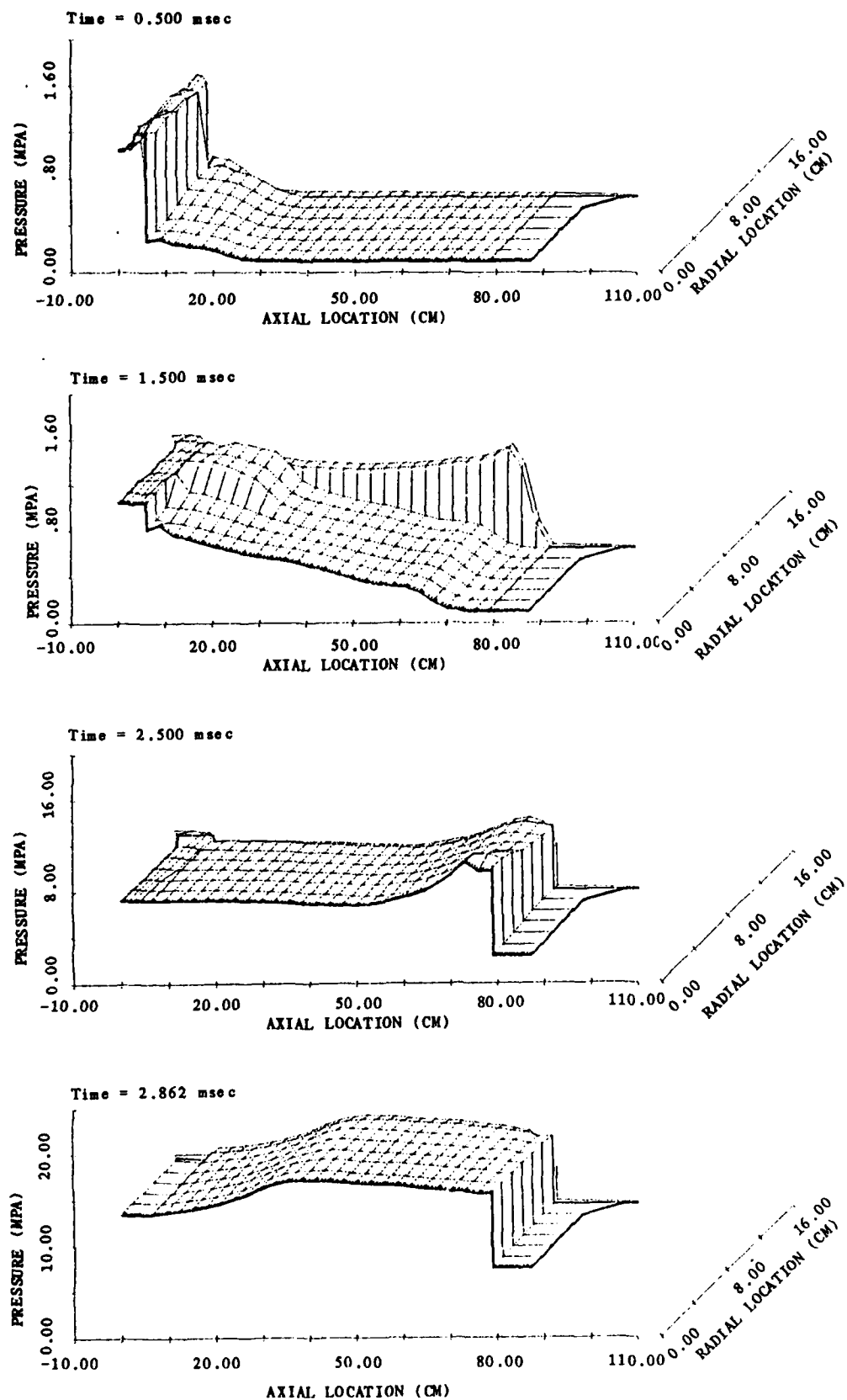


Figure 5.2 Pressure Distributions for the M203E2 Case 1 (Nominal) Data Base

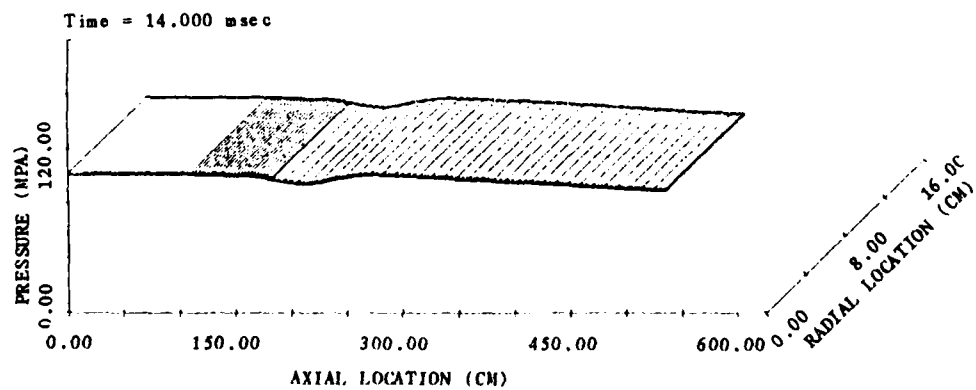
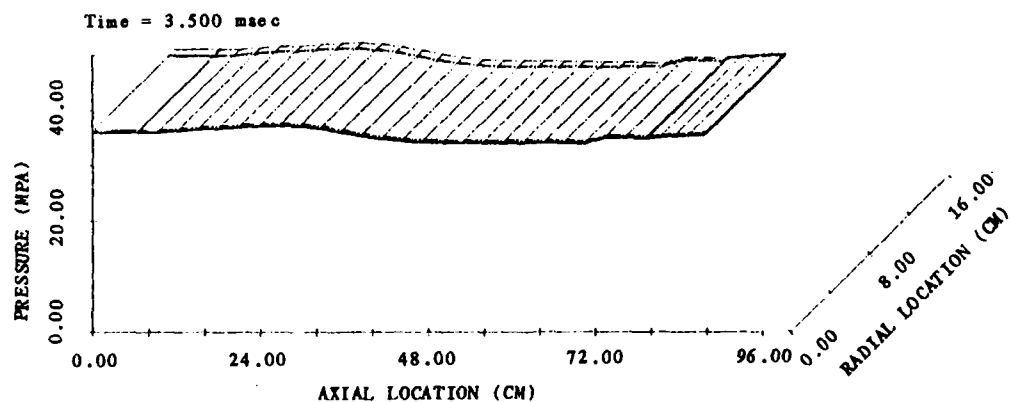
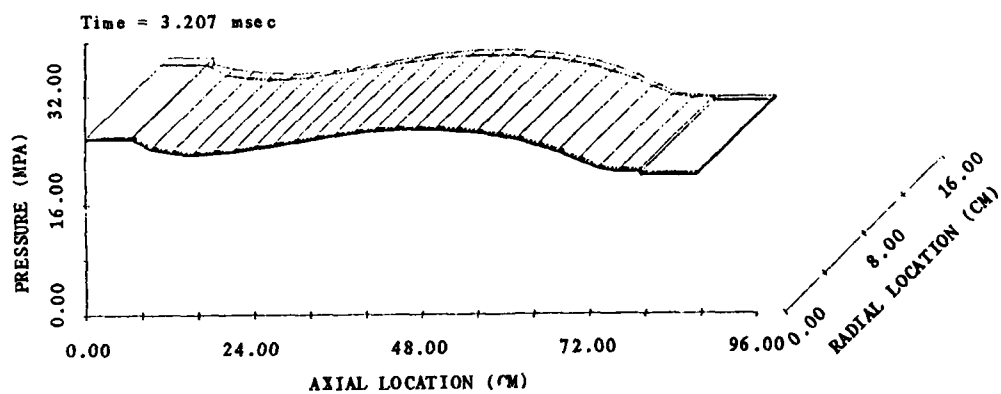
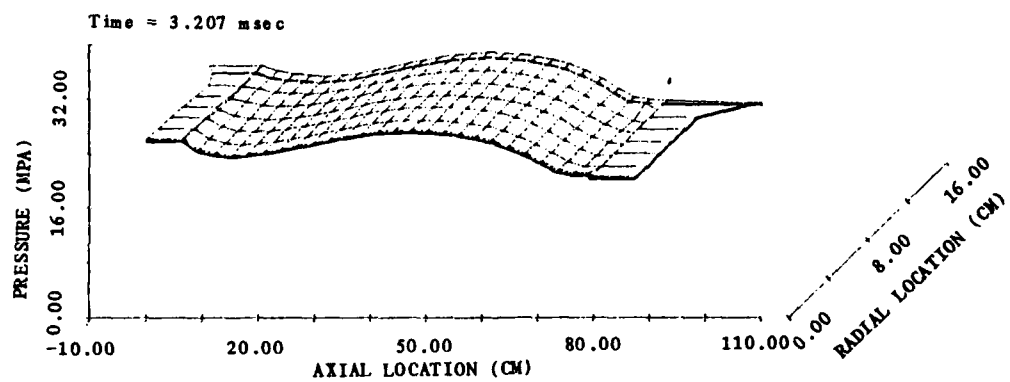


Figure 5.2 Continued

AD-A171 004

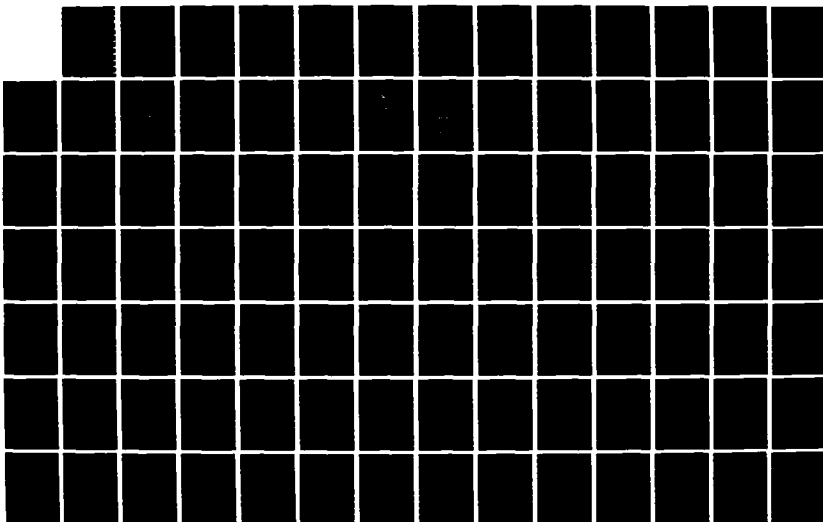
NUMERICAL SIMULATION OF CURRENT ARTILLERY CHARGES USING 2/3
THE TDNOVA CODE(U) GOUGH (PAUL) ASSOCIATES INC
PORTSMOUTH NH P S GOUGH JUN 86 BRL-CR-555

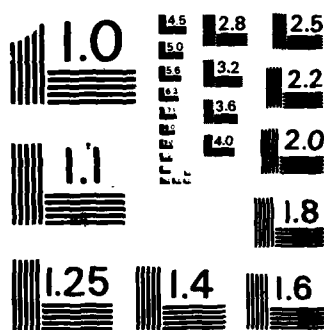
UNCLASSIFIED

DAK11-83-C-0051

F/O 19/4

NL





MICROCOPY RESOLUTION TEST CHART
NATIONAL BUREAU OF STANDARDS - 1963 - A

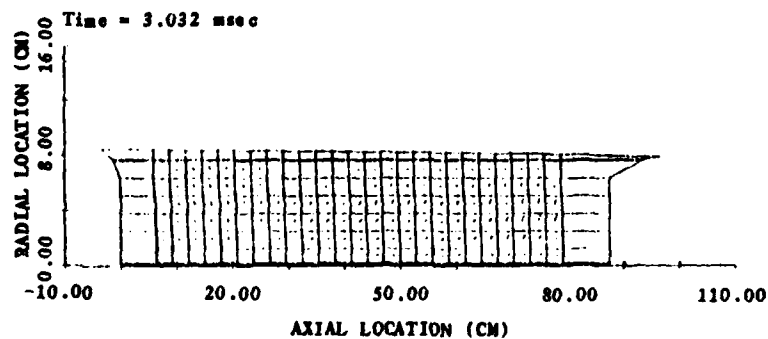
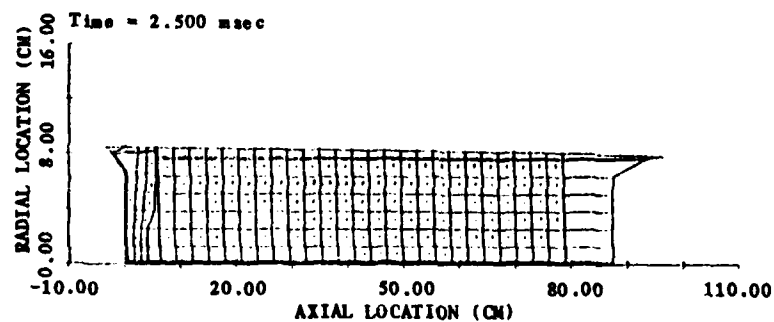
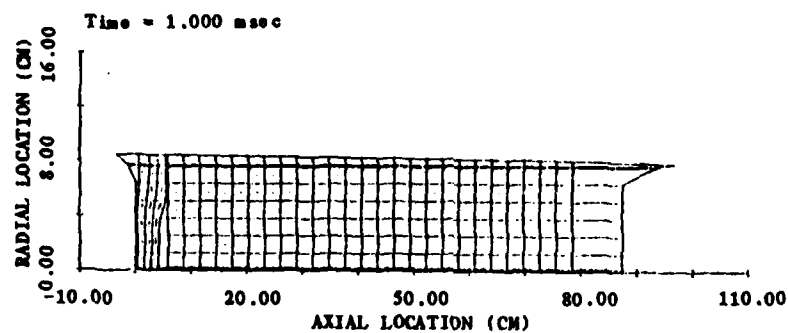
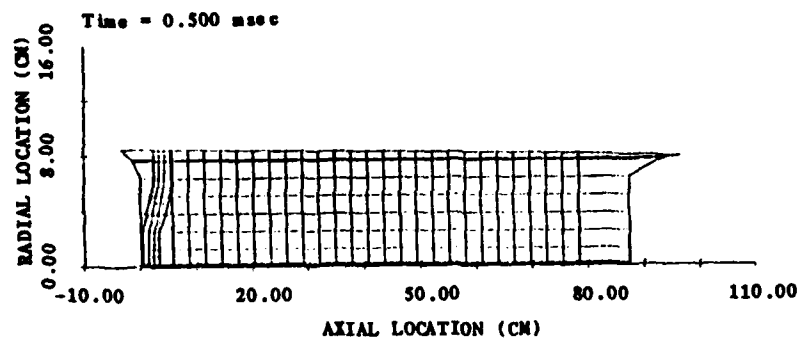


Figure 5.3 Solid-Phase Velocity Fields for the M203E2 Case 1 (Nominal) Data Base

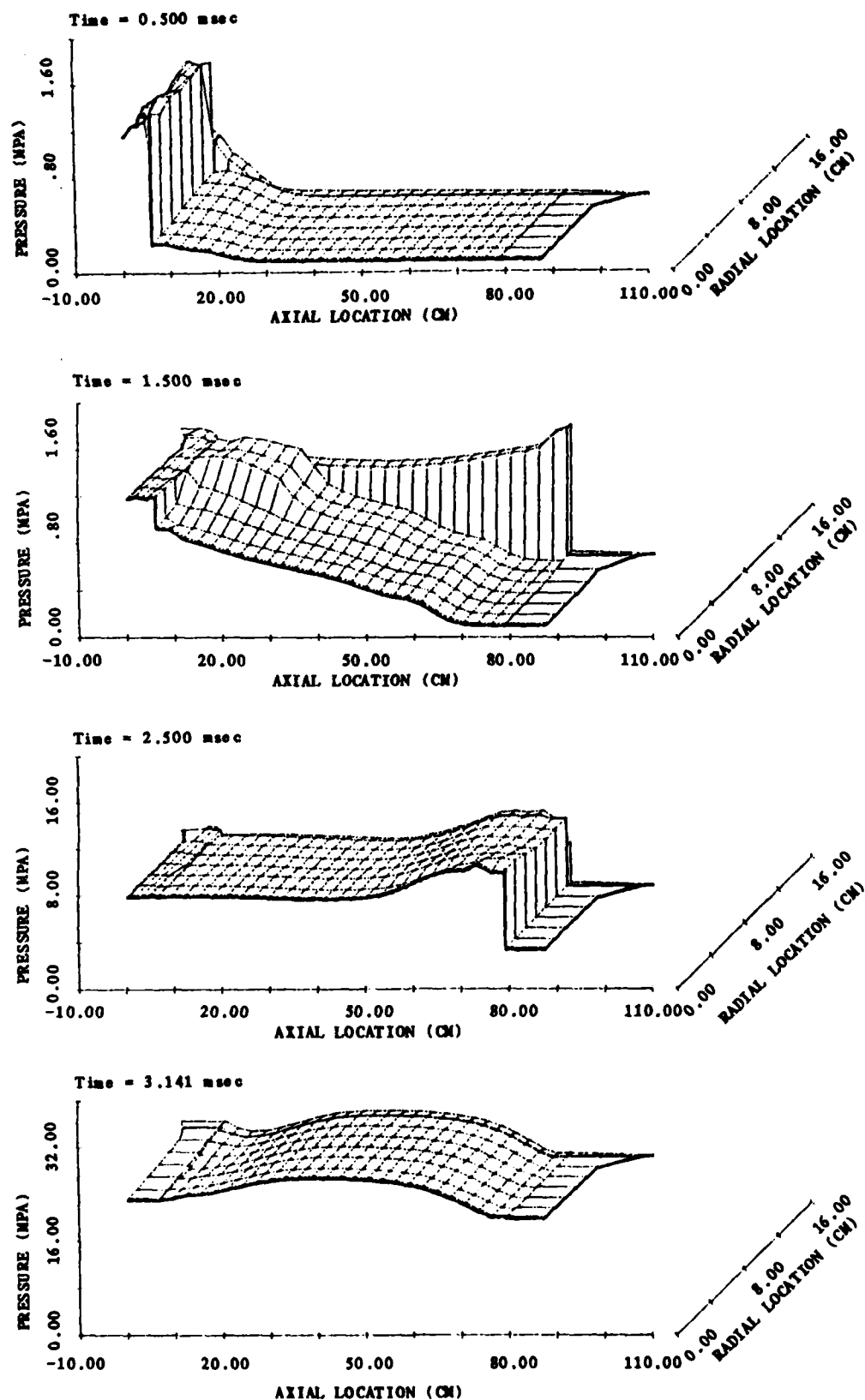


Figure 5.4 Pressure Distributions for the M203E2 Case 2 Data Base

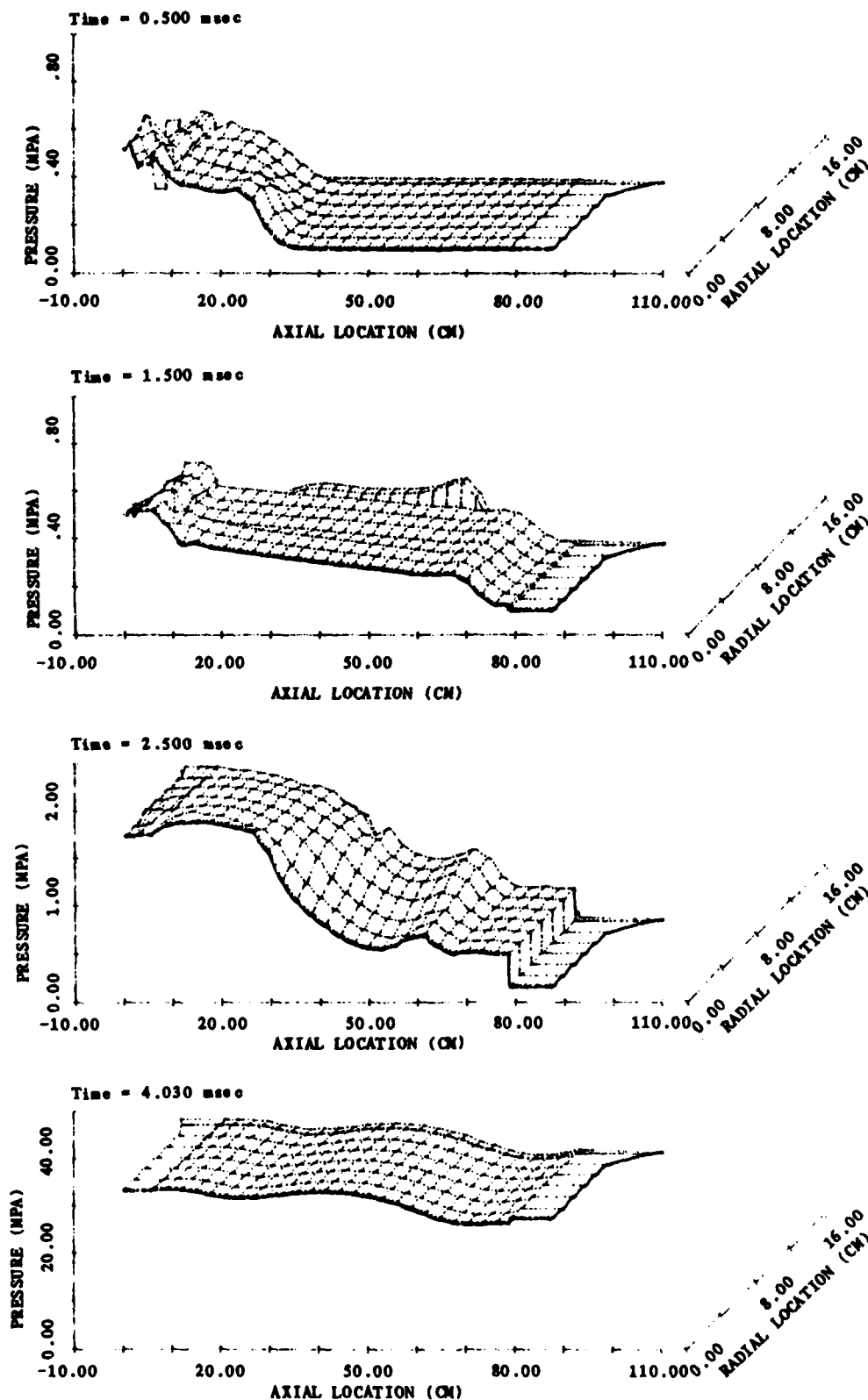


Figure 5.5 Pressure Distributions for the M203E2 Case 3 Data Base

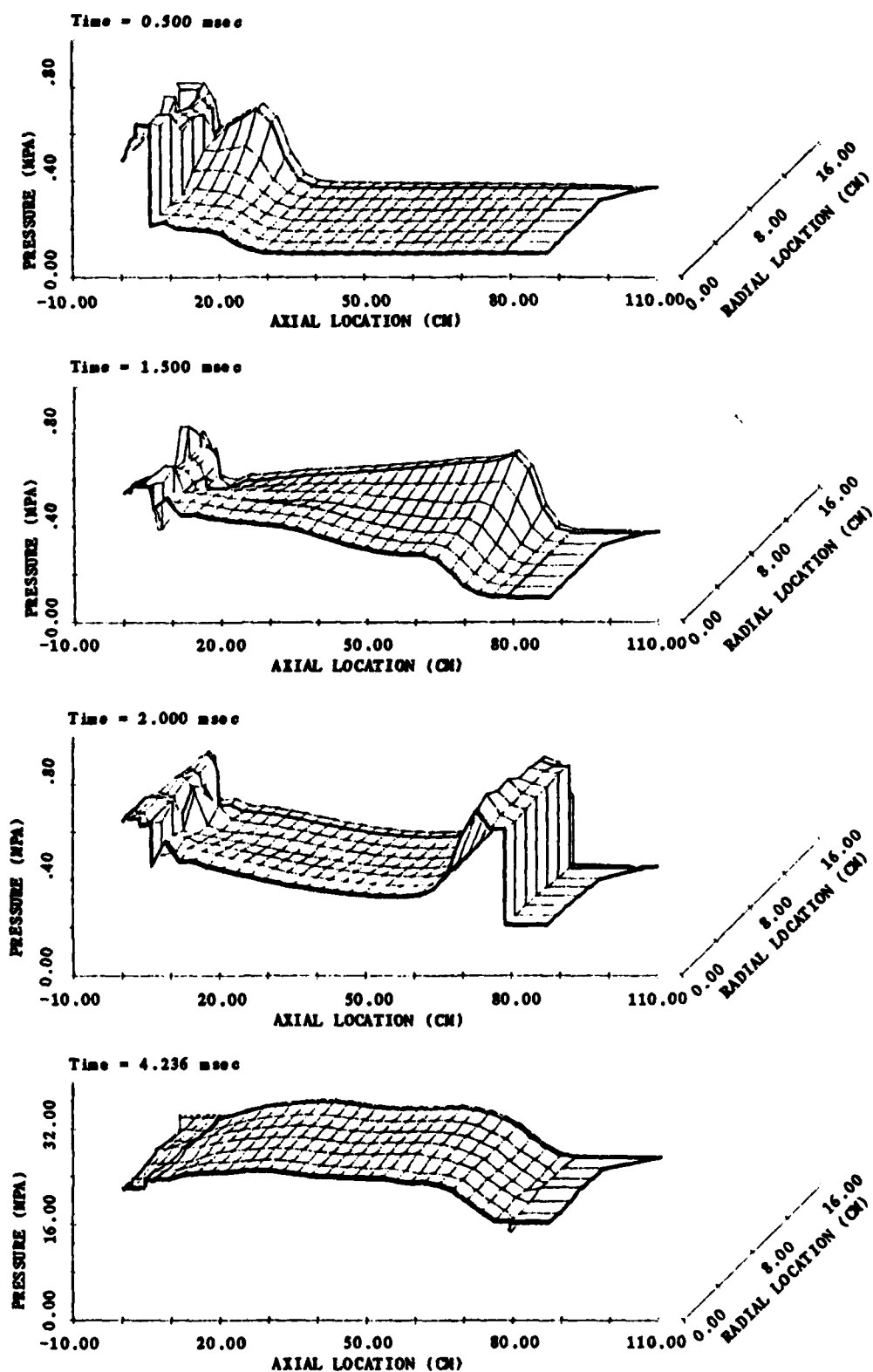


Figure 5.6 Pressure Distributions for the M203E2 Case 4 Data Base

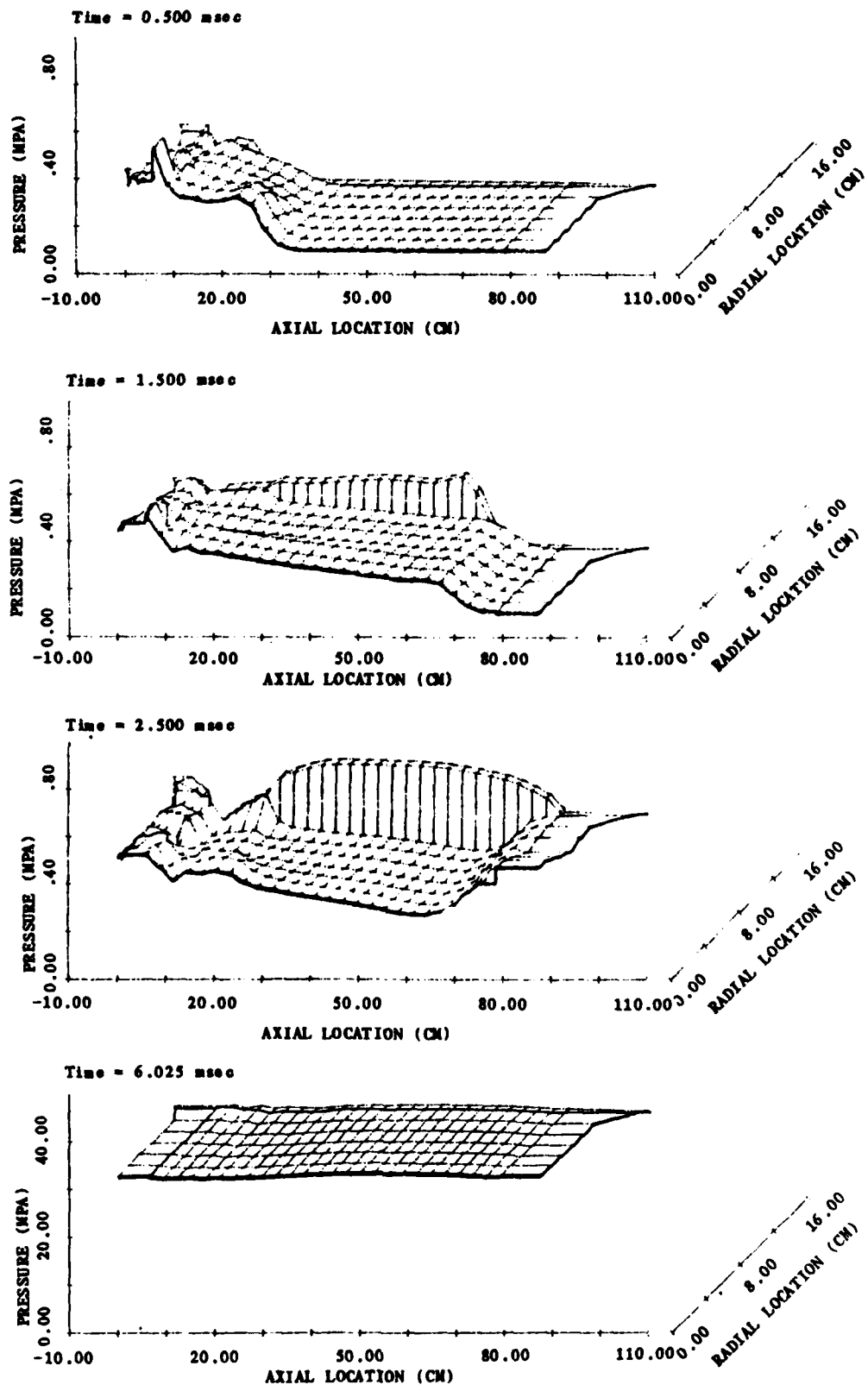


Figure 5.7 Pressure Distributions for the M203E2 Case 5 Data Base

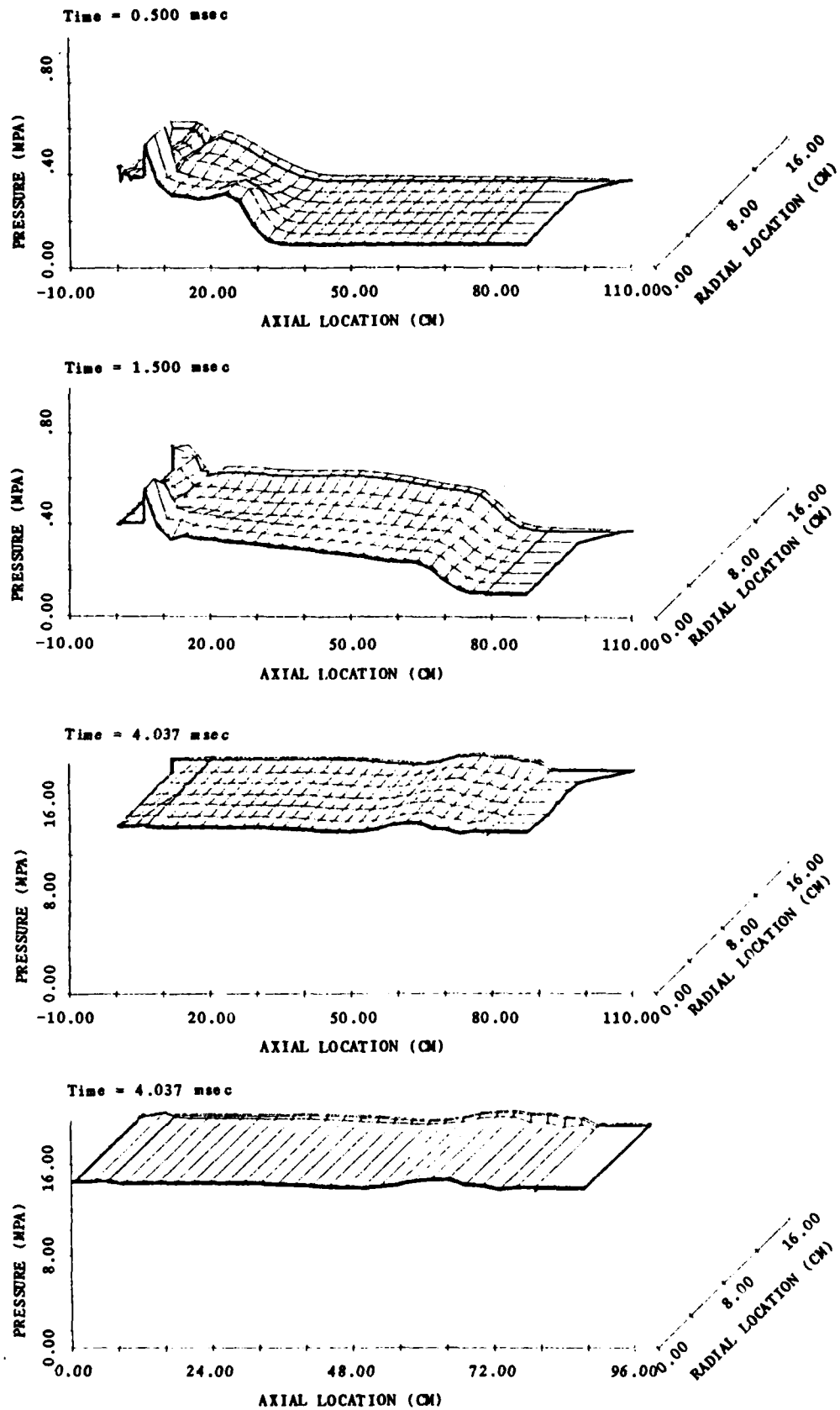


Figure 5.8 Pressure Distributions for the M203E2 Case 6 Data Base

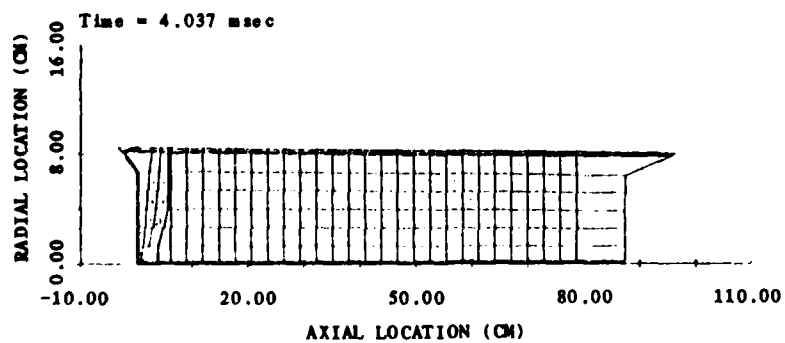
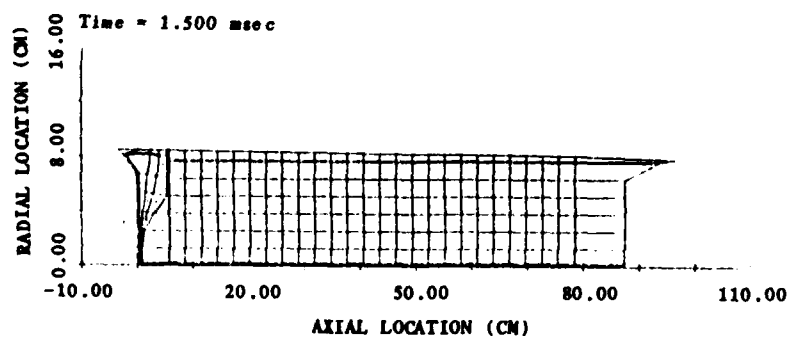
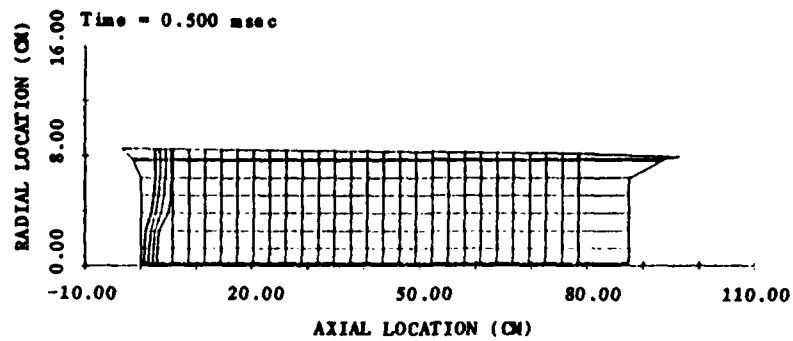


Figure 5.9 Solid-Phase Velocity Fields for the M203E2 Case 6 Data Base

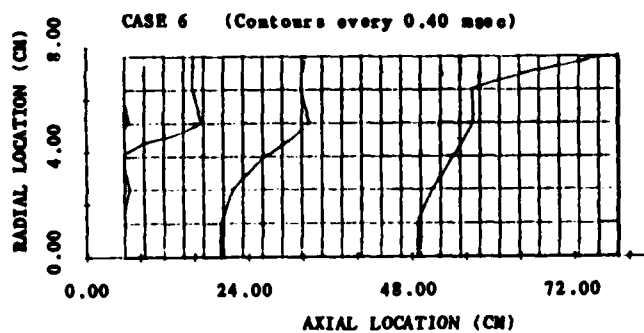
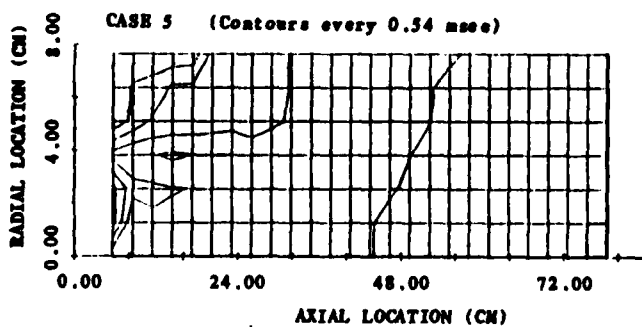
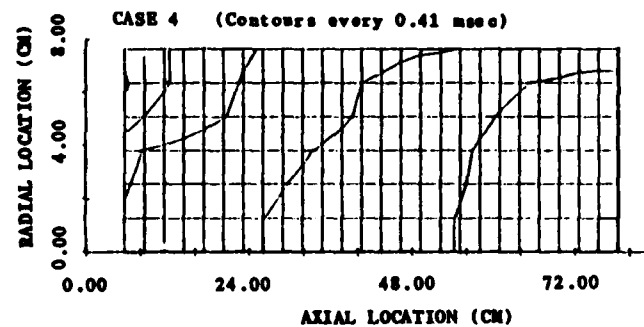
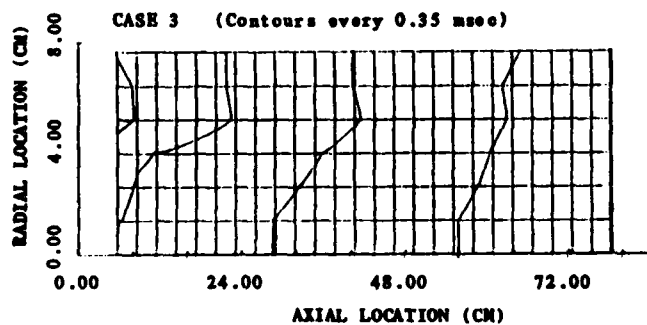
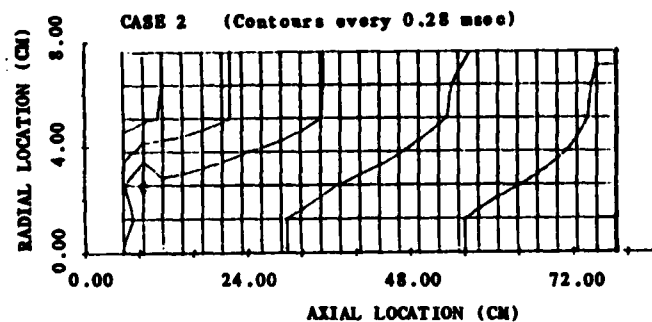
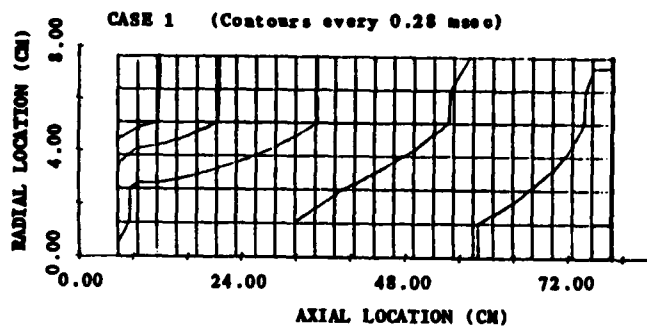


Figure 5.10 Influence of Case Permeability on External (Interstitial) Flamespreading Through M203E2 Charge

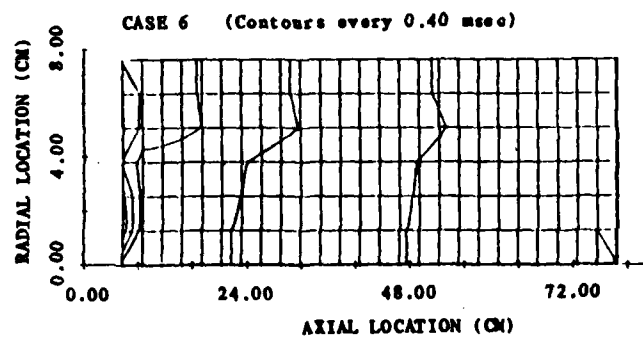
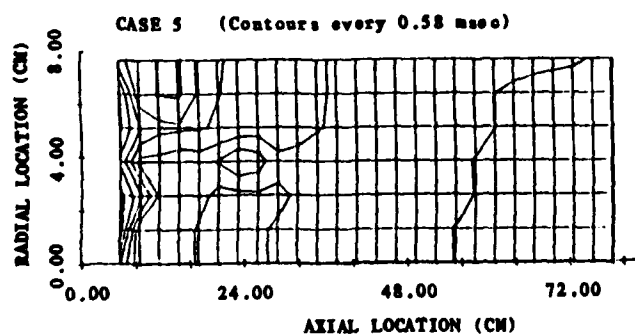
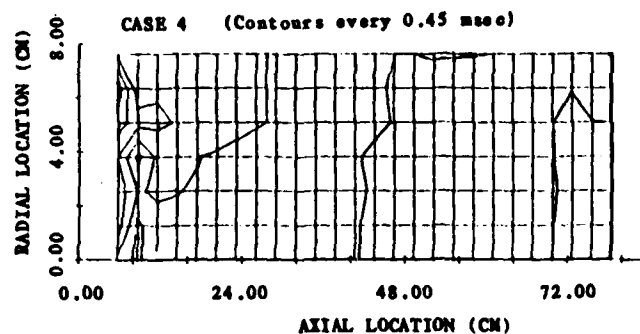
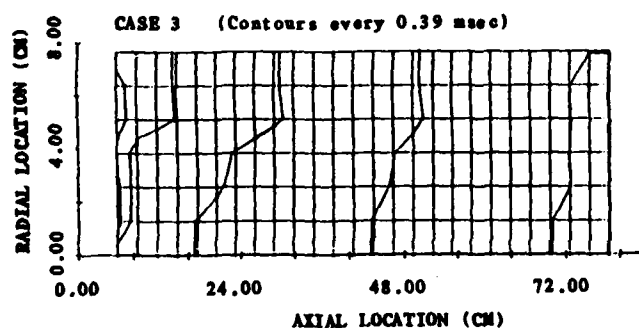
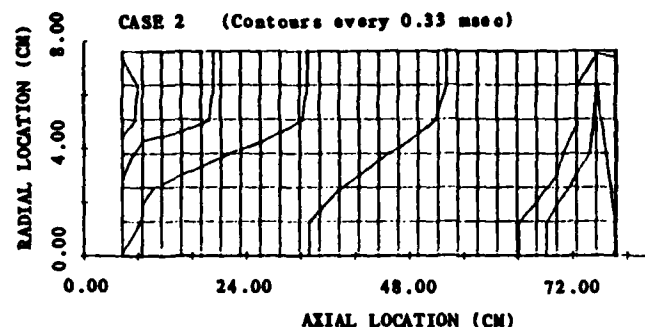
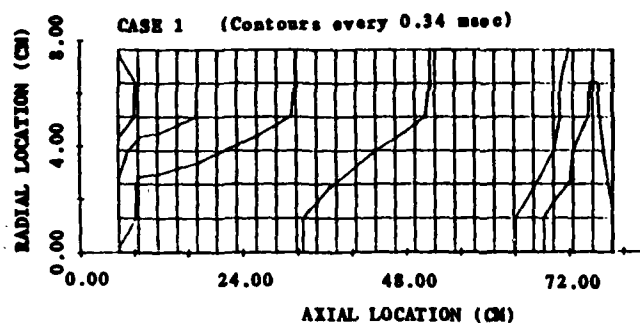


Figure 5.11 Influence of Case Permeability on Internal (Perforation) Flamespreading Through M203E2 Charge

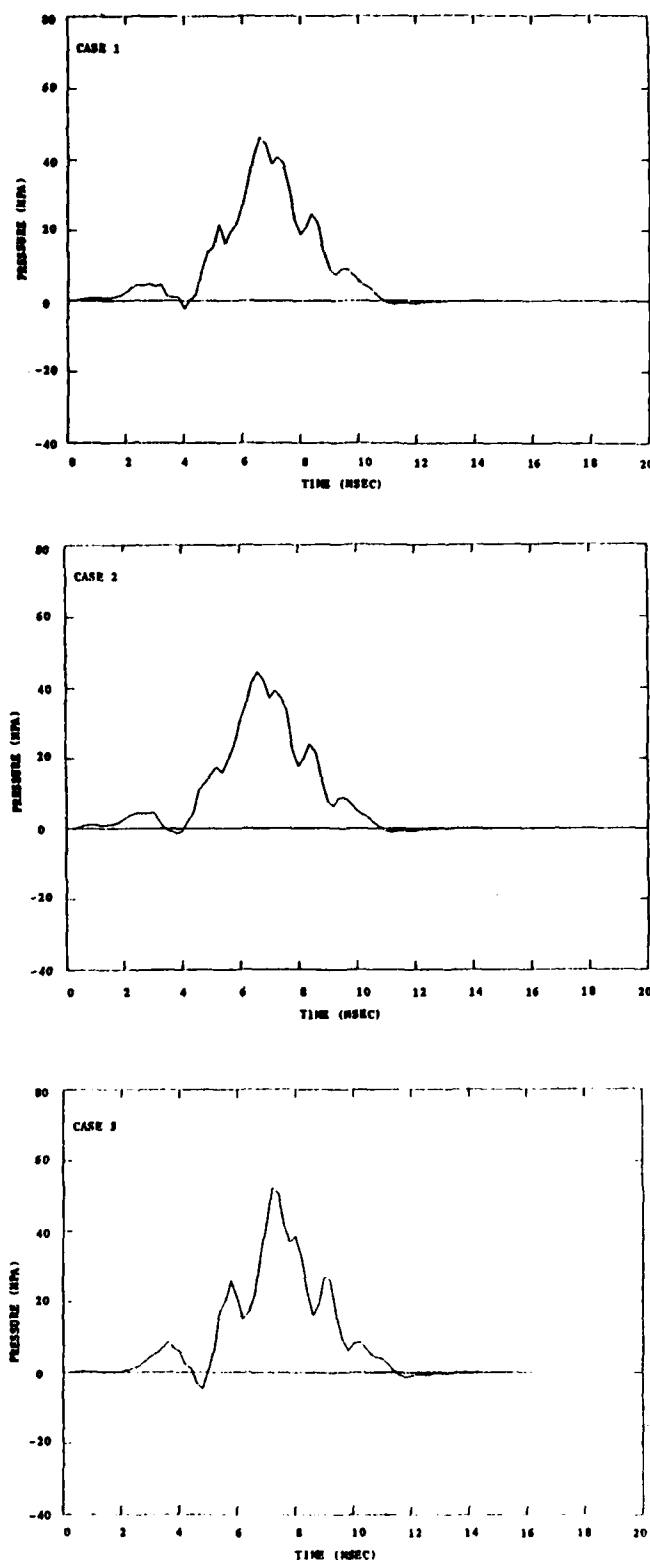


Figure 5.12 Influence of Case Permeability on Pressure Difference History in M203E2 Charge (Pressure at 0.01 cm minus pressure at 87.37 cm on centerline)

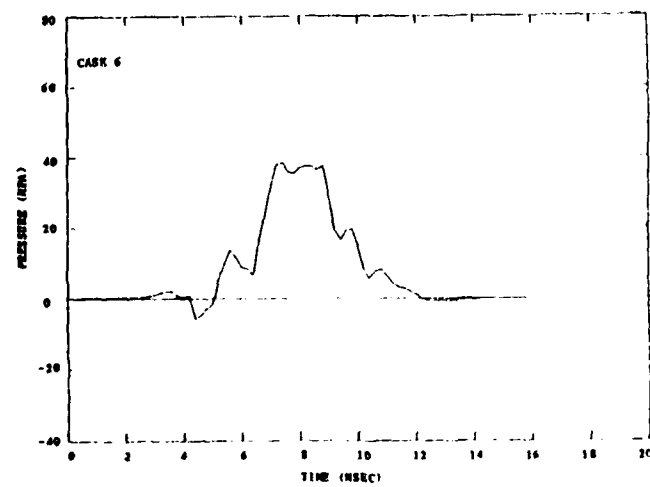
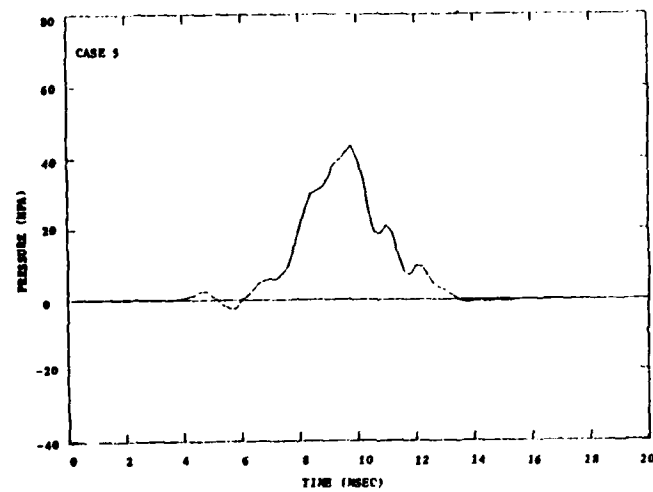
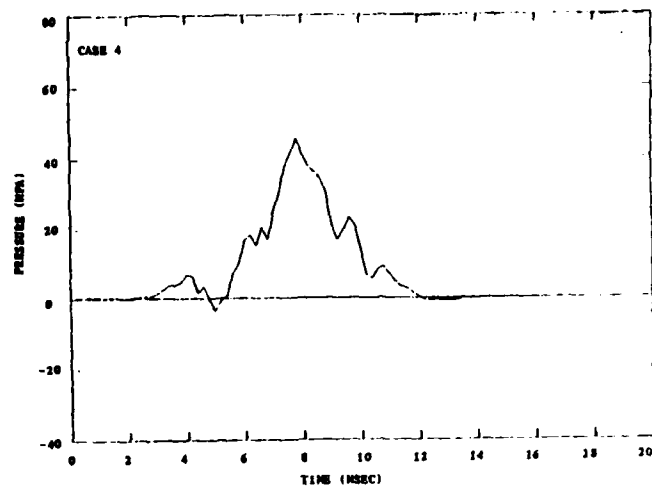


Figure 5.12 Continued

6.0 THE XM216 PROPELLING CHARGE

We turn now to a more demanding computational exercise, namely the simulation of the XM216 Propelling Charge for the 155-mm Howitzer. In contrast to the M203E2 Charge we must now confront a total of three main charge increments, each separately enclosed in its own container. Like the M203E2 Charge, the XM216 Charge has a structurally complex base igniter which we also wish to model as a separate increment. In Section 6.1 we describe the XM216 Charge in more detail, discuss a nominal data base to represent it, and present certain details of the solution. In Section 6.2 we examine the theoretical influence of the properties of the container. As in Chapter 5.0 we consider the effect of the permeability of the various sections of the container. We also examine the influence of the strength of the bonds between the individual containers.

6.1 Nominal Data Base and Solution

The XM216 Charge is illustrated in Figure 6.1. The charge consists of three main increments of M31 slotted stick propellant. The two forward main charge increments are identical and are somewhat shorter than the first main charge increment. They also have a somewhat larger web than the first main charge increment. Ignition is induced by a base igniter increment whose characteristics are similar to those for the M203E2 Charge described in Chapter 4.0. We note that the endwall between the igniter and the first main charge increment is permeable, another point of similarity with the M203E2 Charge. However, the two forward increments are completely enclosed by impermeable containers. The igniter increment is strongly bonded to the first main charge increment. The two forward main charge increments, however, are only lightly bonded to each other and to the first increment. As with the other charges we have considered in this study, ullage is present to the rear of the charge, around it and in front of it. We note that for the XM216 Charge the region of axial ullage between the charge and the projectile is much more extensive than for the M203 or M203E2 Charges.

The nominal representation of this charge is defined by the data base tabulated in Appendix E and is illustrated, in part, by Figure 6.2. Details of the representation are, for the most part, similar to those for the two-increment representation of the M203E2 Charge. All increment containers are rigidized. All the increments of stick propellant are taken to have the slots open at all times so that the pressure in the interstices is always equal to that in the perforations. Combustion of the containers is fully modeled with the exception of the black powder spot located on the outside of the rear endwall of the first main charge increment. The ignition temperature of the CBI, like that of the container segments is set equal to 300°K.

The principal difference between the container representation used here and that for the M203E2 Charge is the present election of the option to initiate container rupture when the main charge is locally ignited. This constitutive modification was made to promote the rate of rupture of the endwalls of the forward increments.

The solution is performed with the computational parameter set 31 X 7 @ 0.05. Some pre-allocation of the axial mesh points was performed in order to ensure that the two forward main charge increments would receive the same number of mesh points. The nominal solution required 1160 CPU seconds on the CYBER 7600 computer. This relatively long run time, as compared with the M203E2 Charge described in Chapter 5.0, reflects the long ignition delay in the present example.

Some details of the nominal solution are presented in Figures 6.3 and 6.4. Figure 6.3 illustrates the pressure distributions at a variety of times throughout the interior ballistic cycle. Figure 6.4 displays the solid-phase velocity fields at various times.

All four containers are modeled as rigidized. The first main charge increment container fails at the rear endwall at about 0.1 msec. Accordingly, the endwall between the igniter and the first main charge increment begins to become fully permeable at this time. The rupture interval, over which the flow resistance drops to zero, is 1.0 msec for all segments of all containers. By 0.2 msec the igniter increment fails at the rear endwall and it too starts to become fully permeable. The second main charge increment fails at the forward endwall at 0.55 msec. The third main charge increment fails at the same time at its rear endwall. Accordingly, the boundary between the second and third main charge increments begins to become fully permeable at this time. The commencement of rupture of all other container segments is gradual and is a result of either overpressure from within the container or the local ignition of the propellant. With regard to the initiation of rupture by overpressure, we note that the load on the container reflects the solid-phase intergranular stress as well as the gas-phase pressure. Furthermore, if the exterior of the container is burning, rupture will be taken to commence whenever the contiguous ullage collapses.

In Figure 6.3 we see that at 0.5 msec the pressure in the igniter increment is significantly higher than that in the first main charge increment. Although the endwall between the increments has ruptured, it still has a finite flow resistance and supports a significant pressure differential. Some pressurization of the outer annular ullage is also seen at 0.5 msec. Due to the impermeability of the sidewall the gas does not penetrate the propellant bed. Instead, the bed is compressed as the radial pressure differential is transmitted through the sidewall of the container and equilibrated by the transverse intergranular stress field on the boundary.

By 1.0 msec the first main charge increment is pressurized. The rear endwall has become almost fully permeable. But the sidewall is still intact. Flamespread has not started. Ignition of the first main charge increment does not occur until roughly 2.5 msec have elapsed. At 1.5 msec we see nearly uniform pressure throughout the first main charge increment and near equilibration across the sidewall even though the sidewall is still

impermeable. Meanwhile the two forward charge increments find themselves being compressed by the pressure in the outer annular ullage. Although the endwalls between the two forward main charge increments are permeable, the increments are in contact and the model does not recognize the possibility of gas leakage from the annular ullage into the collapsed region of axial ullage between the increments.

At 4.0 msec the pressure distribution has not changed appreciably, although we note the pressurization of the forward region of ullage. However, flamespreading through the first main charge increment is nearing completion. By 4.56 msec the first main charge increment is fully ignited on both the outer and inner surfaces of the sticks. At 4.747 msec we see for the first time some pressurization within the two forward main charge increments. At 4.747 msec the igniter increment has been eliminated due to local burnout.

Shortly thereafter, flamespreading begins in the two forward increments. By 5.02 msec the second main charge increment is fully ignited and by 5.16 msec so is the third increment. At 5.5 msec the pressure is nearly uniform throughout all three increments. By 8.944 msec the containers are fully ruptured and the solution satisfies the pressure tolerance criterion for transformation to a quasi-two-dimensional representation. We display the solution directly before and directly after transformation. Figure 6.3 concludes with the pressure distribution at 21.024 msec as the projectile reaches the muzzle of the gun.

Figure 6.4 displays the solid-phase velocity fields at various times. We note that in contrast to the M203E2 Charge of Chapter 5.0, the XM216 Charge involves substantial motion and deformation of the individual increments. At 1.0 msec only the igniter increment has deformed or moved appreciably. But by 4.558 msec, the first main charge increment has expanded to the tube wall. The second main charge increment is beginning to move forward. Although the outer part of the rear endwall of the second increment is ruptured by 4.558 msec, the inner part is not and the inner sticks continue to be pushed forward. They, in turn, push forward the inner sticks of the third main charge increment. At the time of transformation to a quasi-two-dimensional representation the three main charge increments have all separated. The endwalls have developed rather irregular shapes, reflecting the potential for physical instability of the boundaries of the charge.

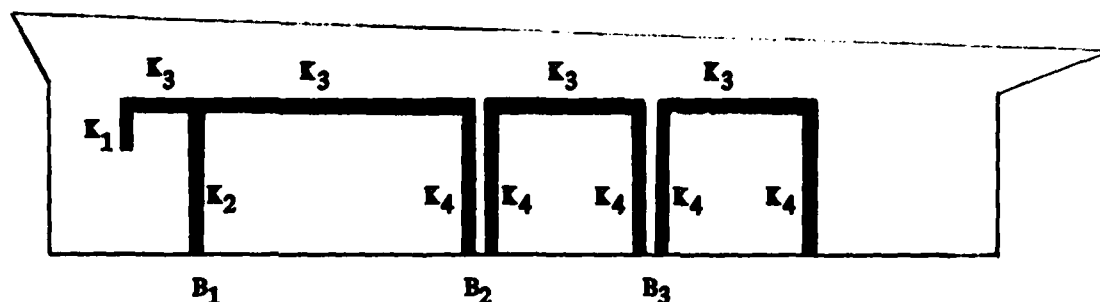
6.2 Effects of Container Properties

Our assessment of the theoretical influence of the properties of the container is similar to that of Chapter 5.0. Here, however, in addition to the effect of the permeability of the container segments we also consider the effect of the bonds between increments. Including the nominal solution of Section 6.1 we consider a total of eight data bases. All data bases are variations of the nominal data base tabulated in Appendix E. Only the bond strengths and segment flow resistance factors differ from case to case.

Table 6.1 presents the parametric values of bond strength and container segment flow resistance coefficients used in the eight simulations. Table 6.2 presents the corresponding ballistic predictions and the maximum, minimum and final values of the percent mass defect. Details of the solutions for Cases 4 through 8 are presented in Figures 6.5 through 6.12.

Table 6.1 Values of Container Bond Strength and Flow Resistance for Simulations of XM216 Propelling Charge

Case	B_1^* (N)	B_2 (N)	B_3 (N)	K_1	K_2	K_3	K_4
1	10^6	10	10	101	10	101	101
2	2×10^6	20	20	101	10	101	101
3	0	0	0	101	10	101	101
4	10^6	10	10	101	20	101	101
5	10^6	10	10	101	0	101	101
6	10^6	10	10	101	10	0	10
7	10^6	10	10	0	0	101	0
8	10^6	10	10	0	0	0	0



* Nomenclature for values of B_1 and K_1 as in sketch

Referring to Table 6.1 we see that Case 1 is the nominal solution which we have already discussed. In Case 2 the strength of the bonds between the increments is doubled while in Case 3 it is set equal to zero. Since only B_1 , the strength of the bond between the igniter increment and the first main charge increment, is appreciably different from zero it is the influence of this single term which is being assessed in Cases 2 and 3. Cases 4 through 8 are analogous to Cases 2 through 6 of Chapter 5.0. In Case 4 we double the flow resistance coefficient for the endwall between the ignition increment and the first main charge increment, in Case 5 we reduce it to zero. In Case 6 the sidewalls are all made fully permeable. Finally, in Case 8 all segments of all containers are made fully permeable.

We draw attention to the value of K_4 in Case 6. Ideally we should have used $K_4 = 101$. However it was not found possible to obtain a complete solution with fully impermeable endwalls. Accordingly, the present choice of $K_4 = 10$ represents a compromise for the sake of numerical tractability.

In general it may be said that all the simulations of the XM216 Charge presented here exhibit signs of numerical strain. This is perhaps not surprising given the geometrical complexity of the charge configuration, the non-analytic conditions due to the container properties and the limited number of mesh points used to represent the solution. While a greater number of mesh points would have been desirable we note that the nominal solution already requires a substantial amount of computer time, almost 20 minutes of CPU time on the CYBER 7600. However, a smoother distribution of container properties could certainly be obtained by means of suitable revisions to the constitutive laws for rupture and permeability. It is recommended that such revisions be made, guided by experimental studies, before more substantial commitments of computer time be regarded as appropriate.

That the simulations of XM216 are less accurate than those of the configurationally simple M203E2 Charge is apparent from the values of percent mass defect ($\Delta m\%$) in Table 6.2. Here we see extremal values as large as 5% for some of the cases. Accordingly, although the values of maximum pressure (p_{max}) vary from 245 to 260 MPa and the values of muzzle velocity (m.v.) vary from 679 to 702 m/s, these variations are not sufficiently large to be discriminated from the influence of numerical inaccuracies in our judgment. We therefore conclude that the overall ballistic behavior of the XM216 Charge is computationally insensitive to the properties of the container studied here.

Table 6.2 Effect of Container Bond Strength and Permeability on Simulations of XM216 Propelling Charge

Case	p_{max} (MPa)	m.v. (m/s)	Δp_{min}^* (MPa)	$\Delta m\%$		
				max	min	final
1	249.5	679.2	-20.5	0.42	-5.40	-5.40
2	249.5	679.2	-20.5	0.42	-5.40	-5.40
3	256.6	695.4	-9.4	1.04	-3.31	-3.31
4	245.1	682.4	-14.0	0.18	-5.66	-5.66
5	260.6	702.4	-2.1	0.97	-2.14	-2.14
6	251.4	688.6	-42.8	0.95	-3.89	-3.89
7	259.4	703.8	-3.4	2.00	-0.82	-0.82
8	255.6	698.4	-4.1	0.59	-2.42	-2.42

* Absolute minimum of pressure at 87.37 cm minus pressure at 0.01 cm on centerline

However, the structure of the longitudinal pressure field does appear to exhibit a real level of sensitivity to the properties of the container. Reductions in the flow resistance due to the endwalls appear to reduce the value of Δp_{\min} , a finding which is in keeping with expectation. Here Δp_{\min} is the absolute minimum of the pressure difference history, not the first minimum as was considered in the preceding chapters.

Figures 6.5 through 6.12 display some details of the solutions for Cases 4 through 8. We present the pressure distributions for each of these solutions at a number of times up to and including the instant of transformation to a quasi-two-dimensional representation. For Cases 5, 6 and 7 we display the solid-phase velocity fields. In general these solutions are easily understood in terms of the parametric values on which they are predicated. Some unexpected features do arise, however, as a result of the limited resolving power of the model. We will draw attention to these anomalies.

Figure 6.5 presents the pressure distributions for Case 4 in which the flow resistance of the endwall between the igniter and the first main charge increment is doubled. As was the case in the corresponding solution for the M203E2 Charge, we see very little difference from the nominal solution, Case 1. The effect of setting the resistance of the endwall between the igniter and the first main charge increment to zero is seen in Figure 6.6. Pressurization of the first main charge increment is seen to occur more slowly since the CBI no longer burns under an initial confinement. The effect of the black powder spot is seen in the distribution at 0.5 msec. Such a pressure excursion would not be expected in practice and reflects the inconsistency of the tabulated rate of discharge with the ambient pressure.

Interestingly, the rupture of the rear endwall of the second increment occurs in a more regular fashion in Case 5 than in Case 1. Accordingly, the two forward increments are not pushed forward as strongly as in Case 1. This is seen clearly in Figure 6.7.

Figure 6.8 presents the pressure distributions for Case 6 in which the sidewalls of all containers are made fully permeable. As we discussed previously, it was necessary to make the endwalls of the main charge increments semi-permeable in order to obtain a stable solution. Figure 6.8 includes details of the quasi-two-dimensional part of the solution. Figure 6.9 illustrates the solid-phase velocity fields.

Considering Figure 6.8 we see at 4.5 msec an unexpected feature of the solution. Although the sidewalls are permeable the two forward main charge increments are unpressurized. The solid-phase velocity field at 4.5 msec shows that the first increment has expanded to the tube wall, closing off the annular ullage. At the same time, the model does not recognize the opening of a gap at the forward endwall. The properties of the endwall are attributed to the charge boundary and therefore result in flow resistance over the entire section of the tube defined by the interface between the first and second main charge increments.

The numerical strain associated with this solution is seen at 8.878 msec where we see pressure wiggles near the corners of the two forward main charge increments. Because the corners are excluded from the set of axial positions at which the pressure tolerance criterion is evaluated, transformation to a quasi-two-dimensional representation occurs at this time in spite of the presence of the corner wiggles.

Comparing Figure 6.9 with Figure 6.4 we see that Case 6 involves even greater displacement and deformation of the forward increments than the nominal solution. Apparently, the rate of compression of the gas in the forward region of axial ullage, behind the projectile base, is sufficiently rapid as to create a significant reverse gradient. This is reflected in Figure 6.8 at 9.0 msec and by the results of Table 6.2.

Figures 6.10 and 6.11 illustrate the pressure distributions and solid-phase velocity fields for Case 7 in which the endwalls of all increments are made fully permeable. As expected, the pressure field remains smooth, except for the excursion due to the representation of the black powder spot, and the charge increments suffer very little displacement during flame-spread. Figure 6.12 presents the pressure distributions for Case 8 in which the containers are fully permeable. No unexpected features are seen.

We conclude with Figure 6.13 which compares the histories of pressure difference for all the eight cases. Only Case 6 exhibits a significant reverse gradient.

155MM, MODULAR CHARGE XM216

MODULAR ZONES 2 THRU 4

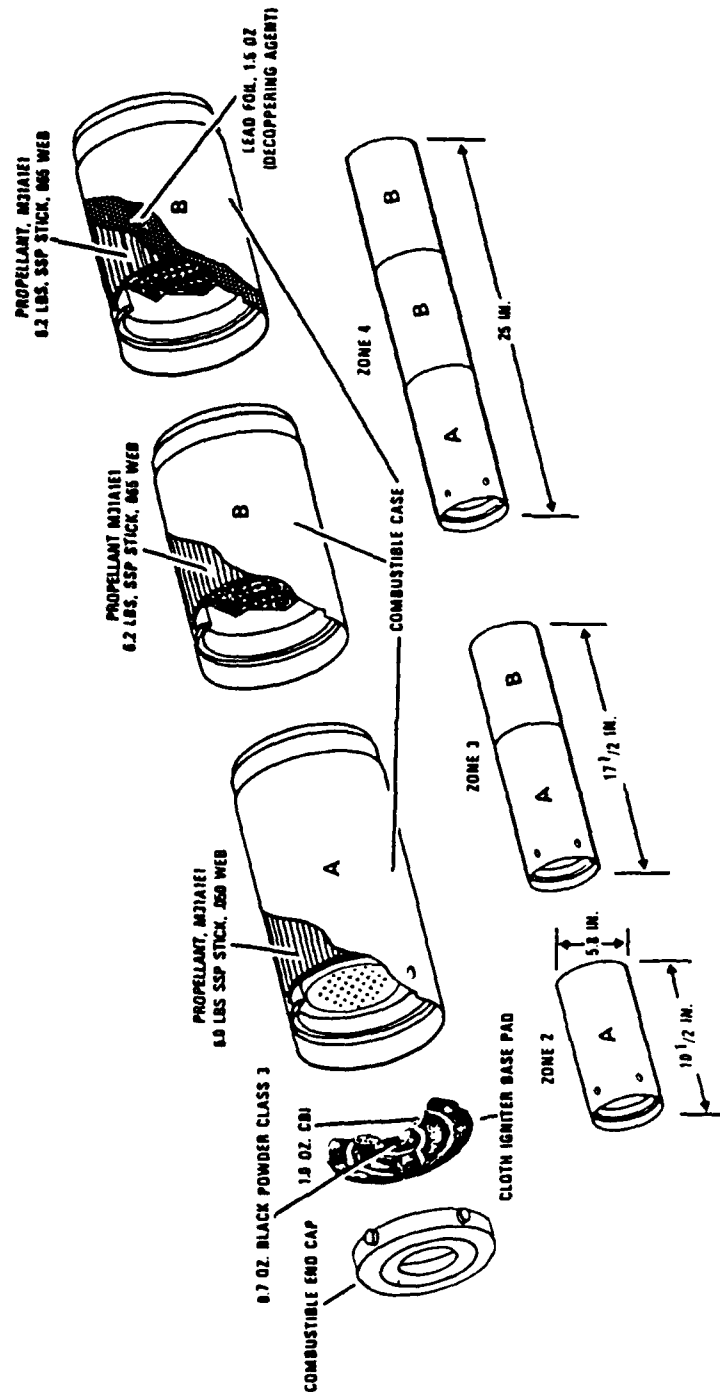


Figure 6.1 The XM216 Propelling Charge

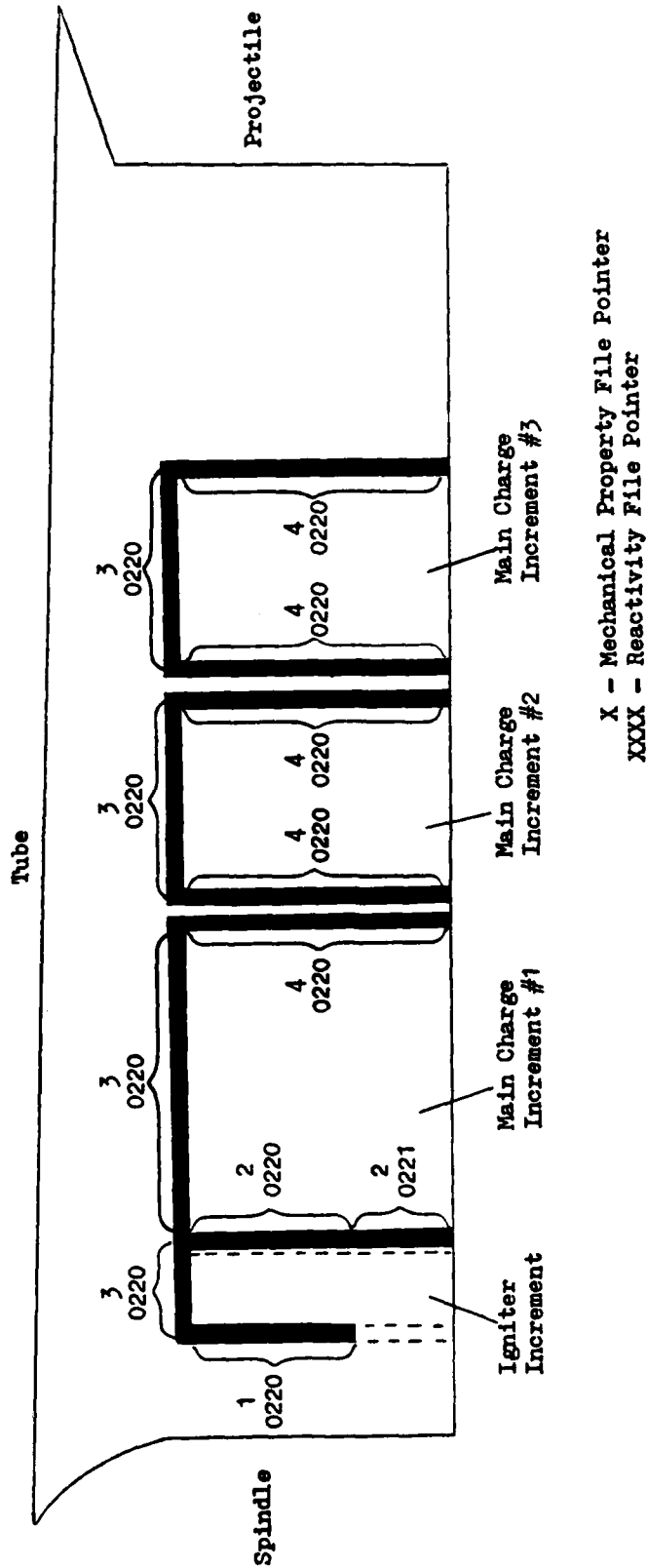


Figure 6.2 Representation of XM216 Charge by TINOVA

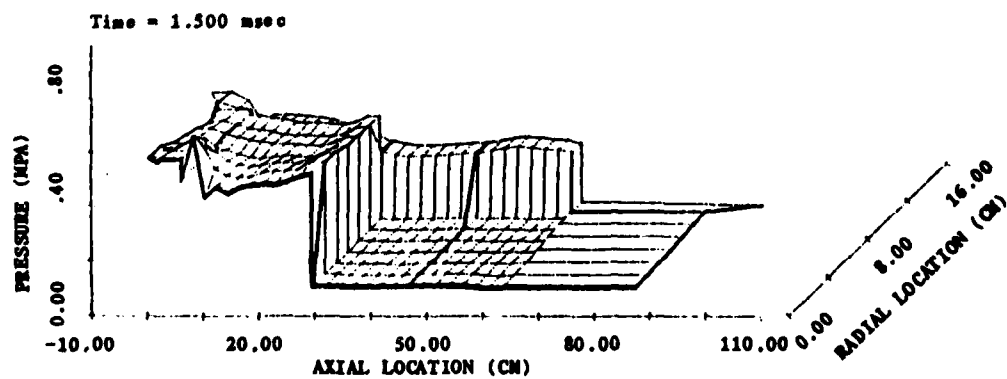
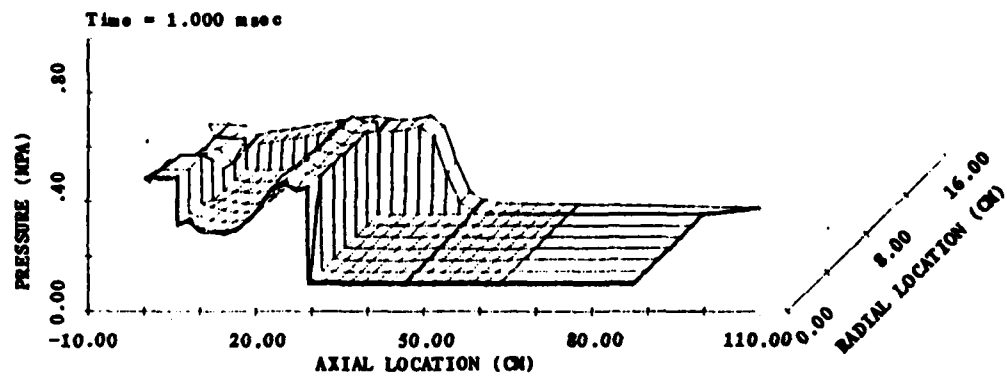
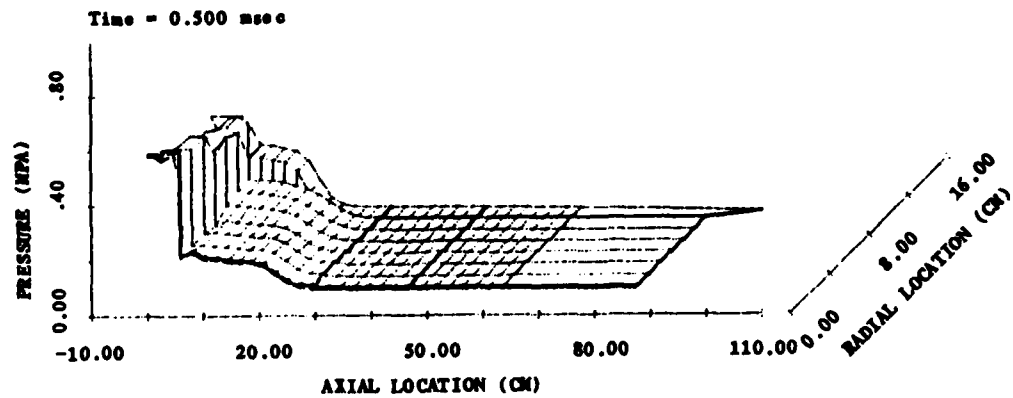


Figure 6.3 Pressure Distributions for the XM216 Case 1 (Nominal) Data Base

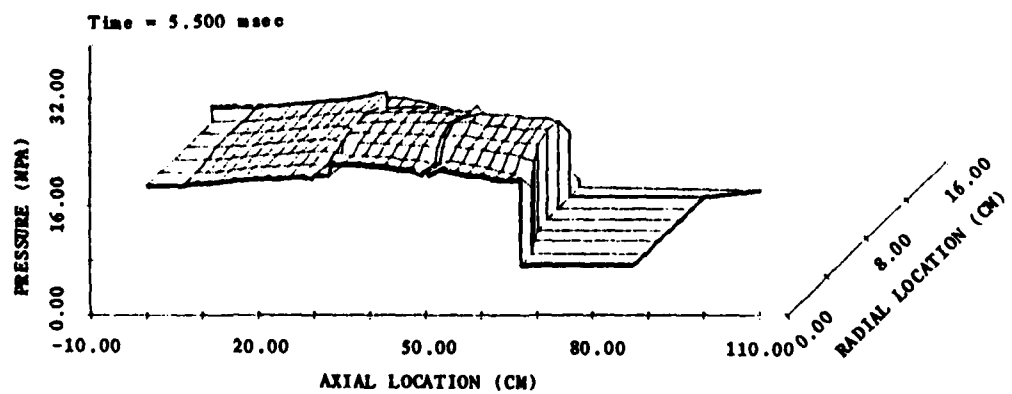
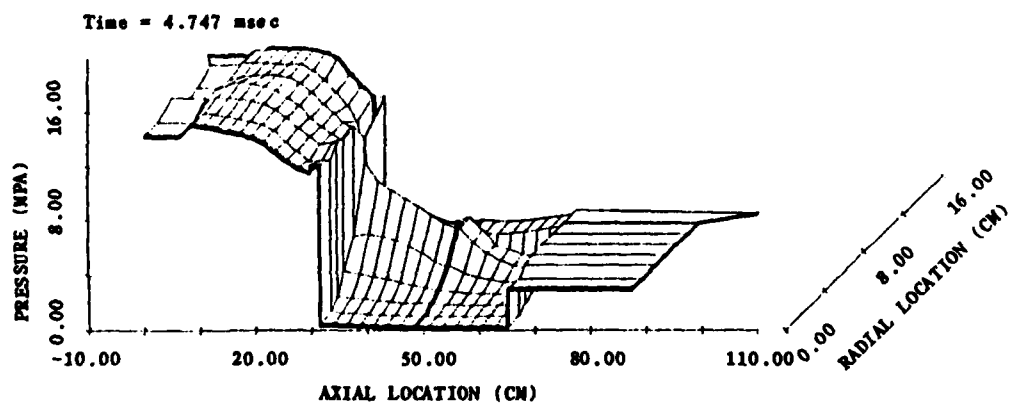
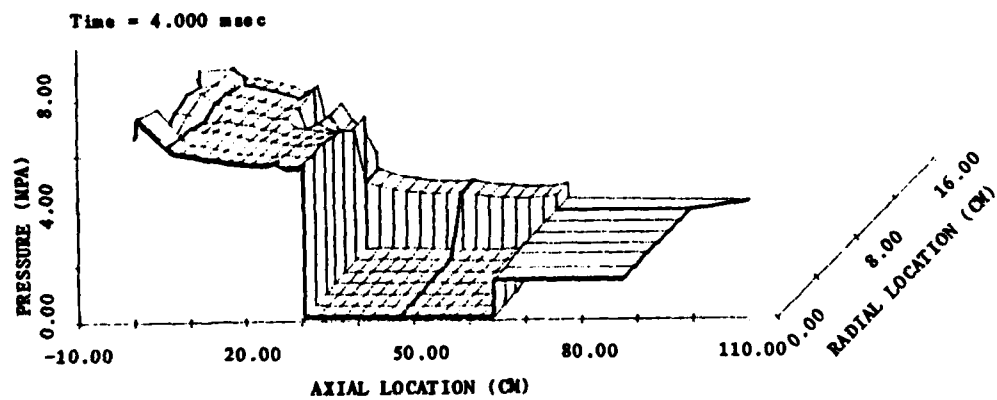


Figure 6.3 Continued

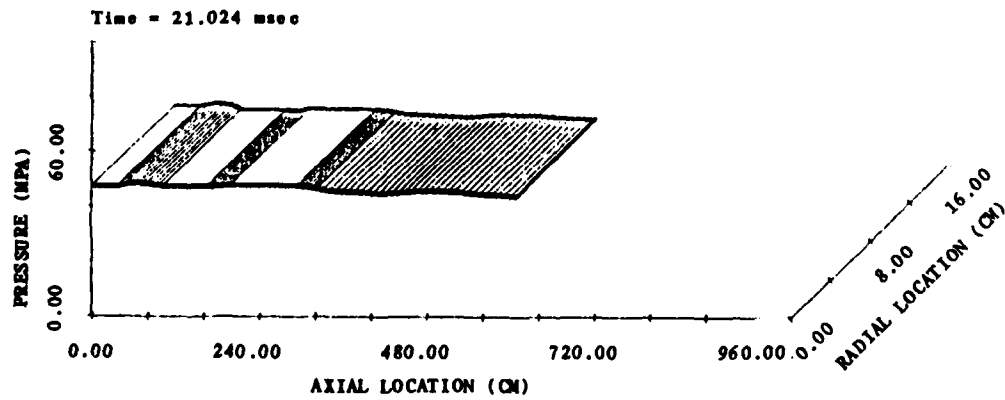
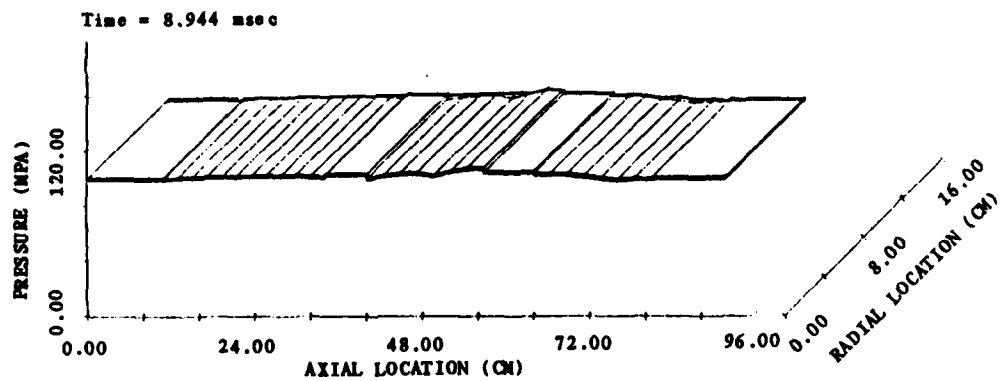
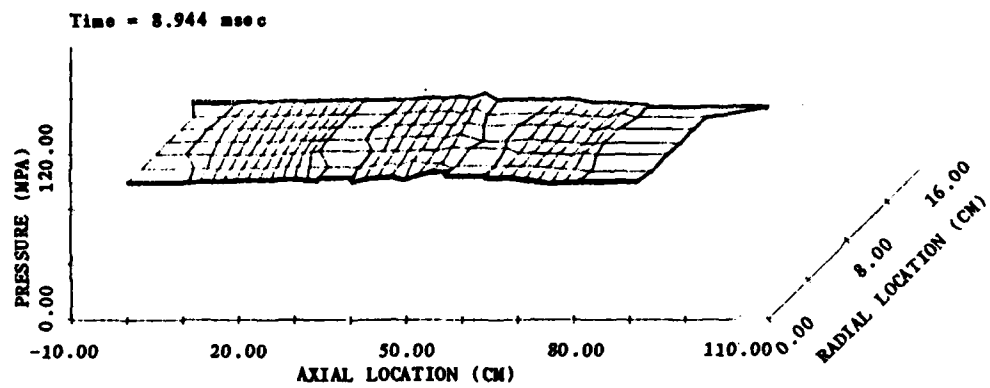


Figure 6.3 Continued

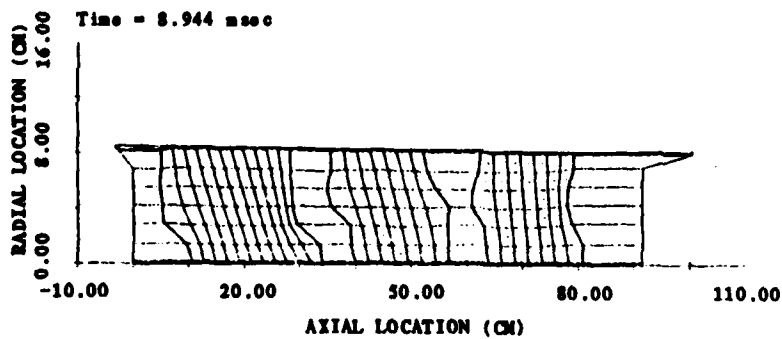
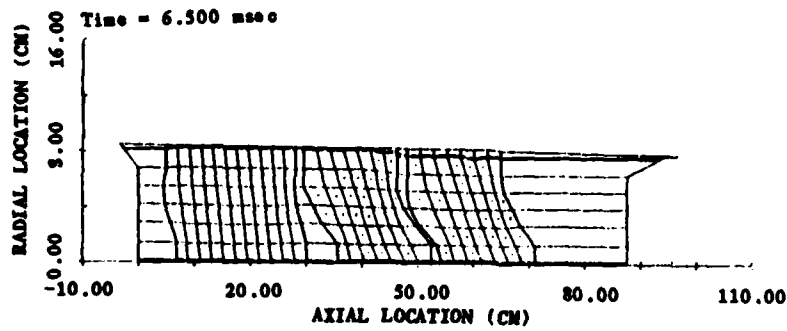
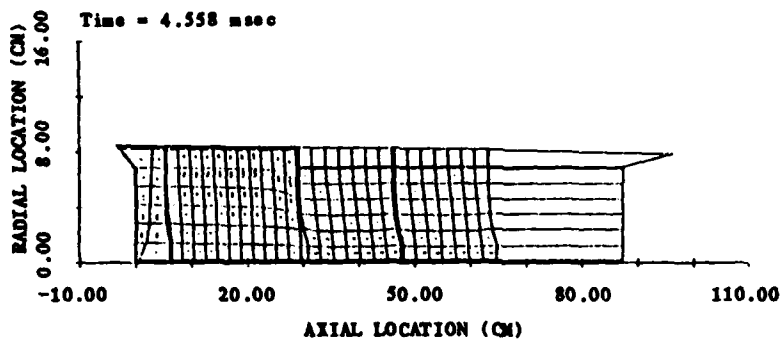
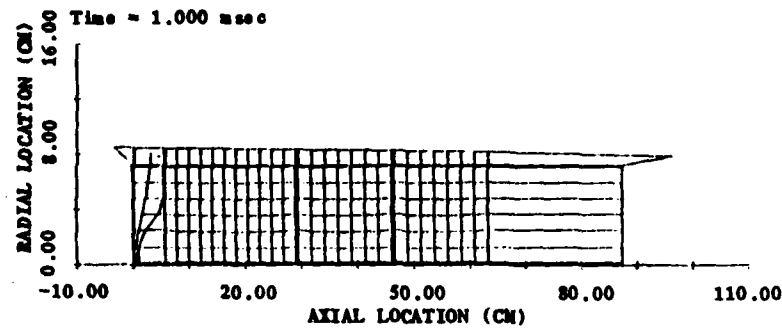


Figure 6.4 Solid-Phase Velocity Fields for the XM216 Case 1 (Nominal) Data Base

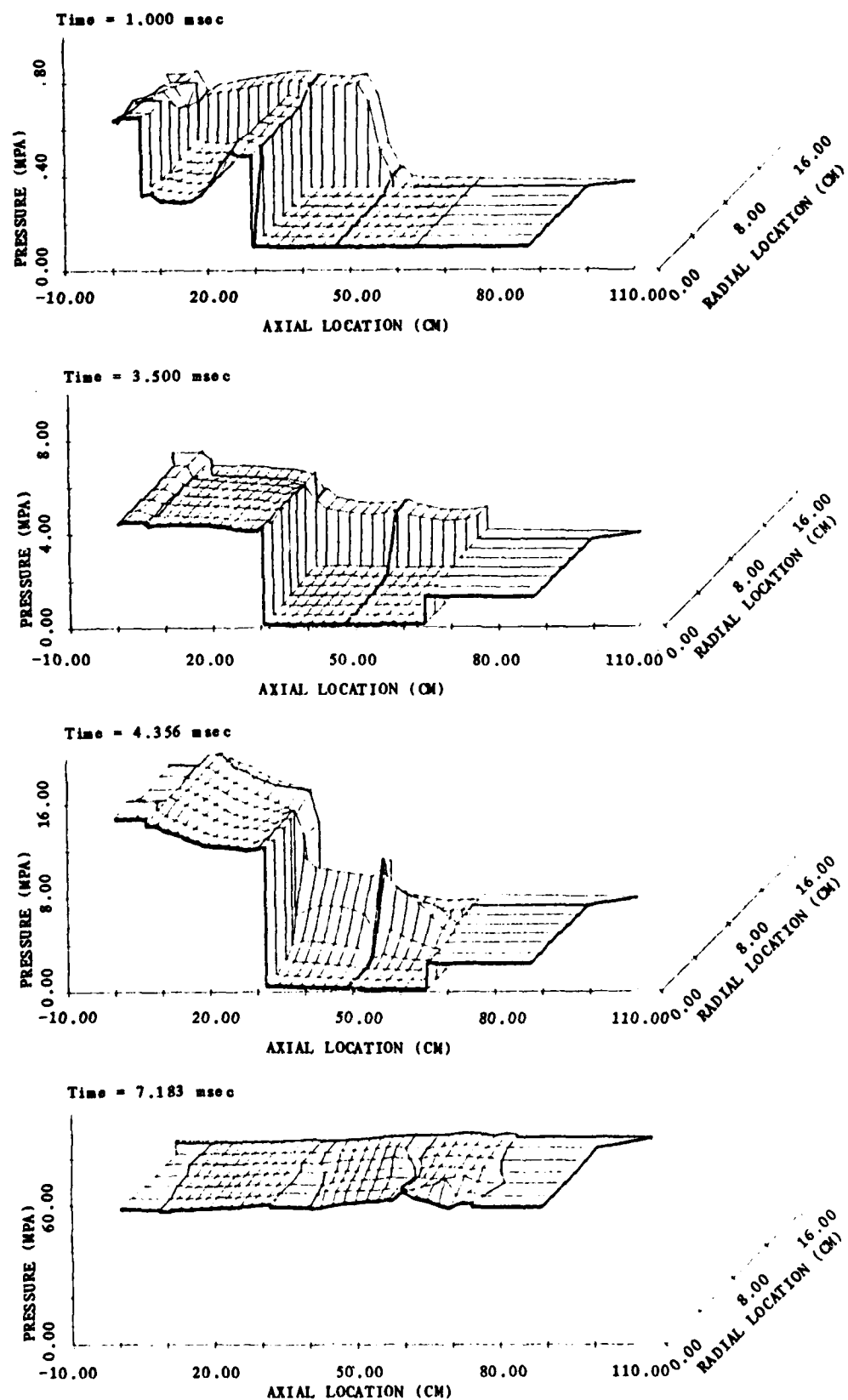


Figure 6.5 Pressure Distributions for the XM216 Case 4 Data Base

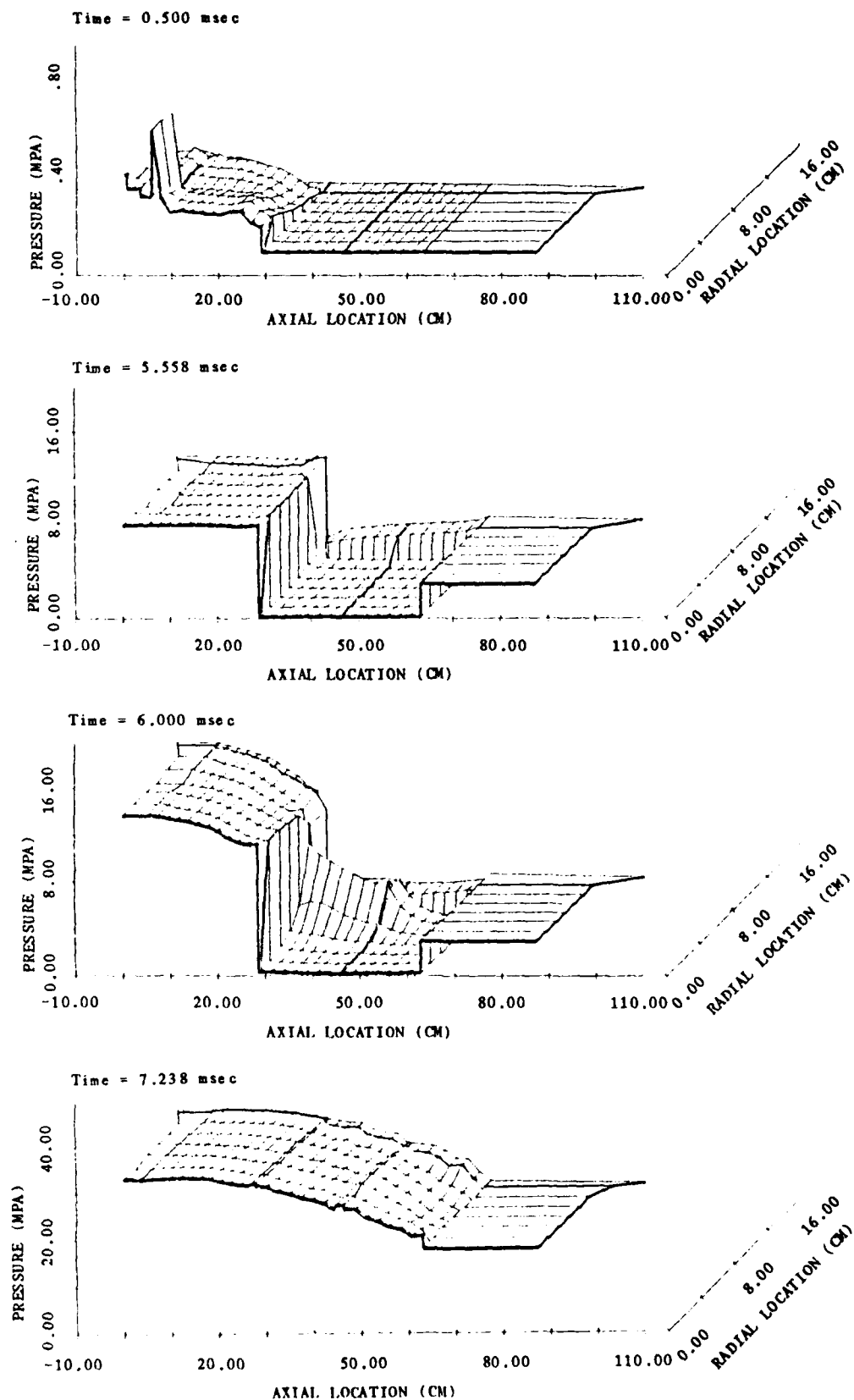


Figure 6.6 Pressure Distributions for the XM216 Case 5 Data Base

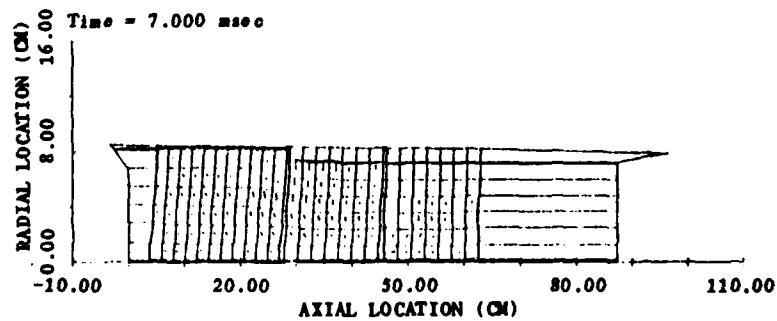
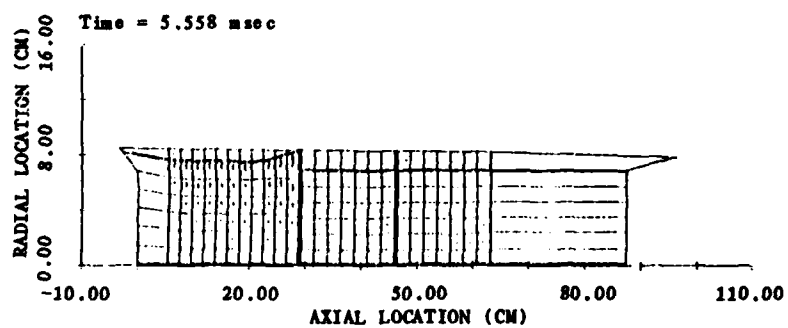
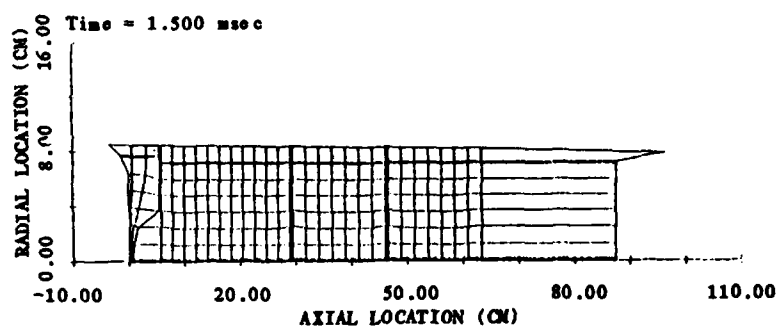
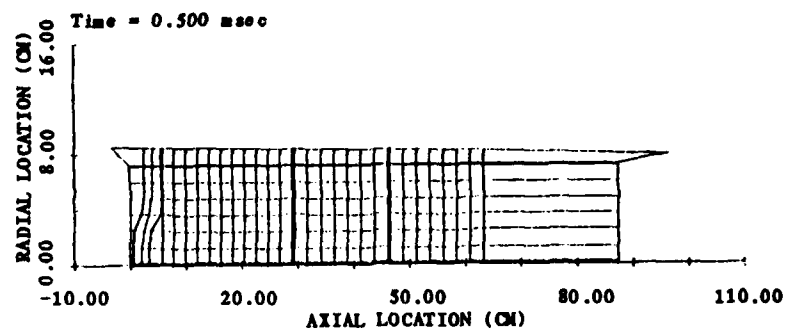


Figure 6.7 Solid-Phase Velocity Fields for the XM216 Case 5 Data Base

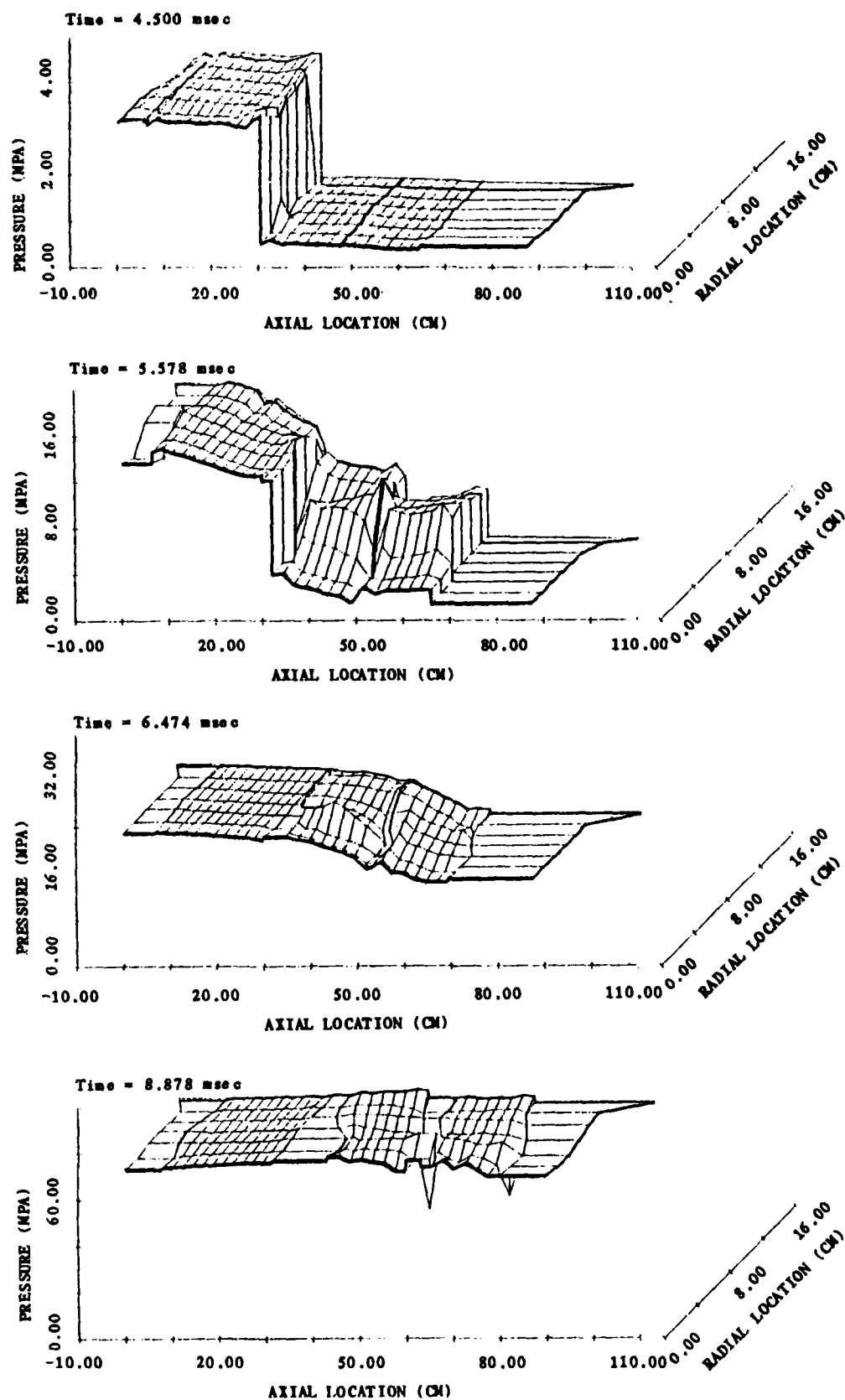


Figure 6.8 Pressure Distributions for the XM216 Case 6 Data Base

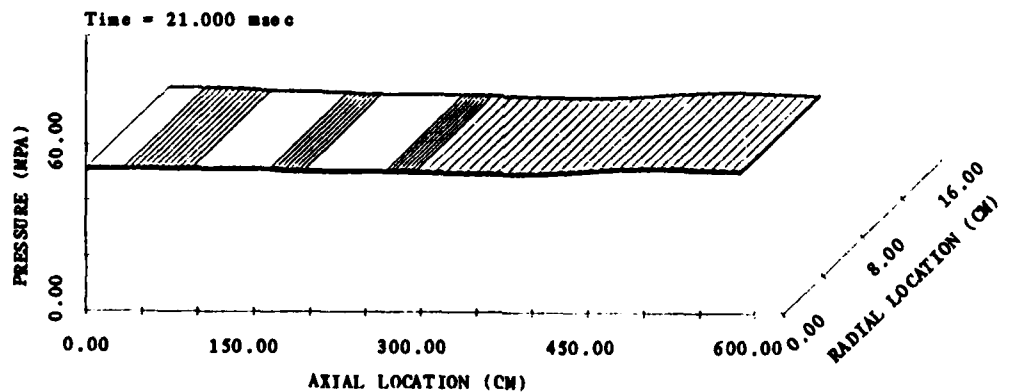
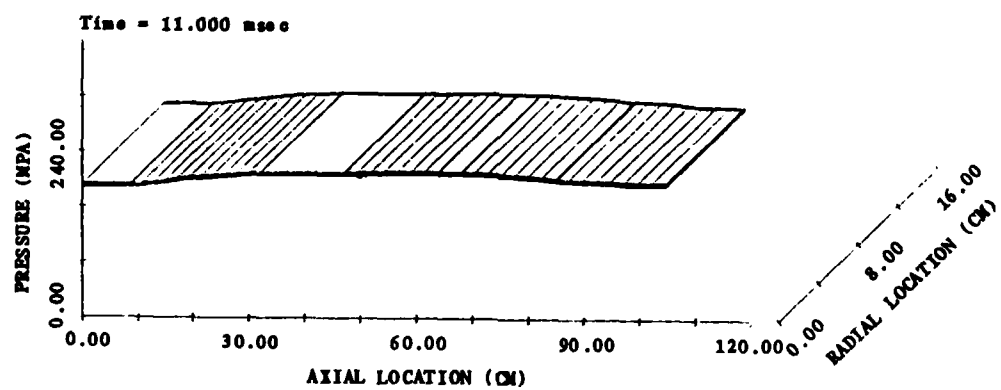
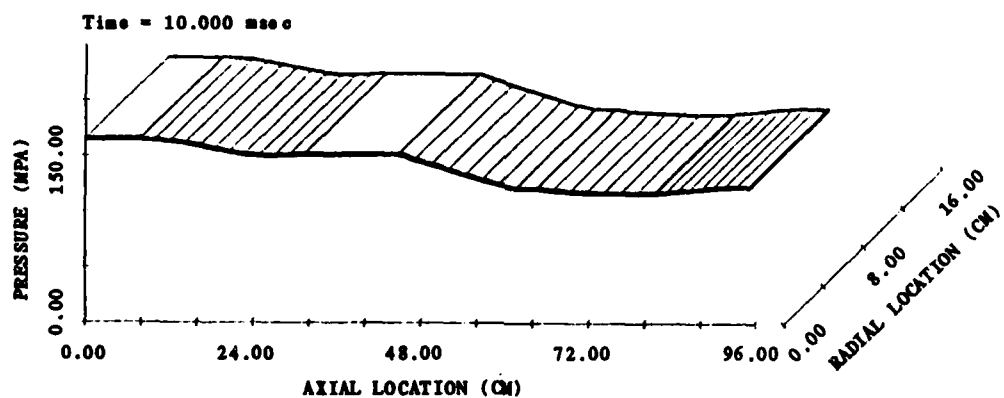
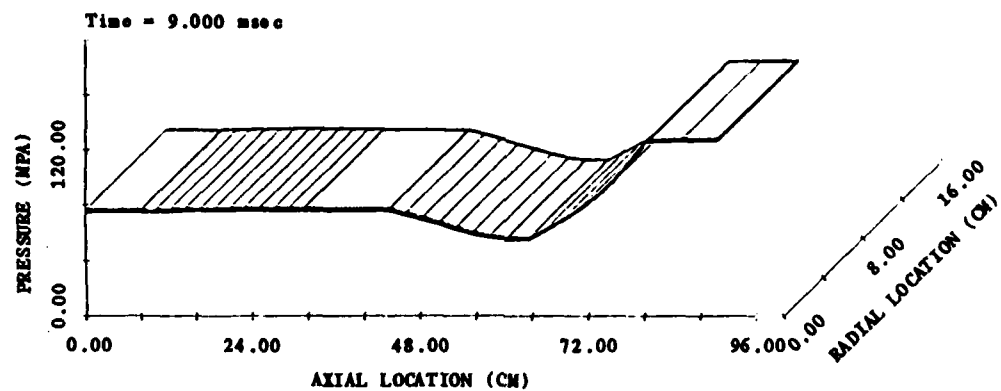


Figure 6.8 Continued

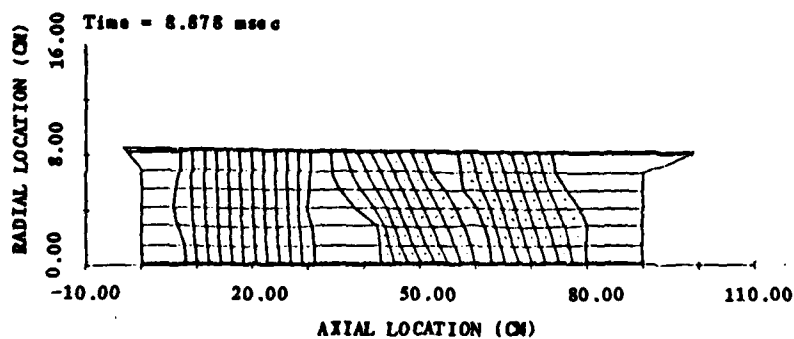
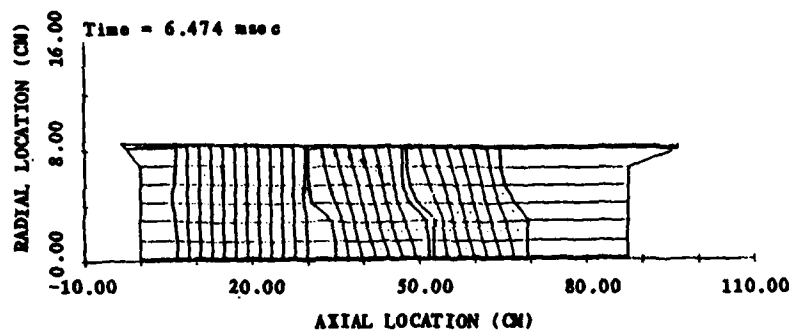
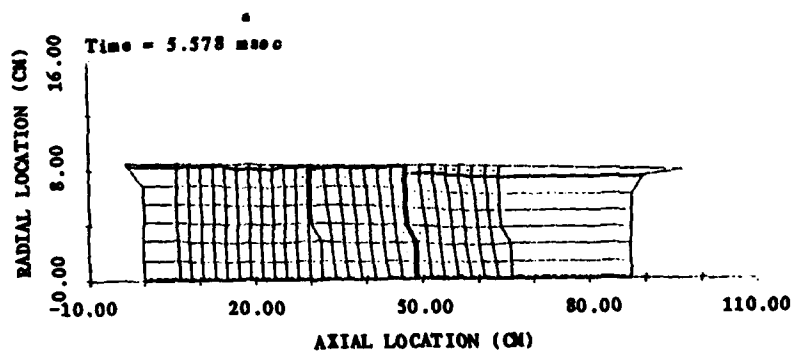
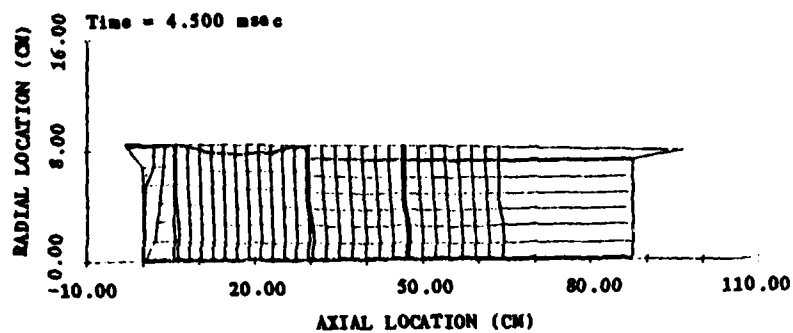


Figure 6.9 Solid Phase Velocity Fields for the XM216 Case 6 Data Base

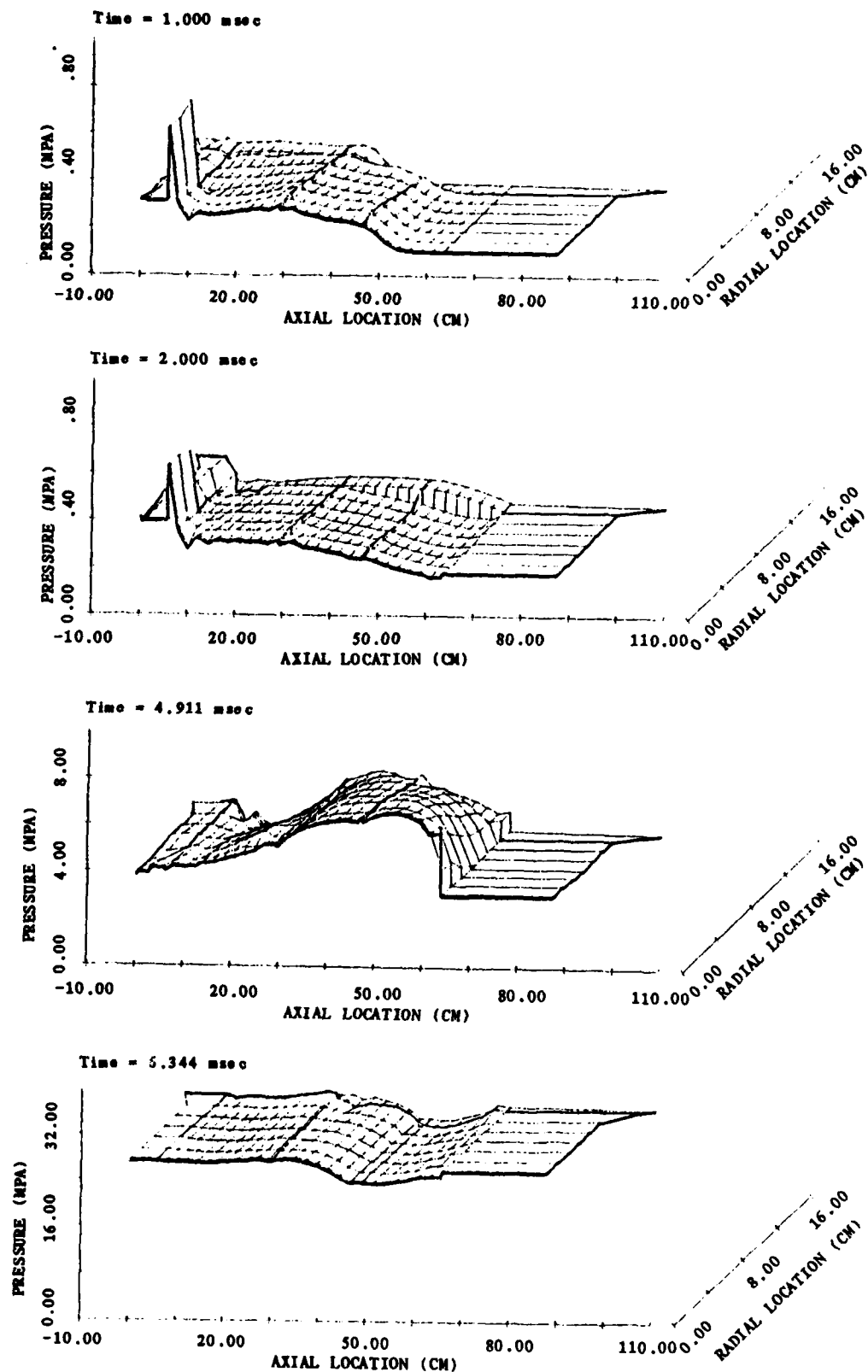


Figure 6.10 Pressure Distributions for the XM216 Case 7 Data Base

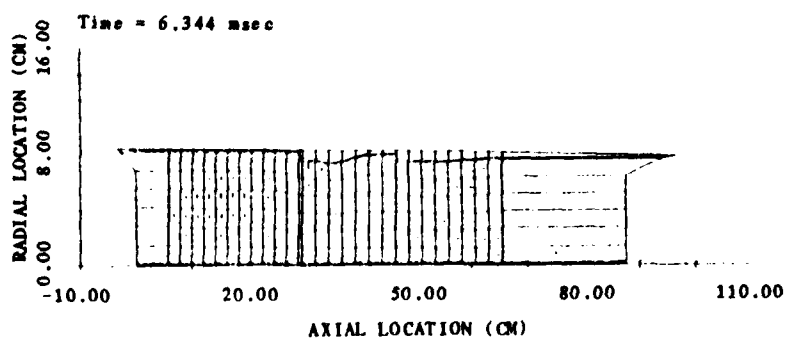
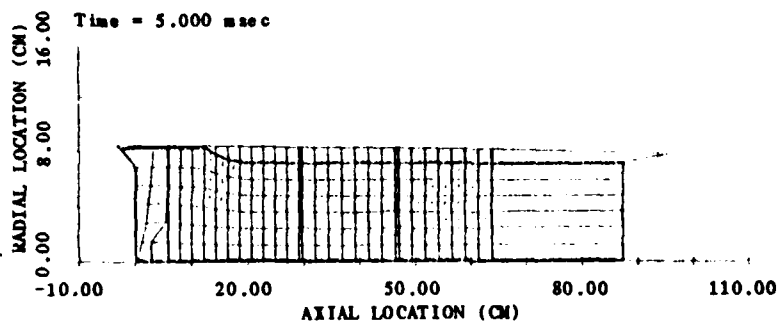
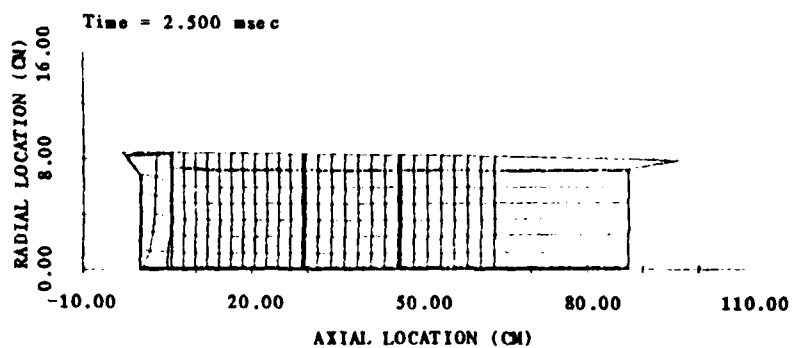
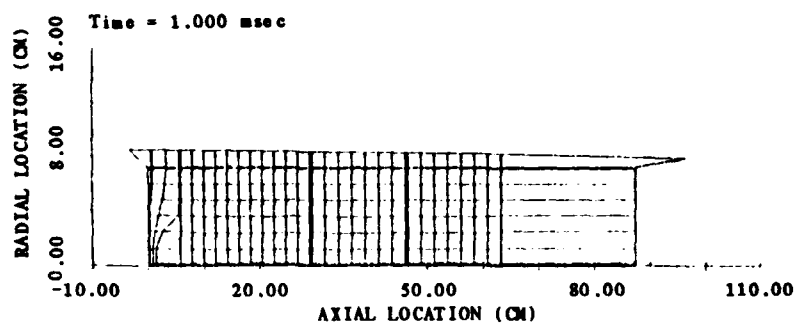


Figure 6.11 Solid-Phase Velocity Fields for the XM216 Case 7 Data Base

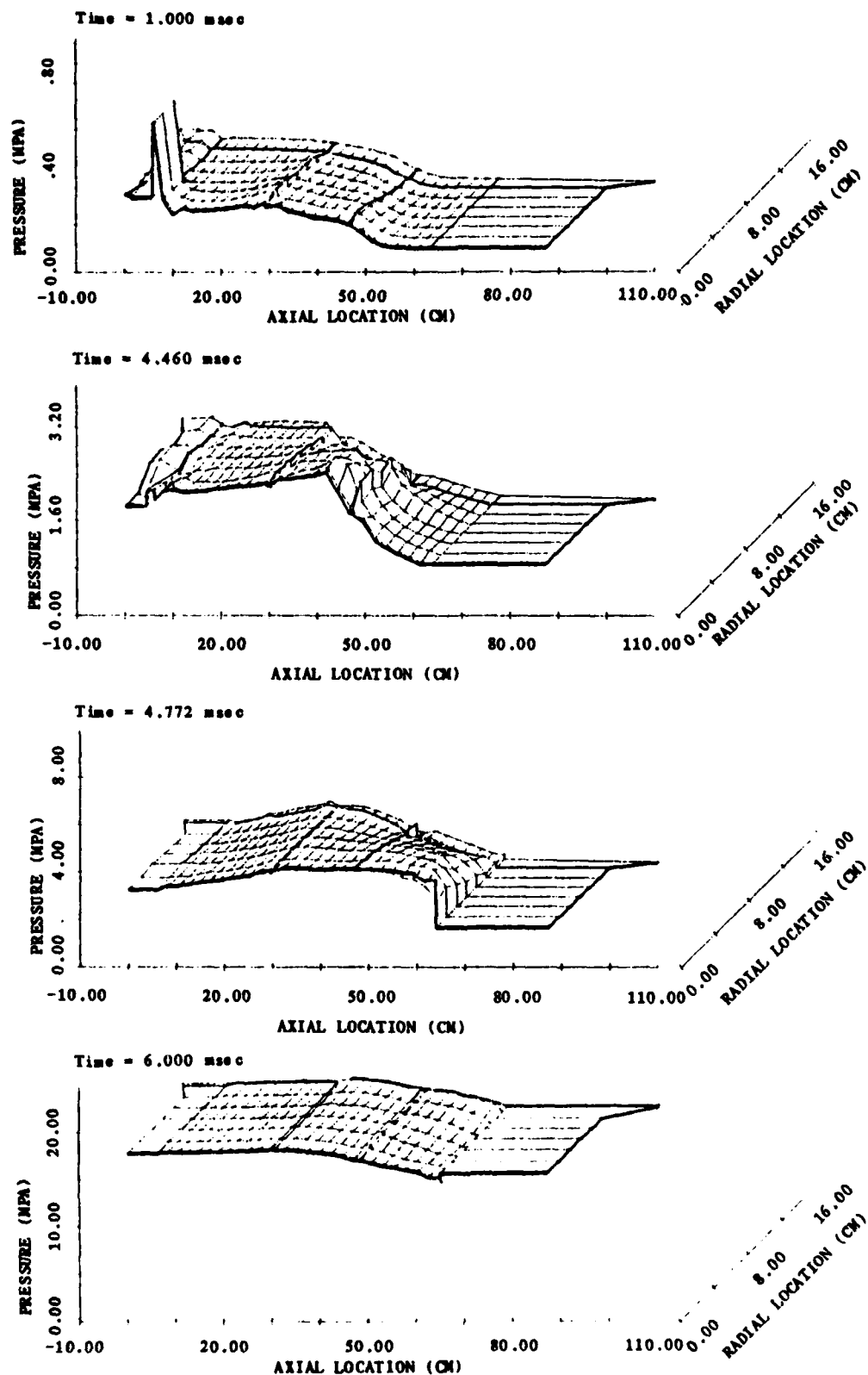


Figure 6.12 Pressure Distributions for the XM216 Case 8 Data Base

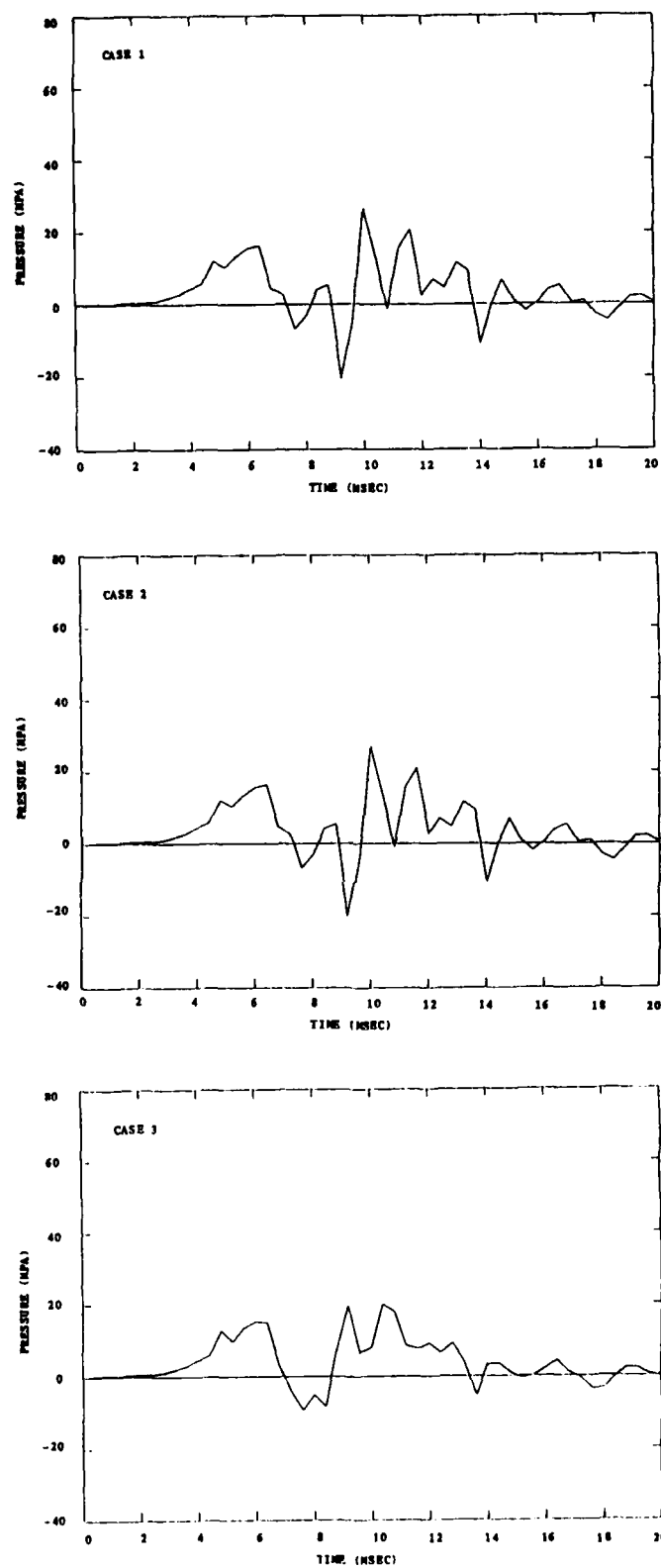


Figure 6.13 Influence of Case Permeability on Pressure Difference History in XM216 Charge (Pressure at 0.01 cm minus pressure at 87.37 cm on centerline)

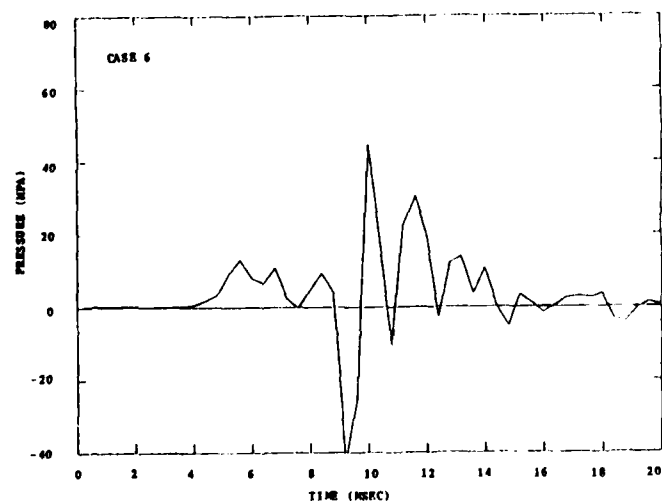
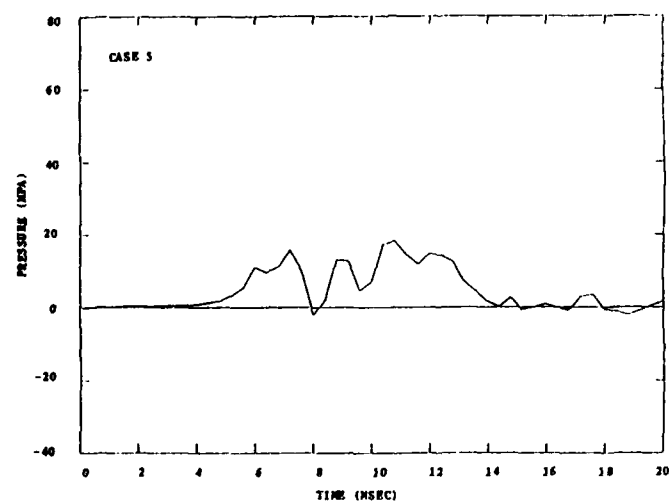
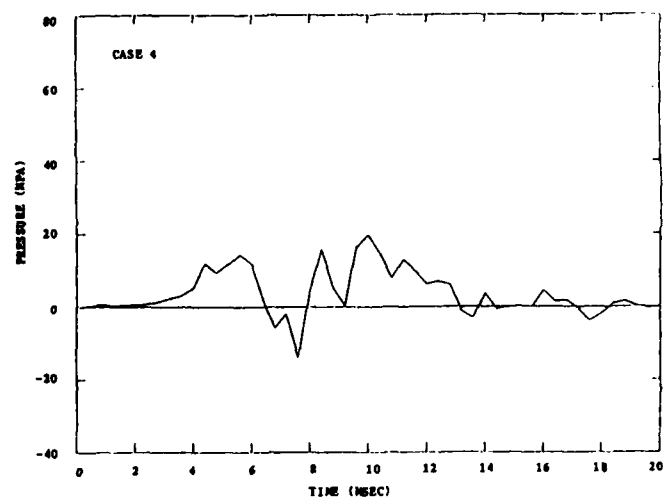


Figure 6.13 Continued

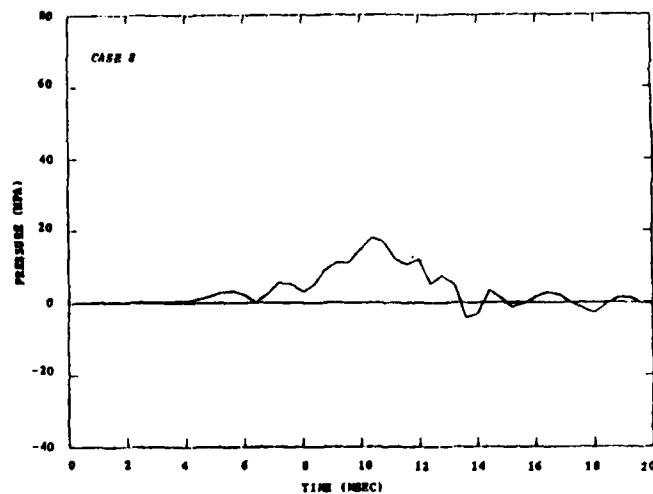
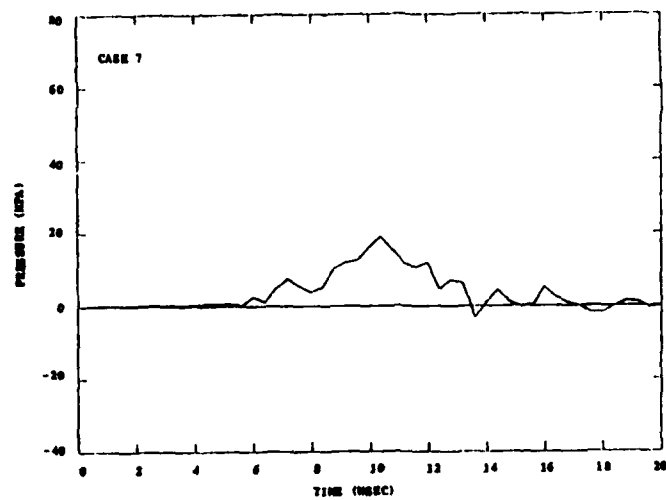


Figure 6.13 Continued

7.0 MISCELLANEOUS APPLICATIONS OF TDNOVA

The purpose of the present Chapter is to illustrate certain special features of TDNOVA. In Section 7.1 we demonstrate the use of the code to model a programmed fracture stick charge in which the sticks are divided lengthwise at various stages of the interior ballistic cycle. The single increment representation of the M203E2 Charge is used to define a data base for this problem. In Section 7.2 we consider a variant of the M203 data base of Chapter 3.0 in which the chemical energy of the propellant is released, in part, at a finite rate in the gas-phase. Finally, in Section 7.3, we use the code to estimate the tube surface temperature associated with firings of the M203 Granular and M203E2 Stick Charges.

7.1 Programmed Fracture Stick Charge

Because of their low axial flow resistance, stick charges minimize the occurrence of ignition anomalies. On the other hand, their tendency to remain in the breech creates a strong blowing condition through the mouth of the chamber which is thought to result in increased heat transfer to the tube.²¹ One possible approach to obtaining the ignition characteristics of stick propellant and the heat transfer characteristics of granular propellant is the programmed fracture stick charge.

Such a charge consists of stick propellant with strategically located stress raisers. When the stress at the midpoint of the stick exceeds a critical value rupture occurs and the stick is divided into two shorter sticks. These, in turn, subdivide at some later time and, eventually, the charge is reduced to a granular form. Thus one has regular packing during ignition, minimizing the development of pressure waves, and random packing subsequently, allowing a uniform distribution of propellant throughout the tube.

The rupture criteria have been presented in Section 2.3.1. For the present illustration of the method we used the M203E2 single-increment representation of Chapter 4.0 as tabulated in Appendix C. The rupture strength was set so that the subdivision would occur in the first few time steps. This means, of course, that the simulation does not represent the ideal behavior which would delay the subdivision until flamespread was complete. Our objective here, however, is simply to demonstrate a computational option, not to design a charge.

When a bundle of sticks has been produced through a three-fold subdivision, and therefore has a length equal to one-eighth of that of the original bundle, it may be converted to a different granulation when the rupture condition is met once again. Here we have allowed each bundle to develop a single-perforation granular form consistent with the original stick form except that the slot is not considered.

Aspects of the solution of this problem are presented in Figures 7.1 and 7.2. Figure 7.1 illustrates the pressure distributions at four times. At 0.006 msec we have already allowed the original bundle to become four smaller bundles. We note that the code recognizes the formation of regions of axial ullage between the bundles. By 0.5 msec the original single bundle of stick propellant has been reduced to eight bundles of single-perforation granular propellant. We observe the pressurization in the rear axial ullage due to the igniter and in the outer annular ullage due to the case. These details are not very different from those of the solution presented in Chapter 4.0. By 2.055 msec flamespread is complete and the case is fully ruptured. Because of the configurational complexity of this problem we used a relatively large pressure tolerance factor of 0.1 which allows conversion to a quasi-two-dimensional representation at this time. Finally, at 14.0 msec we see the solution near burnout. We note the nearly uniform distribution of propellant throughout the tube.

Figure 7.2 illustrates the path of flamespreading, the overall ballistic behavior and the pressure difference history for this charge. The contours of ignition delay show that the flamespread was influenced not only by the base igniter but also by the radial convection through the sidewall and the axial convection through the front endwall. The pressure difference history shows that a detectable pressure wave has been created during ignition, presumably because the data base induces a non-ideal rupture schedule. The fine structure at later times in the pressure difference history is not thought to be of physical significance.

7.2 Finite Rate Chemistry

In the original versions of TDNOVA it was assumed that combustion of the propellant occurred sufficiently rapidly that the full chemical energy could be modeled as released simultaneously with regression of the surface of the solid-phase. In the previous final report¹³ we described an extension to the code according to which the chemical energy could be modeled as released in two steps. Regression of the surface was assumed to result in the instantaneous formation of intermediate products of combustion with a partial release of the chemical energy. We referred to the intermediate products as pyrolysis products of combustion. The pyrolysis products were assumed to react at a finite rate allowing the remaining fraction of the chemical energy to be released gradually in the gas-phase.

Some results with this finite rate chemistry option have already been reported.²⁰ Here we confine our discussion to one data base, a modification of the representation of the M203 Charge which we presented in Chapter 3.0. The data base is as in Appendix B with the addition of the kinetic data presented in Table 7.1.

Table 7.1 Kinetic Data for Finite Rate Chemistry Problem

Fraction of Energy Released at Surface (-)	0.117
Gas-Phase Arrhenius Pre-Exponent ((gm/cc) ** (1-N)/sec)	0.29×10^{10}
Gas-Phase Arrhenius Exponent (J/gmol)	67000.
Gas-Phase Reaction Order (-)	2.0

The specific heats and molecular weight of the pyrolysis products were assumed to be identical with those of the final combustion products.

We present some details of the solution in Figures 7.3, 7.4 and 7.5. Figure 7.3 presents the distributions of pressure at four times up to and including the transformation to a quasi-two-dimensional representation. These have no remarkable characteristics and are similar to those for the nominal M203 solution presented in Chapter 3.0. We do note, however, that the pressure increases at a significantly slower rate when the rate of release of combustion energy follows the data of Table 7.1.

Figure 7.4 illustrates the distributions of the mass fraction of the pyrolysis products at the same set of times that we considered in Figure 7.3. At 1.5 msec we see the first formation of the pyrolysis products near the rear of the charge where ignition has occurred. By 4.0 msec flamespread is almost complete and the mass fraction of the pyrolysis products is as high as 0.3 in some portions of the charge. At the centerline the mass fraction is very small since the combustion of the black powder centercore impresses its own chemical properties on the local solution. On the inner boundary of the charge the value of the mass fraction of the pyrolysis products suffers a discontinuity at those locations where the gas flows from the charge into the centercore. Towards the front of the charge the flow of gas is directed from the centercore into the main charge and the mass fraction remains continuous across the boundary due to the transport condition.

Looking at the solution at 6.562 we see that the mass fraction is taken to be close to zero at the front of the charge directly after the transformation to a quasi-two-dimensional representation. This is due to the code convention of using the values on the inner boundary of the charge to define all gas-phase state variables following transformation. Clearly, this needs to be revised.

Finally, in Figure 7.5 we illustrate the path of flamespreading, the overall ballistics and the pressure difference history corresponding to the present solution. Other than to delay the unfolding of events, there appears to be no significant consequence of the finite rate of energy release.

7.3 Heat Transfer to the Tube

We have already referred to a study by Horst²¹ in which a comparison was made of the rate of heat transfer to the tube due to granular and stick charges. It was shown that ballistically equivalent stick and granular charges of the same propellant formulation produced significantly different rates of heating, that due to the stick charge being significantly higher.

An objective of the previous contract was to incorporate into TDNOVA models of heat transfer similar to those in NOVA. We therefore encoded a total of three models.¹³ The first two are based on empirical correlations; one uses a flat plate correlation while the second uses a pipe flow correlation as in NOVA.⁵ The third is based on an unsteady integral boundary layer formulation, also as in NOVA.

The objective of this section is to present predictions of wall temperature with each of the two empirical correlations and for both stick and granular charges. The solutions presented here are obtained with the M203 data base of Appendix B and the M203E2 data base of Appendix D, modified to exercise the heat transfer options. The data of Table 7.2 were used to characterize the thermal response of the tube. The tube surface

Table 7.2 Thermal Properties of Tube Wall

Thermal Conductivity (J/cm-sec-K)	0.66210
Thermal Diffusivity (cm ² /sec)	0.14710

temperature is computed using an approximate cubic profile solution of the unsteady one-dimensional heat conduction equation.

In Figures 7.6 through 7.9 we present distributions of wall surface temperature at times corresponding to the occurrence of the maximum surface temperatures. These times differ from figure to figure depending on the charge and the heat transfer model.

Comparing Figures 7.6 and 7.7, which pertain to the granular charge, we see that the temperature profiles are similar for the two heat transfer correlations but that the tube flow correlation results in a maximum temperature of approximately 1100°K or roughly 200°K more than that for the plate flow correlation. Obviously, objections can be made to the use of either of these correlations in the gun environment. However, that for the flat plate is more reasonable since it embeds a gradually developing boundary layer.

Figures 7.8 and 7.9 present similar results for the stick charge. Once again, the tube flow correlation produces a prediction of temperature which exceeds that for the flat plate correlation by 200°K. We note that the temperatures produced by the stick charge are actually less than those for the granular charge. This finding is not inconsistent with the results of Horst.²¹ In the present case the flame temperature of the stick propellant is significantly less than that of the granular propellant, thereby offsetting the increased heat transfer coefficient.

We note, in Figure 7.9, an anomaly which should be removed in future studies. The temperature is seen to suffer a discontinuity at a location which corresponds to the forward boundary of the charge. As in NOVA⁵ we have treated the thermal parameter $q_w \delta^3$ as continuous at the internal boundary. Here q_w is the rate of heat transfer to the tube and δ is the thickness of the thermal layer. This internal boundary condition should be revised in terms of surface temperature in both TDNOVA and NOVA.

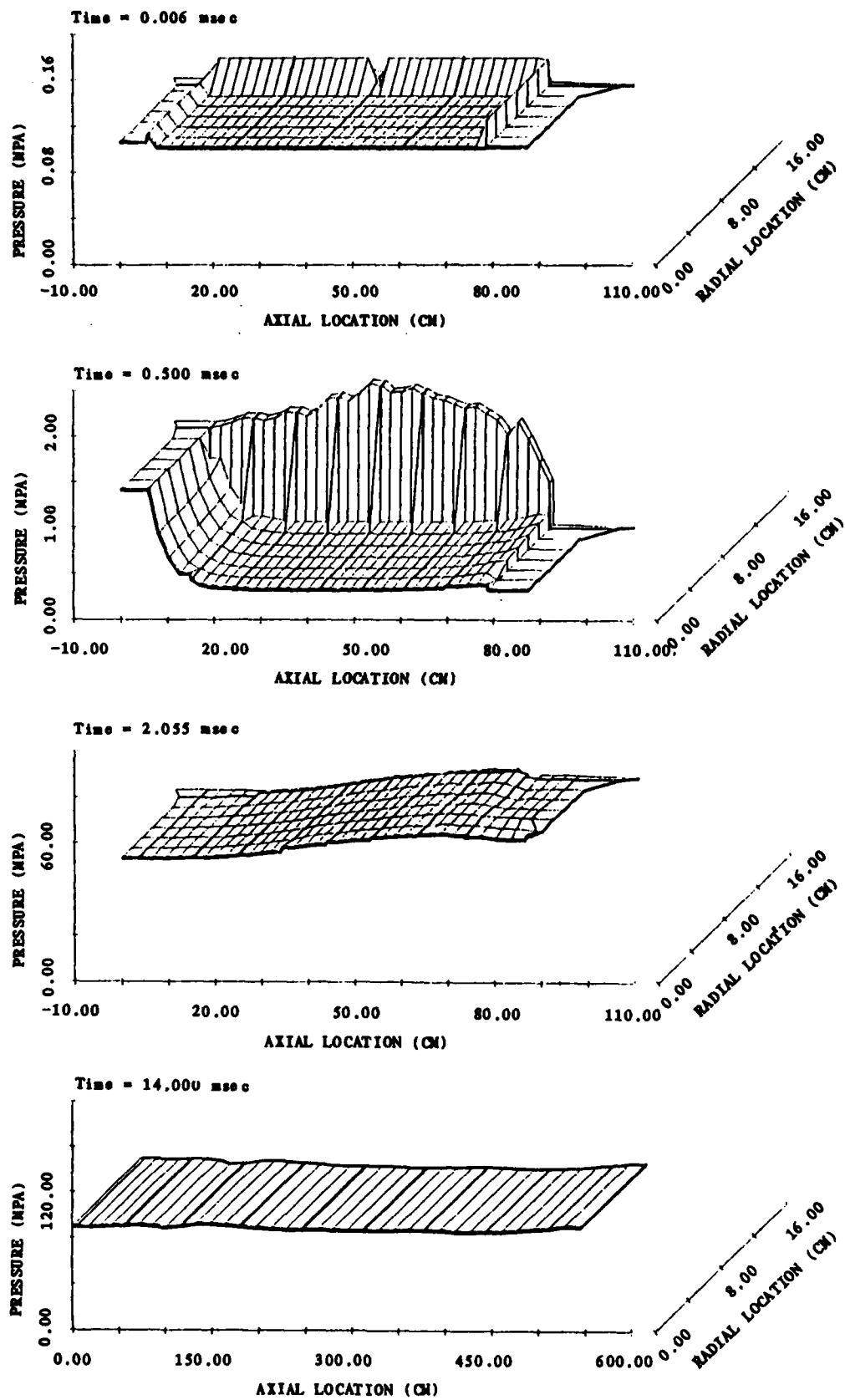
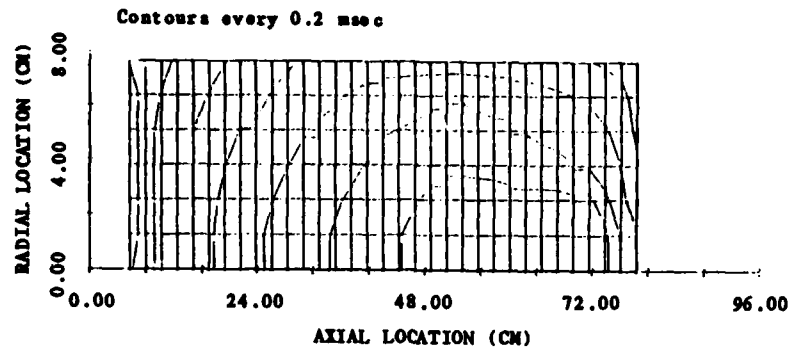
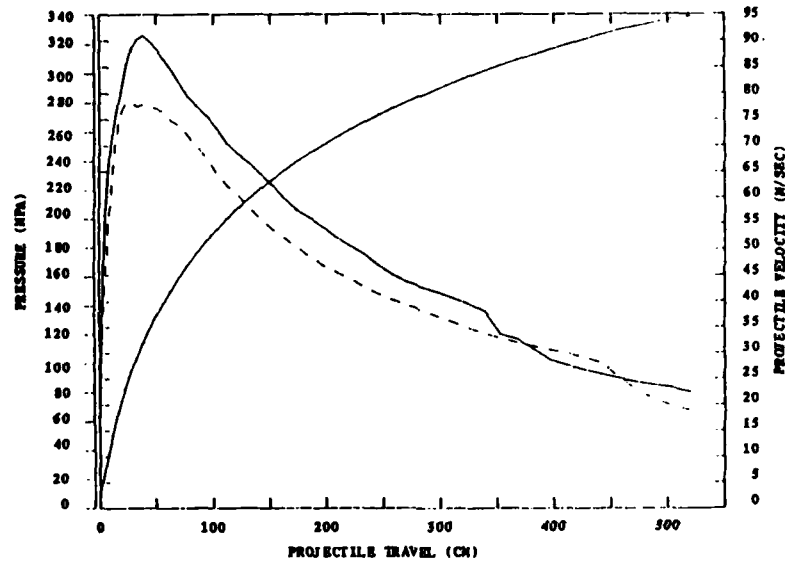


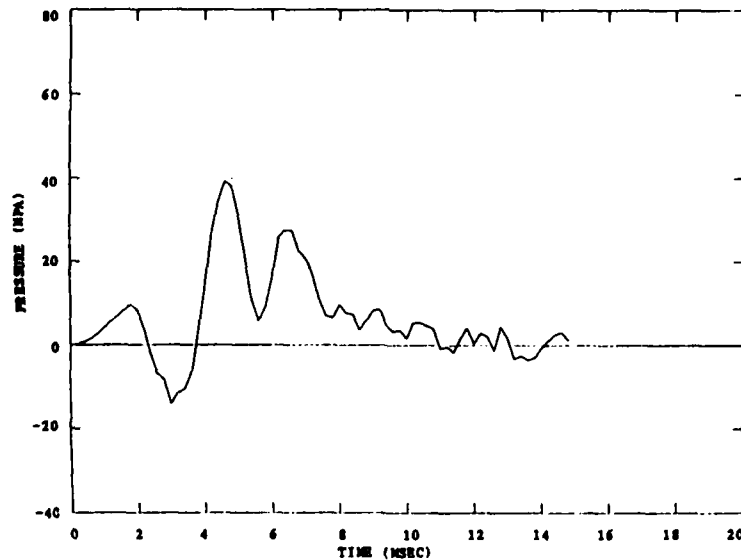
Figure 7.1 Pressure Distributions in Programmed Fracture Stick Charge



(a) Contours of Ignition Delay



(b) Breech and Base Pressure and Projectile Velocity



(c) Pressure at 0.01 cm Minus Pressure at 87.37 cm

Figure 7.2 Flamespreading, Pressure and Projectile Velocity Histories and Pressure Difference History in Programmed Fracture Stick Charge

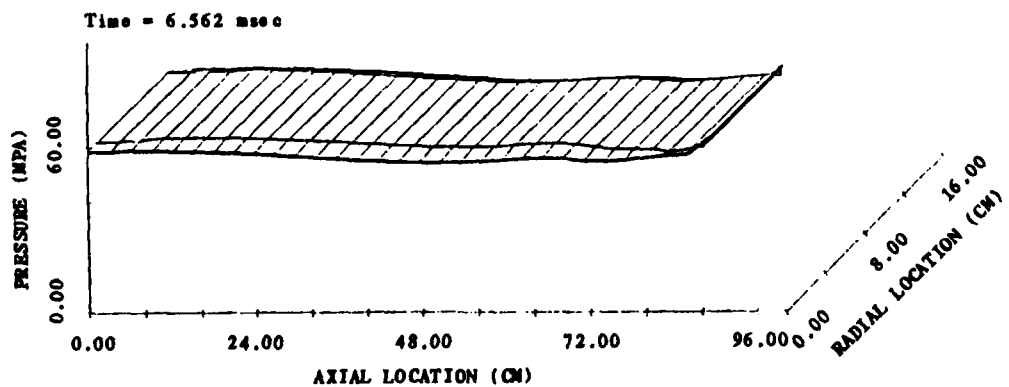
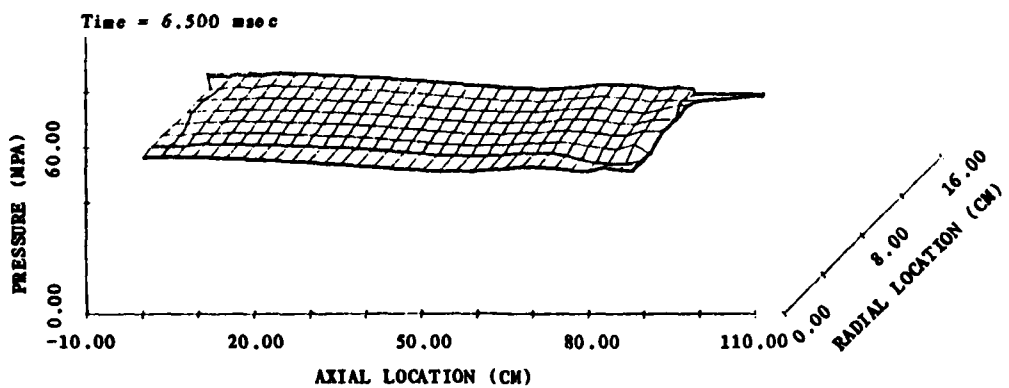
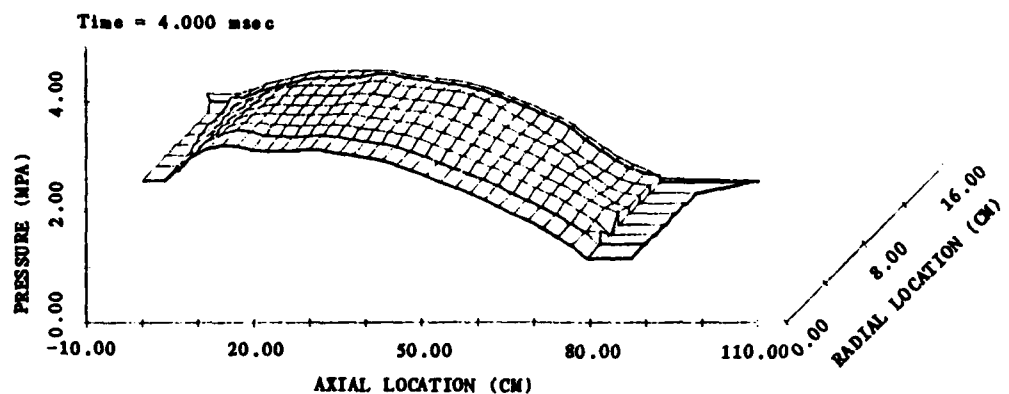
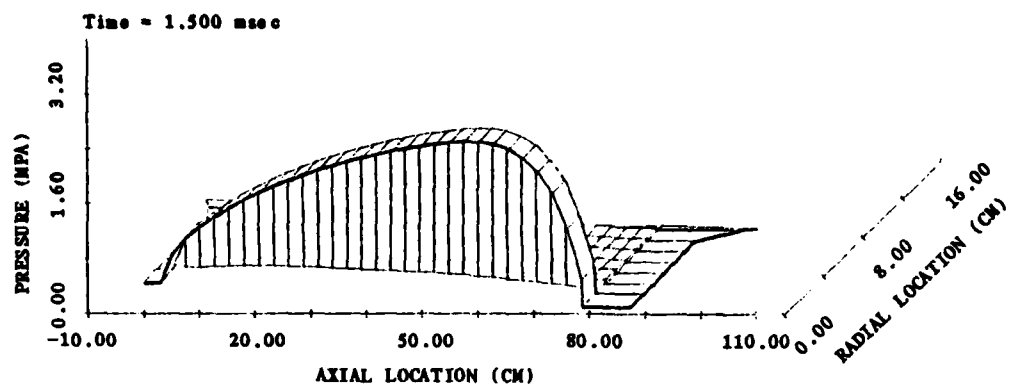


Figure 7.3 Pressure Distributions in the M203 Charge with Finite Rate Gas-Phase Reaction

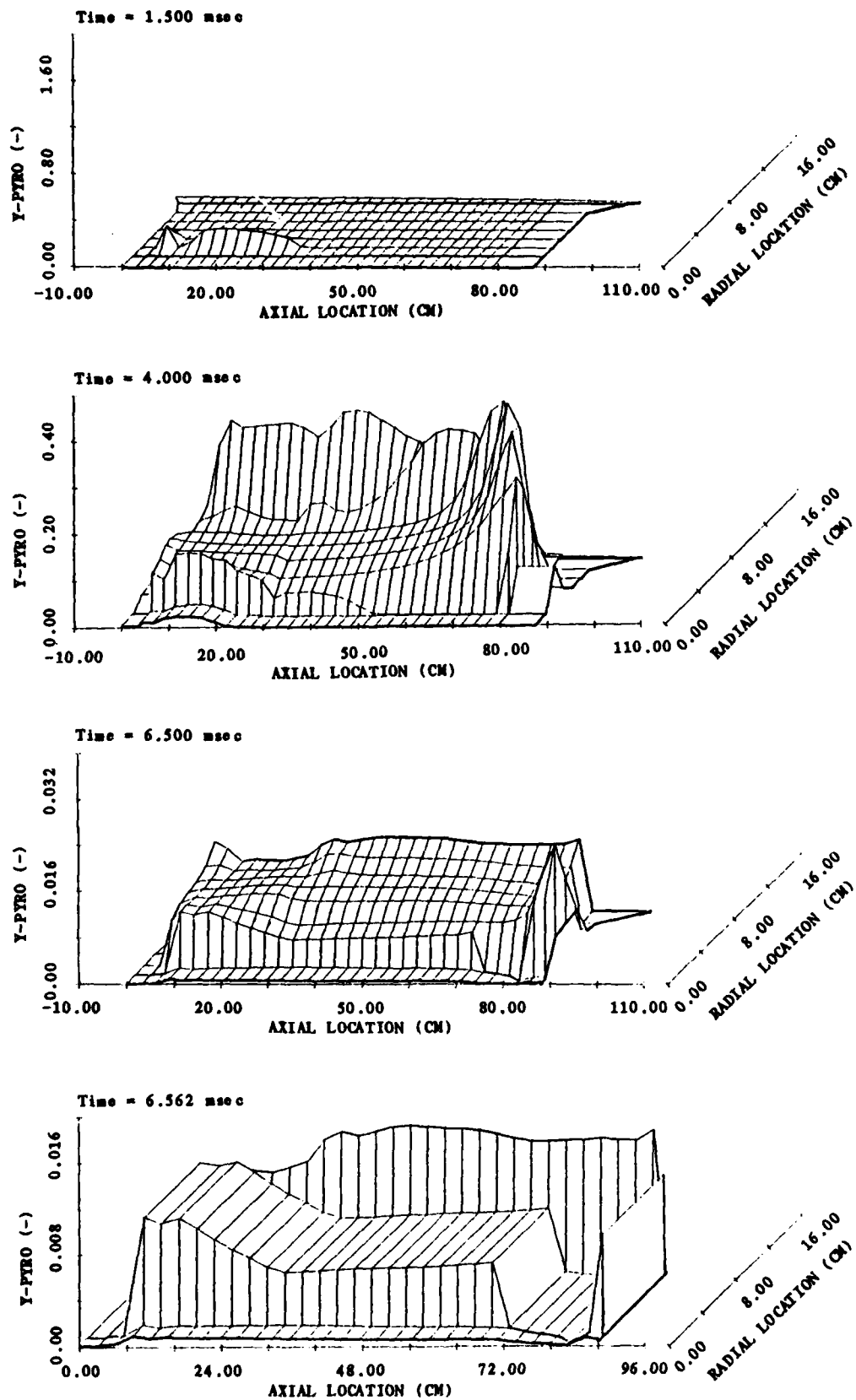
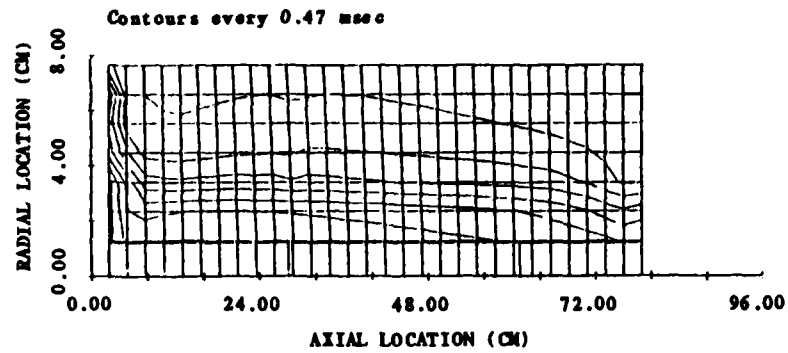
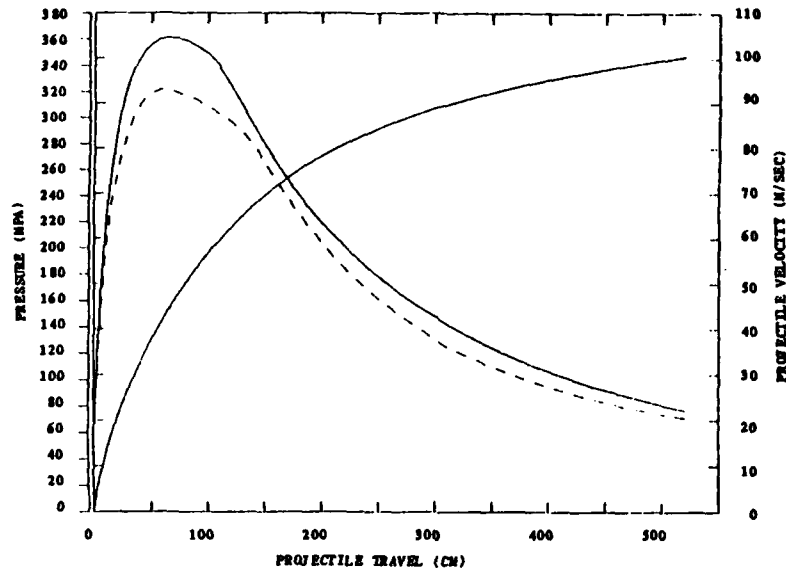


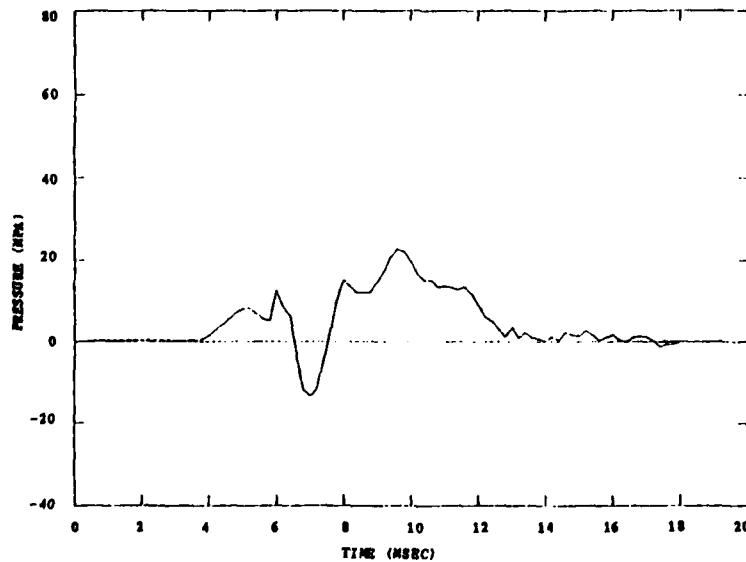
Figure 7.4 Distributions of Pyrolysis Product Mass Fraction in the M203 Charge with Finite Rate Gas-Phase Reaction



(a) Contours of Ignition Delay



(b) Breech and Base Pressure and Projectile Velocity



(c) Pressure at 0.01 cm Minus Pressure at 87.37 cm

Figure 7.5 Flamespreading, Pressure and Projectile Velocity Histories and Pressure Difference History in M203 Charge with Finite Rate Gas-Phase Reaction

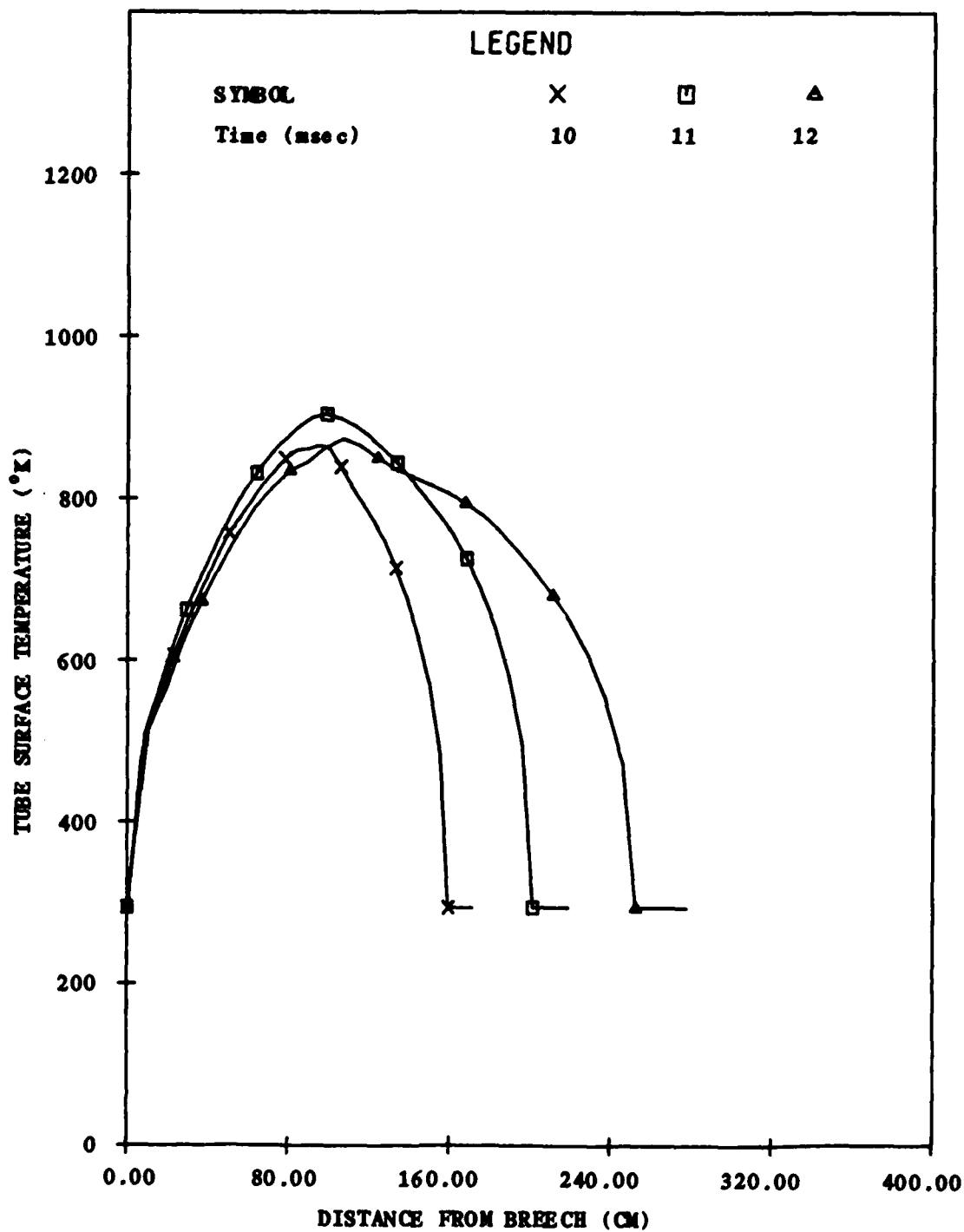


Figure 7.6 Tube Surface Temperature Distributions for M203 Charge and Flat Plate Correlation

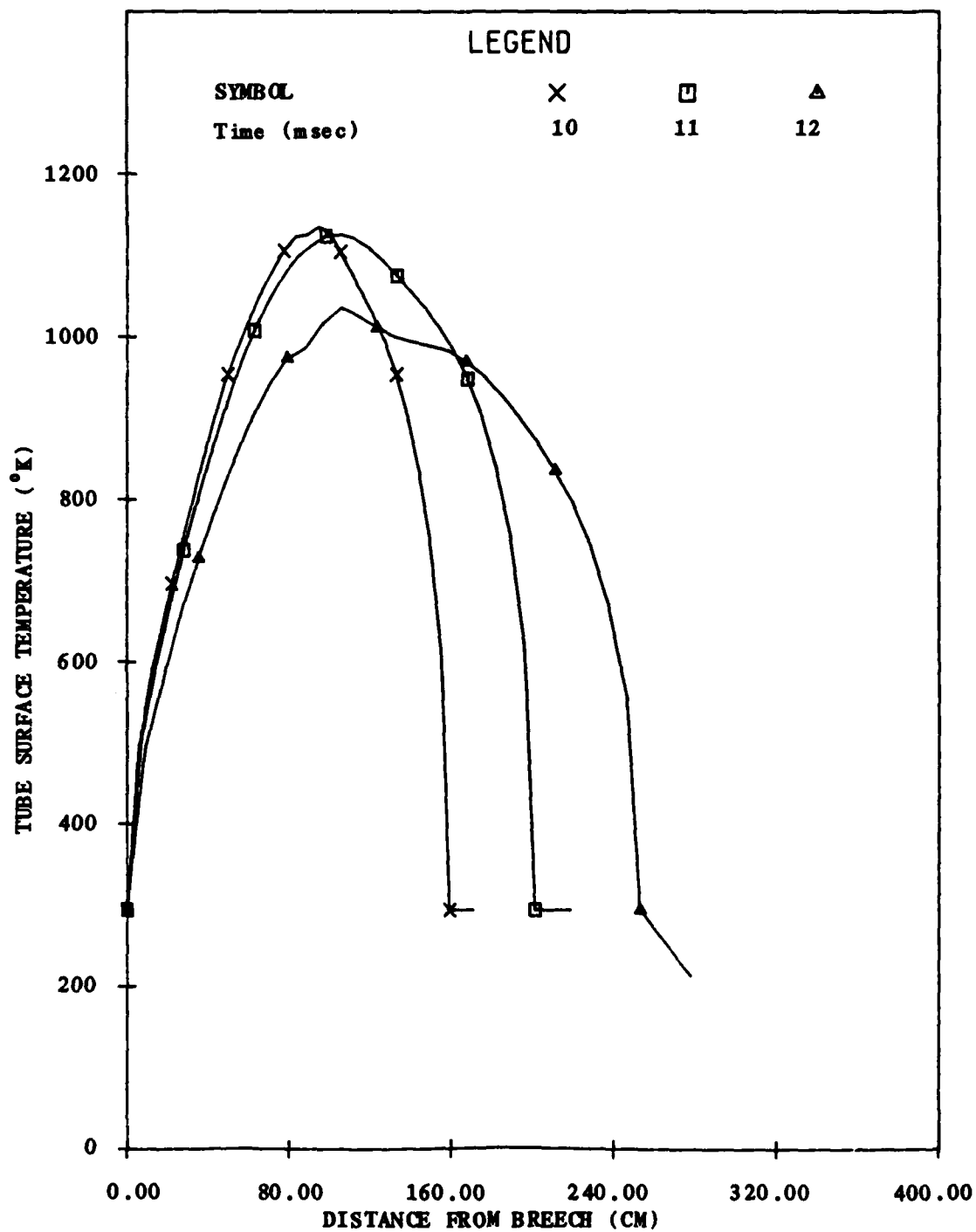


Figure 7.7 Tube Surface Temperature Distributions for M203 Charge and Pipe Flow Correlation

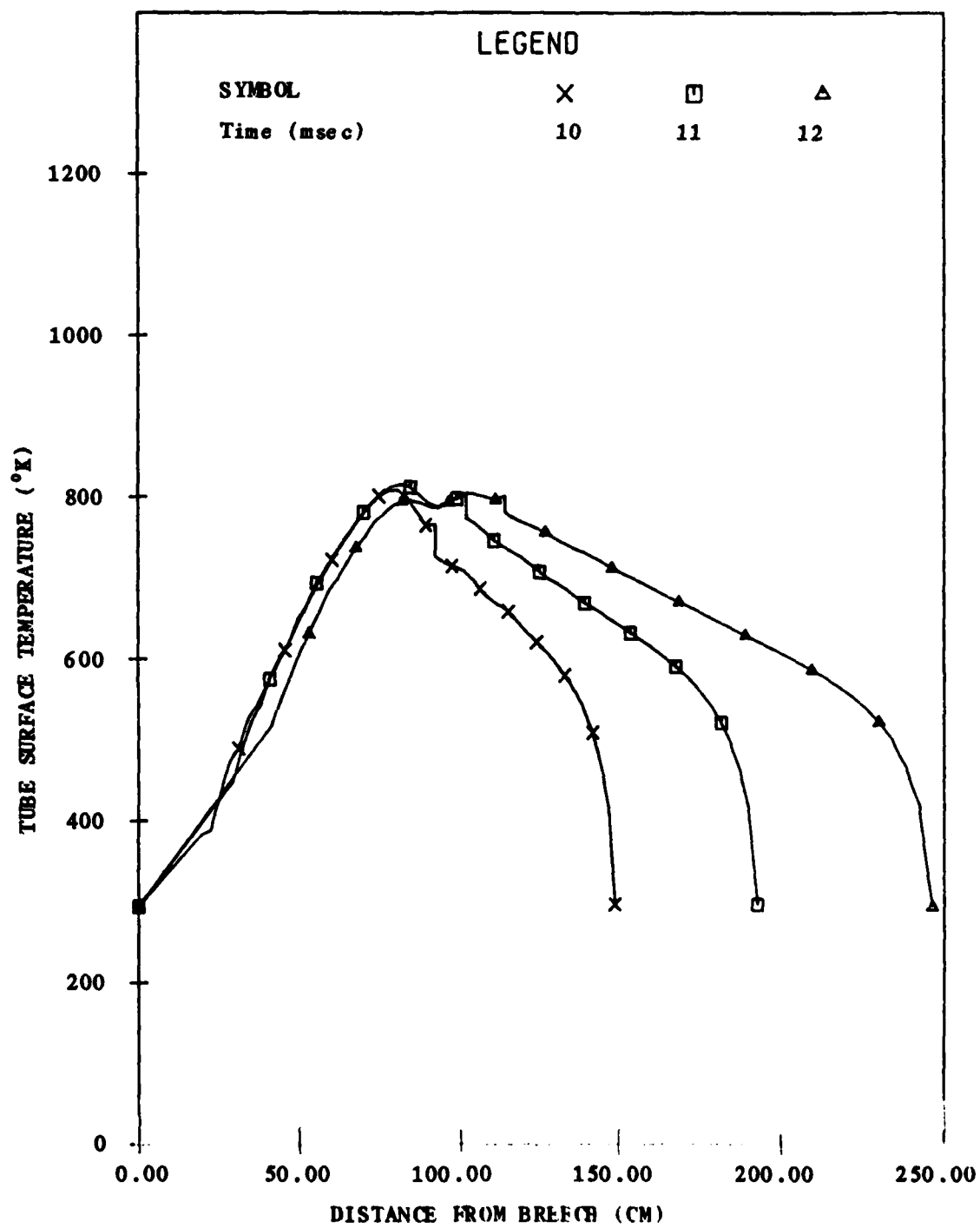


Figure 7.8 Tube Surface Temperature Distributions for M203E2 Charge and Flat Plate Correlation

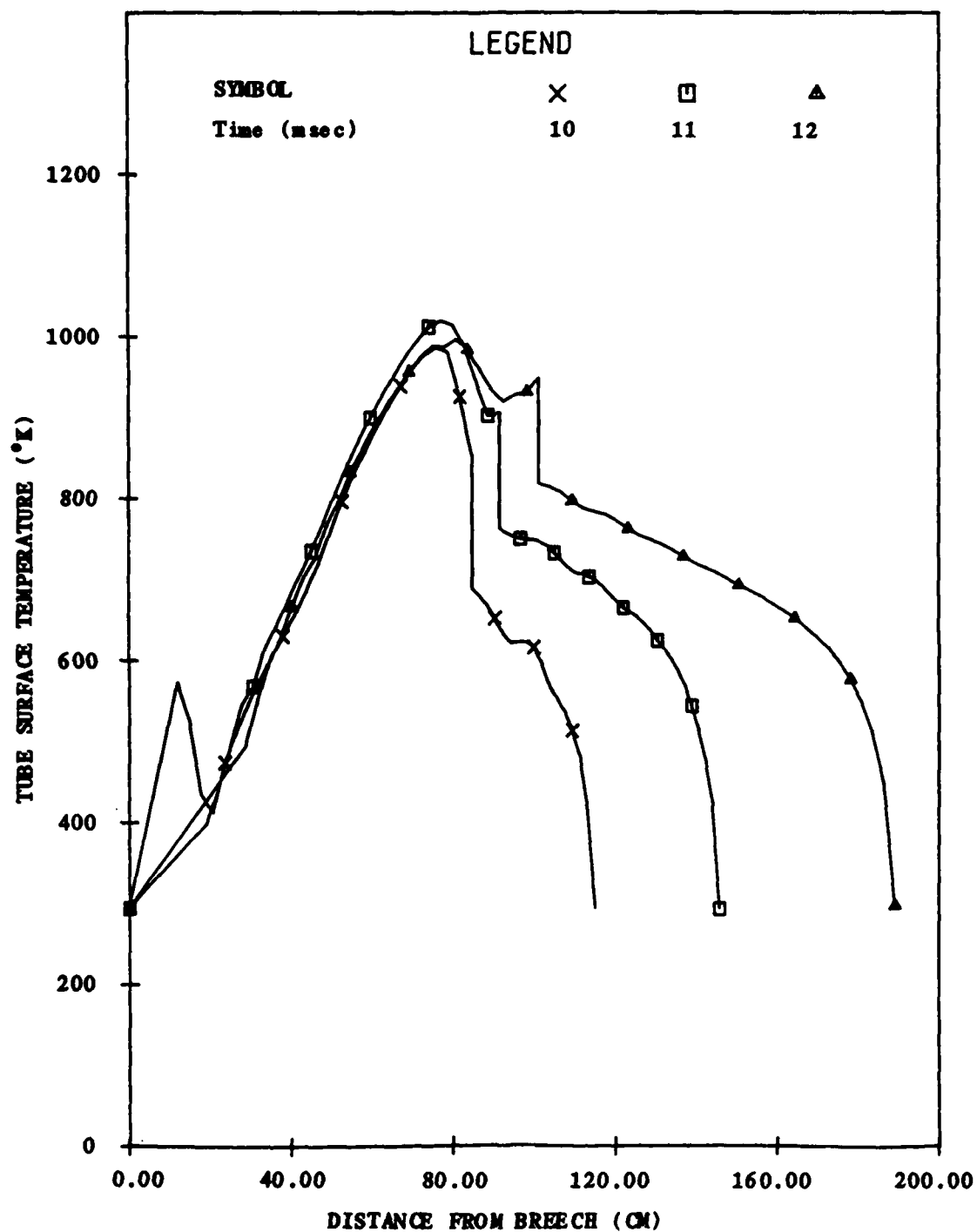


Figure 7.9 Tube Surface Temperature Distributions for M203E2 Charge and Pipe Flow Correlation

8.0 IMPLICIT SOLVER FOR REGIONS OF ULLAGE

The preceding chapters have described the current content of the TDNOVA Code and have illustrated its applicability to a number of propelling charges of current interest. In the present chapter we describe an algorithm which is intended to provide a significant extension to the scope of applicability of TDNOVA. Although we provide evidence of the operability of the algorithm on a stand-alone basis, we emphasize that it does not represent a current TDNOVA capability.

The revised algorithm consists of a Linearized Alternating Direction Implicit (LADI) scheme to solve the two-dimensional, unsteady Navier-Stokes equations with heat conduction in the regions of ullage. This algorithm supersedes an existing explicit solver for the inviscid equations which has been coded but has not been tested. Development of the implicit solver has been motivated by computational experience to date with TDNOVA which strongly suggests the need for physical dissipation in the ullage to assure a well-posed computational problem. Moreover, the inclusion of diffusion terms implies that the resulting code will be applicable to problems of thermal erosion of the tube, at least in cases where the wall boundary layer is confined to the ullage regions.

This chapter contains four sections. In Section 8.1 we discuss the motivation for the algorithm and note the related studies which have contributed to its development. In Section 8.2 we present the equations to be solved. In Section 8.3 we discuss the algorithm itself and in Section 8.4 we present solutions for an idealized problem which admits an analytical solution as a benchmark of accuracy.

8.1 Background Information

The TDNOVA solutions which have been presented in Chapters 3.0 through 7.0 have all treated the regions of ullage as either quasi-one-dimensional or as lumped parameter. This approach has been adopted even during the initial part of the calculations in which the propelling charges are represented as fully two-dimensional. For charges like the M203 Charge or the M203E2 Charge, the neglect of two-dimensional details within the regions of ullage is not unreasonable. For these charges the transverse dimensions of the ullage regions — the distances between the charge boundaries and the external boundaries — are not large during flamespreading. On the other hand, the XM216 Charge involves a region of axial ullage at the front of the chamber which is as large as one of the charge increments. For such a charge, modeling consistency demands a fully two-dimensional treatment of the ullage, at least for the forward region.

TDNOVA has an algorithm to treat two-dimensional regions of ullage.¹¹ Referred to as the dynamic mesh option, the algorithm models regions of ullage as lumped parameter, quasi-one-dimensional inviscid or fully two-dimensional inviscid according to their axial and radial dimensions. As in the simulations presented in the preceding chapters, which have been based on the static mesh option, the ullage is decomposed into regions contiguous with each of the sides of each of the charge increments and corner regions.

As each such region changes in size and shape the dynamic mesh option allows the representation of the region to vary among the three modeling possibilities — lumped parameter, quasi-one-dimensional, fully two-dimensional. In addition, the number of mesh points allocated to the region for a given representation is allowed to vary. This approach has reflected the choice of an explicit solver to integrate the governing equations. The Courant-Lewy-Friedrichs stability criterion requires that the time step be restricted in accordance with the minimal mesh spacing. From the standpoint of economy it is therefore desirable to delete mesh points as the region of ullage collapses and eventually to treat the properties in the compressed direction as lumped.

Although we have noted, in the preceding chapters, certain minor flaws in the static mesh algorithm, and although some of the data bases of interest appeared to be approaching the limits of the algorithm, it may be said that development of the static mesh algorithm is complete. At this time, particularly because of charges like the XM216 Charge, it is of interest to model the ullage in greater detail. The existing dynamic mesh option offers us an avenue to more detailed modeling of the geometrical aspects of the flow in the ullage, but computational ruggedness has not been established. Based on experience with the static mesh option it is thought that the refinement of the dynamic mesh option to assure a level of ruggedness comparable to that of the static mesh option will be a difficult and time-consuming process. At the same time, the absence of physical dissipation from the static mesh option may detract significantly from the benefits of the increased level of geometrical detail.

Testing of the dynamic mesh option has been limited thus far to cycling the code through one or two steps to ensure proper linkages of data and an absence of major coding flaws. Interest in the dynamic mesh option has been limited thus far due to several factors. First, the performance of the matrix of runs presented in Chapters 3.0 through 7.0 required considerable code development effort even though they involved the simpler static mesh option. Second, with the exception of the XM216 Charge, interest has previously been directed towards charges for which the neglect of two-dimensional features of the ullage was reasonable. Third, while both the static and the dynamic mesh options are based on solutions of the inviscid single-phase balance laws, the static option has built into the boundary conditions at the corners a representation of the flow losses due to dissipation. The absence of physical dissipation from the two-dimensional equations has the consequence that while the dynamic mesh option offers a modeling extension in geometric terms it may in fact be less accurate than the static option insofar as computations of pressure losses due to flow around the corners are concerned. Finally, it may be anticipated that the dynamic mode would involve considerable numerical strain in connection with the tangential momentum boundary condition at internal boundaries.

The tangential momentum boundary condition represents a very difficult numerical problem in the static mesh option in which its implications are confined to the consequences of gas entering the mixture. We have circumvented the numerical difficulty in that context by a modification to the boundary condition itself, introducing a tangential momentum loss which assures reasonable consistency of the tangential velocity of the entering

gas with that within the mixture. In the dynamic mesh option we would be confronted with the same numerical problem but we would not be able to take advantage of a similar constitutive revision. Only by the introduction of physical dissipation could we reasonably assure stability in all cases of interest.

But physical dissipation would require that an implicit solver be used in order to avoid the severe time step constraint associated with the diffusion terms, particularly if the mesh were properly refined so as to resolve correctly the structure of the shear layers. On the other hand, if an implicit solver were adopted in place of the existing explicit solver, it would be possible to simplify the dynamic mesh algorithm by working consistently with a two-dimensional mesh for all regions of ullage. Finally, if an implicit solver were used together with a model of both mechanical and thermal diffusion processes in the ullage, the resulting code would allow fresh insights into the problem of thermal erosion of the tube.

TDNOVA presently has the capability to model heat transfer to the tube wall by reference to empirical plate and pipe correlations. In Chapter 7.0 we presented results for the M203 and M203E2 Charges. A significant difference was observed between the wall temperatures predicted with the flat plate and pipe flow correlations, both in the granular M203 Charge and in the stick M203E2 Charge. The need for a more detailed analysis of the wall boundary layer is therefore obvious.

The problem of convective heating of the tube wall has been considered by several other authors. This prior work is of particular relevance here because we adopt the computational approach of the most recent investigations in order to develop the present algorithm revisions to TDNOVA.

The first attempt to analyze the heat loss as a boundary layer phenomenon appears to be that of Hicks and Thornhill as described by Corner.³³ The boundary layer development was assumed to be similar to that for a flat plate. An integral momentum law was used in combination with the assumption that the core flow obeyed the Lagrange laws of uniform density and linear velocity distribution. The idea of modeling the wall boundary layer driven by an independently determined core flow has been elaborated most completely in the TBLIMP code³⁴ which determines the time dependent solution of the partial differential equations for a reacting boundary layer.

-
- 33 Corner, J.
"Theory of the Interior Ballistics of Guns"
John Wiley and Son, Inc. New York 1950
- 34 Evans, R. M.
"User's Manual for Transient Boundary Layer Integral Matrix
Procedure TBLIMP"
Aerotherm Report UM-74-55 1974

The first attempt to couple fully the wall boundary layer to the core flow appears to be that of Shelton et al.³⁵ However, the effect of the boundary layer on the core flow is limited to the incorporation of algebraic momentum and heat loss terms. The core flow is treated as single-phase or as a homogeneous mixture. The boundary layer development is modeled according to a transient integral formulation. The model of Shelton is in fact encoded into both NOVA⁵ and TDNOVA.¹³ However, computational experience has shown it to be unsatisfactory for all but the simplest charge configurations. The boundary layer displacement thickness is found to be susceptible to an unbounded growth mode which appears to be intrinsic to the model. Accordingly, still deeper analysis is required.

More recently, Gibeling et al.³⁶⁻³⁸ have described attempts to obtain solutions of a set of equations which embed both the features of the macroscopic two-phase flow model of Gough and the diffusive terms of the Navier Stokes equations. A solution to these equations would provide a fully coupled analysis of the core and boundary regions. Such solutions as have been presented to date, however, are confined to the so-called Lagrange gun problem in which the projectile is accelerated by a non-reacting gas which is initially at rest and high pressure.^{38,39} Solutions have been presented for the single-phase case and shown to agree well with an analytical solution. Solutions have also been obtained with a dilute suspension of particles and with the effects of the wall boundary layer included.

However, solutions have not yet been presented in which the initial condition is representative of an unmignited propelling charge and in which both the flamespread through the propellant and the development of the wall boundary layer are determined simultaneously.

-
- 35 Shelton, S., Bergles, A. and Saha, P.
"Study of Heat Transfer and Erosion in Gun Barrels"
AFATL-TR-73-69 1973
 - 36 Gibeling, H. J., Buggeln, R. C. and McDonald, H.
"Development of a Two-Dimensional Implicit Interior
Ballistics Code"
BRL Contract Report ARBRL-CR-00411 1980
 - 37 Gibeling, H. J. and McDonald, H.
"Development of a Two-Dimensional Implicit Interior
Ballistics Code"
BRL Contract Report ARBRL-CR-00451 1981
 - 38 Gibeling, H. J. and McDonald, H.
"An Implicit Numerical Analysis for Two-Dimensional
Turbulent Interior Ballistic Flows"
BRL Contract Report ARBRL-CR-00523 1984
 - 39 Schmitt, J. A. and Mann, T. L.
"An Evaluation of the Alpha Code in its One-Phase Mode"
BRL Memorandum Report ARBRL-MR-03081 1981

A model very similar to that of Gibeling et al has been presented by Schmitt.⁴⁰ The major differences between the two models arise in respect to the computational form of the equations and the details of numerical solution. Both models are based on implicit schemes which are updated using a non-iterative, linearized, alternating direction algorithm. The scope of the calculations which have been published to date by Schmitt⁴⁰ and by Heiser and Schmitt^{40,41} does not go beyond those of Gibeling et al.³⁸

In addition, efforts to analyze the boundary layer described by Buckingham and co-workers⁴²⁻⁴⁴ do not appear to go any further than those of Gibeling et al as regards coupling to the combustion of the propellant and recognition of its geometry.

In revising the analysis of the regions of ullage to treat two-dimensional effects we follow the approach of Gibeling et al and of Schmitt. That is to say, we replace the inviscid governing equations by the Navier-Stokes equations with heat conduction. Moreover, we use the computationally efficient linearized alternating direction implicit algorithm. Our immediate purpose in so doing is to provide a better posed computational approach through the inclusion of the appropriate physical terms — mechanical and thermal diffusion — and to achieve simplification of the coding through the use of a two-dimensional representation at all times.

-
- 40 Schmitt, J. A.
 "A Numerical Algorithm for the Multidimensional, Multiphase,
 Viscous Equations of Interior Ballistics"
 Proc. 2nd Army Conference on Applied Mathematics and
 Computing, RPI 1984
 - 41 Heiser, R. and Schmitt, J. A.
 "Simulations of Special Interior Ballistic Phenomena With and
 Without Heat Transfer to the Gun Tube Wall"
 Proc. 2nd Army Conference on Applied Mathematics and
 Computing, RPI 1984
 - 42 Buckingham, A. C.
 "Propellant Driven Turbulent Interior Ballistics and Wall Erosion"
 AIAA Paper 79-0007, 17th Aerospace Sciences Meeting 1979
 - 43 Kang, S. W. and Levatin, J. L.
 "Unsteady Boundary-Layer Flows in Combustion Environments"
 Proc. 17th JANNAF Combustion Meeting 1980
 - 44 Buckingham, A. C. and Levatin, J. L.
 "Additive Thermochemical Effects in Turbulent Erosive
 Boundary Layers"
 Proc. 1983 JANNAF Propulsion Meeting 1983

A more long range goal will be to examine the manner in which the packaging of the charge influences the thermal erosion of the gun tube. Ultimately, this goal will require the resolution of fundamental questions regarding the structure of turbulence in the gun environment, the relationship between thermal diffusion and the macroscopic state variables, and the interpretation of the internal boundary conditions at the boundaries of the mixture regions.

8.2 Governing Equations

The governing equations for the regions of ullage consist of statements of balance of mass, momentum and energy together with a number of constitutive laws. With ρ , density; \mathbf{u} , velocity; σ , stress tensor; e , internal energy; \mathbf{q} , heat flux vector; and g_0 , a constant to reconcile units, the balance equations may be written as follows:

$$\frac{\partial \rho}{\partial t} + \nabla \cdot \rho \mathbf{u} = 0 \quad , \quad (8.1)$$

$$\frac{\partial \mathbf{u}}{\partial t} + (\mathbf{u} \cdot \nabla) \mathbf{u} - \frac{g_0}{\rho} \nabla \cdot \sigma = 0 \quad , \quad (8.2)$$

$$\frac{\partial e}{\partial t} + \mathbf{u} \cdot \nabla e - \frac{1}{\rho} \sigma : \nabla \mathbf{u} + \frac{1}{\rho} \nabla \cdot \mathbf{q} = 0 \quad . \quad (8.3)$$

The stress tensor is assumed to have the form

$$\sigma = -p\mathbf{I} + \left(\lambda - \frac{2}{3}\mu\right)(\nabla \cdot \mathbf{u})\mathbf{I} + \mu(\nabla \mathbf{u} + \nabla \mathbf{u}^T) \quad (8.4)$$

where p is pressure; \mathbf{I} is the identity tensor; μ and λ are the first and second coefficients of viscosity respectively; and we use a superscript T to denote the transpose of a matrix.

Let u be represented in cylindrical coordinates (r, z, θ) by $(v, u, 0)$ for an axisymmetric flow. Then the rate-of-strain tensor may be represented, in physical units, as

$$E = \frac{1}{2} (\nabla u + \nabla u^T) = \begin{bmatrix} \frac{\partial v}{\partial r} & \frac{1}{2} \left[\frac{\partial v}{\partial z} + \frac{\partial u}{\partial r} \right] & 0 \\ \frac{1}{2} \left[\frac{\partial v}{\partial z} + \frac{\partial u}{\partial r} \right] & \frac{\partial u}{\partial z} & 0 \\ 0 & 0 & \frac{v}{r} \end{bmatrix} \quad (8.5)$$

We note that

$$\nabla \cdot u = \frac{\partial v}{\partial r} + \frac{\partial u}{\partial z} + \frac{v}{r} \quad (8.6)$$

Similarly,

$$\nabla \cdot \sigma = \begin{bmatrix} \frac{1}{r} \frac{\partial}{\partial r} (r \sigma_{rr}) + \frac{\partial \sigma_{rz}}{\partial z} - \frac{\sigma_{\theta\theta}}{r} \\ \frac{1}{r} \frac{\partial}{\partial r} (r \sigma_{zr}) + \frac{\partial \sigma_{zz}}{\partial z} \\ 0 \end{bmatrix} \quad (8.7)$$

The heat flux vector is assumed to obey the law

$$\mathbf{q} = -k \nabla T \quad (8.8)$$

where T is the temperature and k is the thermal conductivity. The values of μ , λ and k may be assumed to embed both molecular and turbulent diffusion. The molecular contribution to viscosity is assumed to obey a Sutherland-type law as in previous work¹⁰ and the corresponding thermal conductivity follows from a fixed value of the Prandtl number. The turbulent diffusion processes will be assumed to be governed by algebraic laws as used by Schmitt,⁴⁰ at least for the time being. Finally, we have the equation of state

$$e = e(p, \rho) \quad , \quad (8.9)$$

and equations for the time dependence of the molecular weight and specific heats of the gas. As in previous work,¹⁰ we assume a covolume equation of state. We also use the previous expressions for the evolution of the molecular weight and specific heats.

Making formal use of (8.1) (8.4) and (8.9) enables us to recast the energy balance in the form

$$\frac{Dp}{Dt} + \frac{\rho c^2}{g_0} \nabla \cdot \mathbf{u} = \frac{1}{\left[\frac{\partial e}{\partial p} \right]_\rho} \left[-\frac{1}{\rho} \nabla \cdot \mathbf{q} + \left(\lambda - \frac{2}{3} \mu \right) (\nabla \cdot \mathbf{u})^2 + 2\mu \mathbf{E} : \mathbf{E} \right] \quad (8.10)$$

where c is the isentropic speed of sound.

The balance equations may be written in full, in cylindrical coordinates, as follows. The mass balance is

$$\frac{\partial \rho}{\partial t} + v \frac{\partial \rho}{\partial r} + u \frac{\partial \rho}{\partial z} + \rho \left[\frac{\partial v}{\partial r} + \frac{\partial u}{\partial z} + \frac{v}{r} \right] = 0 \quad . \quad (8.11)$$

The momentum balances are

$$\begin{aligned}
 & \frac{\partial v}{\partial t} + v \frac{\partial v}{\partial r} + u \frac{\partial v}{\partial z} + \frac{s_0}{\rho} \frac{\partial p}{\partial r} \\
 &= - \frac{s_0}{\rho} \left\{ \frac{\partial}{\partial r} \left[\frac{2\mu}{3} \left(2 \frac{\partial v}{\partial r} - \frac{v}{r} - \frac{\partial u}{\partial z} \right) \right] + 2\mu \frac{\partial}{\partial r} \left[\frac{v}{r} \right] \right. \\
 & \quad \left. + \frac{\partial}{\partial r} \left[\lambda \left(\frac{1}{r} \frac{\partial}{\partial r} (rv) + \frac{\partial u}{\partial z} \right) \right] + \frac{\partial}{\partial z} \left[\mu \left[\frac{\partial v}{\partial z} + \frac{\partial u}{\partial r} \right] \right] \right\} \quad (8.12)
 \end{aligned}$$

$$\begin{aligned}
 & \frac{\partial u}{\partial t} + v \frac{\partial u}{\partial r} + u \frac{\partial u}{\partial z} + \frac{s_0}{\rho} \frac{\partial p}{\partial z} \\
 &= - \frac{s_0}{\rho} \left\{ \frac{\partial}{\partial r} \left[\mu \left(\frac{\partial v}{\partial z} + \frac{\partial u}{\partial r} \right) \right] + \frac{\mu}{r} \left[\frac{\partial v}{\partial z} + \frac{\partial u}{\partial r} \right] \right. \\
 & \quad \left. + \frac{\partial}{\partial z} \left[\frac{2\mu}{3} \left[2 \frac{\partial u}{\partial z} - \frac{\partial v}{\partial r} - \frac{v}{r} \right] + \lambda \left[\frac{\partial u}{\partial z} + \frac{\partial v}{\partial r} + \frac{v}{r} \right] \right] \right\} \quad (8.13)
 \end{aligned}$$

The energy balance is

$$\frac{\partial p}{\partial t} + v \frac{\partial p}{\partial r} + u \frac{\partial p}{\partial z} - \frac{\rho c^2}{s_0} \left[\frac{\partial v}{\partial r} + \frac{\partial u}{\partial z} + \frac{v}{r} \right] = \frac{1}{\left[\frac{\partial e}{\partial p} \right] \rho} (\dot{q} + \dot{q}) \quad (8.14)$$

where the mechanical dissipation rate is

$$\begin{aligned} \dot{\Phi} = & \frac{4}{3} \mu \left[\left[\frac{\partial v}{\partial r} \right]^2 + \left[\frac{v}{r} \right]^2 + \left[\frac{\partial u}{\partial z} \right]^2 - \left[\frac{v}{r} \frac{\partial v}{\partial r} + \frac{\partial v}{\partial r} \frac{\partial u}{\partial z} + \frac{v}{r} \frac{\partial u}{\partial z} \right] \right] \\ & + \mu \left[\frac{\partial u}{\partial r} + \frac{\partial v}{\partial z} \right]^2 + \lambda \left[\frac{\partial v}{\partial r} + \frac{v}{r} + \frac{\partial u}{\partial z} \right]^2 \end{aligned} \quad (8.15)$$

and the thermal dissipation rate is

$$\dot{Q} = \frac{1}{\rho} \left[\frac{1}{r} \frac{\partial}{\partial r} \left[k r \frac{\partial T}{\partial r} \right] + \frac{\partial}{\partial z} \left[k \frac{\partial T}{\partial z} \right] \right] \quad (8.16)$$

8.3 Method of Solution

Our approach is similar to that of Schmitt⁴⁰ and we adopt his nomenclature in the present discussion. Like Schmitt we use a Linearized Alternating Direction Implicit Algorithm to solve the balance equations. The idea of replacing a multidimensional implicit integrator by a series of fractional steps each involving implicitness in only one of the coordinate directions is referred to as the Alternating Direction Implicit Method and is discussed in such standard texts of those of Richtmyer et al³⁰ and of Roache.⁴⁵ The further step of linearizing the equations so that each fractional step may be completed without iteration has been pioneered and described by Briley and MacDonald⁴⁶ and by Beam and Warming.⁴⁷

⁴⁵ Roache, P.J.
"Computational Fluid Mechanics"
Hermosa Publishers, Albuquerque 1972

⁴⁶ Briley, W.R. and McDonald, H.
"Solution of the Multi-Dimensional Compressible Navier-Stokes
Equations by a Generalized Implicit Method"
J. Comp. Phys. 24 pp 372-397 1977

⁴⁷ Beam, R.M. and Warming, R.F.
"An Implicit Finite-Difference Algorithm for Hyperbolic Systems
in Conservation Form"
J. Comp. Phys. 22 pp 87-110 1976

Let y be a vector whose elements are the dependent variables. Then we assume that we are required to solve the system

$$y_t = G(y, y_r, y_z, y_{rr}, y_{rz}, y_{zz}) \quad (8.17)$$

where $y_t = \partial y / \partial t$ and similarly for the other subscripts. Unlike Schmitt,⁴⁰ we assume that G has no explicit dependence on t , r or z . A second, and more significant, difference from the approach of Schmitt relates to the coordinate system. We assume a transformation from the physical coordinate frame (t, r, z) to the computational frame (τ, η, ξ) in which the physical boundaries are mapped onto lines of constant η or ξ and in which the mesh is rectangular. We reflect the transformation formally by writing, instead of 8.17, the system

$$y_\tau = G(y, y_\eta, y_\xi, y_{\eta\eta}, y_{\eta\xi}, y_{\xi\xi}) \quad (8.18)$$

where the vector function G is understood to have a different form from its counterpart in 8.17.

We use a superscript n to denote values corresponding to a new or future time and superscript c to denote current or present values. Thus $y^n = y(\eta, \xi, \tau^n)$ and $y^c = y(\eta, \xi, \tau^c)$. We assume for the time being that the transformation of coordinates is known at both the new and the current times. This assumption is expected to be satisfactory unless we determine the necessity for an adaptive mesh which is so tightly coupled to the physical solution that it must be determined simultaneously with the internal flowfield. No fundamental revision to the method would be required in such a case. Whereas we presently assume $y = [\rho, v, u, p]^T$, we could just as well include r and z in the list of dependent variables.

We also note that since we do not employ the conservative form of the balance equations we do not need to consider the geometric conservation law as described by Thomas et al.⁴⁸

⁴⁸ Thomas, P.D. and Lombard, C.K.

"Geometric Conservation Law and Its Application to Flow Computations on Moving Grids"

AIAA J 17 pp 1030-1036

1979

Let $\Delta\tau = \tau^n - \tau^c$, then expanding y about τ^n and τ^c by means of Taylor's theorem and introducing the integration parameter β one may show⁴⁰

$$y^n - \beta G^n \Delta\tau = y^c + (1 - \beta) G^c \Delta\tau + (\beta - 1/2) O(\Delta\tau^2) + E_T(\Delta\tau^3) \quad (8.19)$$

where $E_T(\Delta\tau^3)$ is a truncation error term of order $\Delta\tau^3$. Evidently, when $\beta = 1/2$ one has the standard Crank-Nicolson scheme with truncation error of third order. For values of β other than $1/2$ the truncation error is second order in time.

Linearization of 8.19 is accomplished through a Taylor expansion of G^n about G^c

$$G^n = G^{c,n} + D^c \Delta y + DR^c \Delta y_\eta + DZ^c \Delta y_\xi + DRR^c \Delta y_{\eta\eta} + DZZ^c \Delta y_{\eta\xi} + DZZ^c \Delta y_{\xi\xi} + E_L(\Delta\tau^2) \quad (8.20)$$

Here $G^{c,n}$ denotes an evaluation of G based on current values of y and new values of the metric derivatives associated with the coordinate transformation. We have introduced the Jacobian matrices

$$D_{ij}^c = \left[\frac{\partial G_i}{\partial y_j} \right]^c, \quad DR_{ij}^c = \left[\frac{\partial G_i}{\partial y_{\eta_j}} \right]^c, \quad DRR_{ij}^c = \left[\frac{\partial G_i}{\partial y_{\eta\eta_j}} \right]^c$$

and similarly for DZ , DZ and DZZ .

In order to facilitate factorization of the system of equations into an equivalent system of one-dimensional equations it is assumed that $\Delta y_{\eta\xi}$ is negligible. Alternatively, the cross-derivatives can be viewed as evaluated only at the current level. Then 8.19 becomes

$$\left[I - \beta(D_\eta^n + D_\xi^n) \right] y^n = \left[I - \beta(D_\eta^c + D_\xi^c) \right] y^c + L y^c, \quad (8.21)$$

where

$$D_\eta^n = \Delta\tau \left[D^c + DR^c \left[\frac{\partial}{\partial \eta} \right]^* + DRR^c \left[\frac{\partial^2}{\partial \eta^2} \right]^* \right]$$

$$D_{\xi}^* = \Delta \tau \left[DZ^C \left[\frac{\partial}{\partial \xi} \right]^* + DZZ^C \left[\frac{\partial^2}{\partial \xi^2} \right]^* \right] ,$$

$$Ly^C = \Delta \tau \left[(1 - \beta) G^C + \beta G^{C,n} \right] ,$$

and I is the identity matrix.

Equation 8.21 is decomposed into the following pair of equations which are equivalent to 8.21 to a level of accuracy consistent with the truncation error of Equation 8.21. We have

$$(I - \beta D_{\eta}^n) y^I = (I - \beta D_{\eta}^C) y^C + Ly^C , \quad (8.22)$$

$$(I - \beta D_{\xi}^n) y^F = (I - \beta D_{\xi}^C) y^C + (y^I - y^C) . \quad (8.23)$$

We refer to 8.22 as the radial equation and 8.23 as the axial equation. When the spacewise derivatives are approximated by finite differences each of these equations becomes an algebraic system. We use the standard centered differences to represent the first and second derivatives at internal mesh points, namely

$$\left. \frac{\partial y}{\partial \eta} \right|_i = \frac{y_{i+1} - y_{i-1}}{2\Delta\eta} , \quad (8.24)$$

$$\left. \frac{\partial^2 y}{\partial \eta^2} \right|_i = \frac{y_{i+1} - 2y_i + y_{i-1}}{(\Delta\eta)^2} . \quad (8.25)$$

At the boundaries we use the usual three point approximations which involve the boundary point and its two neighbors. Thus far solutions have been obtained only for problems involving impermeable boundaries and inviscid flow. For these problems the physical boundary condition is the requirement that the normal velocity component vanish. This condition replaces the momentum equation for the corresponding component at the boundary.

The result is a system of linear equations which is nearly block tridiagonal, the departure from exact tridiagonality occurring only in the first and last block rows as a result of the approximation of derivatives at the boundaries. The linear systems are solved using the algorithms developed by Hindmarsh et al.^{49,50}

8.4 A Sample Calculation

The analysis described in Section 8.3 has been encoded into a subroutine called LADIS (Linearized Alternating Direction Implicit Solver). Subroutine LADIS has been coded to be fully compatible with the existing structure of TDNOVA. In order to exercise LADIS we have coupled it to a version of TDNOVA in which the pre-existing integration scheme is suppressed. The resulting code is referred to as TDLADIS and accordingly makes use of all the existing TDNOVA input/output conventions and is structured around the existing TDNOVA arrays and storage procedures. For the present TDLADIS is restricted to rectangular physical domains for which the mesh is readily constructed by interpolation between opposing pairs of boundaries. However, the equipotential algorithm of TDNOVA may be invoked for the analysis of more complex configurations by simply unmasking a few lines of code.

At present the physical boundary conditions are confined to a requirement that the normal velocity component vanish and the tangential velocity component be equal to the value determined by the tangential equation of motion multiplied by a coefficient of accommodation. When the coefficient of accommodation is zero a no-slip condition is obtained; when it is equal to one the slip condition applies. Only the molecular viscosity and thermal conductivity are presently encoded.

It will be a goal of subsequent work to reproduce the single-phase results obtained thus far by Schmitt⁴⁰ and by Gibeling et al.³⁸ For the present we have simply exercised TDLADIS by reference to the Lagrange Ballistic Problem for which an analytical solution was obtained by Love and Pidduck.⁵¹ This is the same problem which previous investigators have used to validate the TDNOVA,¹⁵ ALPHA³⁹ and DELTA⁴⁰ codes.

-
- 49 Hindmarsh, A.C.
 "Solution of Block-Tridiagonal Systems of Linear Algebraic Equations"
 Lawrence Livermore Laboratory, UCID-30150 1977
- 50 Hindmarsh, A.C., Sloan, L.J., Fong, K.W. and Rodrigue, G.H.
 "DEC/SOL: Solution of Dense Systems of Linear Algebraic Equations"
 Lawrence Livermore Laboratory, UCID-30137 1976
- 51 Love, A.E.A. and Pidduck, F.B.
 "Lagrange Ballistic Problem"
 Phil. Trans. Roy. Soc., Vol. 222, pp 167-226 1921-1922

This problem has been fully described by these previous investigators and requires no particular discussion here. We are given a quiescent, pressurized gas which propels a projectile through a cylindrical, frictionless tube. The essential data are given in Table 8.1.

Table 8.1 Definition of Lagrange Ballistic Problem

Bore Diameter (cm)	15.0
Initial Projectile Displacement (m)	1.698
Maximum Travel of Projectile (m)	6.0
Projectile Mass (kg)	50.0
Covolume (cm ³ /gm)	1.0
Ratio of Specific Heats (-)	1.22
Initial Pressure (MPa)	621.09
Initial Temperature (K)	2666.80

Two numerical solutions are discussed here. The first is generated by TDNOVA using the 16 X 3 (axial X radial) mesh in the quasi-two-dimensional mode as described by Robbins.¹⁵ The second is generated by TELADIS using a 26 X 5 mesh and an integration parameter $\beta = 0.8$. The time step for the TELADIS calculation was computed using the existing TDNOVA C-F-L criterion with a safety factor of 1.1 so that the maximum Courant number did not exceed 0.91. In Table 8.2 we compare the predictions of TDNOVA and TELADIS with those of the analytical solution for the instant at which the projectile exits the gun. Although the accuracy of the implicit scheme is not as good as that of TDNOVA, which is specifically oriented towards wave propagation problems, the agreement between TELADIS and the analytical results is certainly acceptable. Moreover, the accuracy appears to be at

Table 8.2 Conditions at Muzzle Exit According to Analytical Solution, TDNOVA and TELADIS

	Analytical	TDNOVA	TELADIS
Muzzle Exit Time (msec)	10.58	10.58 (0.00)*	10.57 (0.09)
Projectile Velocity (m/s)	807.7	807.9 (0.025)	809.6 (0.24)
Base Pressure (MPa)	54.2	54.4 (0.37)	54.8 (1.11)
Mass Defect (%)	----	-0.135	0.218

*Percent deviation from analytical value

least as good as that reported by Schmitt in connection with the DELTA code⁴⁰ and to be better than that reported for the ALPHA code.³⁹ We also note that the global mass balancing was quite satisfactory for both the TDNOVA and TILADIS calculations. Final values for the two codes were -0.135% and 0.218% respectively, and these were also extremal values.

To obtain further evidence of the operability and accuracy of TILADIS we compare the histories of breech and base pressure as computed by the two codes. Table 8.3 presents the computed values at every millisecond during the ballistic cycle. The breech pressures never differ by more than 0.58% and the base pressures never differ by more than 0.71%.

Table 8.3 Comparison of TDNOVA and TILADIS Predictions of Breech and Base Pressure for Lagrange Ballistic Problem

Time (msec)	Breech Pressure (MPa)		Difference (%)	Base Pressure (MPa)		Difference (%)
	TDNOVA	TILADIS		TDNOVA	TILADIS	
1.0	605.4	606.5	-0.18	495.4	495.2	0.04
2.0	424.7	425.2	-0.12	407.9	408.0	-0.02
3.0	317.0	317.6	-0.19	281.1	282.0	-0.32
4.0	241.5	243.0	-0.62	203.9	204.5	-0.29
5.0	177.7	178.5	-0.45	156.8	157.3	-0.32
6.0	136.8	137.6	-0.58	125.5	126.0	-0.40
7.0	109.8	110.4	-0.55	102.4	103.1	-0.68
8.0	90.8	91.2	-0.44	84.3	84.9	-0.71
9.0	76.8	77.1	-0.39	70.2	70.6	-0.57
10.0	66.1	66.4	-0.45	59.4	59.7	-0.51

9.0 CONCLUSIONS AND RECOMMENDATIONS

The following conclusions are drawn from the preceding discussion.

[1] The TDNOVA Code has been revised and shown to be applicable to three propelling charges of current interest. Both computational and physical elements of the data base have been varied to determine their influence on the solution.

[2] The influence of computational elements of the data base has been studied for the M203 Charge, which consists of granular propellant, and the M203E2 Charge, which consists of slotted stick propellant. Excellent indifference is seen in respect to the number of axial and radial mesh points. Overall accuracy is also confirmed by studies of the mass balance defect. However, complete indifference was not demonstrated in respect to the time at which transformation from a two-dimensional to a quasi-two-dimensional representation is made. Because stable fully two-dimensional solutions have not yet been made, it is not known whether the apparent dependence on the time of transformation is reflective of latent instability of the two-dimensional solution or of constitutive modeling assumptions in the quasi-two-dimensional mode of calculation.

[3] The influence of the properties of the charge containers has been studied for the M203E2 and XM216 Charges. In these studies the base igniter was treated as a separate two-phase charge increment. Although variations in the permeability of various segments of the containers had a significant effect on the path of flamespreading and the detailed pressure distribution during the ignition of the charge, the overall ballistics of both the M203E2 and XM216 Charges were found to be essentially indifferent to the container properties. In one case, however, the XM216 Charge did exhibit a significant level of pressure waves, due to the persistence of flow resistance between the increments.

[4] Additional features of the TDNOVA Code have been demonstrated including the treatment of finite rate gas-phase chemistry, programmed fracture of stick charges, and the calculation of heat transfer to the tube according to empirical correlations.

[5] An implicit solver for regions of ullage has been developed based on a Linearized Alternating Direction Implicit algorithm for the two-dimensional Navier-Stokes equations. The solver has been shown to be operable by reference to a simplified ballistic problem for which an analytical solution is available.

The following recommendations are made.

[1] Although TDNOVA was originally formulated with the expectation that the charge would be modeled as fully two-dimensional only through the ignition phase it is now apparent that a complete two-dimensional simulation of the interior ballistic cycle is required. Achieving this goal may necessitate the performance of basic studies of two-phase flow instability.

[2] Further research is required in respect to the characterization of the properties of the containers. Many computational difficulties could be eliminated if the properties of the containers were allowed to vary analytically over the surface rather than suffering discontinuities.

[3] Further testing of the implicit solver is recommended so that it can be linked to TDNOVA to support fully two-dimensional solutions of charges in which the ullage represents a significant fraction of the chamber volume.

REFERENCES

1. Budka, A.J. and Knapton, J.D.
 "Pressure Wave Generation in Gun Systems — A Survey"
 Ballistic Research Laboratory Memorandum Report 2567
 (AD B008893L) 1975
2. May, I.W. and Horst, A.W.
 "Charge Design and Pressure Waves in Guns"
 Progress in Astronautics and Aeronautics, Vol. 68,
Interior Ballistics of Guns, edited by H. Krier and M. Summerfield 1979
3. Kent, R.H.
 "Study of Ignition of 155-mm Gun"
 Ballistic Research Laboratory Report 22 (AD 494703) 1935
4. Heddon, S.E. and Nance, G.A.
 "An Experimental Study of Pressure Waves in Gun Chambers"
 Naval Proving Ground Report 1534 1957
5. Gough, P.S.
 "The NOVA Code: A User's Manual"
 Naval Ordnance Station Contract Report IHCR 80-8 1980
6. Horst, A.W., Smith, T.C. and Mitchell, S.E.
 "Key Design Parameters in Controlling Gun Environment Pressure
 Wave Phenomena — Theory versus Experiment"
 Proc. 13th JANNAF Combustion Meeting 1976
7. Horst, A.W. and Gough, P.S.
 "Influence of Propellant Packaging on Performance of Navy Case
 Gun Ammunition"
 J. Ballistics Vol. 1, p. 229 1977
8. Gough, P.S.
 "Theoretical Study of Two-Phase Flow Associated with Granular
 Bag Charges"
 Ballistic Research Laboratory Contract Report ARBRL-CR-00381
 (AD A062144) 1978
9. Horst, A.W. and Gough, P.S.
 "Modeling Ignition and Flamespread Phenomena in Bagged
 Artillery Charges"
 Ballistic Research Laboratory Technical Report ARBRL-TR-02263
 (AD 091790) 1980
10. Gough, P.S.
 "Two-Dimensional Convective Flamespreading in Packed Beds of
 Granular Propellant"
 Ballistic Research Laboratory Contract Report ARBRL-CR-00404
 (AD A075326) 1979

11. Gough, P.S.
"A Two-Dimensional Model of the Interior Ballistics of Bagged Artillery Charges"
Ballistic Research Laboratory Contract Report ARBRL-CR-00452
(AD A100751) 1981
12. Gough, P.S.
"Two-Dimensional, Two-Phase Modeling of Multi-Increment Bagged Artillery Charges"
Ballistic Research Laboratory Contract Report ARBRL-CR-00503
(AD A125482) 1982
13. Gough, P.S.
"Modeling of Rigidized Gun Propelling Charges"
Ballistic Research Laboratory Contract Report ARBRL-CR-00518
(AD A135860) 1983
14. Horst, A.W.
"Baseline Evaluation of the TDNOVA Code"
Ballistic Research Laboratory Memorandum Report ARBRL-MR-03198
(AD A120718) 1982
15. Robbins, F.W.
"Comparison of TDNOVA Results with an Analytic Solution"
Ballistic Research Laboratory Memorandum Report ARBRL-MR-03299
(AD A132969) 1983
16. Horst, A.W., Robbins, F.W. and Gough, P.S.
"A Two-Dimensional, Two-Phase Flow Simulation of Ignition, Flamespread, and Pressure-Wave Phenomena in the 155-mm Howitzer"
Ballistic Research Laboratory Technical Report ARBRL-TR-02414
(AD A119148) 1982
17. Horst, A.W., Robbins, F.W. and Gough, P.S.
"Multidimensional, Multiphase Flow Analysis of Flamespreading in a Stick Propelling Charge"
Ballistic Research Laboratory Memorandum Report ARBRL-MR-03372
(AD A145731) 1984
18. Gough, P.S.
"Theoretical Effects of Packaging on Two-Dimensional Flamespread Through Slotted Stick Propelling Charges"
Proc. 21st JANNAF Combustion Meeting 1984
19. Minor, T.C. and Horst, A.W.
"Theoretical and Experimental Investigation of Flamespreading Processes in Combustible-Cased, Stick Propellant Charges"
Proc. 21st JANNAF Combustion Meeting 1984

20. Fickie, K.D. and Keller, G.E.
 "Analysis of Solid Propellants as a Reactive-Diffusive System:
 Dynamics of Ignition"
 Proc. 21st JANNAF Combustion Meeting 1984

21. Horst, A.W.
 "A Comparison of Barrel-Heating Processes for Granular and
 Stick Propellant Charges"
 Ballistic Research Laboratory Memorandum Report ARBRL-MR-03193
 (AD A118394) 1982

22. Thompson, J.F., Thames, F.C. and Mastin, C.W.
 "Automatic Numerical Generation of Body-Fitted Curvilinear
 Coordinate Systems for Field Containing Any Number of
 Arbitrary Two-Dimensional Bodies"
 J. Comp. Phys. Vol. 15, p. 299 1974

23. McCormack, R.W.
 "The Effect of Viscosity in Hypervelocity Impact Cratering"
 AIAA Paper No. 69-354 1969

24. Gough, P.S.
 "Continuum Modeling of Stick Charge Combustion"
 Proc. 20th JANNAF Combustion Meeting 1983

25. Gelperin, N.I. and Einstein, V.G.
 "Heat Transfer in Fluidized Beds"
Fluidization, edited by Davidson, J.F. and Harrison, D.
 Academic Press, N.Y. 1971

26. Ergun, S.
 "Fluid Flow Through Packed Columns"
 Chem. Eng. Progr. Vol. 48, p.89 1952

27. Robbins, F.W. and Gough, P.S.
 "Influence of Length and Diameter of Cylinders on Packed
 Bed Flow Resistance"
 Proc. 16th JANNAF Combustion Meeting 1979

28. Andersson, K.E.B.
 "Pressure Drop in Ideal Fluidization"
 Chem. Eng. Sci. Vol. 15, p. 276 1961

29. Kutateladze, S.S. and Borishanskii, V.M.
 "A Concise Encyclopedia of Heat Transfer"
 Pergamon Press 1966

30. Richtmyer, R.D. and Morton, K.W.
 "Difference Methods for Initial Value Problems"
 Interscience 1967

31. Minor, T.C.
 "MultiDimensional Influences on Ignition, Flamespread and
 Pressurization in Artillery Propelling Charges"
 Proc. 20th JANNAF Combustion Meeting 1983

32. Minor, T.C. and Horst, A.W.
 "Ignition Phenomena in Developmental, Stick Propellant, Combustible-
 Cased, 155-mm, M203E2 Propelling Charges"
 Ballistic Research Laboratory Report ARBRL-TR-02568 1984

33. Corner, J.
 "Theory of the Interior Ballistics of Guns"
 John Wiley and Son, Inc. New York 1950

34. Evans, R.M.
 "User's Manual for Transient Boundary Layer Integral Matrix
 Procedure TBLIMP"
 Aerotherm Report UM-74-55 1974

35. Shelton, S., Bergles, A. and Saha, P.
 "Study of Heat Transfer and Erosion in Gun Barrels"
 AFATL-TR-73-69 1973

36. Gibeling, H.J., Buggeln, R.C. and McDonald, H.
 "Development of a Two-Dimensional Implicit Interior
 Ballistics Code"
 BRL Contract Report ARBRL-CR-00411 1980

37. Gibeling, H.J. and McDonald, H.
 "Development of a Two-Dimensional Implicit Interior
 Ballistics Code"
 BRL Contract Report ARBRL-CR-00451 1981

38. Gibeling, H.J. and McDonald, H.
 "An Implicit Numerical Analysis for Two-Dimensional
 Turbulent Interior Ballistic Flows"
 BRL Contract Report ARBRL-CR-00523 1984

39. Schmitt, J.A. and Mann, T.L.
 "An Evaluation of the Alpha Code in its One-Phase Mode"
 BRL Memorandum Report ARBRL-MR-03081 1981

40. Schmitt, J.A.
 "A Numerical Algorithm for the Multidimensional, Multiphase,
 Viscous Equations of Interior Ballistics"
 Proc. 2nd Army Conference on Applied Mathematics and
 Computing, RPI 1984

41. Heiser, R. and Schmitt, J.A.
 "Simulations of Special Interior Ballistic Phenomena With and
 Without Heat Transfer to the Gun Tube Wall"
 Proc. 2nd Army Conference on Applied Mathematics and
 Computing, RPI 1984

42. Buckingham, A.C.
 "Propellant Driven Turbulent Interior Ballistics and Wall Erosion"
 AIAA Paper 79-0007, 17th Aerospace Sciences Meeting 1979
43. Kang, S.W. and Levatin, J.L.
 "Unsteady Boundary-Layer Flows in Combustion Environments"
 Proc. 17th JANNAF Combustion Meeting 1980
44. Buckingham, A.C. and Levatin, J.L.
 "Additive Thermochemical Effects in Turbulent Erosive
 Boundary Layers"
 Proc. 1983 JANNAF Propulsion Meeting 1983
45. Roache, P.J.
 "Computational Fluid Mechanics"
 Hermosa Publishers, Albuquerque 1972
46. Briley, W.R. and McDonald, H.
 "Solution of the Multi-Dimensional Compressible Navier-Stokes
 Equations by a Generalized Implicit Method"
 J. Comp. Phys. 24 pp 372-397 1977
47. Beam, R.M. and Warming, R.F.
 "An Implicit Finite-Difference Algorithm for Hyperbolic Systems
 in Conservation Form"
 J. Comp. Phys. 22 pp 87-110 1976
48. Thomas, P.D. and Lombard, C.K.
 "Geometric Conservation Law and Its Application to Flow
 Computations on Moving Grids"
 AIAA J 17 pp 1030-1036 1979
49. Hindmarsh, A.C.
 "Solution of Block-Tridiagonal Systems of Linear Algebraic
 Equations"
 Lawrence Livermore Laboratory, UCID-30150 1977
50. Hindmarsh, A.C., Sloan, L.J., Fong, K.W. and Rodrigue, G.H.
 "DEC/SOL: Solution of Dense Systems of Linear Algebraic Equations"
 Lawrence Livermore Laboratory, UCID-30137 1976
51. Love, A.E.A. and Pidduck, F.B.
 "Lagrange Ballistic Problem"
 Phil. Trans. Roy. Soc., Vol. 222, pp 167-226 1921-1922
52. Gough, P.S.
 "Theoretical Modeling of Navy Propelling Charges"
 Final Report for Contract N00174-83-C-0241 PGA-TR-84-1 1984

APPENDIX A

SOLUTION OF THE GAS-PHASE MECHANICAL BOUNDARY CONDITIONS

APPENDIX A: SOLUTION OF THE GAS-PHASE MECHANICAL BOUNDARY CONDITIONS

The overall method of determination of the boundary values for both phases remains as described in Reference 13 and as outlined in Chapter 2.0 of the present report. In this appendix we focus attention on the solution of the gas-phase mechanical boundary conditions. These boundary conditions are understood to embrace the continuity and momentum balances and are solved subject to the acoustic characteristic constraints between the pressures and the normal velocity components. The further assumption is made that the equations can be linearized by the neglect of changes in the thermodynamically influenced coefficients such as density and isentropic sound speed. Since, however, an implicit expression of the boundary conditions in terms of future level properties is desirable, the analysis described herein is performed iteratively at each time step. In each iteration the density and sound speed are modified in accordance with the solution of the finite energy balance and material characteristic equations.

We first discuss the mechanical boundary conditions, making the implicit assumption that all the fluxes are subsonic. We then consider the two separate cases in which the region of ullage which terminates all the continuum fluxes is either open or closed. In each of these cases we note the special considerations which pertain when some of the fluxes are sonic. We conclude by discussing the special case of a slotted stick charge in which the slot is open at the boundary so that the internal (perforation) and external (interstitial) pressures are equilibrated.

A.1 The Boundary Conditions

At a discontinuity in porosity which connects a gas-phase continuum state i with an exterior state n , we have the following approximate expression of the finite balance of momentum¹³

$$p_i + \frac{\epsilon_i \rho_i}{g_o} u_i^2 - \frac{K_i}{g_o \rho_i \epsilon_i} \left[\dot{m}_i + \sum_{j=1}^{J_1} \dot{m}_{s_{ji}} \right] \left| \dot{m}_i + \sum_{j=1}^{J_1} \dot{m}_{s_{ji}} \right| = p_n + \frac{\epsilon_n \rho_n}{g_o} u_n^2 \quad (A.1)$$

Here we have p , pressure; ϵ , porosity; ρ , density; g_o , a constant to reconcile units; K , the dimensionless surface flow resistance factor; u , the normal component of gas-phase velocity; $\dot{m} = \epsilon \rho u$, the corresponding mass flux; $\dot{m}_{s_{ji}}$, a surface mass source; J_1 , the number of mass sources located on the inner (mixture) side of the boundary. State n is to be thought of as corresponding to the region of ullage which terminates each of the continua

corresponding to $i = 1, \dots, n-1$ at a common macroscopic point. In all cases of interest here the velocity u_n is not an explicitly modeled quantity. Even if the ullage is open its properties will be lumped in the direction normal to the surface. We evaluate u_n from the finite mass balance

$$\varepsilon_n \rho_n u_n = \dot{m}_i + \sum_{j=1}^J \dot{m}_{s_{ji}}, \quad (A.2)$$

where $J \geq J_1$ is the total number of surface source terms.

It is convenient therefore to recast (A.1) in terms of \dot{m}_i as follows.

$$\begin{aligned} p_i + \frac{\dot{m}_i^2}{g_0 \varepsilon_i \rho_i} - \frac{K_i}{g_0 \varepsilon_i \rho_i} \left[\dot{m}_i + \sum_{j=1}^{J_1} \dot{m}_{s_{ji}} \right] \left[\dot{m}_i + \sum_{j=1}^{J_1} \dot{m}_{s_{ji}} \right] \\ = p_n + \frac{\left[\dot{m}_i + \sum_{j=1}^{J_1} \dot{m}_{s_{ji}} \right]^2}{g_0 \varepsilon_n \rho_n} \end{aligned} \quad (A.3)$$

We distinguish three separate computational regimes according to the value of K_i .

[1] If $K_i \geq 100$ we take the surface to be impermeable to flux i . The boundary condition reduces to

$$\dot{m}_i + \sum_{j=1}^{J_1} \dot{m}_{s_{ji}} = 0.$$

[2] If $K_i < 0.1$ we assume that the normal loss due to flow resistance is comparable in magnitude to the momentum flux term and that the quadratic dependence on \dot{m}_i is no longer significant. A linearized scheme is used as discussed previously¹³ and as noted below.

[3] If $0.1 \leq K_i < 100$ we assume that the quadratic relation between p_i and \dot{m}_i cannot be ignored. This is the case which interests us here.

We further recast (A.3) as

$$p_i \left[1 + \frac{\dot{m}_i^2}{s_o s_i \rho_i p_i} \right] - \frac{\bar{K}}{s_o \rho_i s_i^2} \left[\dot{m}_i + \sum_{j=1}^{J_1} \dot{m}_{s_{ji}} \right]^2$$

$$= p_n \left\{ 1 + \frac{\left[\dot{m}_i + \sum_{j=1}^J \dot{m}_{s_{ji}} \right]^2}{s_o s_n \rho_n p_n} \right\} \quad (A.4)$$

where $\bar{K} = \pm K$ according as $\dot{m}_i + \sum_{j=1}^{J_1} \dot{m}_{s_{ji}} \gtrless 0$. (A.5)

We now introduce quantities ϕ_i and φ_i which are understood to be defined in terms of current storage, thereby linearizing equation (A.4) except for the through-flux term. We put

$$\phi_i = \frac{1 + \frac{\left[\dot{m}_i + \sum_{j=1}^J \dot{m}_{s_{ji}} \right]^2}{s_o s_n \rho_n p_n}}{1 + \frac{\dot{m}_i^2}{s_o s_i \rho_i p_i}} \quad (A.6)$$

$$\varphi_i = \frac{\frac{\bar{K}}{s_o \rho_i s_i^2}}{1 + \frac{\left[\dot{m}_i + \sum_{j=1}^J \dot{m}_{s_{ji}} \right]^2}{s_o s_n \rho_n p_n}} \quad (A.7)$$

and we introduce $\dot{\mu}_i$ such that

$$\dot{\mu}_i = \dot{m}_i + \sum_{j=1}^{J_1} \dot{m}_{s_{ji}} \quad (A.8)$$

Then the momentum balance is put into the form

$$\frac{p_i}{\phi_i} - \varphi_i \dot{\mu}_i^2 = p_n \quad (A.9)$$

We note that if $\varphi_i = 0$, as would be the case if $K_i < 0.1$, then (A.9) would define a relationship between p_i and p_n which may be viewed as linear from a computational standpoint.

The $n - 1$ relationships of the form (A.9) are used in combination with the conditions of compatibility between pressure and mass flux for all n states to obtain the future level values of p_n , $\dot{\mu}_i$, p_i , $i = 1, \dots, n - 1$. The transport equations for enthalpy and the other state variables then determine the remaining thermodynamic properties for fluxes which are found to enter their respective continuum regions. The material characteristics serve the same purpose for exiting fluxes.

The compatibility conditions between pressure and mass flux depend on whether the exterior state n corresponds to an open or a closed region and also whether the continuum state is subsonic or sonic. Supersonic states are not presently considered.

The exterior region is considered to be closed if its extension normal to the boundary element is less than 1 mm. Somewhat larger exterior regions may also be treated as closed if the flow through the ullage is large. This second criterion is applied only to regions of axial ullage which separate charge increments during the fully two-dimensional part of the solution. If Δt is the time step, the exterior state will be treated as closed if

$$\frac{\Delta t}{\rho_n} \sum_{\dot{m}_i > 0} \left[\dot{m}_i \frac{\partial \rho_n}{\partial \dot{m}_i} \right] > 0.1$$

where ρ_n is the density in the ullage region.

A.2 Exterior State Open

In this case state n has lumped properties in the normal direction. The compatibility relation for state n may be written as

$$p_n = p_n' + \sum_{i=1}^{n-1} \beta_i (\dot{m}_i - \dot{m}_i') \quad , \quad (A.10)$$

where p_n' is the trial future level value computed from the balance equations for the ullage on the basis of trial fluxes \dot{m}_i' . Since the \dot{m}_{sji} are given it follows from (A.8) that

$$p_n = p_n' + \sum_{i=1}^{n-1} \beta_i (\dot{\mu}_i - \dot{\mu}_i') \quad . \quad (A.11)$$

A.2.1 Subsonic Fluxes

The compatibility relation between p_i and $\dot{\mu}_i$ is the acoustic characteristic condition

$$p_i = p_i' + \frac{\alpha_i}{C_i} (\dot{\mu}_i - \dot{\mu}_i') \quad , \quad (A.12)$$

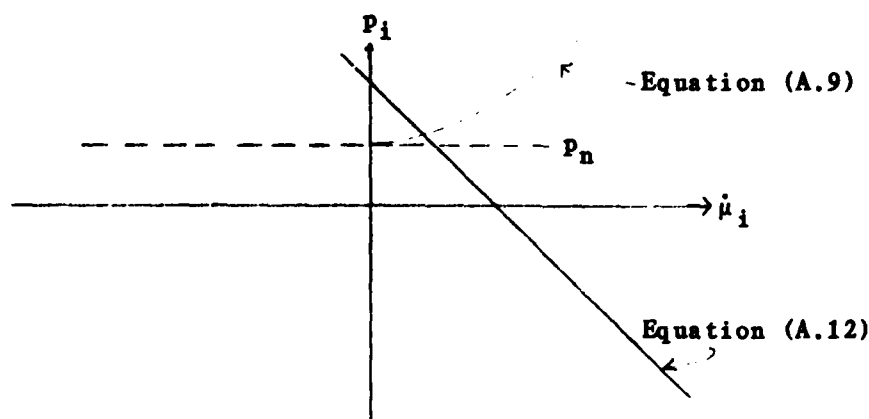
where $C_i = \partial \dot{M}_i / \partial u_i$ and α_i is the characteristic derivative $\partial p_i / \partial u_i$. We

substitute (A.12) into (A.9) to obtain $\dot{\mu}_i$ as a function of p_n and the trial or present storage quantities:

$$\dot{\mu}_i = \frac{\alpha_i}{2\phi C \psi_{i i i}} \pm \left[\left[\frac{\alpha_i}{2\phi C \psi_{i i i}} \right]^2 + \frac{1}{\psi_i} \left[\frac{\alpha_i \mu_{i i}}{C_i} - p_n \right] \right]^{1/2} \quad (A.13)$$

Care must be exercised in respect to the choice of signs in equation (A.13). Apart from the correct selection of the physical solution from the pair defined by the quadratic roots, there is the uncertainty concerning the sign of ψ_i as embedded in K . Particularly when the direction of the flux is near reversal the sign of ψ_i may not be known a priori and experience shows that the numerical determination of the boundary values may become unstable if an incorrect guess is made.

Although (A.13) allows two roots, we may see from graphical construction that (A.9) and (A.12) can have only one intersection. We observe that (A.9) describes a parabola with $\psi_i > 0$ if $\dot{\mu}_i > 0$ and $\psi_i < 0$ if $\dot{\mu}_i < 0$. Also we have $\alpha_i/C_i < 0$ in all cases. Hence (A.12) describes a straight line with negative slope. We sketch the situation below. One and only one intersection can occur.



Assuming that ψ_i is small, and performing a binomial expansion, the condition $\lim_{\psi_i \rightarrow 0} \dot{\mu}_i$ be bounded shows that the minus sign is correct.

We proceed as follows. We set $\bar{K} = \pm K$ according as

$$p_i' - \frac{a_i \dot{\mu}_i'}{C_i} - \phi_i p_n > 0, \text{ thereby using the solution for } \phi_i = 0 \text{ as a guide}$$

to the sign of $\dot{\mu}_i$. Given \bar{K} and hence ϕ_i we have a functional relationship between $\dot{\mu}_i$ and p_n :

$$\dot{\mu}_i(p_n) = \frac{a_i}{2\phi_i C_i \phi_i} \left\{ 1 - \left[1 + \frac{1}{\phi_i \phi_i} \left[\frac{2\phi_i C_i \phi_i}{a_i} \right]^2 \left[p_i' - \frac{a_i \dot{\mu}_i'}{C_i} - \phi_i p_n \right]^2 \right]^{1/2} \right\} \quad (A.14)$$

The $n-1$ equations of the form (A.14) may be substituted into (A.11) to obtain

$$f(p_n) = p_n - p_n' + \sum_{i=1}^{n-1} \beta_i \left[\dot{\mu}_i' - \dot{\mu}_i(p_n) \right] = 0 \quad (A.15)$$

This equation may be solved by Newton's method according to which the trial value \bar{p}_n is replaced by the improved value p_n such that

$$p_n = \bar{p}_n - \frac{f(\bar{p}_n)}{f'(\bar{p}_n)} \quad (A.16)$$

Evidently

$$f'(p_n) = 1 - \sum_{i=1}^{n-1} \frac{\beta_i}{2\psi_i} \left[\frac{2\phi_i C_i \psi_i}{a_i} \right] \left\{ 1 + \frac{1}{\psi_i \phi_i} \left[\frac{2\phi_i C_i \psi_i}{a_i} \right] \left[p_i' - \frac{a_i \dot{\mu}_i'}{C_i} - \phi_i p_n \right] \right\}^{-1/2} \quad (A.17)$$

If it happens that $\phi_i = 0$ for a given flux we may use the solution

$$\dot{\mu}_i = \frac{C_i}{a_i} \left[\phi_i p_n - p_i' \right] + \dot{\mu}_i' \quad \text{and} \quad \frac{\partial \dot{\mu}_i}{\partial p_n} = \frac{C_i \phi_i}{a_i} \quad \text{in forming the sums in (A.15)}$$

and (A.17).

A.2.2 Sonic Fluxes

Equation (A.15) is first solved assuming that all the fluxes are subsonic. Once the updated fluxes are determined from (A.14) they are tested to see if they are indeed subsonic. If any normal velocity is found to be supersonic, based on the value of the speed of sound computed using current storage data, the corresponding $\dot{\mu}_i$ is replaced by the sonic value. Equation (A.15) is then solved once again. Only the subsonic fluxes are included in the sum over i since $\dot{\mu}_i = \dot{\mu}_i'$ for a sonic flux. It is assumed, of course, that p_n' has been made compatible with $\dot{\mu}_i'$ prior to the second pass.

At present, the uniqueness of solutions involving sonic fluxes has not been established.

We note the role played by the condition of sonic flow. For an efflux, the sonic condition replaces the condition of exterior compatibility as expressed by Equation (A.9). That is, the exterior pressure p_n no longer affects the interior of continuum region i . For an influx, the sonic condition replaces the condition of interior compatibility as expressed by the characteristic relation (A.12). The boundary values are determined by the exterior state and not by the interior flow.

A.3 Exterior State Closed

In this case the state of the external region is not modeled and Equation (A.11) cannot be used. Instead, we use directly the finite balance of mass

$$\sum_{i=1}^{n-1} \left[\dot{m}_i + \sum_{j=1}^J \dot{m}_{s_{ji}} \right] = 0 \quad . \quad (\text{A.18})$$

A.3.1 Subsonic Fluxes

As in the case when the exterior region is open, Equations (A.9) and (A.12) lead to the determination of the \dot{m}_i according to (A.14). In this case the quantity p_n is to be thought of as a reference pressure which may not be realized by any real local state but which emerges formally from the analysis. From (A.18) we see that we must solve

$$f(p_n) = \sum_{i=1}^{n-1} \left[\dot{m}_i(p_n) + \sum_{j=J_1+1}^J \dot{m}_{s_{ji}} \right] = 0 \quad . \quad (\text{A.19})$$

We use (A.16) and we note that

$$f'(p_n) = \sum_{i=1}^{n-1} \frac{1}{2\phi_i} \left[\frac{2\rho_i C_i \phi_i}{\alpha_i} \right] \left\{ 1 + \frac{1}{\phi_i \phi_i} \left[\frac{2\rho_i C_i \phi_i}{\alpha_i} \right] \left[p_i' - \frac{\alpha_i \dot{m}_i'}{C_i} - \phi_i p_n \right] \right\}^{-1/2} \quad . \quad (\text{A.20})$$

The situation when $\phi_i = 0$ is treated in the same way as the case when the exterior region is open.

A.3.2 Sonic Fluxes

As with the case of the open exterior region, it is initially assumed that all fluxes are subsonic. Subsonic fluxes are replaced by sonic values and the solution of (A.19) is repeated with the sum in (A.20) confined to subsonic states. If all the fluxes are found to be sonic, the sum in (A.20) only excludes those fluxes which correspond to inflows to their respective continuum regions. Further discussion of this topic may be found in Reference 52.

A.4 Treatment of Slotted Sticks

When the slot is open the interior (perforation) and exterior (interstitial) fluxes are assumed to have the same pressure. We assume that the values of ρ and ϕ for the interstitial flux define compatibility with the ullage region which terminates the continuum. If we adopt the convention that the perforation flow has label i and the interstitial flow has label $i-1$ then (A.9) is replaced by

$$p_i = p_{i-1} \quad (A.21)$$

for flux i . We consider first the case when the ullage region is open. Provided that both \dot{m}_i and \dot{m}_{i-1} are subsonic it follows that the contribution of flux i to the sum in (A.15) is

$$\Delta f_i = \frac{\beta_i C_i}{\alpha_i} \frac{\alpha_{i-1}}{C_{i-1} \beta_{i-1}} \Delta f_{i-1} \quad (A.22)$$

where Δf_{i-1} is the contribution corresponding to flux $i-1$. Similarly, the contribution to the sum in (A.17) is

$$\Delta f_i' = \frac{\beta_i C_i}{\alpha_i} \frac{\alpha_{i-1}}{C_{i-1} \beta_{i-1}} \Delta f_{i-1}' \quad (A.23)$$

52

Gough, P.S.

"Theoretical Modeling of Navy Propelling Charges"

Final Report for Contract N00174-83-C-0241, PGA-TR-84-1

1984

When the ullage is closed we have the following contributions to the sums in (A.19) and (A.20) respectively.

$$\Delta f_i = \frac{C_i}{a_i} \frac{a_{i-1}}{C_{i-1}} \left[\dot{\mu}_{i-1} - \dot{\mu}_{i-1}' \right] + \dot{\mu}_i' + \sum_{j=J_1+1}^J h_{s_{ji}} \quad , \quad (A.24)$$

$$\Delta f_i' = \frac{C_i}{a_i} \frac{a_{i-1}}{C_{i-1}} \frac{d\dot{\mu}_{i-1}}{dp_n} \quad , \quad (A.25)$$

where $\frac{d\dot{\mu}_{i-1}}{dp_n}$ follows from (A.14).

In the event that either flux i or flux $i-1$ turns out to be sonic, the algorithm uses the previously discussed procedure for sonic fluxes and the equilibration condition (A.21) may fail to be satisfied.

APPENDIX B

INPUT DATA FOR NOMINAL SIMULATION OF M203 CHARGE

CONTROL PARAMETERS

NPRINT (0=NO PRINT, 1=PRINT)	1
NSUMRY (0=NO SUMMARY TABLES, 1=YES)	1
NPLOT (0=NO ISOMETRIC CARPET PLOTS, 1=PLOT)	1
NVHL (0=HIDDEN LINES DELETED, 1=RETAINED)	0
NPLCON (0=NO CONTOUR PLOTS, 1=PLOT)	0
NPLFLO (0=NO FLOW PLOTS, 1=PLOT)	1
NPLFLM (0=NO FLAMESREAD PLOT, 1=PLOT)	1
NDSKW (0=NO DISC SAVE, 1=DISC SAVE)	0
NDSKR (0=NO DISC START, >0=DISC START AT STEP NDSKR)	0

ISOMETRICALLY PLOTTED QUANTITIES (1=YES, 0=NO)

MESH 0	POROSITY 0	GRANULAR STRESS 0
PRESSURE 1	DENSITY 0	GAS AXIAL VELOCITY 0
SOLID AXIAL VELOCITY 0	GAS RADIAL VELOCITY 0	SOLID RADIAL VELOCITY 0
GAS TEMPERATURE 0	PARTICLE SURFACE TEMPERATURE 0	
PYROLYSIS PRODUCT MASS FRACTION 0		

CONTOUR PLOTTED QUANTITIES (1=YES, 0=NO)

MESH 0	POROSITY 0	GRANULAR STRESS 0
PRESSURE 1	DENSITY 0	GAS AXIAL VELOCITY 0
SOLID AXIAL VELOCITY 0	GAS RADIAL VELOCITY 0	SOLID RADIAL VELOCITY 0
GAS TEMPERATURE 0	PARTICLE SURFACE TEMPERATURE 0	
PYROLYSIS PRODUCT MASS FRACTION 0		

SCALE FACTOR FOR PLOTTING(-)	.40
LENGTH OF Z-AXIS IN CALCOMP PLOTS(IN)	12.01
LENGTH OF R-AXIS(IN)	4.01
LENGTH OF ORDINATE AXIS(IN)	5.00

LOGOUT PARAMETERS

PARAMETERS PRIOR TO Q-2-D TRANSFORMATION

NUMBER OF STEPS BEFORE LOGOUT	2000
N.B. A NEGATIVE ENTRY FOR THE ABOVE DATUM IMPLIES THAT VARIABLE LOGOUT SCHEDULING IS INTENDED.	
TIME INCREMENT BEFORE LOGOUT(MSEC)	.5000

PARAMETERS AFTER Q-2-D TRANSFORMATION

NUMBER OF STEPS BEFORE LOGOUT	2000
TIME INCREMENT BEFORE LOGOUT(MSEC)	1.0000

SUMMARY TABLE PARAMETERS

NUMBER OF PRESSURE SUMMARY STATIONS	2
TIME INCREMENT FOR PRESSURE SUMMARY STORAGE (MSEC)	.200
DEBUG PRINT REQUIRED (0=NO, 1=YES)	0
EXTENDED PRINT REQUIRED (0=NO, 1=YES)	0

TERMINATION PARAMETERS

MAXIMUM NUMBER OF STEPS BEFORE TERMINATION	2500
MAXIMUM INTEGRATION TIME(MSEC)	25.0000
MAXIMUM PROJECTILE TRAVEL (CM)	520.7

CHARGE REPRESENTATION PARAMETERS

NUMBER OF PROPELLANTS IN CHARGE	2
NUMBER OF BAGS IN CHARGE	1
MESH ALLOCATION MODE (0=STATIC, 1=DYNAMIC)	0
MAXIMUM NUMBER OF STORAGE POINTS FOR DYNAMIC MESH ALLOCATION	0
NUMBER OF MESH POINTS IN AXIAL DIRECTION	30
NUMBER OF MESH POINTS IN RADIAL DIRECTION	7
NUMBER OF ITERATIONS TO DETERMINE INITIAL MESH	200
EQUIPOTENTIAL (0) OR LAGRANGIAN (1) MESH	0
QUASI-TWO-DIMENSIONAL FLAMESPREADING (0=NO, 1=YES)	0
NEW(0) OR OLD (1) INTERPHASE DRAG AND HEAT TRANSFER FOR GRANULAR PROPELLANT	1
BED IGNITION RUPTURES CASE (0=NO, 1=YES) (GLOBAL OPTION)	0
SAFETY FACTOR FOR C-F-L CRITERION	1.1000
MAXIMUM FRACTIONAL DISPLACEMENT FOR CON- VERGENCE OF INITIAL MESH DISTRIBUTION	.100E-04
OVER-RELAXATION FACTOR FOR DETERMINATION OF INITIAL MESH DISTRIBUTION	1.600
PRESSURE TOLERANCE FACTOR FOR REDUCTION TO QUASI-TWO-DIMENSIONAL REPRESENTATION(-)	.010
AXIAL SPATIAL RESOLUTION FACTOR(-)	.100
RADIAL SPATIAL RESOLUTION FACTOR(-)	.100
SOURCE STABILITY FACTOR (-)	0.000
MAX. FRACT. OF TUBE FOR CENTERCORE IN Q2D(-)	0.000

AMBIENT CONDITIONS

INITIAL TEMPERATURE(DEG.K)	294.4
INITIAL PRESSURE(MPA)	.1014
INITIAL RATIO OF SPECIFIC HEATS(-)	1.24300
INITIAL MOLECULAR WEIGHT(GM/GM-MOL)	23.36000

PROPERTIES OF PROPELLANT TYPE 1 MAIN CHARGE

SOLID PHASE CONSTITUTIVE DATA

SETTLING POROSITY OF GRANULAR BED(-)	0.00000
SPEED OF COMPRESSION WAVE(M/SEC)	152.4
SPEED OF EXPANSION WAVE(M/SEC)	1270.0
DENSITY OF SOLID PHASE(GM/CC)	1.5830
THERMAL CONDUCTIVITY(J/CM-SEC-DEG.K)	.160100E-02
THERMAL DIFFUSIVITY(CM**2/SEC)	.645200E-03
LONGITUDINAL WAVE SPEED(M/SEC)	0.0
(STICK PROPELLANT ONLY)	
POISSON RATIO(-)	0.000
(STICK PROPELLANT ONLY)	

GAS PHASE CONSTITUTIVE DATA

RATIO OF SPECIFIC HEATS(-)	1.24300
MOLECULAR WEIGHT(GM/GM-MOL)	23.360
COVOLUME(CC/GM)	1.030

SOLID PHASE COMBUSTION CHARACTERISTICS

NUMBER OF BURN RATE DATA	2
EROSIVE EFFECT CONSIDERED (0=NO, 1=YES)	0
FINITE RATE CHEMISTRY (0=NO, 1=YES)	0
IGNITION TEMPERATURE(DEG.K)	444.4
CHEMICAL ENERGY(J/GM)	4384.
SURFACE FLAMESPREAD DELAY(MSEC)	0.0000
EROSIVE PRE-EXPONENT(CM**2-DEG.K/N)	0.
EROSIVE EXPONENT(-)	0.000
FRACTION OF ENERGY RELEASED AT SURFACE(-)	0.000
GAS-PHASE ARRHENIUS PRE-EXPONENT	
((GM/CC)**(1-N)/SEC)	0.
GAS-PHASE ARRHENIUS EXPONENT(J/GM-MOL)	0.0
GAS-PHASE REACTION ORDER(-)	0.000
RATIO OF SPECIFIC HEATS OF FINAL PRODUCTS(-)	0.00000
MOLECULAR WEIGHT OF FINAL PRODUCTS(GM/GM-MOL)	0.000

MAX. PRESSURE (MPA)	BURN RATE ADDITIVE CONSTANT (CM/SEC)	PRE-EXPONENT (CM/SEC-MPA**BN)	EXPONENT (-)
68.95	0.00000	.41170	.63370
689.50	0.00000	.22180	.78640

GRAIN GEOMETRY

FORM (0=CYLINDER, 1=SPHERE, 2=SOLID STICK, 3=PERFORATED OR SLOTTED STICK)	0
EXTERNAL DIAMETER(CM)	1.060
LENGTH(CM)	2.408
DIAMETER OF PERFORATIONS(CM)	.086
NUMBER OF PERFORATIONS(-)	7.
SLOT WIDTH(CM)	0.000
MAX. PERF. STRESS OR OVERPRESSURE(MPA)	0.000
NXSTR (IF 0, ABOVE VALUE IS HOOP STRESS. IF 1, VALUE IS OVERPRESSURE)	0

PROPERTIES OF PROPELLANT TYPE 2 CENTERCORE

SOLID PHASE CONSTITUTIVE DATA

SETTLING POROSITY OF GRANULAR BED(-)	.40000
SPEED OF COMPRESSION WAVE(M/SEC)	442.0
SPEED OF EXPANSION WAVE(M/SEC)	1270.0
DENSITY OF SOLID PHASE(GM/CC)	1.7990
THERMAL CONDUCTIVITY(J/CM-SEC-DEG.K)	.160000E-02
THERMAL DIFFUSIVITY(CM**2/SEC)	.600000E-03
LONGITUDINAL WAVE SPEED(M/SEC)	0.0
(STICK PROPELLANT ONLY)	
POISSON RATIO(-)	0.000
(STICK PROPELLANT ONLY)	

GAS PHASE CONSTITUTIVE DATA

RATIO OF SPECIFIC HEATS(-)	1.24300
MOLECULAR WEIGHT(GM/GM-MOL)	23.360
COVOLUME(CC/GM)	1.030

SOLID PHASE COMBUSTION CHARACTERISTICS

NUMBER OF BURN RATE DATA	2
EROSIVE EFFECT CONSIDERED (0=NO, 1=YES)	0
FINITE RATE CHEMISTRY (0=NO, 1=YES)	0
IGNITION TEMPERATURE (DEG.K)	300.0
CHEMICAL ENERGY (J/GM)	2489.
SURFACE FLAMES PREAD DELAY (MSEC)	0.0000
EROSIVE PRE-EXPONENT (CM**2-DEG.K/N)	0.
EROSIVE EXPONENT (-)	0.000
FRACTION OF ENERGY RELEASED AT SURFACE (-)	0.000
GAS-PHASE ARRHENIUS PRE-EXPONENT ((GM/CC)**(1-N)/SEC)	0.
GAS-PHASE ARRHENIUS EXPONENT (J/GM-MOL)	0.0
GAS-PHASE REACTION ORDER (-)	0.000
RATIO OF SPECIFIC HEATS OF FINAL PRODUCTS (-)	0.00000
MOLECULAR WEIGHT OF FINAL PRODUCTS (GM/GM-MOL)	0.000

MAX. PRESSURE (MPA)	BURN RATE ADDITIVE CONSTANT (CM/SEC)	PRE-EXPONENT (CM/SEC-MPA**BN)	EXPONENT (-)
.52	0.00000	2.50800	.46200
690.00	0.00000	2.00700	.13300

GRAIN GEOMETRY

FORM (0=CYLINDER, 1=SPHERE, 2=SOLID STICK, 3=PERFORATED OR SLOTTED STICK)	1
EXTERNAL DIAMETER (CM)	.300
LENGTH (CM)	0.000
DIAMETER OF PERFORATIONS (CM)	0.000
NUMBER OF PERFORATIONS (-)	0.
SLOT WIDTH (CM)	0.000
MAX. PERF. STRESS OR OVERPRESSURE (MPA)	0.000
NXSTR (IF 0, ABOVE VALUE IS HOOP STRESS. IF 1, VALUE IS OVERPRESSURE)	0

PROPERTIES OF BAG NUMBER 1

MAIN CHARGE PROPELLANT TYPE	1
CENTERCORE IGNITER PROPELLANT TYPE	2
REAR BASEPAD REACTIVITY DATA	1
FORWARD BASEPAD REACTIVITY DATA	0
REAR OF CENTERCORE PERMITS SOLID EFFLUX (1=YES, 0=NO)	0
FRONT OF CENTERCORE PERMITS SOLID EFFLUX (1=YES, 0=NO)	0
STRONG BAG OPTION (1=YES, 0=NO)	0
CASE IS RIGIDIZED (1=YES, 0=NO)	0
PROGRESSIVE FRACTURE OPTION(0=NO; 1,2=YES)	0
FINAL MAIN CHARGE PROPELLANT TYPE	0
INCREMENT IS IGNITER(0=NO; 1=YES)	0
MASS OF MAIN CHARGE(KG)	11.8600
INITIAL POROSITY OF MAIN CHARGE(-)	0.0000
MASS OF CENTERCORE CHARGE(KG)	.1134
INITIAL POROSITY OF CENTERCORE CHARGE(-)	0.0000
INCREMENT STANDOFF(CM)	0.0000
STRENGTH OF BOND TO NEXT INCREMENT(N)	0.
FRACTURE STRENGTH OF STICK PROPELLANT IN	
PROGRESSIVE FRACTURE OPTION(MPA)	0.0
PERFORATION RELAXATION TIME(MSEC)	0.000

CONFIGURATION OF REAR OF BAG

AXIAL POS(CM)	RADIAL POS(CM)	THICKNESS (CM)	FLOW RES. DATA	REACTIVITY DATA	NO. PTS PRE-ASSIGNED	DATA (0=D, 1=N)
2.540	1.270	0.000	1	1	0	0
2.540	3.400	0.000	1	0	0	0
2.540	7.620	0.000	0	0	0	0

CONFIGURATION OF FRONT OF BAG

AXIAL POS(CM)	RADIAL POS(CM)	THICKNESS (CM)	FLOW RES. DATA	REACTIVITY DATA	NO. PTS PRE-ASSIGNED	DATA (0=D, 1=N)
78.740	1.270	0.000	2	0	0	0
78.740	7.620	0.000	0	0	0	0

CONFIGURATION OF INSIDE OF BAG

AXIAL POS(CM)	RADIAL POS(CM)	THICKNESS (CM)	FLOW RES. DATA	REACTIVITY DATA	NO. PTS PRE-ASSIGNED	DATA (0=D, 1=N)
2.540	1.270	0.000	3	0	0	0
78.740	1.270	0.000	0	0	0	0

CONFIGURATION OF OUTSIDE OF BAG

AXIAL POS(CM)	RADIAL POS(CM)	THICKNESS (CM)	FLOW RES. DATA	REACTIVITY DATA	NO. PTS PRE-ASSIGNED	DATA (0=D,1=N)
2.540	7.620	0.000	1	0	0	0
27.940	7.620	0.000	4	0	0	0
78.740	7.620	0.000	0	0	0	0

CONFIGURATION OF BREECH

AXIAL POSITION(CM)	RADIAL POSITION(CM)
0.000	0.000
0.000	7.060
-3.450	8.480

CONFIGURATION OF PROJECTILE BASE

AXIAL POSITION(CM)	RADIAL POSITION(CM)
87.380	0.000
87.380	7.140
96.420	7.850

CONFIGURATION OF INSIDE BOUNDARY

AXIAL POSITION(CM)	RADIAL POSITION(CM)
0.000	0.000
87.380	0.000

CONFIGURATION OF OUTSIDE BOUNDARY

AXIAL POSITION(CM)	RADIAL POSITION(CM)
-3.450	8.480
92.460	8.050
96.420	7.850

PROPERTIES OF PROJECTILE

PROJECTILE MASS(KG)	46.720
NUMBER OF ENTRIES IN BORE RESISTANCE TABLE	7
RESISTANCE LAW NUMBER	1
N.B. IF <1 OR >3, VALUE WILL DEFAULT TO 2 INTERNALLY	
NUMBER OF FILLER ELEMENTS	0
WALL HEAT LOSS OPTION (0=IGNORE, 1=PLATE, 2=TUBE, 3=SHELTON)	0
WALL TEMPERATURE UPDATE OPTION (0=IGNORE, 1=CUBIC, 2= CUBIC PLUS INV. EMB.)	0

BORE RESISTANCE DATA

PROJECTILE TRAVEL(CM)	RESISTIVE PRESSURE(MPA)
0.000	1.720
1.016	23.100
2.540	34.100
3.937	25.000
5.207	22.400
11.430	17.200
520.700	10.300

BAG SEGMENT MECHANICAL PROPERTIES

TYPE(-)	1	2	3	4
RUPTURE IF BED IGNITED (0=N, 1=Y)	1	0	0	0
INITIAL FRICTION FACTOR(-)	.010	101.000	101.000	101.000
MAX. PRESSURE DIFF.(MPA)	.300	.600	.600	.300
RUPTURE INTERVAL(MSEC)	0.000	2.000	2.000	0.000
THICKNESS(CM)	0.000	0.000	0.000	0.000
STRUCTURAL THICKNESS(CM)	0.000	0.000	0.000	0.000
DENSITY OF STRUCTURAL PART (GM/CC)	0.000	0.000	0.000	0.000
LONGITUDINAL TENSILE MODULUS (MPA)	0.000	0.000	0.000	0.000
LONGITUDINAL COMPRESSIVE MODULUS(MPA)	0.000	0.000	0.000	0.000
POISSON RATIO(-)	0.000	0.000	0.000	0.000
MAX. LONGITUDINAL STRESS(MPA)	0.000	0.000	0.000	0.000
COEFFICIENT OF FRICTION(-)	0.000	0.000	0.000	0.000

DATA TO DESCRIBE REACTIVITY OF BAG SUBSTRATE 1

ENERGY RELEASED DURING DECOMPOSITION(J/GM)	2489.
DENSITY OF DECOMPOSING SOLID-PHASE(GM/CC)	1.7990
RATIO OF SPECIFIC HEATS(-)	1.2430
MOLECULAR WEIGHT(GM/GMOL)	23.3600

BAG SUBSTRATE DISCHARGE CHARACTERISTICS

TIME(MSEC)	RATE OF DISCHARGE(GM/CM**2-SEC)
0.000	2.620
.100	26.200
30.000	26.200

LOCATION OF POINTS FOR PRESSURE SUMMARY TABLE

AXIAL LOCATION(CM)	WALL(0) OR AXIS(1)
.010	0
87.370	0

APPENDIX C

**INPUT DATA FOR NOMINAL SIMULATION OF M203E2 CHARGE
(SINGLE-INCREMENT REPRESENTATION)**

AD-A171 004

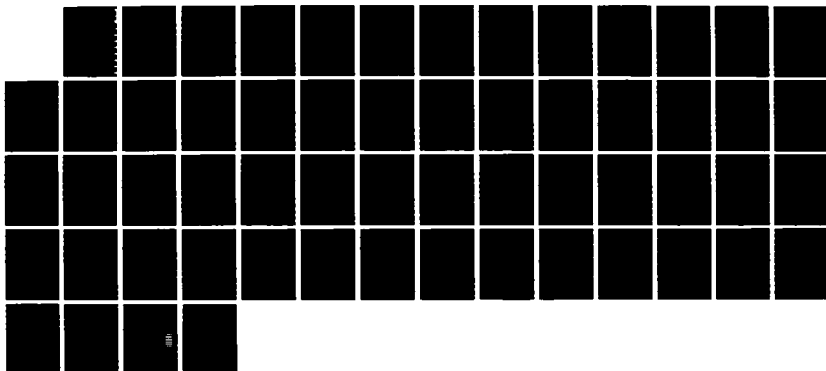
NUMERICAL SIMULATION OF CURRENT ARTILLERY CHARGES USING 3/3
THE TDNOVA CODE(U) GOUGH (PAUL) ASSOCIATES INC
PORTSMOUTH NH P S GOUGH JUN 86 BRL-CR-335

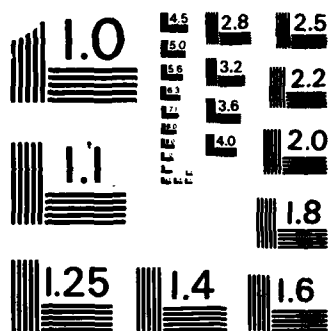
UNCLASSIFIED

DAAK11-83-C-0051

F/G 19/4

NL





MICROCOPY RESOLUTION TEST CHART
NATIONAL BUREAU OF STANDARDS-1963-A

CONTROL PARAMETERS

NPRINT (0=NO PRINT, 1=PRINT)	1
NSUMRY (0=NO SUMMARY TABLES, 1=YES)	2
NPLOT (0=NO ISOMETRIC CARPET PLOTS, 1=PLOT)	0
NVHL (0=HIDDEN LINES DELETED, 1=RETAINED)	0
NPLCON (0=NO CONTOUR PLOTS, 1=PLOT)	0
NPLFLO (0=NO FLOW PLOTS, 1=PLOT)	0
NPLFLM (0=NO FLAMESPREAD PLOT, 1=PLOT)	0
NDSKW (0=NO DISC SAVE, 1=DISC SAVE)	0
NDSKR (0=NO DISC START, >0=DISC START AT STEP NDSKR)	0

ISOMETRICALLY PLOTTED QUANTITIES (1=YES, 0=NO)

MESH 0	POROSITY 0	GRANULAR STRESS 0
PRESSURE 1	DENSITY 0	GAS AXIAL VELOCITY 0
SOLID AXIAL VELOCITY 0	GAS RADIAL VELOCITY 0	SOLID RADIAL VELOCITY 0
GAS TEMPERATURE 0	PARTICLE SURFACE TEMPERATURE 0	
PYROLYSIS PRODUCT MASS FRACTION 0		

CONTOUR PLOTTED QUANTITIES (1=YES, 0=NO)

MESH 0	POROSITY 0	GRANULAR STRESS 0
PRESSURE 1	DENSITY 0	GAS AXIAL VELOCITY 0
SOLID AXIAL VELOCITY 0	GAS RADIAL VELOCITY 0	SOLID RADIAL VELOCITY 0
GAS TEMPERATURE 0	PARTICLE SURFACE TEMPERATURE 0	
PYROLYSIS PRODUCT MASS FRACTION 0		
SCALE FACTOR FOR PLOTTING(-)		.40
LENGTH OF Z-AXIS IN CALCOMP PLOTS(IN)		12.00
LENGTH OF R-AXIS(IN)		4.00
LENGTH OF ORDINATE AXIS(IN)		5.00

LOGOUT PARAMETERS

PARAMETERS PRIOR TO Q-2-D TRANSFORMATION

NUMBER OF STEPS BEFORE LOGOUT	2000
N.B. A NEGATIVE ENTRY FOR THE ABOVE DATUM IMPLIES THAT VARIABLE LOGOUT SCHEDULING IS INTENDED.	
TIME INCREMENT BEFORE LOGOUT(MSEC)	.5000

PARAMETERS AFTER Q-2-D TRANSFORMATION

NUMBER OF STEPS BEFORE LOGOUT	2000
TIME INCREMENT BEFORE LOGOUT(MSEC)	1.0000

SUMMARY TABLE PARAMETERS

NUMBER OF PRESSURE SUMMARY STATIONS	2
TIME INCREMENT FOR PRESSURE SUMMARY STORAGE (MSEC)	.200
DEBUG PRINT REQUIRED (0=NO, 1=YES)	0
EXTENDED PRINT REQUIRED (0=NO, 1=YES)	0

TERMINATION PARAMETERS

MAXIMUM NUMBER OF STEPS BEFORE TERMINATION	2500
MAXIMUM INTEGRATION TIME(MSEC)	25.0000
MAXIMUM PROJECTILE TRAVEL (CM)	520.7

CHARGE REPRESENTATION PARAMETERS

NUMBER OF PROPELLANTS IN CHARGE	4
NUMBER OF BAGS IN CHARGE	1
MESH ALLOCATION MODE (0=STATIC, 1=DYNAMIC)	0
MAXIMUM NUMBER OF STORAGE POINTS FOR DYNAMIC MESH ALLOCATION	0
NUMBER OF MESH POINTS IN AXIAL DIRECTION	30
NUMBER OF MESH POINTS IN RADIAL DIRECTION	7
NUMBER OF ITERATIONS TO DETERMINE INITIAL MESH	200
EQUIPOTENTIAL (0) OR LAGRANGIAN (1) MESH	0
QUASI-TWO-DIMENSIONAL FLAMESPREADING (0=NO, 1=YES)	0
NEW(0) OR OLD (1) INTERPHASE DRAG AND HEAT TRANSFER FOR GRANULAR PROPELLANT	1
BED IGNITION RUPTURES CASE (0=NO, 1=YES) (GLOBAL OPTION)	0
SAFETY FACTOR FOR C-F-L CRITERION	1.1000
MAXIMUM FRACTIONAL DISPLACEMENT FOR CON- VERGENCE OF INITIAL MESH DISTRIBUTION	.100E-04
OVER-RELAXATION FACTOR FOR DETERMINATION OF INITIAL MESH DISTRIBUTION	1.600
PRESSURE TOLERANCE FACTOR FOR REDUCTION TO QUASI-TWO-DIMENSIONAL REPRESENTATION(-)	.010
AXIAL SPATIAL RESOLUTION FACTOR(-)	.100
RADIAL SPATIAL RESOLUTION FACTOR(-)	.100
SOURCE STABILITY FACTOR (-)	0.000
MAX. FRACT. OF TUBE FOR CENTERCORE IN Q2D(-)	0.000

AMBIENT CONDITIONS

INITIAL TEMPERATURE(DEG.K)	294.4
INITIAL PRESSURE(MPA)	.1014
INITIAL RATIO OF SPECIFIC HEATS(-)	1.40000
INITIAL MOLECULAR WEIGHT(GM/GM-MOL)	29.00000

PROPERTIES OF PROPELLANT TYPE 1 CBI

SOLID PHASE CONSTITUTIVE DATA

SETTLING POROSITY OF GRANULAR BED(-)	0.00000
SPEED OF COMPRESSION WAVE(M/SEC)	442.0
SPEED OF EXPANSION WAVE(M/SEC)	1270.0
DENSITY OF SOLID PHASE(GM/CC)	1.6500
THERMAL CONDUCTIVITY(J/CM-SEC-DEG.K)	.160000E-02
THERMAL DIFFUSIVITY(CM**2/SEC)	.600000E-03
LONGITUDINAL WAVE SPEED(M/SEC)	0.0
(STICK PROPELLANT ONLY)	
POISSON RATIO(-)	0.000
(STICK PROPELLANT ONLY)	

GAS PHASE CONSTITUTIVE DATA

RATIO OF SPECIFIC HEATS(-)	1.23400
MOLECULAR WEIGHT(GM/GM-MOL)	24.200
COVOLUME(CC/GM)	1.097

SOLID PHASE COMBUSTION CHARACTERISTICS

NUMBER OF BURN RATE DATA	1
EROSIVE EFFECT CONSIDERED (0=NO, 1=YES)	0
FINITE RATE CHEMISTRY (0=NO, 1=YES)	0
IGNITION TEMPERATURE(DEG.K)	300.0
CHEMICAL ENERGY(J/GM)	4372.
SURFACE FLAMESREAD DELAY(MSEC)	0.0000
EROSIVE PRE-EXPONENT(CM**2-DEG.K/N)	0.
EROSIVE EXPONENT(-)	0.000
FRACTION OF ENERGY RELEASED AT SURFACE(-)	0.000
GAS-PHASE ARRHENIUS PRE-EXPONENT	
((GM/CC)**(1-N)/SEC)	0.
GAS-PHASE ARRHENIUS EXPONENT(J/GM-MOL)	0.0
GAS-PHASE REACTION ORDER(-)	0.000
RATIO OF SPECIFIC HEATS OF FINAL PRODUCTS(-)	0.00000
MOLECULAR WEIGHT OF FINAL PRODUCTS(GM/GM-MOL)	0.000

MAX. PRESSURE (MPA)	BURN RATE ADDITIVE CONSTANT (CM/SEC)	PRE-EXPONENT (CM/SEC-MPA**BN)	EXPONENT (-)
690.00	0.00000	.40000	1.00000

GRAIN GEOMETRY

FORM (0=CYLINDER, 1=SPHERE, 2=SOLID STICK, 3=PERFORATED OR SLOTTED STICK)	0
EXTERNAL DIAMETER(CM)	.071
LENGTH(CM)	.013
DIAMETER OF PERFORATIONS(CM)	0.000
NUMBER OF PERFORATIONS(-)	0.
SLOT WIDTH(CM)	0.000
MAX. PERF. STRESS OR OVERPRESSURE(MPA)	0.000
NXSTR (IF 0, ABOVE VALUE IS HOOP STRESS. IF 1, VALUE IS OVERPRESSURE)	0

PROPERTIES OF PROPELLANT TYPE 2 MAIN CHARGE

SOLID PHASE CONSTITUTIVE DATA

SETTLING POROSITY OF GRANULAR BED(-)	0.00000
SPEED OF COMPRESSION WAVE(M/SEC)	152.4
SPEED OF EXPANSION WAVE(M/SEC)	1270.0
DENSITY OF SOLID PHASE(GM/CC)	1.6500
THERMAL CONDUCTIVITY(J/CM-SEC-DEG.K)	.160100E-02
THERMAL DIFFUSIVITY(CM**2/SEC)	.645200E-03
LONGITUDINAL WAVE SPEED(M/SEC) (STICK PROPELLANT ONLY)	1270.0
POISSON RATIO(-) (STICK PROPELLANT ONLY)	.500

GAS PHASE CONSTITUTIVE DATA

RATIO OF SPECIFIC HEATS(-)	1.26000
MOLECULAR WEIGHT(GM/GM-MOL)	22.200
COVOLUME(CC/GM)	1.084

SOLID PHASE COMBUSTION CHARACTERISTICS

NUMBER OF BURN RATE DATA	1
EROSIVE EFFECT CONSIDERED (0=NO, 1=YES)	0
FINITE RATE CHEMISTRY (0=NO, 1=YES)	0
IGNITION TEMPERATURE(DEG.K)	445.0
CHEMICAL ENERGY(J/GM)	3794.
SURFACE FLAMESREAD DELAY(MSEC)	0.0000
EROSIVE PRE-EXPONENT(CM**2-DEG.K/N)	0.
EROSIVE EXPONENT(-)	0.000
FRACTION OF ENERGY RELEASED AT SURFACE(-)	0.000
GAS-PHASE ARRHENIUS PRE-EXPONENT ((GM/CC)**(1-N)/SEC)	0.
GAS-PHASE ARRHENIUS EXPONENT(J/GM-MOL)	0.0
GAS-PHASE REACTION ORDER(-)	0.000
RATIO OF SPECIFIC HEATS OF FINAL PRODUCTS(-)	0.00000
MOLECULAR WEIGHT OF FINAL PRODUCTS(GM/GM-MOL)	0.000

MAX. PRESSURE (MPA)	BURN RATE ADDITIVE CONSTANT (CM/SEC)	PRE-EXPONENT (CM/SEC-MPA**BN)	EXPONENT (-)
690.00	0.00000	.23672	.70000

GRAIN GEOMETRY

FORM (0=CYLINDER, 1=SPHERE, 2=SOLID STICK, 3=PERFORATED OR SLOTTED STICK)	3
EXTERNAL DIAMETER(CM)	.640
LENGTH(CM)	73.660
DIAMETER OF PERFORATIONS(CM)	.234
NUMBER OF PERFORATIONS(-)	1.
SLOT WIDTH(CM)	.025
MAX. PERF. STRESS OR OVERPRESSURE(MPA)	-1000.000
NISTR (IF 0, ABOVE VALUE IS HOOP STRESS. IF 1, VALUE IS OVERPRESSURE)	0

PROPERTIES OF PROPELLANT TYPE 3 CASE MATERIAL

SOLID PHASE CONSTITUTIVE DATA

SETTLING POROSITY OF GRANULAR BED(-)	0.00000
SPEED OF COMPRESSION WAVE(M/SEC)	152.4
SPEED OF EXPANSION WAVE(M/SEC)	1270.0
DENSITY OF SOLID PHASE(GM/CC)	1.0000
THERMAL CONDUCTIVITY(J/CM-SEC-DEG.K)	.160100E-02
THERMAL DIFFUSIVITY(CM**2/SEC)	.645200E-03
LONGITUDINAL WAVE SPEED(M/SEC)	1270.0
(STICK PROPELLANT ONLY)	
POISSON RATIO(-)	.500
(STICK PROPELLANT ONLY)	

GAS PHASE CONSTITUTIVE DATA

RATIO OF SPECIFIC HEATS(-)	1.27500
MOLECULAR WEIGHT(GM/GM-MOL)	21.400
COVOLUME(CC/GM)	1.180

SOLID PHASE COMBUSTION CHARACTERISTICS

NUMBER OF BURN RATE DATA	1
EROSIVE EFFECT CONSIDERED (0=NO, 1=YES)	0
FINITE RATE CHEMISTRY (0=NO, 1=YES)	0
IGNITION TEMPERATURE(DEG.K)	300.0
CHEMICAL ENERGY(J/GM)	2350.
SURFACE FLAMES PREAD DELAY(MSEC)	0.0000
EROSIVE PRE-EXPONENT(CM**2-DEG.K/N)	0.
EROSIVE EXPONENT(-)	0.000
FRACTION OF ENERGY RELEASED AT SURFACE(-)	0.000
GAS-PHASE ARRHENIUS PRE-EXPONENT ((GM/CC)**(1-N)/SEC)	0.
GAS-PHASE ARRHENIUS EXPONENT(J/GM-MOL)	0.0
GAS-PHASE REACTION ORDER(-)	0.000
RATIO OF SPECIFIC HEATS OF FINAL PRODUCTS(-)	0.00000
MOLECULAR WEIGHT OF FINAL PRODUCTS(GM/GM-MOL)	0.000

MAX. PRESSURE (MPA)	BURN RATE ADDITIVE CONSTANT (CM/SEC)	PRE-EXPONENT (CM/SEC-MPA**BN)	EXPONENT (-)
690.00	0.00000	.04000	1.28700

GRAIN GEOMETRY

FORM (0=CYLINDER, 1=SPHERE, 2=SOLID STICK, 3=PERFORATED OR SLOTTED STICK)	0
EXTERNAL DIAMETER(CM)	0.000
LENGTH(CM)	0.000
DIAMETER OF PERFORATIONS(CM)	0.000
NUMBER OF PERFORATIONS(-)	0.
SLOT WIDTH(CM)	0.000
MAX. PERF. STRESS OR OVERPRESSURE(MPA)	0.000
NXSTR (IF 0, ABOVE VALUE IS HOOP STRESS. IF 1, VALUE IS OVERPRESSURE)	0

PROPERTIES OF PROPELLANT TYPE 4 CASE MATERIAL

SOLID PHASE CONSTITUTIVE DATA

SETTLING POROSITY OF GRANULAR BED(-)	0.00000
SPEED OF COMPRESSION WAVE(M/SEC)	152.4
SPEED OF EXPANSION WAVE(M/SEC)	1270.0
DENSITY OF SOLID PHASE(GM/CC)	1.0000
THERMAL CONDUCTIVITY(J/CM-SEC-DEG.K)	.160100E-02
THERMAL DIFFUSIVITY(CM**2/SEC)	.645200E-03
LONGITUDINAL WAVE SPEED(M/SEC)	1270.0
(STICK PROPELLANT ONLY)	
POISSON RATIO(-)	.500
(STICK PROPELLANT ONLY)	

GAS PHASE CONSTITUTIVE DATA

RATIO OF SPECIFIC HEATS(-)	1.26000
MOLECULAR WEIGHT(GM/GM-MOL)	24.000
COVOLUME(CC/GM)	.920

SOLID PHASE COMBUSTION CHARACTERISTICS

NUMBER OF BURN RATE DATA	1
EROSIVE EFFECT CONSIDERED (0=NO, 1=YES)	0
FINITE RATE CHEMISTRY (0=NO, 1=YES)	0
IGNITION TEMPERATURE(DEG.K)	300.0
CHEMICAL ENERGY(J/GM)	1880.
SURFACE FLAMESPREAD DELAY(MSEC)	0.0000
EROSIVE PRE-EXPONENT(CM**2-DEG.K/N)	0.
EROSIVE EXPONENT(-)	0.000
FRACTION OF ENERGY RELEASED AT SURFACE(-)	0.000
GAS-PHASE ARRHENIUS PRE-EXPONENT ((GM/CC)**(1-N)/SEC)	0.
GAS-PHASE ARRHENIUS EXPONENT(J/GM-MOL)	0.0
GAS-PHASE REACTION ORDER(-)	0.000
RATIO OF SPECIFIC HEATS OF FINAL PRODUCTS(-)	0.00000
MOLECULAR WEIGHT OF FINAL PRODUCTS(GM/GM-MOL)	0.000

MAX. PRESSURE (MPA)	BURN RATE ADDITIVE CONSTANT (CM/SEC)	PRE-EXPONENT (CM/SEC-MPA**BN)	EXPONENT (-)
690.00	0.00000	.04000	1.28700

GRAIN GEOMETRY

FORM (0=CYLINDER, 1=SPHERE, 2=SOLID STICK, 3=PERFORATED OR SLOTTED STICK)	0
EXTERNAL DIAMETER(CM)	0.000
LENGTH(CM)	0.000
DIAMETER OF PERFORATIONS(CM)	0.000
NUMBER OF PERFORATIONS(-)	0.
SLOT WIDTH(CM)	0.000
MAX. PERF. STRESS OR OVERPRESSURE(MPA)	0.000
NXSTR (IF 0, ABOVE VALUE IS HOOP STRESS. IF 1, VALUE IS OVERPRESSURE)	0

PROPERTIES OF BAG NUMBER 1

MAIN CHARGE PROPELLANT TYPE	2
CENTERCORE IGNITER PROPELLANT TYPE	0
REAR BASEPAD REACTIVITY DATA	0
FORWARD BASEPAD REACTIVITY DATA	0
REAR OF CENTERCORE PERMITS SOLID EFFLUX (1=YES, 0=NO)	0
FRONT OF CENTERCORE PERMITS SOLID EFFLUX (1=YES, 0=NO)	0
STRONG BAG OPTION (1=YES, 0=NO)	0
CASE IS RIGIDIZED (1=YES, 0=NO)	1
PROGRESSIVE FRACTURE OPTION(0=NO; 1,2=YES)	0
FINAL MAIN CHARGE PROPELLANT TYPE	0
INCREMENT IS IGNITER(0=NO; 1=YES)	0
MASS OF MAIN CHARGE(KG)	12.7000
INITIAL POROSITY OF MAIN CHARGE(-)	0.0000
MASS OF CENTERCORE CHARGE(KG)	0.0000
INITIAL POROSITY OF CENTERCORE CHARGE(-)	0.0000
INCREMENT STANDOFF(CM)	2.5400
STRENGTH OF BOND TO NEXT INCREMENT(N)	0.
FRACTURE STRENGTH OF STICK PROPELLANT IN PROGRESSIVE FRACTURE OPTION(MPA)	0.0
PERFORATION RELAXATION TIME(MSEC)	0.000

CONFIGURATION OF REAR OF BAG

AXIAL POS (CM)	RADIAL POS (CM)	THICKNESS (CM)	FLOW RES. DATA	REACTIVITY DATA	NO. PTS PRE-ASSIGNED	DATA (0=D, 1=N)
2.240	0.000	.940	6	224	0	0
2.240	2.540	.940	6	224	0	0
2.240	7.940	.940	0	0	0	0

CONFIGURATION OF FRONT OF BAG

AXIAL POS (CM)	RADIAL POS (CM)	THICKNESS (CM)	FLOW RES. DATA	REACTIVITY DATA	NO. PTS PRE-ASSIGNED	DATA (0=D, 1=N)
76.210	0.000	.320	4	330	0	0
76.210	2.540	.320	4	330	0	0
76.210	7.940	.320	0	0	0	0

CONFIGURATION OF INSIDE OF BAG

AXIAL POS (CM)	RADIAL POS (CM)	THICKNESS (CM)	FLOW RES. DATA	REACTIVITY DATA	NO. PTS PRE-ASSIGNED	DATA (0=D, 1=N)
2.240	0.000	0.000	0	0	0	0
76.210	0.000	0.000	0	0	0	0

CONFIGURATION OF OUTSIDE OF BAG

AXIAL POS (CM)	RADIAL POS (CM)	THICKNESS (CM)	FLOW RES. DATA	REACTIVITY DATA	NO. PTS PRE-ASSIGNED	DATA (0=D, 1=N)
2.240	7.940	.320	5	330	0	0
76.210	7.940	.320	0	0	0	0

CONFIGURATION OF BREECH

AXIAL POSITION (CM)	RADIAL POSITION (CM)
0.000	0.000
0.000	7.060
-3.450	8.480

CONFIGURATION OF PROJECTILE BASE

AXIAL POSITION (CM)	RADIAL POSITION (CM)
87.380	0.000
87.380	7.140
96.420	7.850

CONFIGURATION OF INSIDE BOUNDARY

AXIAL POSITION(CM)	RADIAL POSITION(CM)
0.000	0.000
87.380	0.000

CONFIGURATION OF OUTSIDE BOUNDARY

AXIAL POSITION(CM)	RADIAL POSITION(CM)
-3.450	8.480
92.460	8.050
96.420	7.850

PROPERTIES OF PROJECTILE

PROJECTILE MASS(KG)	46.720
NUMBER OF ENTRIES IN BORE RESISTANCE TABLE	7
RESISTANCE LAW NUMBER	1
N.B. IF <1 OR >3, VALUE WILL DEFAULT TO 2 INTERNALLY	
NUMBER OF FILLER ELEMENTS	0
WALL HEAT LOSS OPTION (0=IGNORE, 1=PLATE, 2=TUBE, 3=SHELTON)	0
WALL TEMPERATURE UPDATE OPTION (0=IGNORE, 1=CUBIC, 2=CUBIC PLUS INV. EMB.)	0

BORE RESISTANCE DATA

PROJECTILE TRAVEL(CM)	RESISTIVE PRESSURE(MPA)
0.000	1.720
1.016	23.100
2.540	34.100
3.937	25.000
5.207	22.400
11.430	17.200
520.700	10.300

BAG SEGMENT MECHANICAL PROPERTIES

TYPE(-)	1	2	3	4	5	6
RUPTURE IF BED IGNITED (0=N, 1=Y)	0	0	0	0	0	0
INITIAL FRICTION FACTOR(-)	101.000	10.000	101.000	101.000	101.000	10.000
MAX. PRESSURE DIFF. (MPA)	.860	.860	.860	.860	.860	.860
RUPTURE INTERVAL (MSEC)	0.000	0.000	0.000	0.000	0.000	0.000
THICKNESS(CM)	.320	.320	.320	.320	.320	.940
STRUCTURAL THICKNESS (CM)	.320	.320	.320	.320	.320	.320
DENSITY OF STRUCTURAL PART (GM/CC)	1.000	1.000	1.000	1.000	1.000	1.000
LONGITUDINAL TENSILE MODULUS (MPA)	1000.000	1000.000	1000.000	1000.000	1000.000	1000.000
LONGITUDINAL COMPRESSIVE MODULUS(MPA)	1000.000	1000.000	1000.000	1000.000	1000.000	1000.000
POISSON RATIO(-)	.500	.500	.500	.500	.500	.500
MAX. LONGITUDINAL STRESS (MPA)	20.680	20.680	20.680	20.680	20.680	20.680
COEFFICIENT OF FRICTION(-)	.500	.500	.500	.500	.500	.500

DATA TO DESCRIBE REACTIVITY OF BAG SUBSTRATE 1

ENERGY RELEASED DURING DECOMPOSITION(J/GM)	1352.
DENSITY OF DECOMPOSING SOLID-PHASE(GM/CC)	1.7990
RATIO OF SPECIFIC HEATS(-)	1.2190
MOLECULAR WEIGHT(GM/GMOL)	34.8600

BAG SUBSTRATE DISCHARGE CHARACTERISTICS

TIME(MSEC)	RATE OF DISCHARGE(GM/CM**2-SEC)
0.000	1.000
.100	98.000
10.000	98.000

DATA TO DESCRIBE REACTIVITY OF BAG SUBSTRATE 2

ENERGY RELEASED DURING DECOMPOSITION(J/GM)	2350.
DENSITY OF DECOMPOSING SOLID-PHASE(GM/CC)	1.0000
RATIO OF SPECIFIC HEATS(-)	1.2750
MOLECULAR WEIGHT(GM/GMOL)	23.0000

BAG SUBSTRATE DISCHARGE CHARACTERISTICS

TIME(MSEC)	RATE OF DISCHARGE(GM/CM**2-SEC)
0.000	1.000
1.000	5.000
5.000	5.000

DATA TO DESCRIBE REACTIVITY OF BAG SUBSTRATE 3

ENERGY RELEASED DURING DECOMPOSITION(J/GM)	1880.
DENSITY OF DECOMPOSING SOLID-PHASE(GM/CC)	1.0000
RATIO OF SPECIFIC HEATS(-)	1.2600
MOLECULAR WEIGHT(GM/GMOL)	24.0000

BAG SUBSTRATE DISCHARGE CHARACTERISTICS

TIME(MSEC)	RATE OF DISCHARGE(GM/CM**2-SEC)
0.000	1.000
1.000	5.000
5.000	5.000

DATA TO DESCRIBE REACTIVITY OF BAG SUBSTRATE 4

ENERGY RELEASED DURING DECOMPOSITION(J/GM)	4372.
DENSITY OF DECOMPOSING SOLID-PHASE(GM/CC)	1.6500
RATIO OF SPECIFIC HEATS(-)	1.2340
MOLECULAR WEIGHT(GM/GMOL)	24.2000

BAG SUBSTRATE DISCHARGE CHARACTERISTICS

TIME(MSEC)	RATE OF DISCHARGE(GM/CM**2-SEC)
0.000	1.000
1.000	50.000
10.000	50.000

LOCATION OF POINTS FOR PRESSURE SUMMARY TABLE

AXIAL LOCATION(CM)	WALL(0) OR AXIS(1)
.010	0
87.370	0

APPENDIX D

**INPUT DATA FOR NOMINAL SIMULATION OF M203E2 CHARGE
(TWO-INCREMENT REPRESENTATION)**

CONTROL PARAMETERS

NPRINT (0=NO PRINT, 1=PRINT)	1
NSUMRY (0=NO SUMMARY TABLES, 1=YES)	2
NPLOT (0=NO ISOMETRIC CARPET PLOTS, 1=PLOT)	1
NVHL (0=HIDDEN LINES DELETED, 1=RETAINED)	0
NPLCON (0=NO CONTOUR PLOTS, 1=PLOT)	0
NPLFLO (0=NO FLOW PLOTS, 1=PLOT)	1
NPLFLM (0=NO FLAMESPREAD PLOT, 1=PLOT)	1
NDSKW (0=NO DISC SAVE, 1=DISC SAVE)	0
NDSKR (0=NO DISC START, >0=DISC START AT STEP NDSKR)	0

ISOMETRICALLY PLOTTED QUANTITIES (1=YES, 0=NO)

MESH 0	POROSITY 0	GRANULAR STRESS 0
PRESSURE 1	DENSITY 0	GAS AXIAL VELOCITY 0
SOLID AXIAL VELOCITY 0	GAS RADIAL VELOCITY 0	SOLID RADIAL VELOCITY 0
GAS TEMPERATURE 0	PARTICLE SURFACE TEMPERATURE 0	
PYROLYSIS PRODUCT MASS FRACTION 0		

CONTOUR PLOTTED QUANTITIES (1=YES, 0=NO)

MESH 0	POROSITY 0	GRANULAR STRESS 0
PRESSURE 1	DENSITY 0	GAS AXIAL VELOCITY 0
SOLID AXIAL VELOCITY 0	GAS RADIAL VELOCITY 0	SOLID RADIAL VELOCITY 0
GAS TEMPERATURE 0	PARTICLE SURFACE TEMPERATURE 0	
PYROLYSIS PRODUCT MASS FRACTION 0		

SCALE FACTOR FOR PLOTTING(-)	.40
LENGTH OF Z-AXIS IN CALCOMP PLOTS(IN)	12.00
LENGTH OF R-AXIS(IN)	4.00
LENGTH OF ORDINATE AXIS(IN)	5.00

LOGOUT PARAMETERS

PARAMETERS PRIOR TO Q-2-D TRANSFORMATION

NUMBER OF STEPS BEFORE LOGOUT	2000
N.B. A NEGATIVE ENTRY FOR THE ABOVE DATUM IMPLIES THAT VARIABLE LOGOUT SCHEDULING IS INTENDED.	
TIME INCREMENT BEFORE LOGOUT(MSEC)	.5000

PARAMETERS AFTER Q-2-D TRANSFORMATION

NUMBER OF STEPS BEFORE LOGOUT	2000
TIME INCREMENT BEFORE LOGOUT(MSEC)	1.0000

SUMMARY TABLE PARAMETERS

NUMBER OF PRESSURE SUMMARY STATIONS	2
TIME INCREMENT FOR PRESSURE SUMMARY STORAGE (MSEC)	.200
DEBUG PRINT REQUIRED (0=NO, 1=YES)	0
EXTENDED PRINT REQUIRED (0=NO, 1=YES)	0

TERMINATION PARAMETERS

MAXIMUM NUMBER OF STEPS BEFORE TERMINATION	2500
MAXIMUM INTEGRATION TIME(MSEC)	25.0000
MAXIMUM PROJECTILE TRAVEL (CM)	520.7

CHARGE REPRESENTATION PARAMETERS

NUMBER OF PROPELLANTS IN CHARGE	4
NUMBER OF BAGS IN CHARGE	2
MESH ALLOCATION MODE (0=STATIC, 1=DYNAMIC)	0
MAXIMUM NUMBER OF STORAGE POINTS FOR DYNAMIC MESH ALLOCATION	0
NUMBER OF MESH POINTS IN AXIAL DIRECTION	30
NUMBER OF MESH POINTS IN RADIAL DIRECTION	7
NUMBER OF ITERATIONS TO DETERMINE INITIAL MESH	200
EQUIPOTENTIAL (0) OR LAGRANGIAN (1) MESH	0
QUASI-TWO-DIMENSIONAL FLAMESPREADING (0=NO, 1=YES)	0
NEW(0) OR OLD (1) INTERPHASE DRAG AND HEAT TRANSFER FOR GRANULAR PROPELLANT	1
BED IGNITION RUPTURES CASE (0=NO, 1=YES) (GLOBAL OPTION)	0
SAFETY FACTOR FOR C-F-L CRITERION	1.1000
MAXIMUM FRACTIONAL DISPLACEMENT FOR CON- VERGENCE OF INITIAL MESH DISTRIBUTION	.100E-04
OVER-RELAXATION FACTOR FOR DETERMINATION OF INITIAL MESH DISTRIBUTION	1.600
PRESSURE TOLERANCE FACTOR FOR REDUCTION TO QUASI-TWO-DIMENSIONAL REPRESENTATION(-)	.050
AXIAL SPATIAL RESOLUTION FACTOR(-)	.100
RADIAL SPATIAL RESOLUTION FACTOR(-)	.100
SOURCE STABILITY FACTOR (-)	0.000
MAX. FRACT. OF TUBE FOR CENTERCORE IN Q2D(-)	0.000

AMBIENT CONDITIONS

INITIAL TEMPERATURE(DEG.K)	294.4
INITIAL PRESSURE(MPA)	.1014
INITIAL RATIO OF SPECIFIC HEATS(-)	1.40000
INITIAL MOLECULAR WEIGHT(GM/GM-MOL)	29.00000

PROPERTIES OF PROPELLANT TYPE 1 CBI

SOLID PHASE CONSTITUTIVE DATA

SETTLING POROSITY OF GRANULAR BED(-)	1.00000
SPEED OF COMPRESSION WAVE(M/SEC)	1270.0
SPEED OF EXPANSION WAVE(M/SEC)	1270.0
DENSITY OF SOLID PHASE(GM/CC)	1.6500
THERMAL CONDUCTIVITY(J/CM-SEC-DEG.K)	.160000E-02
THERMAL DIFFUSIVITY(CM**2/SEC)	.600000E-03
LONGITUDINAL WAVE SPEED(M/SEC)	0.0
(STICK PROPELLANT ONLY)	
POISSON RATIO(-)	0.000
(STICK PROPELLANT ONLY)	

GAS PHASE CONSTITUTIVE DATA

RATIO OF SPECIFIC HEATS(-)	1.23400
MOLECULAR WEIGHT(GM/GM-MOL)	24.200
COVOLUME(CC/GM)	1.097

SOLID PHASE COMBUSTION CHARACTERISTICS

NUMBER OF BURN RATE DATA	1
EROSIVE EFFECT CONSIDERED (0=NO, 1=YES)	0
FINITE RATE CHEMISTRY (0=NO, 1=YES)	0
IGNITION TEMPERATURE(DEG.K)	300.0
CHEMICAL ENERGY(J/GM)	4372.
SURFACE FLAMESREAD DELAY(MSEC)	0.0000
EROSIVE PRE-EXPONENT(CM**2-DEG.K/N)	0.
EROSIVE EXPONENT(-)	0.000
FRACTION OF ENERGY RELEASED AT SURFACE(-)	0.000
GAS-PHASE ARRHENIUS PRE-EXPONENT	
((GM/CC)**(1-N)/SEC)	0.
GAS-PHASE ARRHENIUS EXPONENT(J/GM-MOL)	0.0
GAS-PHASE REACTION ORDER(-)	0.000
RATIO OF SPECIFIC HEATS OF FINAL PRODUCTS(-)	0.00000
MOLECULAR WEIGHT OF FINAL PRODUCTS(GM/GM-MOL)	0.000

MAX. PRESSURE (MPA)	BURN RATE ADDITIVE CONSTANT (CM/SEC)	PRE-EXPONENT (CM/SEC-MPA**BN)	EXPONENT (-)
690.00	0.00000	.40000	1.00000

GRAIN GEOMETRY

FORM (0-CYLINDER, 1-SPHERE, 2-SOLID STICK, 3-PERFORATED OR SLOTTED STICK)	0
EXTERNAL DIAMETER(CM)	.071
LENGTH(CM)	.013
DIAMETER OF PERFORATIONS(CM)	0.000
NUMBER OF PERFORATIONS(-)	0.
SLOT WIDTH(CM)	0.000
MAX. PERF. STRESS OR OVERPRESSURE(MPA)	0.000
NISTR (IF 0, ABOVE VALUE IS HOOP STRESS. IF 1, VALUE IS OVERPRESSURE)	0

PROPERTIES OF PROPELLANT TYPE 2 M31

SOLID PHASE CONSTITUTIVE DATA

SETTLING POROSITY OF GRANULAR BED(-)	0.00000
SPEED OF COMPRESSION WAVE(M/SEC)	152.4
SPEED OF EXPANSION WAVE(M/SEC)	1270.0
DENSITY OF SOLID PHASE(GM/CC)	1.6500
THERMAL CONDUCTIVITY(J/CM-SEC-DEG.K)	.160100E-02
THERMAL DIFFUSIVITY(CM**2/SEC)	.645200E-03
LONGITUDINAL WAVE SPEED(M/SEC)	1270.0
(STICK PROPELLANT ONLY)	
POISSON RATIO(-)	.500
(STICK PROPELLANT ONLY)	

GAS PHASE CONSTITUTIVE DATA

RATIO OF SPECIFIC HEATS(-)	1.26000
MOLECULAR WEIGHT(GM/GM-MOL)	22.200
COVOLUME(CC/GM)	1.084

SOLID PHASE COMBUSTION CHARACTERISTICS

NUMBER OF BURN RATE DATA	1
EROSIVE EFFECT CONSIDERED (0=NO, 1=YES)	0
FINITE RATE CHEMISTRY (0=NO, 1=YES)	0
IGNITION TEMPERATURE(DEG.K)	445.0
CHEMICAL ENERGY(J/GM)	3794.
SURFACE FLAMESREAD DELAY(MSEC)	0.0000
EROSIVE PRE-EXPONENT(CM**2-DEG.K/N)	0.
EROSIVE EXPONENT(-)	0.000
FRACTION OF ENERGY RELEASED AT SURFACE(-)	0.000
GAS-PHASE ARRHENIUS PRE-EXPONENT ((GM/CC)**(1-N)/SEC)	0.
GAS-PHASE ARRHENIUS EXPONENT(J/GM-MOL)	0.0
GAS-PHASE REACTION ORDER(-)	0.000
RATIO OF SPECIFIC HEATS OF FINAL PRODUCTS(-)	0.00000
MOLECULAR WEIGHT OF FINAL PRODUCTS(GM/GM-MOL)	0.000

MAX. PRESSURE (MPA)	BURN RATE ADDITIVE CONSTANT (CM/SEC)	PRE-EXPONENT (CM/SEC-MPA**BN)	EXPONENT (-)
690.00	0.00000	.23672	.70000

GRAIN GEOMETRY

FORM (0-CYLINDER, 1-SPHERE, 2-SOLID STICK, 3-PERFORATED OR SLOTTED STICK)	3
EXTERNAL DIAMETER(CM)	.640
LENGTH(CM)	73.660
DIAMETER OF PERFORATIONS(CM)	.234
NUMBER OF PERFORATIONS(-)	1.
SLOT WIDTH(CM)	.025
MAX. PERF. STRESS OR OVERPRESSURE(MPA)	-1000.000
NXSTR (IF 0, ABOVE VALUE IS HOOP STRESS. IF 1, VALUE IS OVERPRESSURE)	0

PROPERTIES OF PROPELLANT TYPE 3 72% NC CASE

SOLID PHASE CONSTITUTIVE DATA

SETTLING POROSITY OF GRANULAR BED(-)	0.00000
SPEED OF COMPRESSION WAVE(M/SEC)	152.4
SPEED OF EXPANSION WAVE(M/SEC)	1270.0
DENSITY OF SOLID PHASE(GM/CC)	1.0000
THERMAL CONDUCTIVITY(J/CM-SEC-DEG.K)	.160100E-02
THERMAL DIFFUSIVITY(CM**2/SEC)	.645200E-03
LONGITUDINAL WAVE SPEED(M/SEC) (STICK PROPELLANT ONLY)	1270.0
POISSON RATIO(-) (STICK PROPELLANT ONLY)	.500

GAS PHASE CONSTITUTIVE DATA

RATIO OF SPECIFIC HEATS(-)	1.27500
MOLECULAR WEIGHT(GM/GM-MOL)	21.400
COVOLUME(CC/GM)	1.180

SOLID PHASE COMBUSTION CHARACTERISTICS

NUMBER OF BURN RATE DATA	1
EROSIVE EFFECT CONSIDERED (0=NO, 1=YES)	0
FINITE RATE CHEMISTRY (0=NO, 1=YES)	0
IGNITION TEMPERATURE(DEG.K)	300.0
CHEMICAL ENERGY(J/GM)	2350.
SURFACE FLAMES PREAD DELAY(MSEC)	0.0000
EROSIVE PRE-EXPONENT(CM**2-DEG.K/N)	0.
EROSIVE EXPONENT(-)	0.000
FRACTION OF ENERGY RELEASED AT SURFACE(-)	0.000
GAS-PHASE ARRHENIUS PRE-EXPONENT ((GM/CC)**(1-N)/SEC)	0.
GAS-PHASE ARRHENIUS EXPONENT(J/GM-MOL)	0.0
GAS-PHASE REACTION ORDER(-)	0.000
RATIO OF SPECIFIC HEATS OF FINAL PRODUCTS(-)	0.00000
MOLECULAR WEIGHT OF FINAL PRODUCTS(GM/GM-MOL)	0.000

MAX. PRESSURE (MPA)	BURN RATE ADDITIVE CONSTANT (CM/SEC)	PRE-EXPONENT (CM/SEC-MPA**BN)	EXPONENT (-)
690.00	0.00000	.04000	1.28700

GRAIN GEOMETRY

FORM (0=CYLINDER, 1=SPHERE, 2=SOLID STICK, 3=PERFORATED OR SLOTTED STICK)	0
EXTERNAL DIAMETER(CM)	0.000
LENGTH(CM)	0.000
DIAMETER OF PERFORATIONS(CM)	0.000
NUMBER OF PERFORATIONS(-)	0.
SLOT WIDTH(CM)	0.000
MAX. PERF. STRESS OR OVERPRESSURE(MPA)	0.000
NXSTR (IF 0, ABOVE VALUE IS HOOP STRESS. IF 1, VALUE IS OVERPRESSURE)	0

PROPERTIES OF PROPELLANT TYPE 4 52% NC CASE

SOLID PHASE CONSTITUTIVE DATA

SETTLING POROSITY OF GRANULAR BED(-)	0.00000
SPEED OF COMPRESSION WAVE(M/SEC)	152.4
SPEED OF EXPANSION WAVE(M/SEC)	1270.0
DENSITY OF SOLID PHASE(GM/CC)	1.0000
THERMAL CONDUCTIVITY(J/CM-SEC-DEG.K)	.160100E-02
THERMAL DIFFUSIVITY(CM**2/SEC)	.645200E-03
LONGITUDINAL WAVE SPEED(M/SEC)	1270.0
(STICK PROPELLANT ONLY)	
POISSON RATIO(-)	.500
(STICK PROPELLANT ONLY)	

GAS PHASE CONSTITUTIVE DATA

RATIO OF SPECIFIC HEATS(-)	1.26000
MOLECULAR WEIGHT(GM/GM-MOL)	24.000
COVOLUME(CC/GM)	.920

SOLID PHASE COMBUSTION CHARACTERISTICS

NUMBER OF BURN RATE DATA	1
EROSIVE EFFECT CONSIDERED (0=NO, 1=YES)	0
FINITE RATE CHEMISTRY (0=NO, 1=YES)	0
IGNITION TEMPERATURE(DEG.K)	300.0
CHEMICAL ENERGY(J/GM)	1880.
SURFACE FLAMESREAD DELAY(MSEC)	0.0000
EROSIVE PRE-EXPONENT(CM**2-DEG.K/N)	0.
EROSIVE EXPONENT(-)	0.000
FRACTION OF ENERGY RELEASED AT SURFACE(-)	0.000
GAS-PHASE ARRHENIUS PRE-EXPONENT ((GM/CC)**(1-N)/SEC)	0.
GAS-PHASE ARRHENIUS EXPONENT(J/GM-MOL)	0.0
GAS-PHASE REACTION ORDER(-)	0.000
RATIO OF SPECIFIC HEATS OF FINAL PRODUCTS(-)	0.00000
MOLECULAR WEIGHT OF FINAL PRODUCTS(GM/GM-MOL)	0.000

MAX. PRESSURE (MPA)	BURN RATE ADDITIVE CONSTANT (CM/SEC)	PRE-EXPONENT (CM/SEC-MPA**BN)	EXPONENT (-)
690.00	0.00000	.04000	1.28700

GRAIN GEOMETRY

FORM (0=CYLINDER, 1=SPHERE, 2=SOLID STICK, 3=PERFORATED OR SLOTTED STICK)	0
EXTERNAL DIAMETER(CM)	0.000
LENGTH(CM)	0.000
DIAMETER OF PERFORATIONS(CM)	0.000
NUMBER OF PERFORATIONS(-)	0.
SLOT WIDTH(CM)	0.000
MAX. PERF. STRESS OR OVERPRESSURE(MPA)	0.000
NXSTR (IF 0, ABOVE VALUE IS HOOP STRESS. IF 1, VALUE IS OVERPRESSURE)	0

PROPERTIES OF BAG NUMBER 1

MAIN CHARGE PROPELLANT TYPE	1
CENTERCORE IGNITER PROPELLANT TYPE	0
REAR BASEPAD REACTIVITY DATA	0
FORWARD BASEPAD REACTIVITY DATA	0
REAR OF CENTERCORE PERMITS SOLID EFFLUX (1=YES, 0=NO)	0
FRONT OF CENTERCORE PERMITS SOLID EFFLUX (1=YES, 0=NO)	0
STRONG BAG OPTION (1=YES, 0=NO)	0
CASE IS RIGIDIZED (1=YES, 0=NO)	1
PROGRESSIVE FRACTURE OPTION(0=NO; 1,2=YES)	0
FINAL MAIN CHARGE PROPELLANT TYPE	0
INCREMENT IS IGNITER(0=NO; 1=YES)	1
MASS OF MAIN CHARGE(KG)	.0283
INITIAL POROSITY OF MAIN CHARGE(-)	0.0000
MASS OF CENTERCORE CHARGE(KG)	0.0000
INITIAL POROSITY OF CENTERCORE CHARGE(-)	0.0000
INCREMENT STANDOFF(CM)	2.5400
STRENGTH OF BOND TO NEXT INCREMENT(N)	1000000.
FRACTURE STRENGTH OF STICK PROPELLANT IN PROGRESSIVE FRACTURE OPTION(MPA)	0.0
PERFORATION RELAXATION TIME(MSEC)	0.000

CONFIGURATION OF REAR OF BAG

AXIAL POS (CM)	RADIAL POS (CM)	THICKNESS (CM)	FLOW RES. DATA	REACTIVITY DATA	NO. PTS PRE-ASSIGNED	DATA (0=D, 1=N)
0.000	0.000	.320	0	0	0	0
0.000	2.540	.320	1	220	0	0
0.000	7.940	.320	0	0	0	0

CONFIGURATION OF FRONT OF BAG

AXIAL POS (CM)	RADIAL POS (CM)	THICKNESS (CM)	FLOW RES. DATA	REACTIVITY DATA	NO. PTS PRE-ASSIGNED	DATA (0=D, 1=N)
2.860	0.000	0.000	0	0	0	0
2.860	2.540	0.000	0	0	0	0
2.860	7.940	0.000	0	0	0	0

CONFIGURATION OF INSIDE OF BAG

AXIAL POS (CM)	RADIAL POS (CM)	THICKNESS (CM)	FLOW RES. DATA	REACTIVITY DATA	NO. PTS PRE-ASSIGNED	DATA (0=D, 1=N)
0.000	0.000	0.000	0	0	0	0
2.860	0.000	0.000	0	0	0	0

CONFIGURATION OF OUTSIDE OF BAG

AXIAL POS (CM)	RADIAL POS (CM)	THICKNESS (CM)	FLOW RES. DATA	REACTIVITY DATA	NO. PTS PRE-ASSIGNED	DATA (0=D, 1=N)
0.000	7.940	.320	3	220	0	0
2.860	7.940	.320	0	0	0	0

PROPERTIES OF BAG NUMBER 2

MAIN CHARGE PROPELLANT TYPE	2
CENTERCORE IGNITER PROPELLANT TYPE	0
REAR BASEPAD REACTIVITY DATA	0
FORWARD BASEPAD REACTIVITY DATA	0
REAR OF CENTERCORE PERMITS SOLID EFFLUX (1=YES, 0=NO)	0
FRONT OF CENTERCORE PERMITS SOLID EFFLUX (1=YES, 0=NO)	0
STRONG BAG OPTION (1=YES, 0=NO)	0
CASE IS RIGIDIZED (1=YES, 0=NO)	1
PROGRESSIVE FRACTURE OPTION(0=NO, 1,2=YES)	0
FINAL MAIN CHARGE PROPELLANT TYPE	0
INCREMENT IS IGNITER(0=NO, 1=YES)	0
MASS OF MAIN CHARGE(KG)	12.7000
INITIAL POROSITY OF MAIN CHARGE(-)	0.0000
MASS OF CENTERCORE CHARGE(KG)	0.0000
INITIAL POROSITY OF CENTERCORE CHARGE(-)	0.0000
INCREMENT STANDOFF(CM)	0.0000
STRENGTH OF BOND TO NEXT INCREMENT(N)	0.
FRACTURE STRENGTH OF STICK PROPELLANT IN PROGRESSIVE FRACTURE OPTION(MPA)	0.0
PERFORATION RELAXATION TIME(MSEC)	0.000

CONFIGURATION OF REAR OF BAG

AXIAL POS(CM)	RADIAL POS(CM)	THICKNESS (CM)	FLOW RES. DATA	REACTIVITY DATA	NO. PTS PRE-ASSIGNED	DATA (0=D, 1=N)
2.860	0.000	.320	2	221	0	0
2.860	2.540	.320	2	220	0	0
2.860	7.940	.320	0	0	0	0

CONFIGURATION OF FRONT OF BAG

AXIAL POS(CM)	RADIAL POS(CM)	THICKNESS (CM)	FLOW RES. DATA	REACTIVITY DATA	NO. PTS PRE-ASSIGNED	DATA (0=D, 1=N)
76.210	0.000	.320	4	330	0	0
76.210	2.540	.320	4	330	0	0
76.210	7.940	.320	0	0	0	0

CONFIGURATION OF INSIDE OF BAG

AXIAL POS(CM)	RADIAL POS(CM)	THICKNESS (CM)	FLOW RES. DATA	REACTIVITY DATA	NO. PTS PRE-ASSIGNED	DATA (0=D, 1=N)
2.860	0.000	0.000	0	0	0	0
76.210	0.000	0.000	0	0	0	0

CONFIGURATION OF OUTSIDE OF BAG

AXIAL POS(CM)	RADIAL POS(CM)	THICKNESS (CM)	FLOW RES. DATA	REACTIVITY DATA	NO. PTS PRE-ASSIGNED	DATA (0=D, 1=N)
2.860	7.940	.320	5	330	0	0
76.210	7.940	.320	0	0	0	0

CONFIGURATION OF BREECH

AXIAL POSITION(CM)	RADIAL POSITION(CM)
0.000	0.000
0.000	7.060
-3.450	8.480

CONFIGURATION OF PROJECTILE BASE

AXIAL POSITION(CM)	RADIAL POSITION(CM)
87.380	0.000
87.380	7.140
96.420	7.850

CONFIGURATION OF INSIDE BOUNDARY

AXIAL POSITION(CM)	RADIAL POSITION(CM)
0.000	0.000
87.380	0.000

CONFIGURATION OF OUTSIDE BOUNDARY

AXIAL POSITION(CM)	RADIAL POSITION(CM)
-3.450	8.480
92.460	8.050
96.420	7.850

PROPERTIES OF PROJECTILE

PROJECTILE MASS(KG)	43.170
NUMBER OF ENTRIES IN BORE RESISTANCE TABLE	7
RESISTANCE LAW NUMBER	1
N.B. IF <1 OR >3, VALUE WILL DEFAULT TO 2 INTERNALLY	
NUMBER OF FILLER ELEMENTS	0
WALL HEAT LOSS OPTION (0=IGNORE, 1=PLATE, 2=TUBE, 3=SHELTON)	0
WALL TEMPERATURE UPDATE OPTION (0=IGNORE, 1=CUBIC, 2= CUBIC PLUS INV. EMB.)	0

BORE RESISTANCE DATA

PROJECTILE TRAVEL(CM)	RESISTIVE PRESSURE(MPA)
0.000	1.720
1.016	23.100
2.540	34.100
3.937	25.000
5.207	22.400
11.430	17.200
520.700	10.300

BAG SEGMENT MECHANICAL PROPERTIES

TYPE(-)	1	2	3	4	5
RUPTURE IF BED IGNITED (0=N, 1=Y)	0	0	0	0	0
INITIAL FRICTION FACTOR(-)	101.000	10.000	101.000	101.000	101.000
MAX. PRESSURE DIFF.(MPA)	.860	.860	.860	.860	.860
RUPTURE INTERVAL(MSEC)	1.000	1.000	1.000	1.000	1.000
THICKNESS(CM)	.320	.320	.320	.320	.320
STRUCTURAL THICKNESS(CM)	.320	.320	.320	.320	.320
DENSITY OF STRUCTURAL PART (GM/CC)	1.000	1.000	1.000	1.000	1.000
LONGITUDINAL TENSILE MODULUS (MPA)	1000.000	1000.000	1000.000	1000.000	1000.000
LONGITUDINAL COMPRESSIVE MODULUS (MPA)	1000.000	1000.000	1000.000	1000.000	1000.000
POISSON RATIO(-)	.500	.500	.500	.500	.500
MAX. LONGITUDINAL STRESS(MPA)	20.680	20.680	20.680	20.680	20.680
COEFFICIENT OF FRICTION(-)	.500	.500	.500	.500	.500

DATA TO DESCRIBE REACTIVITY OF BAG SUBSTRATE 1

ENERGY RELEASED DURING DECOMPOSITION(J/GM)	1352.
DENSITY OF DECOMPOSING SOLID-PHASE(GM/CC)	1.7990
RATIO OF SPECIFIC HEATS(-)	1.2190
MOLECULAR WEIGHT(GM/GMOL)	34.8600

BAG SUBSTRATE DISCHARGE CHARACTERISTICS

TIME(MSEC)	RATE OF DISCHARGE(GM/CM**2-SEC)
0.000	1.000
.100	98.000
10.000	98.000

DATA TO DESCRIBE REACTIVITY OF BAG SUBSTRATE 2

ENERGY RELEASED DURING DECOMPOSITION(J/GM)	23 50 .
DENSITY OF DECOMPOSING SOLID-PHASE(GM/CC)	1.0000
RATIO OF SPECIFIC HEATS(-)	1.27 50
MOLECULAR WEIGHT(GM/GMOL)	21.4000

SUBSTRATE DISCHARGE CHARACTERISTICS MODELED AS IGNITION AND COMBUSTION OF PROPELLANT TYPE 3

DATA TO DESCRIBE REACTIVITY OF BAG SUBSTRATE 3

ENERGY RELEASED DURING DECOMPOSITION(J/GM)	1880 .
DENSITY OF DECOMPOSING SOLID-PHASE(GM/CC)	1.0000
RATIO OF SPECIFIC HEATS(-)	1.26 00
MOLECULAR WEIGHT(GM/GMOL)	24.0000

SUBSTRATE DISCHARGE CHARACTERISTICS MODELED AS IGNITION AND COMBUSTION OF PROPELLANT TYPE 4

LOCATION OF POINTS FOR PRESSURE SUMMARY TABLE

AXIAL LOCATION(CM)	WALL(0) OR AXIS(1)
.010	0
87.370	0

APPENDIX E

INPUT DATA FOR NOMINAL SIMULATION OF XM216 CHARGE

CONTROL PARAMETERS

NPRINT (0=NO PRINT, 1=PRINT)	1
NSUMRY (0=NO SUMMARY TABLES, 1=YES)	1
NFLOT (0=NO ISOMETRIC CARPET PLOTS, 1=PLOT)	1
NVHL (0=HIDDEN LINES DELETED, 1=RETAINED)	0
NFLCON (0=NO CONTOUR PLOTS, 1=PLOT)	0
NFLFLO (0=NO FLOW PLOTS, 1=PLOT)	1
NFLFLM (0=NO FLAMES PREAD PLOT, 1=PLOT)	1
NDSKW (0=NO DISC SAVE, 1=DISC SAVE)	0
NDSKR (0=NO DISC START, >0=DISC START AT STEP NDSKR)	0

ISOMETRICALLY PLOTTED QUANTITIES (1=YES, 0=NO)

MESH 0	POROSITY 0	GRANULAR STRESS 0
PRESSURE 1	DENSITY 0	GAS AXIAL VELOCITY 0
SOLID AXIAL VELOCITY 0	GAS RADIAL VELOCITY 0	SOLID RADIAL VELOCITY 0
GAS TEMPERATURE 0	PARTICLE SURFACE TEMPERATURE 0	
PYROLYSIS PRODUCT MASS FRACTION 0		

CONTOUR PLOTTED QUANTITIES (1=YES, 0=NO)

MESH 0	POROSITY 0	GRANULAR STRESS 0
PRESSURE 1	DENSITY 0	GAS AXIAL VELOCITY 0
SOLID AXIAL VELOCITY 0	GAS RADIAL VELOCITY 0	SOLID RADIAL VELOCITY 0
GAS TEMPERATURE 0	PARTICLE SURFACE TEMPERATURE 0	
PYROLYSIS PRODUCT MASS FRACTION 0		

SCALE FACTOR FOR PLOTTING(-)	.40
LENGTH OF Z-AXIS IN CALCOMP PLOTS(IN)	12.00
LENGTH OF R-AXIS(IN)	4.00
LENGTH OF ORDINATE AXIS(IN)	5.00

LOGOUT PARAMETERS

PARAMETERS PRIOR TO Q-2-D TRANSFORMATION

NUMBER OF STEPS BEFORE LOGOUT	5000
N.B. A NEGATIVE ENTRY FOR THE ABOVE DATUM IMPLIES THAT VARIABLE LOGOUT SCHEDULING IS INTENDED.	
TIME INCREMENT BEFORE LOGOUT(MSEC)	.5000

PARAMETERS AFTER Q-2-D TRANSFORMATION

NUMBER OF STEPS BEFORE LOGOUT	5000
TIME INCREMENT BEFORE LOGOUT(MSEC)	1.0000

SUMMARY TABLE PARAMETERS

NUMBER OF PRESSURE SUMMARY STATIONS	2
TIME INCREMENT FOR PRESSURE SUMMARY STORAGE (MSEC)	.200
DEBUG PRINT REQUIRED (0=NO, 1=YES)	0
EXTENDED PRINT REQUIRED (0=NO, 1=YES)	0

TERMINATION PARAMETERS

MAXIMUM NUMBER OF STEPS BEFORE TERMINATION	2500
MAXIMUM INTEGRATION TIME (MSEC)	25.0000
MAXIMUM PROJECTILE TRAVEL (CM)	520.7

CHARGE REPRESENTATION PARAMETERS

NUMBER OF PROPELLANTS IN CHARGE	5
NUMBER OF BAGS IN CHARGE	4
MESH ALLOCATION MODE (0=STATIC, 1=DYNAMIC)	0
MAXIMUM NUMBER OF STORAGE POINTS FOR DYNAMIC MESH ALLOCATION	0
NUMBER OF MESH POINTS IN AXIAL DIRECTION	31
NUMBER OF MESH POINTS IN RADIAL DIRECTION	7
NUMBER OF ITERATIONS TO DETERMINE INITIAL MESH	200
EQUIPOTENTIAL (0) OR LAGRANGIAN (1) MESH	0
QUASI-TWO-DIMENSIONAL FLAMES PREADING (0=NO, 1=YES)	0
NEW(0) OR OLD (1) INTERPHASE DRAG AND HEAT TRANSFER FOR GRANULAR PROPELLANT	1
BED IGNITION RUPTURES CASE (0=NO, 1=YES) (GLOBAL OPTION)	1
SAFETY FACTOR FOR C-F-L CRITERION	1.1000
MAXIMUM FRACTIONAL DISPLACEMENT FOR CON- VERGENCE OF INITIAL MESH DISTRIBUTION	.100E-04
OVER-RELAXATION FACTOR FOR DETERMINATION OF INITIAL MESH DISTRIBUTION	1.600
PRESSURE TOLERANCE FACTOR FOR REDUCTION TO QUASI-TWO-DIMENSIONAL REPRESENTATION(-)	.050
AXIAL SPATIAL RESOLUTION FACTOR(-)	.100
RADIAL SPATIAL RESOLUTION FACTOR(-)	.100
SOURCE STABILITY FACTOR (-)	0.000
MAX. FRACT. OF TUBE FOR CENTERCORE IN Q2D(-)	0.000

AMBIENT CONDITIONS

INITIAL TEMPERATURE(DEG.K)	294.4
INITIAL PRESSURE(MPA)	.1014
INITIAL RATIO OF SPECIFIC HEATS(-)	1.40000
INITIAL MOLECULAR WEIGHT(GM/GM-MOL)	29.00000

PROPERTIES OF PROPELLANT TYPE 1 CBI

SOLID PHASE CONSTITUTIVE DATA

SETTLING POROSITY OF GRANULAR BED(-)	1.00000
SPEED OF COMPRESSION WAVE(M/SEC)	1270.0
SPEED OF EXPANSION WAVE(M/SEC)	1270.0
DENSITY OF SOLID PHASE(GM/CC)	1.6500
THERMAL CONDUCTIVITY(J/CM-SEC-DEG.K)	.160000E-02
THERMAL DIFFUSIVITY(CM**2/SEC)	.600000E-03
LONGITUDINAL WAVE SPEED(M/SEC)	0.0
(STICK PROPELLANT ONLY)	
POISSON RATIO(-)	0.000
(STICK PROPELLANT ONLY)	

GAS PHASE CONSTITUTIVE DATA

RATIO OF SPECIFIC HEATS(-)	1.23400
MOLECULAR WEIGHT(GM/GM-MOL)	24.200
COVOLUME(CC/GM)	1.097

SOLID PHASE COMBUSTION CHARACTERISTICS

NUMBER OF BURN RATE DATA	1
EROSIVE EFFECT CONSIDERED (0=NO, 1=YES)	0
FINITE RATE CHEMISTRY (0=NO, 1=YES)	0
IGNITION TEMPERATURE(DEG.K)	300.0
CHEMICAL ENERGY(J/GM)	4372.
SURFACE FLAMESPREAD DELAY(MSEC)	0.0000
EROSIVE PRE-EXPONENT(CM**2-DEG.K/N)	0.
EROSIVE EXPONENT(-)	0.000
FRACTION OF ENERGY RELEASED AT SURFACE(-)	0.000
GAS-PHASE ARRHENIUS PRE-EXPONENT ((GM/CC)**(1-N)/SEC)	0.
GAS-PHASE ARRHENIUS EXPONENT(J/GM-MOL)	0.0
GAS-PHASE REACTION ORDER(-)	0.000
RATIO OF SPECIFIC HEATS OF FINAL PRODUCTS(-)	0.00000
MOLECULAR WEIGHT OF FINAL PRODUCTS(GM/GM-MOL)	0.000

MAX. PRESSURE (MPA)	BURN RATE ADDITIVE CONSTANT (CM/SEC)	PRE-EXPONENT (CM/SEC-MPA**BN)	EXPONENT (-)
690.00	0.00000	.40000	1.00000

GRAIN GEOMETRY

FORM (0=CYLINDER, 1=SPHERE, 2=SOLID STICK, 3=PERFORATED OR SLOTTED STICK)	0
EXTERNAL DIAMETER(CM)	.071
LENGTH(CM)	.013
DIAMETER OF PERFORATIONS(CM)	0.000
NUMBER OF PERFORATIONS(-)	0.
SLOT WIDTH(CM)	0.000
MAX. PERF. STRESS OR OVERPRESSURE(MPA)	0.000
NXSTR (IF 0, ABOVE VALUE IS HOOP STRESS. IF 1, VALUE IS OVERPRESSURE)	0

PROPERTIES OF PROPELLANT TYPE 2 M31

SOLID PHASE CONSTITUTIVE DATA

SETTLING POROSITY OF GRANULAR BED(-)	0.00000
SPEED OF COMPRESSION WAVE(M/SEC)	152.4
SPEED OF EXPANSION WAVE(M/SEC)	1270.0
DENSITY OF SOLID PHASE(GM/CC)	1.6500
THERMAL CONDUCTIVITY(J/CM-SEC-DEG.K)	.160100E-02
THERMAL DIFFUSIVITY(CM**2/ SEC)	.645200E-03
LONGITUDINAL WAVE SPEED(M/SEC)	1270.0
(STICK PROPELLANT ONLY)	
POISSON RATIO(-)	.500
(STICK PROPELLANT ONLY)	

GAS PHASE CONSTITUTIVE DATA

RATIO OF SPECIFIC HEATS(-)	1.26000
MOLECULAR WEIGHT(GM/GM-MOL)	22.200
COVOLUME(CC/GM)	1.084

SOLID PHASE COMBUSTION CHARACTERISTICS

NUMBER OF BURN RATE DATA	1
EROSIVE EFFECT CONSIDERED (0=NO, 1=YES)	0
FINITE RATE CHEMISTRY (0=NO, 1=YES)	0
IGNITION TEMPERATURE(DEG.K)	445.0
CHEMICAL ENERGY(J/GM)	3794.
SURFACE FLAMESREAD DELAY(MSEC)	0.0000
EROSIVE PRE-EXPONENT(CM**2-DEG.K/N)	0.
EROSIVE EXPONENT(-)	0.000
FRACTION OF ENERGY RELEASED AT SURFACE(-)	0.000
GAS-PHASE ARRHENIUS PRE-EXPONENT ((GM/CC)**(1-N)/SEC)	0.
GAS-PHASE ARRHENIUS EXPONENT(J/GM-MOL)	0.0
GAS-PHASE REACTION ORDER(-)	0.000
RATIO OF SPECIFIC HEATS OF FINAL PRODUCTS(-)	0.00000
MOLECULAR WEIGHT OF FINAL PRODUCTS(GM/GM-MOL)	0.000

MAX PRESSURE (MPA)	BURN RATE ADDITIVE CONSTANT (CM/SEC)	PRE-EXPONENT (CM/SEC-MPA**BN)	EXPONENT (-)
690.00	0.00000	.23672	.70000

GRAIN GEOMETRY

FORM (0-CYLINDER, 1-SPHERE, 2-SOLID STICK, 3-PERFORATED OR SLOTTED STICK)	3
EXTERNAL DIAMETER(CM)	.399
LENGTH(CM)	22.451
DIAMETER OF PERFORATIONS(CM)	.152
NUMBER OF PERFORATIONS(-)	1.
SLOT WIDTH(CM)	.025
MAX. PERF. STRESS OR OVERPRESSURE(MPA)	-1000.000
NXSTR (IF 0, ABOVE VALUE IS HOOP STRESS. IF 1, VALUE IS OVERPRESSURE)	0

PROPERTIES OF PROPELLANT TYPE 3 M31

SOLID PHASE CONSTITUTIVE DATA

SETTLING POROSITY OF GRANULAR BED(-)	0.00000
SPEED OF COMPRESSION WAVE(M/SEC)	152.4
SPEED OF EXPANSION WAVE(M/SEC)	1270.0
DENSITY OF SOLID PHASE(GM/CC)	1.6500
THERMAL CONDUCTIVITY(J/CM-SEC-DEG.K)	.160100E-02
THERMAL DIFFUSIVITY(CM**2/SEC)	.645200E-03
LONGITUDINAL WAVE SPEED(M/SEC)	1270.0
(STICK PROPELLANT ONLY)	
POISSON RATIO(-)	.500
(STICK PROPELLANT ONLY)	

GAS PHASE CONSTITUTIVE DATA

RATIO OF SPECIFIC HEATS(-)	1.26000
MOLECULAR WEIGHT(GM/GM-MOL)	22.200
COVOLUME(CC/GM)	1.084

SOLID PHASE COMBUSTION CHARACTERISTICS

NUMBER OF BURN RATE DATA	1
EROSIVE EFFECT CONSIDERED (0=NO, 1=YES)	0
FINITE RATE CHEMISTRY (0=NO, 1=YES)	0
IGNITION TEMPERATURE(DEG.K)	445.0
CHEMICAL ENERGY(J/GM)	3794.
SURFACE FLAMESPREAD DELAY(MSEC)	0.0000
EROSIVE PRE-EXPONENT(CM**2-DEG.K/N)	0.
EROSIVE EXPONENT(-)	0.000
FRACTION OF ENERGY RELEASED AT SURFACE(-)	0.000
GAS-PHASE ARRHENIUS PRE-EXPONENT ((GM/CC)**(1-N)/SEC)	0.
GAS-PHASE ARRHENIUS EXPONENT(J/GM-MOL)	0.0
GAS-PHASE REACTION ORDER(-)	0.000
RATIO OF SPECIFIC HEATS OF FINAL PRODUCTS(-)	0.00000
MOLECULAR WEIGHT OF FINAL PRODUCTS(GM/GM-MOL)	0.000

MAX. PRESSURE (MPA)	BURN RATE ADDITIVE CONSTANT (CM/SEC)	PRE-EXPONENT (CM/SEC-MPA**BN)	EXPONENT (-)
690.00	0.00000	.23672	.70000

GRAIN GEOMETRY

FORM (0=CYLINDER, 1=SPHERE, 2=SOLID STICK, 3=PERFORATED OR SLOTTED STICK)	3
EXTERNAL DIAMETER(CM)	.498
LENGTH(CM)	16.358
DIAMETER OF PERFORATIONS(CM)	.175
NUMBER OF PERFORATIONS(-)	1.
SLOT WIDTH(CM)	.025
MAX. PERF. STRESS OR OVERPRESSURE(MPA)	-1000.000
NXSTR (IF 0, ABOVE VALUE IS HOOP STRESS. IF 1, VALUE IS OVERPRESSURE)	0

PROPERTIES OF PROPELLANT TYPE 4 M31

SOLID PHASE CONSTITUTIVE DATA

SETTLING POROSITY OF GRANULAR BED(-)	0.00000
SPEED OF COMPRESSION WAVE(M/SEC)	152.4
SPEED OF EXPANSION WAVE(M/SEC)	1270.0
DENSITY OF SOLID PHASE(GM/CC)	1.6500
THERMAL CONDUCTIVITY(J/CM-SEC-DEG.K)	.160100E-02
THERMAL DIFFUSIVITY(CM**2/ SEC)	.645200E-03
LONGITUDINAL WAVE SPEED(M/SEC)	1270.0
(STICK PROPELLANT ONLY)	
POISSON RATIO(-)	.500
(STICK PROPELLANT ONLY)	

GAS PHASE CONSTITUTIVE DATA

RATIO OF SPECIFIC HEATS(-)	1.26000
MOLECULAR WEIGHT(GM/GM-MOL)	22.200
COVOLUME(CC/GM)	1.084

SOLID PHASE COMBUSTION CHARACTERISTICS

NUMBER OF BURN RATE DATA	1
EROSIVE EFFECT CONSIDERED (0=NO, 1=YES)	0
FINITE RATE CHEMISTRY (0=NO, 1=YES)	0
IGNITION TEMPERATURE(DEG.K)	445.0
CHEMICAL ENERGY(J/GM)	3794.
SURFACE FLAMESPREAD DELAY(MSEC)	0.0000
EROSIVE PRE-EXPONENT(CM**2-DEG.K/N)	0.
EROSIVE EXPONENT(-)	0.000
FRACTION OF ENERGY RELEASED AT SURFACE(-)	0.000
GAS-PHASE ARRHENIUS PRE-EXPONENT ((GM/CC)**(1-N)/SEC)	0.
GAS-PHASE ARRHENIUS EXPONENT(J/GM-MOL)	0.0
GAS-PHASE REACTION ORDER(-)	0.000
RATIO OF SPECIFIC HEATS OF FINAL PRODUCTS(-)	0.00000
MOLECULAR WEIGHT OF FINAL PRODUCTS(GM/GM-MOL)	0.000

MAX. PRESSURE (MPA)	BURN RATE ADDITIVE CONSTANT (CM/SEC)	PRE-EXPONENT (CM/SEC-MPA**BN)	EXPONENT (-)
690.00	0.00000	.23672	.70000

GRAIN GEOMETRY

FORM (0=CYLINDER, 1=SPHERE, 2=SOLID STICK, 3=PERFORATED OR SLOTTED STICK)	3
EXTERNAL DIAMETER(CM)	.498
LENGTH(CM)	16.358
DIAMETER OF PERFORATIONS(CM)	.175
NUMBER OF PERFORATIONS(-)	1.
SLOT WIDTH(CM)	.025
MAX. PERF. STRESS OR OVERPRESSURE(MPA)	-1000.000
NXSTR (IF 0, ABOVE VALUE IS HOOP STRESS. IF 1, VALUE IS OVERPRESSURE)	0

PROPERTIES OF PROPELLANT TYPE 5 72% NC CASE

SOLID PHASE CONSTITUTIVE DATA

SETTLING POROSITY OF GRANULAR BED(-)	0.00000
SPEED OF COMPRESSION WAVE(M/SEC)	152.4
SPEED OF EXPANSION WAVE(M/SEC)	1270.0
DENSITY OF SOLID PHASE(GM/CC)	1.0000
THERMAL CONDUCTIVITY(J/CM-SEC-DEG.K)	.160000E-02
THERMAL DIFFUSIVITY(CM**2/ SEC)	.600000E-03
LONGITUDINAL WAVE SPEED(M/SEC)	0.0
(STICK PROPELLANT ONLY)	
POISSON RATIO(-)	0.000
(STICK PROPELLANT ONLY)	

GAS PHASE CONSTITUTIVE DATA

RATIO OF SPECIFIC HEATS(-)	1.27500
MOLECULAR WEIGHT(GM/GM-MOL)	21.400
COVOLUME(CC/GM)	1.180

SOLID PHASE COMBUSTION CHARACTERISTICS

NUMBER OF BURN RATE DATA	1
EROSIVE EFFECT CONSIDERED (0=NO, 1=YES)	0
FINITE RATE CHEMISTRY (0=NO, 1=YES)	0
IGNITION TEMPERATURE(DEG.K)	300.0
CHEMICAL ENERGY(J/GM)	2350.
SURFACE FLAMES PREAD DELAY(MSEC)	0.0000
EROSIVE PRE-EXPONENT(CM**2-DEG.K/N)	0.
EROSIVE EXPONENT(-)	0.000
FRACTION OF ENERGY RELEASED AT SURFACE(-)	0.000
GAS-PHASE ARRHENIUS PRE-EXPONENT ((GM/CC)**(1-N)/SEC)	0.
GAS-PHASE ARRHENIUS EXPONENT(J/GM-MOL)	0.0
GAS-PHASE REACTION ORDER(-)	0.000
RATIO OF SPECIFIC HEATS OF FINAL PRODUCTS(-)	0.00000
MOLECULAR WEIGHT OF FINAL PRODUCTS(GM/GM-MOL)	0.000

MAX. PRESSURE (MPA)	BURN RATE ADDITIVE CONSTANT (CM/SEC)	PRE-EXPONENT (CM/SEC-MPA**BN)	EXPONENT (-)
690.00	0.00000	.04000	1.28700

GRAIN GEOMETRY

FORM (0=CYLINDER, 1=SPHERE, 2=SOLID STICK, 3=PERFORATED OR SLOTTED STICK)	0
EXTERNAL DIAMETER(CM)	0.000
LENGTH(CM)	0.000
DIAMETER OF PERFORATIONS(CM)	0.000
NUMBER OF PERFORATIONS(-)	0.
SLOT WIDTH(CM)	0.000
MAX. PERF. STRESS OR OVERPRESSURE(MPA)	0.000
NXSTR (IF 0, ABOVE VALUE IS HOOP STRESS. IF 1, VALUE IS OVERPRESSURE)	0

PROPERTIES OF BAG NUMBER 1

MAIN CHARGE PROPELLANT TYPE	1
CENTERCORE IGNITER PROPELLANT TYPE	0
REAR BASEPAD REACTIVITY DATA	0
FORWARD BASEPAD REACTIVITY DATA	0
REAR OF CENTERCORE PERMITS SOLID EFFLUX (1=YES, 0=NO)	0
FRONT OF CENTERCORE PERMITS SOLID EFFLUX (1=YES, 0=NO)	0
STRONG BAG OPTION (1=YES, 0=NO)	0
CASE IS RIGIDIZED (1=YES, 0=NO)	1
PROGRESSIVE FRACTURE OPTION (0=NO, 1,2=YES)	0
FINAL MAIN CHARGE PROPELLANT TYPE	0
INCREMENT IS IGNITER (0=NO, 1=YES)	1
MASS OF MAIN CHARGE(KG)	.0283
INITIAL POROSITY OF MAIN CHARGE(-)	0.0000
MASS OF CENTERCORE CHARGE(KG)	0.0000
INITIAL POROSITY OF CENTERCORE CHARGE(-)	0.0000
INCREMENT STANDOFF(CM)	2.5400
STRENGTH OF BOND TO NEXT INCREMENT(N)	1000000.
FRACTURE STRENGTH OF STICK PROPELLANT IN PROGRESSIVE FRACTURE OPTION(MPA)	0.0
PERFORATION RELAXATION TIME(MSEC)	0.000

CONFIGURATION OF REAR OF BAG

AXIAL POS(CM)	RADIAL POS(CM)	THICKNESS (CM)	FLOW RES. DATA	REACTIVITY DATA	NO. PTS PRE-ASSIGNED	DATA (0=D, 1=N)
0.000	0.000	.200	0	0	0	0
0.000	2.540	.200	1	220	0	0
0.000	7.300	.200	0	0	0	0

CONFIGURATION OF FRONT OF BAG

AXIAL POS(CM)	RADIAL POS(CM)	THICKNESS (CM)	FLOW RES. DATA	REACTIVITY DATA	NO. PTS PRE-ASSIGNED	DATA (0=D, 1=N)
2.980	0.000	0.000	0	0	0	0
2.980	2.540	0.000	0	0	0	0
2.980	7.300	0.000	0	0	0	0

CONFIGURATION OF INSIDE OF BAG

AXIAL POS(CM)	RADIAL POS(CM)	THICKNESS (CM)	FLOW RES. DATA	REACTIVITY DATA	NO. PTS PRE-ASSIGNED	DATA (0=D, 1=N)
0.000	0.000	0.000	0	0	0	0
2.980	0.000	0.000	0	0	0	0

CONFIGURATION OF OUTSIDE OF BAG

AXIAL POS(CM)	RADIAL POS(CM)	THICKNESS (CM)	FLOW RES. DATA	REACTIVITY DATA	NO. PTS PRE-ASSIGNED	DATA (0=D,1=N)
0.000	7.300	.200	3	220	10	0
2.980	7.300	.200	0	0	0	0

PROPERTIES OF BAG NUMBER 2

MAIN CHARGE PROPELLANT TYPE	2
CENTERCORE IGNITER PROPELLANT TYPE	0
REAR BASEPAD REACTIVITY DATA	0
FORWARD BASEPAD REACTIVITY DATA	0
REAR OF CENTERCORE PERMITS SOLID EFFLUX (1=YES, 0=NO)	0
FRONT OF CENTERCORE PERMITS SOLID EFFLUX (1=YES, 0=NO)	0
STRONG BAG OPTION (1=YES, 0=NO)	0
CASE IS RIGIDIZED (1=YES, 0=NO)	1
PROGRESSIVE FRACTURE OPTION (0=NO, 1,2=YES)	0
FINAL MAIN CHARGE PROPELLANT TYPE	0
INCREMENT IS IGNITER (0=NO, 1=YES)	0
MASS OF MAIN CHARGE(KG)	2.7200
INITIAL POROSITY OF MAIN CHARGE(-)	0.0000
MASS OF CENTERCORE CHARGE(KG)	0.0000
INITIAL POROSITY OF CENTERCORE CHARGE(-)	0.0000
INCREMENT STANDOFF(CM)	0.0000
STRENGTH OF BOND TO NEXT INCREMENT(N)	10.
FRACTURE STRENGTH OF STICK PROPELLANT IN PROGRESSIVE FRACTURE OPTION(MPA)	0.0
PERFORATION RELAXATION TIME(MSEC)	0.000

CONFIGURATION OF REAR OF BAG

AXIAL POS(CM)	RADIAL POS(CM)	THICKNESS (CM)	FLOW RES. DATA	REACTIVITY DATA	NO. PTS PRE-ASSIGNED	DATA (0=D,1=N)
2.980	0.000	.200	2	221	0	0
2.980	2.540	.200	2	220	0	0
2.980	7.300	.200	0	0	0	0

CONFIGURATION OF FRONT OF BAG

AXIAL POS(CM)	RADIAL POS(CM)	THICKNESS (CM)	FLOW RES. DATA	REACTIVITY DATA	NO. PTS PRE-ASSIGNED	DATA (0=D,1=N)
26.670	0.000	.200	4	220	0	0
26.670	2.540	.200	4	220	0	0
26.670	7.300	.200	0	0	0	0

CONFIGURATION OF INSIDE OF BAG

AXIAL POS(CM)	RADIAL POS(CM)	THICKNESS (CM)	FLOW RES. DATA	REACTIVITY DATA	NO. PTS PRE-ASSIGNED	DATA (0=D, 1=N)
2.980	0.000	0.000	0	0	10	0
26.670	0.000	0.000	0	0	0	0

CONFIGURATION OF OUTSIDE OF BAG

AXIAL POS(CM)	RADIAL POS(CM)	THICKNESS (CM)	FLOW RES. DATA	REACTIVITY DATA	NO. PTS PRE-ASSIGNED	DATA (0=D, 1=N)
2.980	7.300	.200	3	220	10	0
26.670	7.300	.200	0	0	0	0

PROPERTIES OF BAG NUMBER 3

MAIN CHARGE PROPELLANT TYPE	3
CENTERCORE IGNITER PROPELLANT TYPE	0
REAR BASEPAD REACTIVITY DATA	0
FORWARD BASEPAD REACTIVITY DATA	0
REAR OF CENTERCORE PERMITS SOLID EFFLUX (1=YES, 0=NO)	0
FRONT OF CENTERCORE PERMITS SOLID EFFLUX (1=YES, 0=NO)	0
STRONG BAG OPTION (1=YES, 0=NO)	0
CASE IS RIGIDIZED (1=YES, 0=NO)	1
PROGRESSIVE FRACTURE OPTION (0=NO, 1,2=YES)	0
FINAL MAIN CHARGE PROPELLANT TYPE	0
INCREMENT IS IGNITER (0=NO, 1=YES)	0
MASS OF MAIN CHARGE(KG)	2.8600
INITIAL POROSITY OF MAIN CHARGE(-)	0.0000
MASS OF CENTERCORE CHARGE(KG)	0.0000
INITIAL POROSITY OF CENTERCORE CHARGE(-)	0.0000
INCREMENT STANDOFF(CM)	0.0000
STRENGTH OF BOND TO NEXT INCREMENT(N)	10.
FRACTURE STRENGTH OF STICK PROPELLANT IN PROGRESSIVE FRACTURE OPTION(MPA)	0.0
PERFORATION RELAXATION TIME(MSEC)	0.000

CONFIGURATION OF REAR OF BAG

AXIAL POS(CM)	RADIAL POS(CM)	THICKNESS (CM)	FLOW RES. DATA	REACTIVITY DATA	NO. PTS PRE-ASSIGNED	DATA (0=D, 1=N)
26.670	0.000	.200	4	220	0	0
26.670	2.540	.200	4	220	0	0
26.670	7.300	.200	0	0	0	0

CONFIGURATION OF FRONT OF BAG

AXIAL POS(CM)	RADIAL POS(CM)	THICKNESS (CM)	FLOW RES. DATA	REACTIVITY DATA	NO. PTS PRE-ASSIGNED	DATA (0=D, 1=N)
43.820	0.000	.200	4	220	0	0
43.820	2.540	.200	4	220	0	0
43.820	7.300	.200	0	0	0	0

CONFIGURATION OF INSIDE OF BAG

AXIAL POS(CM)	RADIAL POS(CM)	THICKNESS (CM)	FLOW RES. DATA	REACTIVITY DATA	NO. PTS PRE-ASSIGNED	DATA (0=D, 1=N)
26.670	0.000	0.000	0	0	6	0
43.820	0.000	0.000	0	0	0	0

CONFIGURATION OF OUTSIDE OF BAG

AXIAL POS(CM)	RADIAL POS(CM)	THICKNESS (CM)	FLOW RES. DATA	REACTIVITY DATA	NO. PTS PRE-ASSIGNED	DATA (0=D, 1=N)
26.670	7.300	.200	3	220	6	0
43.820	7.300	.200	0	0	0	0

PROPERTIES OF BAG NUMBER 4

MAIN CHARGE PROPELLANT TYPE	4
CENTERCORE IGNITER PROPELLANT TYPE	0
REAR BASEPAD REACTIVITY DATA	0
FORWARD BASEPAD REACTIVITY DATA	0
REAR OF CENTERCORE PERMITS SOLID EFFLUX (1=YES, 0=NO)	0
FRONT OF CENTERCORE PERMITS SOLID EFFLUX (1=YES, 0=NO)	0
STRONG BAG OPTION (1=YES, 0=NO)	0
CASE IS RIGIDIZED (1=YES, 0=NO)	1
PROGRESSIVE FRACTURE OPTION (0=NO, 1,2=YES)	0
FINAL MAIN CHARGE PROPELLANT TYPE	0
INCREMENT IS IGNITER (0=NO, 1=YES)	0
MASS OF MAIN CHARGE(KG)	2.8600
INITIAL POROSITY OF MAIN CHARGE(-)	0.0000
MASS OF CENTERCORE CHARGE(KG)	0.0000
INITIAL POROSITY OF CENTERCORE CHARGE(-)	0.0000
INCREMENT STANDOFF(CM)	0.0000
STRENGTH OF BOND TO NEXT INCREMENT(N)	0.
FRACTURE STRENGTH OF STICK PROPELLANT IN PROGRESSIVE FRACTURE OPTION(MPA)	0.0
PERFORATION RELAXATION TIME(MSEC)	0.000

CONFIGURATION OF REAR OF BAG

AXIAL POS(CM)	RADIAL POS(CM)	THICKNESS (CM)	FLOW RES. DATA	REACTIVITY DATA	NO. PTS PRE-ASSIGNED	DATA (0=D, 1=N)
43.820	0.000	.200	4	220	0	0
43.820	2.540	.200	4	220	0	0
43.820	7.300	.200	0	0	0	0

CONFIGURATION OF FRONT OF BAG

AXIAL POS(CM)	RADIAL POS(CM)	THICKNESS (CM)	FLOW RES. DATA	REACTIVITY DATA	NO. PTS PRE-ASSIGNED	DATA (0=D, 1=N)
60.970	0.000	.200	4	220	0	0
60.970	2.540	.200	4	220	0	0
60.970	7.300	.200	0	0	0	0

CONFIGURATION OF INSIDE OF BAG

AXIAL POS(CM)	RADIAL POS(CM)	THICKNESS (CM)	FLOW RES. DATA	REACTIVITY DATA	NO. PTS PRE-ASSIGNED	DATA (0=D, 1=N)
43.820	0.000	0.000	0	0	6	0
60.970	0.000	0.000	0	0	0	0

CONFIGURATION OF OUTSIDE OF BAG

AXIAL POS(CM)	RADIAL POS(CM)	THICKNESS (CM)	FLOW RES. DATA	REACTIVITY DATA	NO. PTS PRE-ASSIGNED	DATA (0=D, 1=N)
43.820	7.300	.200	3	220	6	0
60.970	7.300	.200	0	0	0	0

CONFIGURATION OF BREECH

AXIAL POSITION(CM)	RADIAL POSITION(CM)
0.000	0.000
0.000	7.060
-3.450	8.480

CONFIGURATION OF PROJECTILE BASE

AXIAL POSITION(CM)	RADIAL POSITION(CM)
87.380	0.000
87.380	7.140
96.420	7.850

CONFIGURATION OF INSIDE BOUNDARY

AXIAL POSITION(CM)	RADIAL POSITION(CM)
0.000	0.000
87.380	0.000

CONFIGURATION OF OUTSIDE BOUNDARY

AXIAL POSITION(CM)	RADIAL POSITION(CM)
-3.450	8.480
92.460	8.050
96.420	7.850

PROPERTIES OF PROJECTILE

PROJECTILE MASS(KG)	43.170
NUMBER OF ENTRIES IN BORE RESISTANCE TABLE	7
RESISTANCE LAW NUMBER	1
N.B. IF <1 OR >3, VALUE WILL DEFAULT TO 2 INTERNALLY	
NUMBER OF FILLER ELEMENTS	0
WALL HEAT LOSS OPTION (0=IGNORE, 1=PLATE, 2=TUBE, 3=SHELTON)	0
WALL TEMPERATURE UPDATE OPTION (0=IGNORE, 1=CUBIC, 2=CUBIC PLUS INV. EMB.)	0

BORE RESISTANCE DATA

PROJECTILE TRAVEL(CM)	RESISTIVE PRESSURE(MPA)
0.000	1.720
1.016	23.100
2.540	34.100
3.937	25.000
5.207	22.400
11.430	17.200
520.700	10.300

BAG SEGMENT MECHANICAL PROPERTIES

TYPE(-)	1	2	3	4
RUPTURE IF BED IGNITED (0=N, 1=Y)	0	0	0	0
INITIAL FRICTION FACTOR(-)	101.000	10.000	101.000	101.000
MAX. PRESSURE DIFF.(MPA)	.860	.860	.860	.860
RUPTURE INTERVAL(MSEC)	1.000	1.000	1.000	1.000
THICKNESS(CM)	.200	.200	.200	.200
STRUCTURAL THICKNESS(CM)	.200	.200	.200	.200
DENSITY OF STRUCTURAL PART (GM/CC)	1.000	1.000	1.000	1.000
LONGITUDINAL TENSILE MODULUS (MPA)	1000.000	1000.000	1000.000	1000.000
LONGITUDINAL COMPRESSIVE MODULUS(MPA)	1000.000	1000.000	1000.000	1000.000
POISSON RATIO(-)	.500	.500	.500	.500
MAX. LONGITUDINAL STRESS(MPA)	20.680	20.680	20.680	20.680
COEFFICIENT OF FRICTION(-)	.500	.500	.500	.500

DATA TO DESCRIBE REACTIVITY OF BAG SUBSTRATE 1

ENERGY RELEASED DURING DECOMPOSITION(J/GM)	1352.
DENSITY OF DECOMPOSING SOLID-PHASE(GM/CC)	1.7990
RATIO OF SPECIFIC HEATS(-)	1.2190
MOLECULAR WEIGHT(GM/GMOL)	34.8600

BAG SUBSTRATE DISCHARGE CHARACTERISTICS

TIME(MSEC)	RATE OF DISCHARGE(GM/CM**2-SEC)
0.000	1.000
.100	98.000
10.000	98.000

DATA TO DESCRIBE REACTIVITY OF BAG SUBSTRATE 2

ENERGY RELEASED DURING DECOMPOSITION(J/GM)	2350.
DENSITY OF DECOMPOSING SOLID-PHASE(GM/CC)	1.0000
RATIO OF SPECIFIC HEATS(-)	1.2750
MOLECULAR WEIGHT(GM/GMOL)	21.4000

SUBSTRATE DISCHARGE CHARACTERISTICS MODELED AS IGNITION AND COMBUSTION OF
PROPELLANT TYPE 5

LOCATION OF POINTS FOR PRESSURE SUMMARY TABLE

AXIAL LOCATION(CM)	WALL(0) OR AXIS(1)
.010	0
87.370	0

NOMENCLATURE

A	Cross-sectional area
E	Rate-of-strain tensor
e	Internal energy
g_0	Constant to reconcile units
I	Unit tensor
K	Friction factor associated with normal flux of gas through the container
k	Thermal conductivity
\dot{m}	Mass flux
\dot{m}_s	Surface source term
p	Pressure
q	Heat flux vector
r	Radial coordinate
t	Time
u	Velocity vector with components $u_r = v$, $u_z = u$, $u_\theta = 0$
V	Volume
z	Axial coordinate

Greek Symbols

α_i	Characteristic derivative
β	Integration parameter for implicit algorithm
β_i	Derivative of lumped parameter ullage pressure with respect to mass flux

Nomenclature continued

Δm	Percent mass defect
$\Delta \tau$	Time increment
ϵ	Porosity
ζ	Computational coordinate
η	Computational coordinate
λ	Second coefficient of viscosity
μ	First coefficient of viscosity
ξ	Computational coordinate
ρ	Density
σ	Stress tensor
σ_p	Solid-phase stress
τ	Computational time

DISTRIBUTION LIST

<u>No. Of Copies</u>	<u>Organization</u>	<u>No. Of Copies</u>	<u>Organization</u>
12	Administrator Defense Technical Info Center ATTN: DTIC-DDA Cameron Station Alexandria, VA 22304-6145	1	Commander US Army Materiel Command ATTN: AMCDRA-ST 5001 Eisenhower Avenue Alexandria, VA 22333-5001
1	Commander USA Concepts Analysis Agency ATTN: D. Hardison 8120 Woodmont Avenue Bethesda, MD 20014-2797	1	Commander US Army Materiel Command ATTN: AMCDE-DW 5001 Eisenhower Avenue Alexandria, VA 22333-5001
1	HQDA/ DAMA-ZA Washington, DC 20310-2500	5	Project Manager Cannon Artillery Weapons System, ARDC, AMCCOM ATTN: AMCPM-CW, F. Menke AMCPM-CWJ AMCPM-CWS M. Fisette AMCPM-CWA R. DeKleine H. Hassmann Dover, NJ 07801-5001
1	HQDA, DAMA-CSM, E. Lippi Washington, DC 20310-2500		
1	HQDA/SARDA Washington, DC 20310-2500		
1	Commander US Army War College ATTN: Library-FF229 Carlisle Barracks, PA 17013	2	Project Manager Munitions Production Base Modernization and Expansion ATTN: AMCPM-PBM, A. Siklosi AMCPM-PBM-E, L. Laibson Dover, NJ 07801-5001
1	US Army Ballistic Missile Defense Systems Command Advanced Technology Center P. O. Box 1500 Huntsville, AL 35807-3801	3	Project Manager Tank Main Armament System ATTN: AMCPM-TMA, K. Russell AMCPM-TMA-105 AMCPM-TMA-120 Dover, NJ 07801-5001
1	Chairman DOD Explosives Safety Board Room 856-C Hoffman Bldg. 1 2461 Eisenhower Avenue Alexandria, VA 22331-9999	1	Commander US Army Watervliet Arsenal ATTN: SARVV-RD, R. Thierry Watervliet, NY 12189-5001
1	Commander US Army Materiel Command ATTN: AMCPM-GQM-WF 5001 Eisenhower Avenue Alexandria, VA 22333-5001		

DISTRIBUTION LIST

<u>No. Of</u> <u>Copies</u>	<u>Organization</u>	<u>No. Of</u> <u>Copies</u>	<u>Organization</u>
20	Commander US Army ARDC, AMCCOM ATTN: SMCAR-TSS SMCAR-TDC SMCAR-LC LTC N. Barron SMCAR-LCA A. Beardell D. Downs S. Einstein S. Westley S. Bernstein C. Roller J. Rutkowski SMCAR-LCB-I D. Spring SMCAR-LCE SMCAR-LCM-E S. Kaplowitz SMCAR-LCS SMCAR-LCU-CT E. Barrieres R. Davitt SMCAR-LCU-CV C. Mandala SMCAR-LCW-A M. Salsbury SMCAR-SCA L. Stiefel B. Brodman Dover, NJ 07801-5001	1	HQDA DAMA-ART-M Washington, DC 20310-2500
		1	Director Benet Weapons Laboratory Armament R&D Center US Army AMCCOM ATTN: SMCAR-LCB-TL Watervliet, NY 12189-5001
		1	Commander US Army Aviation Research and Development Command ATTN: AMSAV-E 4300 Goodfellow Blvd. St. Louis, MO 63120-1702
		1	Commander US Army TSARCOM 4300 Goodfellow Blvd. St. Louis, MO 63120-1702
		1	Director US Army Air Mobility Research And Development Laboratory Ames Research Center Moffett Field, CA 94035-1099
1	Commander Armament R&D Center U.S. Army AMCCOM ATTN: SMCAR-TSS Dover, NJ 07801-5001	1	Commander US Army Communications - Electronics Command ATTN: AMSEL-ED Fort Monmouth, NJ 07703-5301
1	Commander Armament R&D Center U.S. Army AMCCOM ATTN: SMCAR-TDC Dover, NJ 07801	1	Commander ERADCOM Technical Library ATTN: DELSD-L (Report Section) Fort Monmouth, NJ 07703-5301
4	Commander US Army Armament Munitions and Chemical Command ATTN: SMCAR-ESP-L Rock Island, IL 61299-7300	1	Commander US Army Harry Diamond Lab. ATTN: DELHD-TA-L 2800 Powder Mill Road Adelphi, MD 20783-1145

DISTRIBUTION LIST

<u>No. Of Copies</u>	<u>Organization</u>	<u>No. Of Copies</u>	<u>Organization</u>
1	Commander US Army Missile Command ATTN: AMSMI-CM Redstone Arsenal, AL 35898-5249	2	Program Manager M1 Abrams Tank System ATTN: AMCPM-GMC-SA, T. Dean Warren, MI 48092-2498
1	Commander US Army Missile and Space Intelligence Center ATTN: AIAMS-YDL Redstone Arsenal, AL 35898-5500	1	Project Manager Fighting Vehicle Systems ATTN: AMCPM-FVS Warren, MI 48092-2498
1	Commander US Army Missile Command Research, Development, and Engineering Center ATTN: AMSMI-RD Redstone Arsenal, AL 35898-5500	1	President US Army Armor & Engineer Board ATTN: ATZK-AD-S Fort Knox, KY 40121-5200
1	Commandant US Army Aviation School ATTN: Aviation Agency Fort Rucker, AL 36360	1	Project Manager M-60 Tank Development ATTN: AMCPM-M60TD Warren, MI 48092-2498
1	Commander US Army Tank Automotive Command ATTN: AMSTA-TSL Warren, MI 48397-5000	1	Director US Army TRADOC Systems Analysis Activity ATTN: ATAA-SL White Sands Missile Range, NM 88002
1	Commander US Army Tank Automotive Command ATTN: AMSTA-OG Warren, MI 48397-5000	1	Commander US Army Training & Doctrine Command ATTN: ATCD-MA/ MAJ Williams Fort Monroe, VA 23651
1	Project Manager Improved TOW Vehicle ATTN: AMCPM-ITV US Army Tank Automotive Command Warren, MI 48397-5000	2	Commander US Army Materials and Mechanics Research Center ATTN: AMXMR-ATL Tech Library Watertown, MA 02172
		1	Commander US Army Research Office ATTN: Tech Library P. O. Box 12211 Research Triangle Park, NC 27709-2211

DISTRIBUTION LIST

<u>No. Of</u> <u>Copies</u>	<u>Organization</u>	<u>No. Of</u> <u>Copies</u>	<u>Organization</u>
1	Commander US Army Belvoir Research & Development Center ATTN: STRBE-WC Fort Belvoir, VA 22060-5606	1	Commander US Army Development and Employment Agency ATTN: MODE-TED-SAB Fort Lewis, WA 98433-5099
1	Commander US Army Logistics Mgmt Ctr Defense Logistics Studies Fort Lee, VA 23801	1	Chief of Naval Material Department of the Navy ATTN: J. Amlie Arlington, VA 20360
1	Commandant US Army Infantry School ATTN: ATSH-CD-CSO-OR Fort Benning, GA 31905	1	Office of Naval Research ATTN: Code 473, R. S. Miller 800 N. Quincy Street Arlington, VA 22217-9999
1	President US Army Artillery Board Ft. Sill, OK 73503-5600	3	Commandant US Army Armor School ATTN: ATZK-CD-MS M. Falkovitch Armor Agency Fort Knox, KY 40121-5215
1	Commandant US Army Command and General Staff College Fort Leavenworth, KS 66027	2	Commander Naval Sea Systems Command ATTN: SEA 62R SEA 64 Washington, DC 20362-5101
1	Commandant US Army Special Warfare School ATTN: Rev & Tng Lit Div Fort Bragg, NC 28307	1	Commander Naval Air Systems Command ATTN: AIR-954-Tech Lib Washington, DC 20360
3	Commander Radford Army Ammunition Plant ATTN: SMCRA-QA/HI LIB Radford, VA 24141-0298	1	Assistant Secretary of the Navy (R, E, and S) ATTN: R. Reichenbach Room 5E787 Pentagon Bldg. Washington, DC 20350
1	Commander US Army Foreign Science & Technology Center ATTN: AMXST-MC-3 220 Seventh Street, NE Charlottesville, VA 22901-5396	1	Naval Research Lab Tech Library Washington, DC 20375
2	Commandant US Army Field Artillery Center & School ATTN: ATSF-CO-MW, B. Willis Ft. Sill, OK 73503-5600		

DISTRIBUTION LIST

<u>No. Of Copies</u>	<u>Organization</u>	<u>No. Of Copies</u>	<u>Organization</u>
5	Commander Naval Surface Weapons Center ATTN: Code G33, J. L. East W. Burrell J. Johndrow Code G23, D. McClure Code DK-21 Tech Lib Dahlgren, VA 22448-5000	1	Program Manager AFOSR Directorate of Aerospace Sciences ATTN: L. H. Caveny Bolling AFB, DC 20332-0001
2	Comander US Naval Surface Weapons Center ATTN: J. P. Consaga C. Gotzmer Indian Head, MD 20640-5000	6	Commander Naval Ordnance Station ATTN: P. L. Stang J. Birkett L Torreyson T. C. Smith D. Brooks Tech Library Indian Head, MD 20640-5000
4	Commander Naval Surface Weapons Center ATTN: S. Jacobs/Code 240 Code 730 K. Kim/Code R-13 R. Bernecker Silver Spring, MD 20903-5000	1	AFSC/SDOA Andrews AFB, MD 20334
2	Commanding Officer Naval Underwater Systems Center Energy Conversion Dept. ATTN: CODE 5B331, R. S. Lazar Tech Lib Newport, RI 02840	3	AFRPL/DY, Stop 24 ATTN: J. Levine/DYCR R. Corley/DYC D. Williams/DYCC Edwards AFB, CA 93523-5000
4	Commander Naval Weapons Center ATTN: Code 388, R. L. Derr C. F. Price T. Boggs Info. Sci. Div. China Lake, CA 93555-6001	1	AFRPL/TSTL (Tech Library) Stop 24 Edwards AFB, CA 93523-5000
2	Superintendent Naval Postgraduate School Dept. of Mechanical Engineering Monterey, CA 93943-5100	1	AFATL/DLYV Eglin AFB, FL 32542-5000
		1	AFATL/DLXP Eglin AFB, FL 32542-5000
		1	AFATL/DLJE Eglin AFB, FL 32542-5000
		1	AFATL/DLODL ATTN: Tech Lib Eglin AFB, FL 32542-5000

DISTRIBUTION LISTS

<u>No. of Copies</u>	<u>Organization</u>	<u>No. of Copies</u>	<u>Organization</u>
1	NASA/Lyndon B. Johnson Space Center ATTN: NHS-22, Library Section Houston, TX 77054	10	Central Intelligence Agency Office of Central Reference Dissemination Branch Room GE-47 HQS Washington, DC 20505
1	AFEIM, the Rand Corporation ATTN: Library D (Required or 1700 Main Street Classified Santa Monica CA Only) 90401-3297	1	General Electric Company Armament Systems Dept. ATTN: M. J. Bulman, Room 1311 128 Lakeside Avenue Burlington, VT 05401-4985
1	General Applied Sciences Lab ATTN: J. Erdos Merrick & Stewart Avenues Westbury Long Isld, NY 11590	1	IITRI ATTN: M. J. Klein 10 W. 35th Street Chicago, IL 60616-3799
2	AAI Corporation ATTN: J. Hebert J. Frankle P. O. Box 6767 Baltimore, MD 21204	1	Hercules Inc. Allegheny Ballistics Laboratory ATTN: R. B. Miller P. O. Box 210 Cumberland, MD 21501-0210
1	Aerojet Ordnance Company ATTN: D. Thatcher 2521 Michelle Drive Tustin, CA 92680-7014	1	Hercules, Inc. Bacchus Works ATTN: K. P. McCarty P. O. Box 98 Magna, UT 84044-0098
1	Aerojet Solid Propulsion Co. ATTN: P. Micheli Sacramento, CA 95813	1	Hercules, Inc. Radford Army Ammunition Plant ATTN: J. Pierce Radford, VA 24141-0299
1	Atlantic Research Corporation ATTN: M. K. King 5390 Cheorokee Avenue Alexandria, VA 22312-2302	1	Honeywell, Inc. - MN64 2200 Defense Systems Division ATTN: C. Hargreaves 6110 Blue Circle Drive Minnetonka MN 55436
1	AVCO Everett Rsch Lab ATTN: D. Stickler 2385 Revere Beach Parkway Everett, MA 02149-5936	1	Lawrence Livermore National Laboratory ATTN: L-355, A. Buckingham M. Finger P. O. Box 808 Livermore, CA 94550-0622
2	Calspan Corporation ATTN: C. Morphy P. O. Box 400 Buffalo, NY 14225-0400		

DISTRIBUTION LIST

<u>No. Of Copies</u>	<u>Organization</u>	<u>No. Of Copies</u>	<u>Organization</u>
1	Lawrence Livermore National Laboratory ATTN: L-324 M. Constantino P. O. Box 808 Livermore, CA 94550-0622	3	Thiokol Corporation Huntsville Division ATTN: D. Flanigan R. Glick Tech Library Huntsville, AL 35807
1	Olin Corporation Badger Army Ammunition Plant ATTN: R. J. Thiede Baraboo, WI 53913	1	Scientific Research Assoc., Inc. ATTN: H. McDonald P.O. Box 498 Glastonbury, CT 06033-0498
1	Olin Corporation Smokeless Powder Operations ATTN: D. C. Mann P.O. Box 222 St. Marks, FL 32355-0222	1	Thiokol Corporation Wasatch Division ATTN: J. A. Peterson P. O. Box 524 Brigham City, UT 84302-0524
1	Paul Gough Associates, Inc. ATTN: P. S. Gough P. O. Box 1614, 1048 South St. Portsmouth, NH 03801-1614	2	Thiokol Corporation Elkton Division ATTN: R. Biddle Tech Lib. P. O. Box 241 Elkton, MD 21921-0241
1	Physics International Company ATTN: Library H. Wayne Wampler 2700 Merced Street San Leandro, CA 94577-5602	2	United Technologies Chemical Systems Division ATTN: R. Brown Tech Library P. O. Box 358 Sunnyvale, CA 94086-9998
1	Princeton Combustion Research Lab., Inc. ATTN: M. Summerfield 475 US Highway One Monmouth Junction, NJ 08852-9650	1	Veritay Technology, Inc. ATTN: E. Fisher 4845 Millersport Hwy. P. O. Box 305 East Amherst, NY 14051-0305
2	Rockwell International Rocketdyne Division ATTN: BA08 J. E. Flanagan J. Gray 6633 Canoga Avenue Canoga Park, CA 91303-2703	1	Universal Propulsion Company ATTN: H. J. McSpadden Black Canyon Stage 1 Box 1140 Phoenix, AZ 85029
1	Science Applications, Inc. ATTN: R. B. Edelman 23146 Cumorah Crest Drive Woodland Hills, CA 91364-3710		

DISTRIBUTION LIST

<u>No. Of</u> <u>Copies</u>	<u>Organization</u>	<u>No. Of</u> <u>Copies</u>	<u>Organization</u>
1	Battelle Memorial Institute ATTN: Tech Library 505 King Avenue Columbus, OH 43201-2693	3	Georgia Institute of Tech School of Aerospace Eng. ATTN: B. T. Zinn E. Price W. C. Strahle Atlanta, GA 30332
1	Brigham Young University Dept. of Chemical Engineering ATTN: M. Beckstead Provo, UT 84601	1	Institute of Gas Technology ATTN: D. Gidaspo 3424 S. State Street Chicago, IL 60616-3896
1	California Institute of Tech 204 Karman Lab Main Stop 301-46 ATTN: F. E. C. Culick 1201 E. California Street Pasadena, CA 91109	1	Johns Hopkins University Applied Physics Laboratory Chemical Propulsion Information Agency ATTN: T. Christian Johns Hopkins Road Laurel, MD 20707-0690
1	California Institute of Tech Jet Propulsion Laboratory ATTN: L. D. Strand 4800 Oak Grove Drive Pasadena, CA 91109-8099	1	Massachusetts Institute of Technology Dept of Mechanical Engineering ATTN: T. Toong 77 Massachusetts Avenue Cambridge, MA 02139-4307
1	University of Illinois Dept of Mech/Indust Engr ATTN: H. Krier 144 MEB; 1206 N. Green St. Urbana, IL 61801-2978	1	G. M. Faeth Pennsylvania State University Applied Research Laboratory University Park, PA 16802-7501
1	University of Massachusetts Dept. of Mechanical Engineering ATTN: K. Jakus Amherst, MA 01002-0014	1	Pennsylvania State University Dept. Of Mech. Engineering ATTN: K. Kuo University Park, PA 16802-7501
1	University of Minnesota Dept. of Mechanical Engineering ATTN: E. Fletcher Minneapolis, MN 55414-3368	1	Purdue University School of Mechanical Engineering ATTN: J. R. Osborn TSPC Chaffee Hall West Lafayette, IN 47907-1199
1	Case Western Reserve University Division of Aerospace Sciences ATTN: J. Tien Cleveland, OH 44135		

DISTRIBUTION LIST

<u>No. Of Copies</u>	<u>Organization</u>	<u>No. Of Copies</u>	<u>Organization</u>
1	SRI International Propulsion Sciences Division ATTN: Tech Library 333 Ravenswood Avenue Menlo Park, CA 94025-3493		<u>Aberdeen Proving Ground</u> Dir, USAMSAA ATTN: AMXSY-D AMXSY-MP, H. Cohen Cdr, USATECOM ATTN: AMSTE-TO-F AMSTE-CM-F, L. Nealley Cdr, CSTA ATTN: STECS-AS-H, R. Hendricksen Cdr, CRDC, AMCCOM ATTN: SMCCR-RSP-A SMCCR-MU SMCCR-SPS-IL
1	Rensselaer Polytechnic Inst. Department of Mathematics Troy, NY 12181		
2	Director Los Alamos Scientific Lab ATTN: T3, D. Butler M. Division, B. Craig P. O. Box 1663 Los Alamos, NM 87544		
1	Stevens Institute of Technology Davidson Laboratory ATTN: R. McAlevy, III Castle Point Station Hoboken, NJ 07030-5907		
1	Rutgers University Dept. of Mechanical and Aerospace Engineering ATTN: S. Temkin University Heights Campus New Brunswick, NJ 08903		
1	University of Southern California Mechanical Engineering Dept. ATTN: OHE200, M. Gerstein Los Angeles, CA 90089-5199		
2	University of Utah Dept. of Chemical Engineering ATTN: A. Baer G. Flandro Salt Lake City, UT 84112-1194		
1	Washington State University Dept. of Mechanical Engineering ATTN: C. T. Crowe Pullman, WA 99163-5201		

UNCLASSIFIED

USER EVALUATION SHEET/CHANGE OF ADDRESS

This Laboratory undertakes a continuing effort to improve the quality of the reports it publishes. Your comments/answers to the items/questions below will aid us in our efforts.

1. BRL Report Number _____ Date of Report _____
2. Date Report Received _____
3. Does this report satisfy a need? (Comment on purpose, related project, or other area of interest for which the report will be used.) _____

4. How specifically, is the report being used? (Information source, design data, procedure, source of ideas, etc.) _____

5. Has the information in this report led to any quantitative savings as far as man-hours or dollars saved, operating costs avoided or efficiencies achieved, etc? If so, please elaborate. _____

6. General Comments. What do you think should be changed to improve future reports? (Indicate changes to organization, technical content, format, etc.) _____

CURRENT ADDRESS	_____
	Name

	Organization

	Address

	City, State, Zip

7. If indicating a Change of Address or Address Correction, please provide the New or Correct Address in Block 6 above and the Old or Incorrect address below.

OLD ADDRESS	_____
	Name

	Organization

	Address

	City, State, Zip

(Remove this sheet along the perforation, fold as indicated, staple or tape closed, and mail.)

UNCLASSIFIED

UNCLASSIFIED

----- FOLD HERE -----

Director
U.S. Army Ballistic Research Laboratory
ATTN: SLCBR-DD-T
Aberdeen Proving Ground, MD 21005-5066

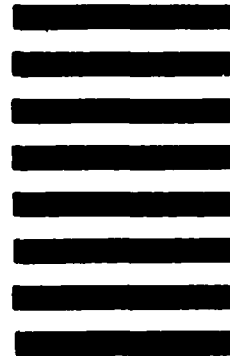


NO POSTAGE
NECESSARY
IF MAILED
IN THE
UNITED STATES

OFFICIAL BUSINESS
PENALTY FOR PRIVATE USE, \$300

BUSINESS REPLY MAIL
FIRST CLASS PERMIT NO 12062 WASHINGTON, DC
POSTAGE WILL BE PAID BY DEPARTMENT OF THE ARMY

Director
U.S. Army Ballistic Research Laboratory
ATTN: SLCBR-DD-T
Aberdeen Proving Ground, MD 21005-9989



----- FOLD HERE -----

UNCLASSIFIED

END

DTIC

9-86